

# **Search for Neutral Higgs Bosons Decaying to Pairs of $\tau$ Leptons at $\sqrt{s} = 7$ TeV**

By

EVAN KLOSE FRIIS

B.S. (University of California at San Diego) 2005

## **DISSERTATION**

Submitted in partial satisfaction of the requirements for the degree of

**DOCTOR OF PHILOSOPHY**

in

Physics

in the

**OFFICE OF GRADUATE STUDIES**

of the

**UNIVERSITY OF CALIFORNIA**

**DAVIS**

Approved:

---

Professor John Conway (Chair)

---

Professor Robin Erbacher

---

Professor Mani Tripathi

Committee in Charge

2011



---

## **3 Abstract**

4 This thesis describes a search for the Higgs boson, a new particle predicted by a theory called  
5 the Minimal Supersymmetric Model (MSSM). The Standard Model of particle physics, the  
6 MSSM, and Higgs phenomenology are introduced briefly. The search presented in this thesis  
7 uses a single final state configuration, in which the Higgs boson decays to two tau leptons,  
8 with one tau decaying to a muon and neutrinos, and the other decays to pions and a single  
9 neutrino. Two new methods are introduced in this analysis, the Tau Neural Classifier tau  
10 identification algorithm, and the Secondary Vertex fit tau pair mass reconstruction method.  
11 Both methods are discussed in detail. The analysis uses the 2010 dataset from the Compact  
12 Muon Solenoid (CMS) experiment, which contains  $36 \text{ pb}^{-1}$  of integrated luminosity at a  
13 center of mass energy of 7 TeV. In total, 573 events are selected in the analysis; this value  
14 is compatible with the Standard Model expectation. No excess of signal events is observed,  
15 and we set an upper limit on cross section times branching ratio of a Higgs boson. We finally  
16 interpret this limit in the parameter space of the MSSM.

---

<sup>17</sup> **Acknowledgments**

<sup>18</sup>

Hooray for everybody.

---

# <sup>19</sup> Table of Contents

<sup>20</sup> <b>Introduction</b>	<sup>1</sup>
<b>1 The Standard Model and Beyond</b>	<b>3</b>
1.1 The Standard Model . . . . .	3
1.1.1 Quantum Electrodynamics and Gauge Invariance . . . . .	4
1.1.2 The Weak Interactions . . . . .	6
1.1.3 Spontaneous Symmetry Breaking . . . . .	8
1.1.4 The Higgs Mechanism . . . . .	10
1.1.5 Electroweak Unification . . . . .	12
1.1.6 Quantum Chromodynamics . . . . .	16
1.2 Beyond the Standard Model . . . . .	18
1.2.1 The Hierarchy Problem . . . . .	19
1.2.2 Supersymmetry . . . . .	20
1.2.3 The Minimal Supersymmetric Model . . . . .	20
1.3 Searches for the Higgs boson . . . . .	23
1.3.1 Standard Model Higgs boson phenomenology . . . . .	23
1.3.2 MSSM Higgs Phenomenology . . . . .	26
1.3.3 Results from LEP and Tevatron . . . . .	27
1.4 The Physics of the Tau Lepton . . . . .	33
<b>2 The Compact Muon Solenoid Experiment</b>	<b>37</b>
2.1 The Large Hadron Collider . . . . .	38
2.2 Solenoid Magnet . . . . .	40
2.3 Charged Particle Tracking Systems . . . . .	41
2.4 Electromagnetic Calorimeter . . . . .	43
2.5 Hadronic Calorimeter . . . . .	45
2.6 Muon System . . . . .	47
2.7 Trigger System . . . . .	49
<b>3 Tau Identification: The Tau Neural Classifier</b>	<b>52</b>
3.1 Geometric Tau Identification Algorithms . . . . .	53
3.2 Decay Mode Tau Identification: Motivation . . . . .	53
3.3 The Tau Neural Classifier . . . . .	54
3.3.1 Decay mode reconstruction . . . . .	55
3.3.2 Neural network classification . . . . .	58
3.4 Summary . . . . .	72
3.5 HPS+TaNC: A Hybrid Algorithm . . . . .	76
3.5.1 Decay mode reconstruction . . . . .	76
3.5.2 Hadronic tau discrimination . . . . .	78

56	3.6 Electron and Muon Rejection . . . . .	79
57	<b>4 Mass Reconstruction: The Secondary Vertex Fit</b>	<b>81</b>
58	4.1 Existing mass reconstruction algorithms . . . . .	81
59	4.2 The Secondary Vertex fit . . . . .	83
60	4.3 Parametrization of tau decays . . . . .	84
61	4.4 Likelihood for tau decay . . . . .	85
62	4.4.1 Likelihood for reconstructed missing transverse momentum . . . . .	85
63	4.4.2 Likelihood for tau lepton transverse momentum balance . . . . .	87
64	4.4.3 Secondary vertex information . . . . .	88
65	4.5 Performance . . . . .	89
66	<b>5 Analysis Selections</b>	<b>93</b>
67	5.1 High Level Trigger . . . . .	93
68	5.2 Particle Identification . . . . .	94
69	5.2.1 Muons . . . . .	94
70	5.2.2 Hadronic Taus . . . . .	95
71	5.2.3 Missing Transverse Energy . . . . .	95
72	5.3 Event Selections . . . . .	96
73	<b>6 Data–Driven Background Estimation</b>	<b>100</b>
74	6.1 Background Enriched Control Regions . . . . .	101
75	6.2 The Fake–rate Method . . . . .	103
76	6.2.1 Parameterization of Fake–rates . . . . .	106
77	6.2.2 Measurement of Fake–rates . . . . .	107
78	6.2.3 Application of Fake–rates . . . . .	108
79	6.2.4 “Simple” weight method . . . . .	109
80	6.2.5 “CDF–type” weights . . . . .	111
81	6.2.6 k–Nearest Neighbor Fake–rate Calculation . . . . .	115
82	6.2.7 Results of Background Estimation . . . . .	116
83	6.3 Template method . . . . .	118
84	<b>7 Monte Carlo Corrections</b>	<b>126</b>
85	7.1 Muon Identification Efficiency . . . . .	126
86	7.2 Hadronic Tau Identification Efficiency . . . . .	129
87	7.3 Muon and Tau Momentum Scale . . . . .	131
88	7.4 Missing Transverse Energy Correction . . . . .	132
89	7.5 Pile-up Event Weighting . . . . .	133
90	<b>8 Systematics and Limit Extraction</b>	<b>135</b>
91	8.1 Signal normalization uncertainties . . . . .	137
92	8.2 Background normalization uncertainties . . . . .	137
93	8.3 Shape uncertainties . . . . .	138
94	8.4 Theory uncertainties . . . . .	139
95	8.5 Limit Extraction Method . . . . .	139
96	<b>9 Results</b>	<b>146</b>
97	9.1 Selected Events . . . . .	146
98	9.2 Limits on Higgs Production . . . . .	147

99	9.3 Interpretation in the MSSM . . . . .	148
100	<b>Conclusions</b>	<b>157</b>
101	<b>Bibliography</b>	<b>157</b>

---

## 102 List of Figures

103	1.1	Fermi contact interaction diagram . . . . .	7
104	1.2	Muon decaying through intermediate gauge boson . . . . .	7
105	1.3	QCD Feynman Diagrams . . . . .	17
106	1.4	Loop corrections to Higgs mass . . . . .	19
107	1.5	Higgstrahlung production diagram at $e^+e^-$ colliders . . . . .	24
108	1.6	Gluon fusion Higgs production diagram . . . . .	24
109	1.7	Vector boson fusion Higgs production diagram . . . . .	24
110	1.8	Parton luminosity comparison of the LHC and Tevatron . . . . .	25
111	1.9	SM Higgs cross sections at the LHC . . . . .	26
112	1.10	SM Higgs branching fractions . . . . .	27
113	1.11	Cross sections of interest at hadron colliders . . . . .	28
114	1.12	MSSM Higgs production with association $b$ -quarks . . . . .	29
115	1.13	MSSM Higgs cross sections at the LHC . . . . .	30
116	1.14	LEP Standard Model Higgs limit plot . . . . .	31
117	1.15	Tevatron low mass Standard Model Higgs limit plot . . . . .	32
118	1.16	Tevatron high mass Standard Model Higgs limit plot . . . . .	33
119	1.17	LEP MSSM exclusion limits . . . . .	34
120	1.18	Tevatron MSSM exclusion limits . . . . .	34
121	2.1	Schematic drawings of the CMS detector . . . . .	39
122	2.2	Material budget of the CMS tracker . . . . .	42
123	2.3	Momentum and impact parameter resolutions of CMS tracker . . . . .	43
124	2.4	Energy resolution of the CMS ECAL . . . . .	45
125	2.5	Muon system material budget and identification efficiency . . . . .	47
126	3.1	Visible invariant mass of $\tau$ lepton decay products . . . . .	54
127	3.2	Invariant mass photon pairs in reconstructed $\pi^0$ mesons . . . . .	56
128	3.3	Neutral energy fraction in visible $\tau$ decays . . . . .	57
129	3.4	Tau decay mode reconstruction performance . . . . .	59
130	3.5	Kinematic dependence of decay mode reconstruction . . . . .	60
131	3.6	Neural network over-training validation plots . . . . .	63
132	3.7	Kinematic weighting of training sample . . . . .	64
133	3.8	Neural network output in each decay mode . . . . .	68
134	3.9	Performance curves for the neural networks used in the TaNC . . . . .	69
135	3.10	Tau Neural Classifier performance curves for different $p_T$ ranges . . . . .	70
136	3.11	Tau Neural Classifier transformation performance . . . . .	72
137	3.12	Transformed neural network output . . . . .	73
138	3.13	Tau Neural Classifier performance comparison . . . . .	74
139	3.14	Tau Neural Classifier kinematic performance . . . . .	75

140	3.15 Invariant mass distribution of PF photon pairs . . . . .	77
141	4.1 Coordinate system of the SVfit . . . . .	86
142	4.2 Effect of $p_T$ -balance term on SVfit performance . . . . .	89
143	4.3 Effect of the visible $p_T$ requirements on muon and hadronic $\tau$ decays . . . . .	90
144	4.4 Effect of the visible $p_T$ requirements for $Z$ and Higgs events . . . . .	91
145	4.5 Comparison of SVfit with the Collinear Approximation algorithm . . . . .	91
146	4.6 Comparison of SVfit with the visible mass observable . . . . .	92
147	5.1 Distributions of $M_T$ and muon isolation discriminants . . . . .	98
148	5.2 Reconstruction of $P_\zeta$ variable . . . . .	98
149	6.1 Visible mass distribution of the backgrounds in the signal and control regions	104
150	6.2 SVfit mass distribution of the backgrounds in the signal and control regions	105
151	6.3 $p_T$ and $\eta$ dependency of tau ID performance . . . . .	106
152	6.4 Comparison of fake-rate contribution from genuine taus in the simple and CDF methods . . . . .	114
153	6.5 Muon transverse momentum in the Fake-rate method . . . . .	120
154	6.6 Tau-jet transverse momentum in the Fake-rate method . . . . .	121
155	6.7 Visible mass in the Fake-rate method . . . . .	122
156	6.8 $k$ -Nearest Neighbor classifier example . . . . .	123
157	6.9 Comparison of visible mass and SVfit mass . . . . .	123
158	6.10 Comparison of background shapes in the signal and control regions . . . . .	124
159	6.11 Visible mass distribution in the final fit of the Template Method . . . . .	125
160		
161	7.1 Tag-probe muon isolation method . . . . .	128
162	7.2 Muon isolation correction factors . . . . .	130
163	7.3 Measurement of hadronic tau identification efficiency . . . . .	131
164	7.4 $Z$ -recoil $E_T^{\text{miss}}$ resolution correction . . . . .	133
165	7.5 Distribution of number of reconstructed primary vertices per event . . . . .	134
166		
167	9.1 Transverse momentum distributions of muon and tau in the final selected events . . . . .	150
168	9.2 Distributions of the $\eta$ and $\phi$ of the muon and tau candidates in the final selected events . . . . .	151
169	9.3 Distributions of final selected events . . . . .	152
170	9.4 Observed and expected limits on Higgs $\sigma \times \text{BR}$ . . . . .	155
171	9.5 Excluded regions of MSSM $\tan\beta - m_{A^0}$ parameter space . . . . .	156
172	9.6 CMS combined exclusion of MSSM $\tan\beta - m_{A^0}$ parameter space . . . . .	158
173		

---

## 174 List of Tables

175	1.1	Chiral supermultiplets in the MSSM . . . . .	21
176	1.2	Gauge supermultiplets in the MSSM . . . . .	21
177	1.3	Higgs search channels at LEP . . . . .	29
178	1.4	Decay modes of the $\tau$ lepton . . . . .	35
179	3.1	Decay mode performance – naive reconstruction . . . . .	58
180	3.2	Decay mode performance – TaNC reconstruction . . . . .	58
181	3.3	Neural network training event statistics . . . . .	62
182	3.4	Variables used in the different TaNC neural networks . . . . .	80
183	5.1	High Level Trigger paths used to select $\mu + \tau_h$ events . . . . .	94
184	5.2	Analysis backgrounds that include fake taus . . . . .	96
185	5.3	Event selection summary . . . . .	99
186	6.1	Criteria used to select background enriched control regions . . . . .	102
187	6.2	Comparison of background control region yields in data and the prediction from simulation . . . . .	103
188	6.3	Fake-rate “simple” method closure test results . . . . .	110
189	6.4	Fake-rate “CDF” method closure test results . . . . .	113
190	6.5	Fake-rate method results . . . . .	117
191	6.6	Fake-rate Method predicted yields in like-sign control region . . . . .	118
192	6.7	Background yields measured using the Template Method . . . . .	119
193	7.1	Muon trigger, identification, and isolation correction factors . . . . .	129
194	8.1	Effect of normalization uncertainties on signal efficiency times acceptance .	140
195	8.2	Correspondence of confidence levels and $2\Delta \ln \mathcal{L}$ intervals . . . . .	142
196	8.3	Summary of systematic uncertainties represented by nuisance parameters in the likelihood, their representation method and magnitudes. . . . .	145
197	9.1	Final analysis yield and background expectations . . . . .	147
198	9.2	Expected signal yields at $\tan \beta = 30$ . . . . .	153
199	9.3	Expected and observed 95% CL $\sigma \times \text{BR}$ upper limits . . . . .	154
200	9.4	Contributions of different MSSM Higgs boson types at different $m_{A^0}$ . . . . .	154

---

## 203 Introduction

204 This thesis describes a search for the Higgs boson, a new particle predicted by a theory  
 205 called the Minimal Supersymmetric Model (MSSM). The analysis uses the 2010 dataset  
 206 from the Compact Muon Solenoid (CMS) experiment, which contains  $36 \text{ pb}^{-1}$  of integrated  
 207 luminosity at a center of mass energy of 7 TeV. The Higgs boson is hypothesized to be the  
 208 catalyst of Electroweak Symmetry Breaking, the phenomenon strongly believed to imparts  
 209 mass to particles.

210 Chapter 1 gives an introduction to the Standard Model (SM) of particle physics. Em-  
 211 phasis is given to Electroweak Symmetry Breaking and the Higgs Mechanism, the theoretical  
 212 phenomena that motivate the presence of a Higgs boson. The theoretical issues which moti-  
 213 vated the development of the MSSM are discussed, and a brief introduction is given. Finally,  
 214 the phenomenology of Higgs bosons in the SM and MSSM is discussed, with an overview  
 215 of Higgs searches performed at LEP and the Tevatron.

216 This thesis then documents the development of a complete search for MSSM Higgs  
 217 bosons at CMS. The CMS experiment is introduced briefly in Chapter 2. Chapters 3 and 4  
 218 document in detail two fundamental components of the search, an advanced tau identifica-  
 219 tion algorithm and a novel method for reconstructing neutrinos associated to tau decays.  
 220 The development of these algorithms was motivated by the challenges of this analysis,  
 221 and precipitated significant improvements in the final result. Finally, in Chapters 5-8, we  
 222 describe the methods and results of the event selection, background estimation, and the  
 223 systematic uncertainties, and finally compute an upper limit on the presence of an MSSM  
 224 Higgs boson.

225 The studies presented herein were part of a larger effort at CMS to search for an MSSM  
 226 Higgs boson decaying to tau lepton pairs. In addition to the  $\mu - \tau_h$  channel described in  
 227 this thesis, final states with an electronic and hadronic tau decay ( $e - \tau$ ) and electronic and

228 muonic ( $e - \mu$ ) were considered. The combination of all three was used to set a limit on  
229 the MSSM [1]. This result has recently been accepted for publication in Physical Review  
230 Letters B. At the time of this writing, the CMS analysis sets the worlds strongest limit on  
231 the MSSM Higgs boson using a direct search.

232

## Chapter 1

### 233 The Standard Model and Beyond

(ch:theory)

#### 234 §1.1 The Standard Model

235 The Standard Model (SM) is a “theory of almost everything” that describes the interactions  
236 of elementary particles. The Standard Model is a *quantum field theory*, first appearing in its  
237 modern form in the middle of the 20th century. The model is the synthesis of the independent  
238 theories of electromagnetism, and the weak and strong nuclear forces. Each of these theories  
239 was used to describe different phenomena, which each have extremely different strengths  
240 and act at different scales. The interaction of light and matter is described by Quantum  
241 Electrodynamics (QED), a relativistic field extension of the theory of electromagnetism.  
242 The physics of radioactivity and nuclear decay was described by the Fermi theory of weak  
243 interactions and the forces that strong nuclear force binds the nuclei of atoms was described  
244 by Yukawa. An overview of these theories will be presented in this chapter.

245 The feature that united the disparate theories into the Standard Model was the appli-  
246 cation of the principle of *local gauge invariance*. The principle of gauge invariance first found  
247 success in QED, which predicted electromagnetic phenomenon with astounding accuracy.  
248 Local gauge invariance is now believed to a fundamental feature of nature that underpins  
249 all theories of elementary particles. Furthermore, the development of the complete Stan-  
250 dard Model as it is known today was precipitated by Goldstones’s work on spontaneous  
251 symmetry breaking [2, 3], which produces an effective Lagrangian with additional massless  
252 “Goldstone” bosons. Higgs (and others) [4, 5, 6] developed these ideas into what isulti-  
253 mately called the “Higgs Mechanism,” which uses a combination of new fields with broken  
254 symmetry to give mass to the Goldstone bosons.

255 In the 1960s, Glashow [7], Weinberg [8], and Salam [9] developed the above ideas into the  
 256 electroweak model, which unified QED with the weak force using intermediate weak bosons  
 257 in a gauge theory whose symmetry was spontaneously broken using the Higgs mechanism.  
 258 This unified theory has been incredibly experimentally successful and is the foundation of  
 259 modern particle theory.

### 260 §1.1.1 Quantum Electrodynamics and Gauge Invariance

QEDandGaugeInvariance) 261 The theory of QED is a modern extension of Maxwell's theory of electromagnetism, describ-  
 262 ing the interaction of matter with light. The development of QED is a result of efforts to  
 263 develop a quantum mechanical formulation of electromagnetism compatible with the theory  
 264 of Special Relativity. QED is a *gauge* theory, which means that the physical observables  
 265 are invariant under local gauge transformations. Requiring local gauge invariance gives rise  
 266 to a “gauge” field, which can be interpreted as particles that are exchanged during an  
 267 interaction.

268 In the following, we first describe the Dirac equation for a free electron, which is the  
 269 relativistic extension of the Schroedinger equation for spin 1/2 particles. We then show that  
 270 requiring the corresponding Lagrangian of the free charged particle to be invariant under  
 271 local gauge transformations creates an effective gauge boson field. This “gauge field” creates  
 272 terms in the Lagrangian that represent interactions between the particles.

The Dirac equation is the equation of motion of a free spin 1/2 particle of mass  $m$  and  
 is derived from the energy–momentum relationship of relativity

$$p^\mu p_\mu - m^2 c^2 = 0. \quad (1.1) \quad \text{[eq:EnergyPRelat]}$$

Dirac sought to express this relationship in the framework of quantum mechanics by applying the transformation

$$p_\mu \rightarrow i\hbar\partial_\mu \quad (1.2) \quad \text{[eq:QuantizeMom]}$$

to equation Equation 1.1, but with the requirement that the resulting equation be first order in time.<sup>1</sup> To achieve this, Dirac factorized Equation 1.1 into

$$(\gamma^\kappa p_\kappa + mc)(\gamma^\mu p_\mu - mc) = 0, \quad (1.3) \quad \text{[eq:DiracEquation]}$$

---

<sup>1</sup>A detailed discussion of this topic is available in [10].

where  $\gamma^\mu$  is a set of four  $4 \times 4$  matrices referred to as the Dirac matrices. The equation of motion is obtained by choosing either term (they are equivalent) from the left hand side of Equation 1.3 and making the substitution in Equation 1.2.

$$i\hbar\gamma^\mu\partial_\mu\psi - mc\psi = 0. \quad (1.4) \quad [\text{eq:DiracEquation}]$$

- <sup>273</sup> The solutions  $\psi$  of the Dirac equation are called “Dirac spinors,” and represent the quantum  
<sup>274</sup> mechanical state of spin 1/2 particles.

The Lagrangian corresponding to the Dirac equation (1.4) is

$$\mathcal{L} = \bar{\psi}(i\hbar c\gamma^\mu\partial_\mu - mc^2)\psi, \quad (1.5) \quad [\text{eq:FreeQEDLagr}]$$

where  $\psi$  is the spinor field of the particle in question,  $\hbar$  is Planck’s constant,  $c$  the speed of light, and  $\gamma^\mu$  are the Dirac matrices. As  $\bar{\psi}$  is the Hermitian conjugate of  $\psi$ , the Lagrangian is invariant under the global gauge transformation

$$\psi' \rightarrow e^{i\theta}\psi. \quad (1.6) \quad [\text{eq:U1GaugeTran}]$$

The Lagrangian is invariant under *local* gauge translations if  $\theta$  can be defined differently at each point in space, i.e. if  $\theta = \theta(x)$  in equation 1.6. However, as the derivative operator  $\partial_\mu$  in equation 1.5 does not commute with  $\theta(x)$ , the Lagrangian must be modified to satisfy local gauge invariance. This modification is accomplished with the use of a “gauge covariant derivative.” By making the replacement

$$\partial_\mu \rightarrow D_\mu = \partial_\mu - \frac{ie}{\hbar}A^\mu \quad (1.7) \quad \{?\}$$

in equation 1.5, where  $A^\mu = \partial^\mu\theta(x)$  and  $e$  is the electric charge, the Lagrangian becomes locally gauge invariant:

$$\mathcal{L} = \bar{\psi}(i\hbar c\gamma^\mu D_\mu - mc^2)\psi. \quad (1.8) \quad [\text{eq:LocalQEDLag}]$$

The difference between the locally (1.8) and the globally (1.5) gauge invariant Lagrangians is then

$$\mathcal{L}_{int} = \frac{e}{\hbar}\bar{\psi}\gamma^\mu\psi A_\mu. \quad (1.9) \quad \{?\}$$

This term can be interpreted as the coupling between the particle and the gauge boson (force carrier) fields. The coupling is proportional to the constant  $e$ , which is associated with the electric charge. This is consistent with the experimental observation that particles with zero electric charge do not interact electromagnetically with each other. In this interpretation, the electromagnetic force between two charged particles is caused by the exchange of gauge bosons (photons). The existence of this “minimal coupling” is *required* if the Lagrangian

is to satisfy local gauge invariance. The addition of a term with the gauge Field Strength Tensor to represent the kinetic term of the gauge (photon) field yields the QED Lagrangian:

$$\mathcal{L}_{QED} = \bar{\psi}(i\hbar c\gamma^\mu D_\mu - mc^2)\psi - \frac{1}{4\mu_0}F_{\mu\nu}F^{\mu\nu}. \quad (1.10) \{?\}$$

The gauge symmetry group of QED is  $U(1)$ , the unitary group of degree 1. This symmetry can be visualized as a rotation of a two-dimensional unit vector. (The application of the gauge transformation  $e^{i\theta}$  rotates a number in the complex plane.) In a gauge theory the symmetry group of the gauge transformation defines the behavior of the gauge bosons and thus the interactions of the theory.

### §1.1.2 The Weak Interactions

*(sec:WeakInteractions)* The theory of Weak Interactions was created to describe the physics of radioactive decay.

The first formulation of the theory was done by Fermi [?] to explain the phenomenon of the  $\beta$  decay of neutrons. The initial theory was a four-fermion “contact” theory. In a contact theory, all four fermions come involved in the  $\beta$ -decay are connected at a single vertex. The Fermi theory Hamiltonian for the  $\beta$ -decay of a proton is then [11]

$$H = \frac{G_\beta}{\sqrt{2}} [\bar{\psi}_p \gamma_\mu (1 - g_A \gamma_5) \psi_n] [[\bar{\psi}_e \gamma^\mu (1 - \gamma_5) \psi_\nu]] + h.c., \quad (1.11) \boxed{\text{eq:FermiTheoryH}}$$

where  $G_\beta$  is the Fermi constant and  $g_A$  is the relative fraction of the interaction with axially Lorentz structure. The value of  $g_A$  was determined experimentally to be 1.26. One of the most notable things discovered about the weak force is that weak interactions violate parity; that is, the physics of the interaction change (or become disallowed) under inversion of the spatial coordinates. This is evidenced by the  $(1 - \gamma_5)$  term in Equation 1.11. This term is the “helicity operator”; the left and right “handed” helicity states are eigenstates states of this term.

$$h = (1 - \gamma_5)/2$$

$$h\psi_R = \frac{1}{2}\psi_R$$

$$h\psi_L = -\frac{1}{2}\psi_L$$

It is observed that only left-handed neutrinos (or right-handed anti-neutrinos) participate in the weak interaction.

The Fermi interaction can describe both nuclear  $\beta$  decay ( $p \rightarrow n + e^+ + \bar{\nu}_e$ ) as well as the decay of a muon into an electron ( $\mu \rightarrow \nu_\mu + e + \bar{\nu}_e$ , Figure 1.1). Furthermore, the

**Fixme:** check handedness is correct

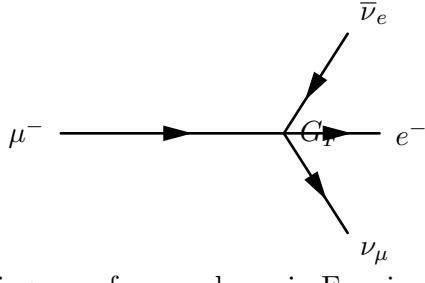


Figure 1.1: Feynmann diagram of muon decay in Fermi contact interaction theory.

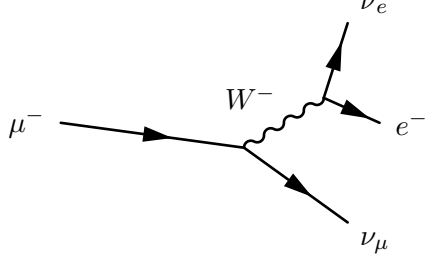


Figure 1.2: Feynmann diagram of muon decay proceeding through an intermediate gauge boson  $W^-$ .

onDecayFeynmanDiagram)

coupling constant  $G$  is found to be a *universal* constant in weak interactions, in that it is the same for interactions regardless of the particle species participating in the interaction. That is,  $G_\mu = G_e = G_F$ . Using an Hamiltonian analogous to Equation 1.11 for muon decay, the decay amplitude  $M$  is found to be

$$M = \frac{G_F}{\sqrt{2}} \left[ \bar{u}_{\nu_\mu} \gamma_\rho \frac{1 - \gamma_5}{2} u_\mu \right] \left[ \bar{u}_{\nu_e} \gamma_\rho \frac{1 - \gamma_5}{2} u_e \right]. \quad (1.12) \quad \text{[eq>ContactAmpli]}$$

290 However, the contact interaction form of Fermi's theory is not complete. When applied  
291 to scattering processes, the interaction violates unitarity: the calculated cross section grows  
292 with the center of mass energy, so that for some energy the probability for an interaction  
293 is greater than one. Furthermore, the techniques successfully used to "renormalize"<sup>2</sup> QED  
294 fail when applied to the Fermi interaction.

The first attempt to solve the problems with the Fermi theory was made by introducing an intermediate weak boson [7]. The contact interaction is replaced by a massive propagator, the  $W^\pm$  bosons. The decay of a muon to an electron and two neutrinos then proceeds as pictured in Figure 1.2 with an amplitude given [11] by

$$M = - \left[ \frac{g}{\sqrt{2}} \bar{u}_{\nu_\mu} \gamma_\rho \frac{1 - \gamma_5}{2} u_\mu \right] \frac{-g^{\rho\sigma} + \frac{q^\rho q^\sigma}{M_W^2}}{q^2 - M_W^2} \left[ \frac{g}{\sqrt{2}} \bar{u}_{\nu_e} \gamma_\rho \frac{1 - \gamma_5}{2} u_e \right]. \quad (1.13) \quad \text{[eq:WeakPropaga]}$$

The presence of the large gauge boson mass term  $M_W^2$  in the denominator of the central

---

<sup>2</sup>Renormalization of quantum field theories is a broad topic beyond the scope of this thesis. Briefly, the process involves "absorbing" infinite divergences that occur in higher-order interactions into physical observables [10].

term of Equation 1.13 is the reason why the contact interaction original formulated by Fermi effectively described low-energy weak phenomenon. When the momentum transfer  $q$  in the interaction is small compared to  $M_W$ , the effect of the propagator is an effective constant. In the low energy limit, the full propagator in equation 1.13 is equivalent to the Fermi contact interaction in 1.12 as

$$\lim_{q/M_W \rightarrow 0} \frac{g^2}{8(q^2 - M_W^2)} = \frac{G_F}{\sqrt{2}}. \quad (1.14) \quad \text{[eq>ContactVersusPropagator]}$$

295 Unfortunately, the weak boson exchange model did not solve the problems of unitarity  
 296 and renormalizability in the weak interaction. However, the form of the boson-exchange  
 297 propagator in Equation 1.14 suggests the observed “weakness” of the weak interactions is  
 298 an artifact of the presence of the massive propagator ( $M_W$ ) and that the fundamental scale  
 299 of the interaction  $g$  is the same order of magnitude as that of QED,  $g \approx e$ . This observation  
 300 lead to the unification of the electromagnetic and weak forces, which we describe in the  
 301 next sections.

### 302 §1.1.3 Spontaneous Symmetry Breaking

303 *(sec:SSB)* In the early 1960s Glashow, Weinberg, and Salam published a series of papers describing  
 304 how the electromagnetic and weak forces could be unified into a common “electroweak”  
 305 force. The fact that at low energy the electromagnetic and weak forces appear to be sep-  
 306 arate phenomena is due to the fact that the symmetry of the electroweak gauge group is  
 307 “spontaneously broken.” Modern field theories (both the Standard Model and beyond) are  
 308 predicated on the idea that the all interactions are part of a single, unified symmetry group  
 309 and the differences between various scales (electromagnetic, weak, etc.) at lower energies  
 310 are due to the unified symmetry being spontaneously broken.

A symmetry of a Lagrangian is spontaneously broken when the ground state, or vacuum, is at a value which about which the Lagrangian is not symmetric. In quantum field theories, a particle is interpreted as quantized fluctuations of its corresponding field about some constant (vacuum) ground state. The “effective” Lagrangian that we observe in the (low energy) laboratory would be the expansion of the Lagrangian about this stable point. The effective Lagrangian no longer obeys the original symmetry, which has been “broken”. We give a brief example of the phenomenological effects of a spontaneously broken symmetry

in a toy model, following the treatment in [11].

$$\mathcal{L} = \frac{1}{2} \partial_\mu \phi_1 \partial^\mu \phi_1 + \frac{1}{2} \partial_\mu \phi_2 \partial^\mu \phi_2 - V(\phi_1^2 + \phi_2^2) \quad (1.15) \boxed{\text{eq:ToySSBLagran}}$$

311 The toy Lagrangian in Equation 1.15 has a global  $U(1)^3$  symmetry and consists of two  
 312 real-valued fields,  $\phi_1$  and  $\phi_2$ . The particle mass spectra of the theory is given by expanding  
 313 the field potential  $V(\phi_1, \phi_2)$  about its minimum,  $(\phi_1^{min}, \phi_2^{min})$ . The first three terms in the  
 314 series are found by

$$\begin{aligned} V(\phi_1, \phi_2) &= V(\phi_1^{min}, \phi_2^{min}) + \sum_{a=1,2} \left( \frac{\partial V}{\partial \phi_a} \right)_0 (\phi_a - \phi_a^{min}) \\ &\quad + \frac{1}{2} \sum_{a,b=1,2} \left( \frac{\partial^2 V}{\partial \phi_a \partial \phi_b} \right)_0 (\phi_a - \phi_a^{min})(\phi_b - \phi_b^{min}) + \dots \end{aligned} \quad (1.16) \boxed{\text{eq:ExpandedPote}}$$

Since at the minimum the partial derivative of  $V$  is zero with respect to all fields, the second term in equation 1.16 is zero. The third term determines the masses of the particles in the theory. Since a mass term for a particle corresponding to a field  $\phi_n$  in the Lagrangian appears as  $\frac{1}{2}m^2\phi_n\phi_n$ , we can identify

$$\left( \frac{\partial^2 V}{\partial \phi_a \partial \phi_b} \right)_{\phi^{min}} \quad (1.17) \boxed{\text{eq:MassMatrixTe}}$$

315 as the  $a$ th row and  $b$ th column in the “mass matrix”. Off diagonal terms in this matrix  
 316 indicate mixing terms between the fields. By diagonalizing the matrix, the combinations of  
 317 fields which correspond to the physical particles (the “mass eigenstates”) are found. The  
 318  $m^2$  of each particle is then the corresponding entry in the diagonal of the mass matrix.

The particle spectra of the model depends heavily on the form of the potential. An illustrative form (that is renormalizable and bounded from below) of a possible configuration for the potential  $V$  in Equation 1.15 is

$$V(\phi_1^2 \phi_2^2) = \frac{m^2}{2}(\phi_1^2 + \phi_2^2) + \frac{\lambda}{4}(\phi_1^2 + \phi_2^2)^2. \quad (1.18) \boxed{\text{eq:SSBPotential}}$$

319 If the parameters  $m^2$  and  $\lambda$  are both positive, then the minimum of  $V$  is at the origin ( $\phi_1 =$   
 320  $\phi_2 = 0$ ). In this case, the mass matrix term in Equation 1.16 takes the form  $\left( \frac{\partial^2 V}{\partial \phi_a \partial \phi_b} \right)_0 =$   
 321  $\frac{m^2}{2} \delta_{ab}$ , where  $\delta_{ab}$  is the Kronecker delta function. Therefore the mass matrix is already  
 322 diagonalized, and the  $\phi_1$  and  $\phi_2$  both correspond to particles with mass  $m$ . If the  $m^2$

---

<sup>3</sup>Technically, the symmetric transformation is

$$\begin{pmatrix} \phi_1 \\ \phi_2 \end{pmatrix} \rightarrow \begin{pmatrix} \phi'_1 \\ \phi'_2 \end{pmatrix} = \begin{pmatrix} \cos \theta & -\sin \theta \\ \sin \theta & \cos \theta \end{pmatrix} \begin{pmatrix} \phi_1 \\ \phi_2 \end{pmatrix},$$

which is  $\mathcal{O}(2)$ . However, this transformation is equivalent to  $U(1)$ , as the two real fields  $\phi_1$  and  $\phi_2$  can be seen to correspond to the real and imaginary parts of a complex field  $\phi$  that does transform according to  $U(1)$ .

323 parameter in Equation 1.18 is negative, the spectrum is dramatically different. After making  
 324 the replacement  $m^2 = -\mu^2 (\mu^2 > 0)$ , the extrema of  $V$  are no longer unique. The requirement  
 325 of  $\frac{\partial V}{\partial \phi_i} = 0$  for all  $i$  is satisfied in two cases:

$$(\phi_1^{min}, \phi_2^{min}) = (0, 0) \quad (1.19) \quad \text{eq:WignerPoint}$$

$$(\phi_1^{min})^2 + (\phi_2^{min})^2 = \frac{\mu^2}{\lambda} = \nu^2. \quad (1.20) \quad \text{eq:NambuGoldst}$$

If the vacuum state is defined at the point in Equation 1.19, the symmetry is unbroken and the mass spectra is unchanged. However, the system is unstable at this point, as it is a local maximum. The true global minimum is defined as the set of points which satisfy Equation 1.20, which form a continuous circle in  $\phi_1 - \phi_2$  space (and is therefore infinitely degenerate). We can choose any point on the circle as the vacuum expectation value (VEV). If the point  $(\phi_1^{min} = \nu, \phi_2^{min} = 0)$ <sup>4</sup> is chosen, evaluating Equation 1.17 yields the mass matrix

**Fixme:**

check matrix

$$\left( \frac{\partial^2 V}{\partial \phi_a \partial \phi_b} \right)_{\phi^{min}} = \begin{pmatrix} v^2 & 0 \\ 0 & 0 \end{pmatrix}.$$

326 Breaking the symmetry has changed the mass spectrum of the physical particles in the  
 327 model. There is now a massive particle with  $m = v^2$  and a massless particle. This massless  
 328 particle is called the “Goldstone boson.” Goldstone found [2] that a massless particle appears  
 329 for each generator in the symmetry group that is broken.

### 330 §1.1.4 The Higgs Mechanism

`sec:HiggsMech` 331 As in section 1.1.1, extending the gauge symmetry requirement to be *locally* invariant creates  
 332 interesting consequences for models that have spontaneously broken symmetry. This gives  
 333 rise to the “Higgs Mechanism,” which we overview here. For simplicity we will again consider  
 334 a model with  $U(1)$  symmetry. The model is identical to the one presented in section 1.1.3,  
 335 with two exceptions. First, we express the two real fields  $\phi_1$  and  $\phi_2$  as a single complex-  
 336 valued field  $\phi$ . Second, the model is required to be locally  $U(1)$  invariant, and so uses the  
 337 gauge-covariant derivatives, minimal coupling to the gauge field, and contains the kinetic

---

<sup>4</sup>The point chosen for the VEV here is not arbitrary. One can chose any point that satisfies Equation 1.20 as the VEV. However, after the mass matrix is diagonalized, there will always be one physical field with a VEV=  $\nu$  and one with a VEV= 0. Therefore the physical content of the theory does not depend on the choice of VEV.

338 term for the gauge field, as discussed in section 1.1.1. The unbroken Lagrangian is

$$\mathcal{L} = -\frac{1}{4}F_{\mu\nu}F^{\mu\nu} + (D_\mu\phi^*)(D^\mu\phi) - V(\phi^*\phi) \quad (1.21)$$

$$V(\phi^*\phi) = -\mu^2\phi^*\phi + \lambda(\phi^*\phi)^2, \quad (1.22)$$

339 where  $F_{\mu\nu}$  is related to the gauge field by  $F_{\mu\nu} = \partial_\mu A_\nu - \partial_\nu A_\mu$ . The Lagrangian is invariant

340 under the local  $U(1)$  gauge transformation

$$\begin{aligned} \phi \rightarrow \phi' &= e^{-i\alpha(x)}\phi \\ A_\mu \rightarrow A'_\mu &= A_\mu - \frac{1}{2}\partial_\mu\alpha(x). \end{aligned} \quad (1.23) \{?\}$$

The potential is minimized when  $\phi^*\phi = \frac{\mu^2}{2\lambda}$ . To simplify the algebra, we can re-parameterize the field into a real part  $\eta(x)$  defined about  $\nu$ , the minimum of  $V$ , and a complex phase parameterized by  $\theta(x)/\nu$

$$\phi(x) = \frac{1}{\sqrt{2}}(\nu + \eta(x))e^{i\theta(x)/\nu}. \quad (1.24)$$

341 If the gauge transform is chosen to be  $\alpha(x) = \theta(x)/\nu$ , the fields of are defined in the so-called

342 “unitary gauge”<sup>5</sup> and have the special forms

$$\begin{aligned} \phi(x) \rightarrow \phi'(x) &= \frac{1}{\sqrt{2}}(\nu + \eta(x)) \\ A_\mu(x) \rightarrow B_\mu(x) &= A_\mu(x) - \frac{1}{e\nu}\partial_\mu\theta(x) \end{aligned} \quad (1.25)$$

343 The kinetic term of the gauge field  $F_{\mu\nu}$  is invariant under this transformation. If the gauge

344 transformations of Equation 1.25 are substituted into the Lagrangian (1.21) the effective

345 Lagrangian at the minimum of  $V$  is

$$\begin{aligned} \mathcal{L} = & \frac{1}{2}\partial_\mu\eta\partial^\mu\eta - \mu^2\eta^2 \\ & - \frac{1}{4}F_{\mu\nu}F^{\mu\nu} + \frac{1}{2}(e\nu)^2B_\mu B^\mu \\ & + \frac{1}{2}e^2B_\mu B^\mu\eta(\eta + 2\nu) - \lambda\nu\eta^3 - \frac{\lambda}{4}\eta^4. \end{aligned} \quad (1.26)$$

346 The breaking of the original symmetry has dramatically altered the physical consequences of

347 the model. In its unbroken form, the model described by Equation 1.21 would produce two

348 real massive particles and one massless gauge boson mandated by local gauge invariance.

349 After symmetry breaking, the effective Lagrangian in Equation 1.26 contains a massive

350 scalar  $\eta$  with  $m = \sqrt{2\mu^2}$  and a *massive* gauge boson  $B_\mu$  with mass  $m = \sqrt{2}e\nu$ . By ac-

351 quiring a mass, the gauge boson  $B_\mu$  has acquired the degree of freedom (as it can now

352 be longitudinally polarized) previously associated to the second degree of freedom in the

---

<sup>5</sup>In the unitary gauge, the choice of gauge ensures that the mass matrix is diagonalized.

353 scalar  $\phi$  field. This phenomenon, known as the “Higgs Mechanism,” is a simplified version  
 354 of the techniques successfully used to unify the electromagnetic and weak forces that we  
 355 will discuss in the next section.

### 356 §1.1.5 Electroweak Unification

ec:ElectroweakUnification) 357 In the 1960s, the ideas of local gauge invariance in field theories, spontaneous symme-  
 358 try breaking, and the Higgs mechanism were combined by Glashow [7], Weinberg [8] and  
 359 Salam [9] to form the unified theory of electroweak interactions, the nucleus of the Stan-  
 360 dard Model. This model successfully unified the electromagnetic and weak interactions into  
 361 a unified theory with a larger symmetry group. The reason for the empirically observed  
 362 difference in scales between two interactions is due to the larger, unified symmetry group  
 363 being broken. This broken symmetry creates heavy gauge bosons via the Higgs mechanism,  
 364 whose large mass decreases the strength of “weak” interactions at low energy, as discussed in  
 365 Section 1.1.2. The model successfully predicted the existence and approximate masses of the  
 366 weak force carriers, the  $W^\pm$  and  $Z$  bosons. These particles were later observed [12, 13, 14, 15]  
 367 with the predicted masses at the UA1 and UA2 experiments.

368 To provide a simple introduction to the mechanisms of the model, we will start with a  
 369 model that includes only one family of leptons, the electron  $e$  and its associated neutrino  
 370  $\nu_e$ . Following once again the treatment of [11], we describe the representation of the  $e$  and  
 371  $\nu_e$  in the chosen symmetry group of the model. We then construct a locally gauge invariant  
 372 Lagrangian with spontaneously broken symmetry, and examine the particle content of the  
 373 resulting model.

The form of the charged current  $J_\mu(x) = \bar{u}_{\nu_e} \gamma_\rho \frac{1-\gamma_5}{2} u_e$  in the weak interaction am-  
 plitudes (1.12) indicates that the left-handed electron and neutrino (remember that the  
 $(1 - \gamma_5)$  kills any right-handed spinors) can be combined into a doublet  $L$  of  $SU(2)$ .

$$L = \frac{1 - \gamma_5}{2} \begin{pmatrix} \nu_e \\ e^- \end{pmatrix} = \begin{pmatrix} \nu_e \\ e^- \end{pmatrix}_L \quad (1.27) \boxed{\text{eq:EWDoubletFc}}$$

<sup>374</sup> The operators that operate on “weak isospin,” the quantum of  $SU(2)_L$ , are

$$\tau^+ = \frac{\tau^1 + i\tau^2}{2} = \begin{pmatrix} 0 & 1 \\ 0 & 0 \end{pmatrix} \quad (1.28) \quad \text{?eq:Su2Generator}$$

$$\tau^- = \frac{\tau^1 - i\tau^2}{2} = \begin{pmatrix} 0 & 0 \\ 1 & 0 \end{pmatrix}, \quad (1.29) \quad \text{[eq:Su2Generator]}$$

where the  $\tau^i$  are the Pauli matrices. The weak currents  $J_\mu^\pm$  can be written by combining equations 1.27–1.29

$$J_\mu^\pm = \bar{L}\gamma_\mu\tau^\pm L. \quad (1.30) \quad \text{[eq:WeakCurrent]}$$

<sup>375</sup> Since  $\tau^1$ ,  $\tau^2$ , and  $\tau^3$  are the generators of the  $SU(2)$  group, we can complete the group

<sup>376</sup> by adding a neutral current to the charged currents of Equation 1.30. The  $\tau^3$  generator is  
<sup>377</sup> diagonal, so the charge of the current is zero and no mixing of the fields occur:

$$\begin{aligned} J_\mu^3 &= \bar{L}\gamma_\mu \frac{\tau^3}{2} L \\ &= \bar{L}\gamma_\mu \frac{1}{2} \begin{pmatrix} 1 & 0 \\ 0 & -1 \end{pmatrix} L \\ &= \frac{1}{2}\bar{\nu}_e\gamma_\mu\nu_e - \frac{1}{2}\bar{e}_L\gamma_\mu e_L. \end{aligned} \quad (1.31) \quad \text{[eq:EWNeutralCu]}$$

<sup>378</sup> Naively one might hope that the neutral current of Equation 1.31 would correspond to the

<sup>379</sup> electromagnetic (photon) current of QED. However, this is impossible for two reasons. First,  
<sup>380</sup> the right-handed component  $e_R$  does not appear in the current, so this interaction violates  
<sup>381</sup> parity, a known symmetry of the electromagnetic interactions. Second, the current couples to  
<sup>382</sup> neutrinos, which have no electric charge. Therefore, the “charge” corresponding to the  $SU(2)$   
<sup>383</sup> gauge symmetry generators  $T^i = \int J_0^i(x)d^3x$  cannot be that of the QED, and the gauge  
<sup>384</sup> group must be enlarged to include an additional  $U(1)$  symmetry. The generator of the new  
<sup>385</sup> symmetry must commute with the generators of the  $SU(2)_L$  group. The symmetry cannot  
<sup>386</sup> be directly extended with  $U(1)_{em}$  as the electromagnetic charge  $Q = \int(e_L^\dagger e_L + e_R^\dagger e_R)d^3x$   
<sup>387</sup> does not commute with  $T^i$ . The solution is to introduce the “weak hypercharge”  $\frac{Y}{2} = Q - T^3$ ,  
<sup>388</sup> which commutes the generators of  $SU(2)_L$ . Thus the symmetry group of the electroweak  
<sup>389</sup> model is  $SU(2)_L \times U(1)_Y$ .

390 The  $SU(2)_L \times U(1)_Y$  gauge invariant Lagrangian is written

$$\begin{aligned}\mathcal{L} &= \bar{L}i\gamma^\mu(\partial_\mu - ig\frac{\vec{\tau}}{2} \cdot \vec{A}_\mu + \frac{i}{2}g'B_\mu)L \\ &+ \bar{R}i\gamma^\mu(\partial_\mu + \frac{i}{2}g'B_\mu)R \\ &- \frac{1}{4}F_{\mu\nu}^iF^{i\mu\nu} - \frac{1}{4}B_{\mu\nu}B^{\mu\nu}.\end{aligned}\quad (1.32) \text{?eq:FermionAndGaugeFields}$$

391 As  $R$  is a singlet in  $SU(2)$ , it does not couple to the  $SU(2)$  gauge bosons  $A_\mu^i$ . For this  
 392 Lagrangian to correspond to empirical observations at low energy, the  $SU(2)_L \times U(1)_Y$   
 393 must be broken. As  $U(1)_{em}$  symmetry is observed to be good symmetry at all scales the  
 394 broken Lagrangian must be invariant under  $U(1)_{em}$ .

395 To accomplish the symmetry breaking, we introduce a new  $SU(2)$  doublet of complex  
 396 Higgs fields  $\phi$  that have hypercharge  $Y = 1$ , and contribute  $\mathcal{L}_S$  to the Lagrangian:

$$\phi = \begin{pmatrix} \phi^+ \\ \phi^0 \end{pmatrix} \quad (1.33) \{?\}$$

$$\mathcal{L}_S = (D_\mu\phi)^\dagger(D^\mu\phi) - V(\phi^\dagger\phi), \quad (1.34) \{?\}$$

where  $D_\mu$  is the gauge covariant derivative containing couplings to both the  $SU(2)_L$  and  
 $U(1)_Y$  gauge fields, and  $V$  has a form analogous to  $V$  in Equation 1.22. At this point we  
also add  $SU(2)_L \times U(1)_Y$  invariant “Yukawa” terms

$$\mathcal{L}_Y = -G_e(\bar{L}\phi R + \bar{R}\phi^\dagger L) + h.c. \quad (1.35) \text{?eq:YukawaTerms}$$

397 to the Lagrangian which couple the fermions ( $L$  and  $R$ ) to the Higgs field. After symmetry  
 398 breaking these terms will allow the fermions to acquire masses. By choosing the  $m^2$  and  $\lambda$   
 399 parameters of  $V$  appropriately, the new  $\phi$  field acquires a non-zero VEV and the symmetry  
 400 is spontaneously broken.

At the minimum of  $V$ , the Higgs field satisfies  $\phi^\dagger\phi = \frac{\nu^2}{2}$  and the Higgs fields has a  
 VEV of

$$\phi_{min} = \begin{pmatrix} 0 \\ v/\sqrt{2} \end{pmatrix}. \quad (1.36) \{?\}$$

The new symmetry of the model can be confirmed by looking at the action of the different  
symmetry generators on the VEV. If the generator acting on the vacuum state has a non-  
zero value, then the corresponding symmetry is broken. It can then be seen that the original  
symmetry generators  $T^+$ ,  $T^-$ ,  $T^3$ , and  $Y$  are all broken. The vacuum *is* invariant under  $Q$ ,

the generator of  $U(1)_{em}$

$$Q\phi_{min} = (T^3 + \frac{Y}{2}) \begin{pmatrix} 0 \\ v/\sqrt{2} \end{pmatrix} = 0,$$

401 so the broken Lagrangian contains the correct symmetry properties.

The gauge boson content of the electroweak interaction is obtained by parameterizing the Higgs field in the magnitude–phase notation of Equation 1.24 and using the unitary gauge (see Section 1.1.4), where the gauge transformation is chosen so Higgs field is real.

The Higgs scalar doublet is then

$$\phi' = \begin{pmatrix} 0 \\ \frac{1}{\sqrt{2}}(\nu + H(x)) \end{pmatrix} = \frac{1}{\sqrt{2}}(\nu + H(x))\chi. \quad (1.37) \quad \text{?eq:HiggsFieldParam}$$

The mass spectrum of the gauge bosons of the electroweak interaction (the photon,  $W^\pm$ , and  $Z$ ) is determined by the interaction of the gauge field terms in the covariant derivative with the non-zero vacuum expectation value  $\nu$  of the scalar Higgs field  $\phi$

$$(D_\mu \phi)' = (\partial_\mu - ig \frac{\vec{\tau}}{2} \cdot \vec{A}'_\mu - \frac{i}{2} g' B'_\mu) \frac{1}{\sqrt{2}}(\nu + H)\chi.$$

The terms in the expansion of the kinetic term of the Higgs field that are quadratic in  $\nu^2$  and a gauge boson field give the mass associated to that boson, and can be written as

$$\mathcal{L}_{mass} = \frac{\nu^2}{8}(g^2 A'_\mu{}^{1\mu} A'^{1\mu} + g^2 A'_\mu{}^{2\mu} A'^{2\mu} + (g A'_\mu{}^{3\mu} - g' B'_\mu)^2). \quad (1.38) \quad \text{?eq:GaugeBosonMass}$$

The  $A'_\mu{}^1$  and  $A'_\mu{}^2$  fields can be combined such that the first two terms in Equation 1.38 are equivalent to the mass term of a charged boson

$$W_\mu^\pm = \frac{A'_\mu{}^1 \mp i A'_\mu{}^2}{2}. \quad (1.39) \quad \{?\}$$

402 This is the familiar  $W^\pm$  boson of  $\beta$  and muon decay, and has mass  $M_W = \frac{1}{2}g\nu$ . The third

403 term in Equation 1.38 can be written in matrix form and then diagonalized into mass

404 eigenstates

$$\begin{aligned} & \frac{\nu^2}{8} (A'_\mu{}^3 \ B'_\mu) \begin{pmatrix} g^2 & -gg' \\ -gg' & g'^2 \end{pmatrix} \begin{pmatrix} A'^{3\mu} \\ B'^\mu \end{pmatrix} \\ & \rightarrow \frac{\nu^2}{8} (Z_\mu \ A_\mu) \begin{pmatrix} g^2 + g'^2 & 0 \\ 0 & 0 \end{pmatrix} \begin{pmatrix} Z^\mu \\ A^\mu \end{pmatrix}, \end{aligned} \quad (1.40) \quad \{?\}$$

giving a massive  $Z$  boson with

$$M_Z = \frac{\nu}{2} \sqrt{g^2 + g'^2} \quad (1.41) \quad \text{?eq:ZBosonMass}$$

and the massless photon  $A_\mu$  of QED. The mass of the  $Z$  is related to the mass of the  $W^\pm$

by

$$M_Z \equiv \frac{M_W}{\cos \theta_W}, \quad (1.42) \{?\}$$

405 where  $\theta_W$  is the “Weinberg angle,” which must be determined from experiment. As the  
 406 Fermi contact interaction of Section 1.1.2 is an effective theory of the weak sector, the value  
 407 of  $G_F$  obtained from  $\beta$  and muon decay experiments give clues to the masses of the  $W$  and  
 408  $Z$ .

$$M_W = \frac{1}{2} \left( \frac{e^2}{\sqrt{2} G_F} \right)^{(1/2)} \frac{1}{\sin \theta_W} \approx \frac{38 \text{ GeV}}{\sin \theta_W} > 37 \text{ GeV} \quad (1.43) \{?\}$$

$$M_Z \approx \frac{76 \text{ GeV}}{\sin 2\theta_W} > 76 \text{ GeV}. \quad (1.44) \{?\}$$

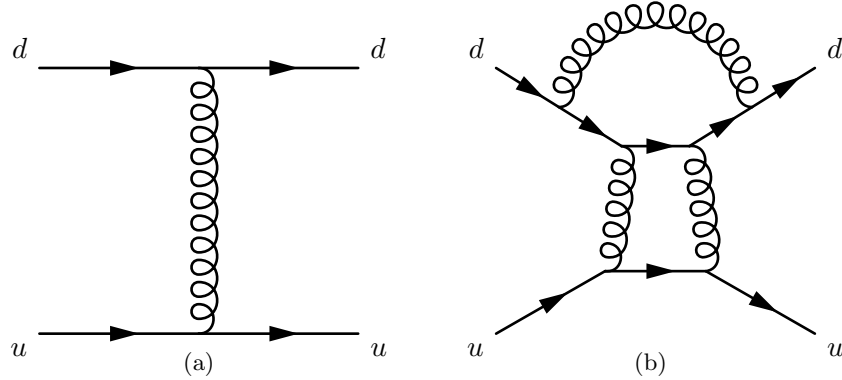
409 The discovery of the  $W$  [12, 13] and  $Z$  [14, 15] at the CERN SPS was a huge triumph for  
 410 the electroweak model.

411 The model that is presented in this section assumes only one species of leptons, the  
 412 electron and its associated neutrino. The electroweak model is trivially extended [11] to  
 413 include the other species ( $\mu, \tau$ ) of leptons and the three families of quarks. The masses of  
 414 the fermions are determined by the Yukawa terms in Equation 1.35. Each particle species  
 415 has a Yukawa term relating the Higgs VEV to its mass that is not constrained by the theory,  
 416 and must be determined by experiment.

### 417 §1.1.6 Quantum Chromodynamics

418 After electroweak unification, the Standard Model is completed by the theory of Quantum  
 419 Chromodynamics (QCD), which describes the interactions between quarks and gluons. QCD  
 420 is a broad field and only a brief introduction to its motivations and the phenomenology  
 421 relevant to the analysis presented in this thesis is contained in this section. The existence  
 422 of quarks as composite particles of hadrons was first proposed by Gell–Man and Zweig to  
 423 explain the spectroscopy of hadrons. QCD is an  $SU(3)$  non–Abelian gauge theory which  
 424 is invariant under *color* transformations. Color is the charge of QCD and comes in three  
 425 types: red, green and blue. The gauge boson that carries the force of QCD is called the  
 426 gluon, which is massless as the  $SU(3)_c$  color symmetry is unbroken.

427 There are three marked differences between the photon of QED and the gluon of QCD.  
 428 First, the gluon carries a color charge, while the photon is electrically neutral. This has  
 429 the consequence that a gluon can couple to other gluons. Secondly, it is found that no



g:QCDFeynmanDiagrams)

Figure 1.3: Feynman diagrams of a first–order (a) QCD interaction and a multi–loop (b) QCD interaction that have the same initial and final states. Each internal gluon propagator contributes a factor of  $g_s$ , the strong coupling constant, to the the amplitude. Since  $g_s > 1$ , multi–loop diagrams have a larger contribution than simpler diagrams.

430 colored object exists in nature. The corollary of this is that it is believed to be impossible  
 431 for a single quark or gluon to be observed. The mechanism that gives rise to this effect  
 432 is called “color confinement.” The strength of the strong force between two interacting  
 433 colored objects increases with distance. If two colored objects in a hadron are pulled apart,  
 434 the energy required to separate them will eventually be large enough to produce new colored  
 435 objects, resulting in two (or more) colorless hadrons. Finally, at low energy, QCD is non–  
 436 perturbative. What this means in practice is that when computing an amplitude from  
 437 a QCD Feynman diagram, additional gluon interactions contribute a value greater than  
 438 one. The dominance of multi–loop diagrams is illustrated in Figure 1.1.6. Thus higher  
 439 order diagrams with many internal loops cannot be ignored in QCD. In practice what is  
 440 done is to “factorize” QCD interaction amplitudes into a perturbative (high–energy) part  
 441 and a non–perturbative part. The perturbative portion is calculable using the Feynman  
 442 calculus; the non–perturbative must be estimated from parameterization functions that are  
 443 experimentally measured.

444 The practical consequence of color confinement to a physicist at a high–energy particle  
 445 physics experiment is the production of quark and gluon “jets,” which are high multi–  
 446 plicity sprays of particles observed in the detector. In a proton–proton collision, quarks  
 447 and gluons can be knocked off the incident protons. These quarks and gluons immediately  
 448 “hadronize,” surrounding themselves with additional hadrons, the majority of which are  
 449 charged and neutral pions. Heavier quarks, such as the charm, beauty, and top quarks un–

450 undergo flavor-changing weak decays, which can give rise to structure (leptons, sub-jets)  
 451 within the jet. Furthermore, due to the relative strength of the strong interaction compared  
 452 that of the electroweak, collision events involving only strong interactions are produced at  
 453 rates many orders of magnitudes larger than that of electroweak interactions. This makes  
 454 life difficult for physicists studying the electroweak force at hadron colliders. Sections 2.7,  
 455 and Chapters 3 and 5 will discuss the techniques used to identify and remove QCD events  
 456 from the data at different stages of the analysis.

## 457 §1.2 Beyond the Standard Model

?⟨sec:BSM⟩?<sup>458</sup> The Standard model is one of the most successful theories of the natural world ever created.  
 459 The predictions of the SM have been tested to many orders of magnitude and no experiment  
 460 to date<sup>6</sup> has found a result statistically incompatible with the Standard Model. However,  
 461 there is a general consensus in the physics community that the Standard Model is not  
 462 complete. It is believed that it is only an effective theory that is valid below some energy  
 463 scale  $\Lambda$ . Above this energy, there must exist some other “new physics,” which unifies the  
 464 forces of the Standard Model and correctly describes the natural world at all scales, while  
 465 maintaining equivalence to the Standard Model at low energy. This concept is analogous to  
 466 the relationship between the effective Fermi contact theory of Section 1.1.2 and the unified  
 467 electroweak theory of Section 1.1.5. The size of the cutoff scale  $\Lambda$  is estimated [11] to be  
 468  $\mathcal{O}(10^{15})$  GeV for a unified theory with  $SU(5)$  symmetry and even larger,  $\mathcal{O}(10^{19})$  GeV =  
 469  $M_{\text{planck}}$  if the theory is unified with gravity.

470 There are many compelling reasons that indicate that the Standard Model is incom-  
 471 plete. One is the fact that the model does not include gravity, which has still not be success-  
 472 fully reformulated into a quantum mechanical theory. Another is that cosmological obser-  
 473 vations indicate the presences of massive amounts of “dark matter” in the universe. Dark  
 474 matter is expected to be composed of a stable massive neutral particle which interacts very  
 475 weakly with other matter; no Standard Model particle fits this description. Finally, there  
 476 is the “hierarchy,” or fine-tuning problem. This problem strongly affects the Higgs sector,

---

<sup>6</sup>The Standard Model predicts that lepton number is a good quantum number and that the neutrinos are massless. It has recently been found that the neutrinos do have non-zero mass, and that they undergo oscillations between different neutrino species, violating lepton number.

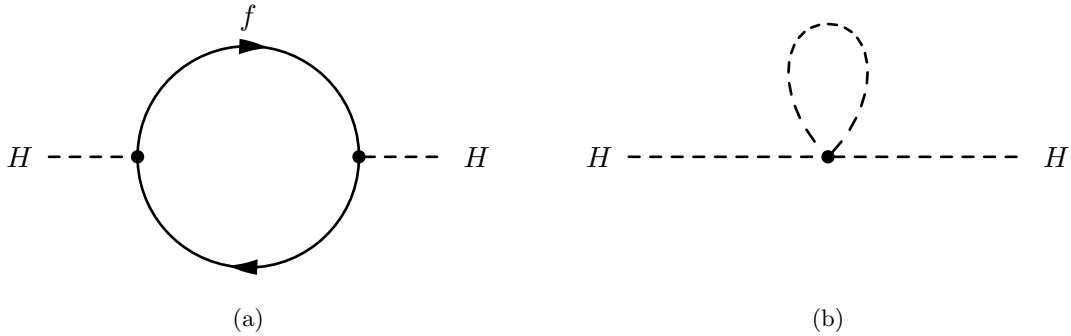


Figure 1.4: Feynman diagram of fermion (a) and scalar (b) loop corrections to Higgs mass.

and motivated the development of Supersymmetry, which are the targets of the search presented in this thesis. An short overview of the hierarchy problem and Supersymmetry are presented in the next sections.

#### §1.2.1 The Hierarchy Problem

The enormous size of the cutoff scale  $\Lambda$  in the Standard Model causes a major theoretical problem in the Standard Model. During renormalization of the Standard Model, amplitudes with divergent integrals are cut off at  $\Lambda$ . These large constant terms are “absorbed” into the physical observables. The cutoff term appears directly in quantum corrections to the Higgs mass [16]. The Yukawa term  $-\lambda_f H \bar{f} f$  coupling the fermion  $f$  to the Higgs  $H$  produces loop corrections to Higgs mass. The two types of corrections due to fermion loops and scalar loops are illustrated in Figure 1.4. The contribution of the loop correction in Figure 1.4(a) is [16]

$$m_H^2 = -\frac{|\lambda_f|^2}{8\pi^2} \Lambda^2 + \dots, \quad (1.45)$$

scales with  $\Lambda^2$ , which is many orders of magnitude larger than the electroweak ( $M_W$ ) scale. The physical mass of the Higgs is expected to have the same scale as  $M_W$ ,  $O(100)$  GeV/ $c^2$ . The fact that each fermion contributes a loop correction (Equation 1.45) requires that the “bare mass” of the Higgs to be tuned to the precision of  $(M_W/\Lambda)^2 \approx 10^{-26}$  for the renormalized mass to be correct! This is the so-called fine-tuning problem: it is believed that in a natural theory there will be only one scale. The electroweak unification analogy is in Equation 1.14, where it was noticed that the difference between the QED and weak scale was due to the massive  $M_W$  propagator term, and that the fundamental scale  $g$  of the

489 intermediate weak boson theory was compatible with QED. The most promising solution  
 490 to the hierarchy problem is the introduction of a new, “super” symmetry.

### 491 §1.2.2 Supersymmetry

492 Supersymmetry extends the Standard Model by positing that there exists a symmetry  
 493 between the integer–spin bosons ( $\gamma, W^\pm, Z, H$ ) and the half integer–spin fermions (quarks  
 494 and leptons). In Supersymmetry, every particle in the Standard Model has a “superpartner”  
 495 with a spin differs by 1/2. All of the other quantum numbers (including mass) of the  
 496 superpartners are the same. The introduction of this symmetry immediately solves the  
 497 hierarchy problem. For every scalar loop correction (Figure 1.4(b)) to the Higgs mass there is  
 498 now a corresponding fermion loop correction (Figure 1.4(a)). As the fermion and the scalar  
 499 have the same quantum numbers (except for spin) it turns out that these two diagrams  
 500 have the same value, but *opposite* sign. Thus the large  $\Lambda^2$  superpartner loop corrections to  
 501 the Higgs mass exactly cancel out the problematic Standard Model corrections. It is clear  
 502 that if Supersymmetry exists, it must be broken. We have not observed a scalar charged  
 503 particle with the same mass as the electron, for example. An excellent overview of possible  
 504 mechanism that create spontaneous symmetry breaking in supersymmetric models is given  
 505 in Chapter 6 of [16].

### 506 §1.2.3 The Minimal Supersymmetric Model

⟨sec:MSSMAndTaus⟩ 507 The simplest possible Supersymmetric extension to the Standard Model is the Minimal  
 508 Supersymmetric Model (MSSM). The model groups superpartner pairs into chiral (a left or  
 509 right–handed fermion field plus a complex scalar field) and gauge (a spin–1 vector boson and  
 510 a left or right–handed *gaugino* fermion) “supermultiplets.” As the weak interactions of the  
 511 Standard Model fermions are chiral, they (and their superpartners) must belong in a chiral  
 512 supermultiplet. It is interesting to note that there is a different superpartner for the left and  
 513 right–handed components of the fermions, even though the superpartners are spin–0 and  
 514 cannot have any handedness. It is found that there must be two Higgs supermultiplets for the  
 515 MSSM to be viable. As there are now fermionic particles in the Higgs sector (the Higgsinos),  
 516 if only one supermultiplet is introduced the MSSM suffers from non–renormalizable gauge

Names		spin 0	spin 1/2	$SU(3)_C, SU(2)_L, U(1)_Y$
squarks, quarks ( $\times 3$ families)	$Q$	$(\tilde{u}_L \ \tilde{d}_L)$	$(u_L \ d_L)$	$(\mathbf{3}, \mathbf{2}, \frac{1}{6})$
	$\bar{u}$	$\tilde{u}_R^*$	$u_R^\dagger$	$(\overline{\mathbf{3}}, \mathbf{1}, -\frac{2}{3})$
	$\bar{d}$	$\tilde{d}_R^*$	$d_R^\dagger$	$(\overline{\mathbf{3}}, \mathbf{1}, \frac{1}{3})$
sleptons, leptons ( $\times 3$ families)	$L$	$(\tilde{\nu} \ \tilde{e}_L)$	$(\nu \ e_L)$	$(\mathbf{1}, \mathbf{2}, -\frac{1}{2})$
	$\bar{e}$	$\tilde{e}_R^*$	$e_R^\dagger$	$(\mathbf{1}, \mathbf{1}, 1)$
Higgs, higgsinos	$H_u$	$(H_u^+ \ H_u^0)$	$(\tilde{H}_u^+ \ \tilde{H}_u^0)$	$(\mathbf{1}, \mathbf{2}, +\frac{1}{2})$
	$H_d$	$(H_d^0 \ H_d^-)$	$(\tilde{H}_d^0 \ \tilde{H}_d^-)$	$(\mathbf{1}, \mathbf{2}, -\frac{1}{2})$

Table 1.1: Chiral supermultiplets in the Minimal Supersymmetric Standard Model. The spin-0 fields are complex scalars, and the spin-1/2 fields are left-handed two-component Weyl fermions. Source: [16]

$\langle \text{tab:chiral} \rangle$

Names	spin 1/2	spin 1	$SU(3)_C, SU(2)_L, U(1)_Y$
gluino, gluon	$\tilde{g}$	$g$	$(\mathbf{8}, \mathbf{1}, 0)$
winos, W bosons	$\widetilde{W}^\pm \ \widetilde{W}^0$	$W^\pm \ W^0$	$(\mathbf{1}, \mathbf{3}, 0)$
bino, B boson	$\tilde{B}^0$	$B^0$	$(\mathbf{1}, \mathbf{1}, 0)$

Table 1.2: Gauge supermultiplets in the Minimal Supersymmetric Standard Model.

Source: [16]

$\langle \text{tab:gauge} \rangle$

517 anomalies.<sup>7</sup> By introducing an additional Higgs supermultiplet with opposite hypercharge,  
 518 the anomaly is canceled. The scalar portion of the MSSM Higgs sector then contains two  
 519 complex doublet fields  $H_u = (H_u^+, H_u^0)$  (up-type) and  $H_d = (H_d^0, H_d^-)$  (down-type). The  
 520 complete chiral and gauge supermultiplets of the MSSM are enumerated in Tables 1.1  
 521 and 1.2, respectively.

The superpotential (like the scalar potential of Section 1.1.3 but invariant under supersymmetric transformations) of the MSSM is then [16]

$$W_{\text{MSSM}} = \bar{u}\mathbf{y}_{\mathbf{u}}QH_u - \bar{d}\mathbf{y}_{\mathbf{d}}QH_d - \bar{e}\mathbf{y}_{\mathbf{e}}LH_d + \mu H_u H_d , \quad (1.46) \{ ? \}$$

522 where  $H_u, H_d, Q, L, \bar{u}, \bar{d}, \bar{e}$  are the superfields defined in Table 1.1. The  $\mathbf{y}$  terms are Yukawa  
 523  $3 \times 3$  matrices which act on the different families. It is important to note that the up-type  
 524 quarks couple to the up-type Higgs  $H_u$ , while the down-type quarks and leptons couple

<sup>7</sup>A gauge anomaly is a linear divergence that occurs in diagrams containing a fermion loop with three gauge bosons (total) in the initial and final states. In the Electroweak model, the sum of the fermion contributions cancel the anomaly. Interestingly, the requirement of anomaly cancellation is only achieved in the SM is achieved only by requiring there be three types of color in QCD.

525 to the down-type Higgs. This feature has large phenomenological consequences, which are  
 526 discussed in 1.3.2. The scalar portion of the  $W_{\text{MSSM}}$  potential defines the spontaneous  
 527 symmetry breaking. Similar to the scalar potential  $V$  symmetry breaking of Section 1.1.3,  
 528 the potential of  $V$  at the minimum is found<sup>8</sup> to be

$$\begin{aligned} V = & \quad (|\mu|^2 + m_{H_u}^2)|H_u^0|^2 + (|\mu|^2 + m_{H_d}^2)|H_d^0|^2 \\ & - (bH_u^0H_d^0 + c.c.) + \frac{1}{8}(g^2 + g'^2)(|H_u^0|^2 - |H_d^0|^2)^2. \end{aligned} \quad (1.47) \quad \text{[eq:MSSMScalarP]}$$

Under suitable choices<sup>9</sup> of the parameters in Equation 1.47, the up-type and down-type neutral Higgs fields acquire a VEV,  $\nu_u$  and  $\nu_d$ , respectively. The VEVs are related to the VEV of electroweak symmetry breaking (Equation 1.41) in the SM,

$$\nu_u^2 + \nu_d^2 = \nu^2 = \frac{2M_Z^2}{g^2 + g'^2} \approx (174 \text{ GeV})^2.$$

The ratio of the VEVs is expressed as

$$\tan \beta \equiv \frac{\nu_u}{\nu_d},$$

529 which is an important parameter of the MSSM. As there are two complex doublets, there are  
 530 a total of eight degrees of freedom in the MSSM Higgs sector. After the symmetry breaking,  
 531 three of the degrees of freedom are (like the Standard Model) eaten by the  $W^\pm$  and  $Z$  weak  
 532 gauge bosons. The remaining five degrees of freedom create five massive Higgs bosons: two  
 533 CP-even neutral scalars  $h^0$  and  $H^0$ , a CP-odd neutral scalar  $A^0$ , and two (positive and  
 534 negative) charged scalars  $H^\pm$ . The masses are of the different Higgs mass eigenstates are  
 535 related to each other and  $\tan \beta$  at tree level by

$$m_{h^0}^2 = \frac{1}{2}(m_{A^0}^2 + m_Z^2 - \sqrt{(m_{A^0}^2 - m_Z^2)^2 + 4m_Z^2m_{A^0}^2 \sin^2(2\beta)}) \quad (1.48) \quad \text{[eq:MSSMLittleH]}$$

$$m_{H^0}^2 = \frac{1}{2}(m_{A^0}^2 + m_Z^2 + \sqrt{(m_{A^0}^2 - m_Z^2)^2 + 4m_Z^2m_{A^0}^2 \sin^2(2\beta)}). \quad (1.49) \quad \text{[eq:MSSMHiggs0]}$$

It can be seen that the tree level mass  $m_{h^0}$  of Equation 1.48 is bounded from above by  $m_{h^0} < m_Z |\cos(2\beta)| < 90 \text{ GeV}/c^2$ . If this is true the model would have been excluded by LEP (see next section). However, there are important quantum corrections to  $m_{h^0}$  from the top-quark and top-squark loop diagrams which increase  $m_{h^0}$ . The Yukawa couplings in the MSSM depend on  $\tan \beta$ . The relationships for the most massive members of each family are

$$m_t = y_t v \sin \beta, \quad m_b = y_b v \cos \beta, \quad m_\tau = y_\tau v \cos \beta. \quad (1.50) \quad \text{[eq:YukawaTanBeta]}$$

---

<sup>8</sup> A clever choice of the  $SU(2)_L$  gauge has removed any contributions from the charged fields. The charged Higgs fields cannot have a VEV without breaking  $U(1)_{em}$ .

<sup>9</sup>See Chapter 7 of [16] for a detailed overview.

536 The Yukawa couplings are free parameters determined by experimentally observed masses.  
 537 This means that when  $\tan\beta$  is large ( $\beta \rightarrow \pi$ ), the Yukawa terms  $y$  for the  $b$  quarks and  $\tau$   
 538 leptons must be enhanced to maintain the observed masses. The effect of  $\tan\beta$  on the Higgs  
 539 mass spectrum and couplings in the MSSM will be discussed further in Section 1.3.2.

## 540 §1.3 Searches for the Higgs boson

?<sec:PreviousSearches>? The potential discovery of the Higgs boson is one of the biggest prizes in science today.  
 541 Dozens of experiments, thousands of scientists and billions of dollars (a human hierarchy  
 542 problem...) have been spent in efforts to discovery the Higgs. In this section we discuss how  
 543 the Higgs and MSSM) could appear in modern colliders (with an emphasis on the LHC)  
 544 and current the limits placed on the Higgs by the LEP and Tevatron experiments.

### 546 §1.3.1 Standard Model Higgs boson phenomenology

(sec:SMHiggsPhenom) The phenomenology of the Higgs boson is strongly coupled to its relationship with mass. The coupling of the Higgs to the fermions is determined by the Yukawa terms (Equation 1.35) in the Lagrangian. Taking the electron as an example, after symmetry breaking, the Yukawa term is found to be

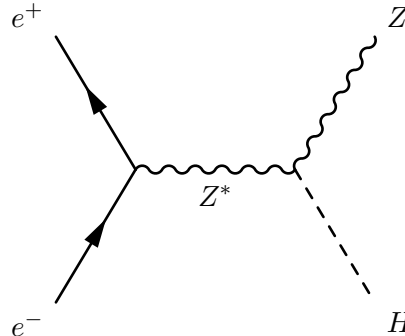
$$\mathcal{L}_e = -\frac{G_e}{\sqrt{2}}(\nu + H(x))\bar{e}e = -\frac{G_e\nu}{\sqrt{2}}\bar{e}e - \frac{G_e}{\sqrt{2}}H(x)\bar{e}e. \quad (1.51)$$

The value of  $G_e$  is a free parameter of the theory and is thus determined by the measurement of the electron mass and  $\nu$ , the VEV of the Higgs field

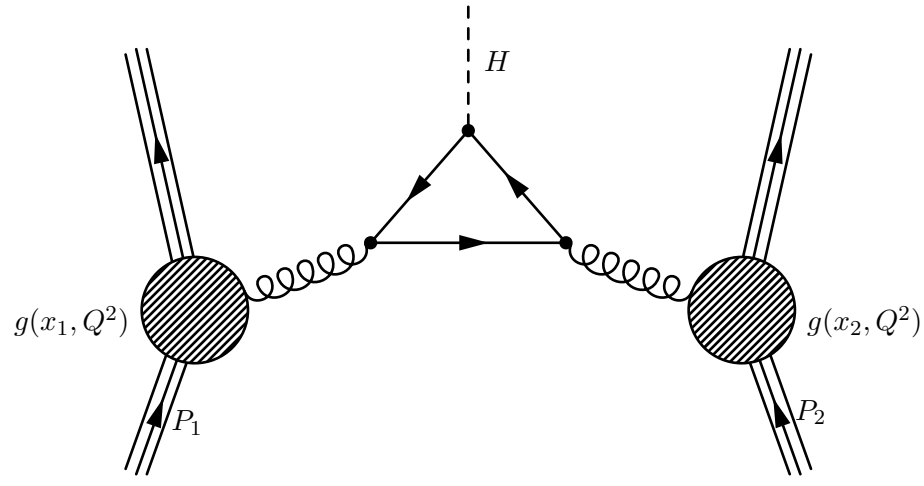
$$\frac{G_e\nu}{\sqrt{2}} = \frac{m_e}{\nu}. \quad (1.52)$$

547 The left-hand side of Equation 1.52 is the same as the constant in the electron–Higgs  $H(x)\bar{e}e$   
 548 coupling term in Equation 1.51. Therefore the coupling between the fermions and Higgs  
 549 boson is proportional to their mass! This remarkable fact shapes the possible production  
 550 modes and the branching fractions of Higgs decays.

551 The dominant modes of Higgs boson production depend on the type of experiment.  
 552 In general, Higgs production is favored through high–mass intermediate states, due to the  
 553 mass–proportional coupling. At the Tevatron and LEP experiments, which will be intro-  
 554 duced in the next section, the dominant SM Higgs production mode is “Higgstrahlung,”

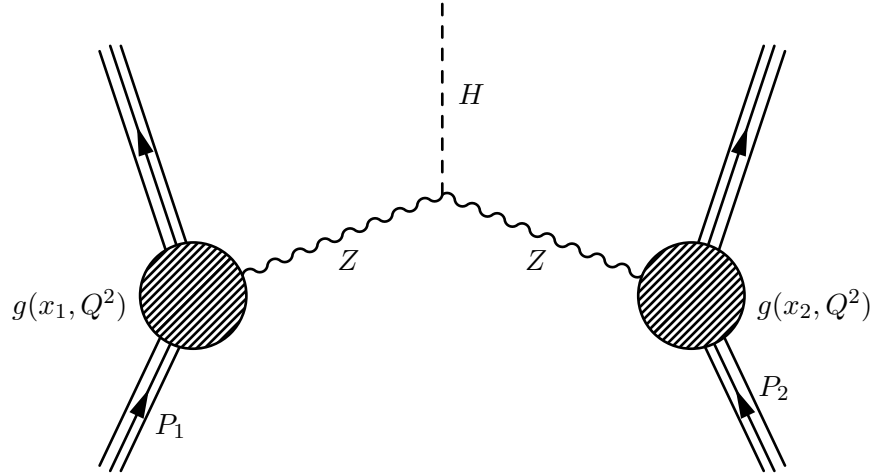


{fig:HiggsStrahlung}

Figure 1.5: Higgstrahlung production diagram at  $e^+e^-$  colliders

{fig:GluonFusion}

Figure 1.6: Gluon fusion Higgs production mechanism in a proton–proton collision. The Higgs mass coupling favors heavy quarks in the central loop. Image credit: [17]



{fig:VBFProdDiagram}

Figure 1.7: Vector boson fusion (VBF) Higgs production mechanism in proton–proton collisions. The VBF mechanism is notable for the lack of color–flow between the two incident protons.

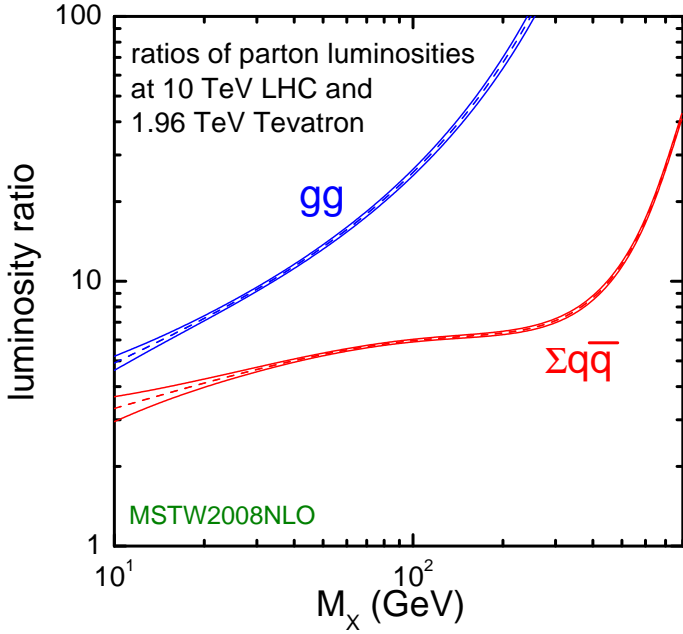


Figure 1.8: Ratio of the parton luminosity (the amount of luminosity contributed by the different species that compose the proton) of the LHC (at  $\sqrt{s} = 10$  TeV) and the Tevatron. The large increase in gluon–gluon luminosity affects the favored production mechanisms of the Higgs boson.

(fig:GluonLumiRatio)

555 where a virtual  $W^\pm$  or  $Z$  gauge boson is produced and then radiates a Higgs boson. Hig-  
 556 gstrahlung is illustrated in Figure 1.3.1. At the Large Hadron Collider, higher gluon lumi-  
 557 nosities (See Figure 1.8) result in the favored cross section being “gluon fusion,” (illustrated  
 558 in Figure 1.3.1) where two gluons from the incident protons combine in a quark (dominated  
 559 by the massive top quark) loop which then radiates a Higgs boson. Another important  
 560 channel [18] is “vector boson fusion,” (Figure 1.3.1) where weak gauge bosons ( $W^\pm$  or  $Z$ )  
 561 are radiated from the incoming quarks and fuse to produce a Higgs. This is a notable chan-  
 562 nel due to the lack of “color-flow” (gluons) between the two protons, producing an event  
 563 with low central jet activity and two “tag-jets” in the forward and backward regions. The  
 564 theoretical cross sections for the SM Higgs at the LHC are shown in Figure 1.9.

565 The branching fractions of the different decay modes of the SM Higgs boson depend  
 566 strongly on the mass of the Higgs boson. In general, the Higgs prefers (due to the Yukawa  
 567 couplings) to decay pairs of the particles with the highest mass possible. Below the threshold  
 568 to decay to pairs of weak bosons ( $M_H < 160 \text{ GeV}/c^2$ ), the Higgs decays predominantly to  
 569 either  $b$ -quarks ( $b\bar{b}$ , 90%) or a pair of  $\tau$  leptons ( $\tau^+\tau^-$ ,  $\approx 10$ ). Above the  $W^\pm W^\mp$  threshold,

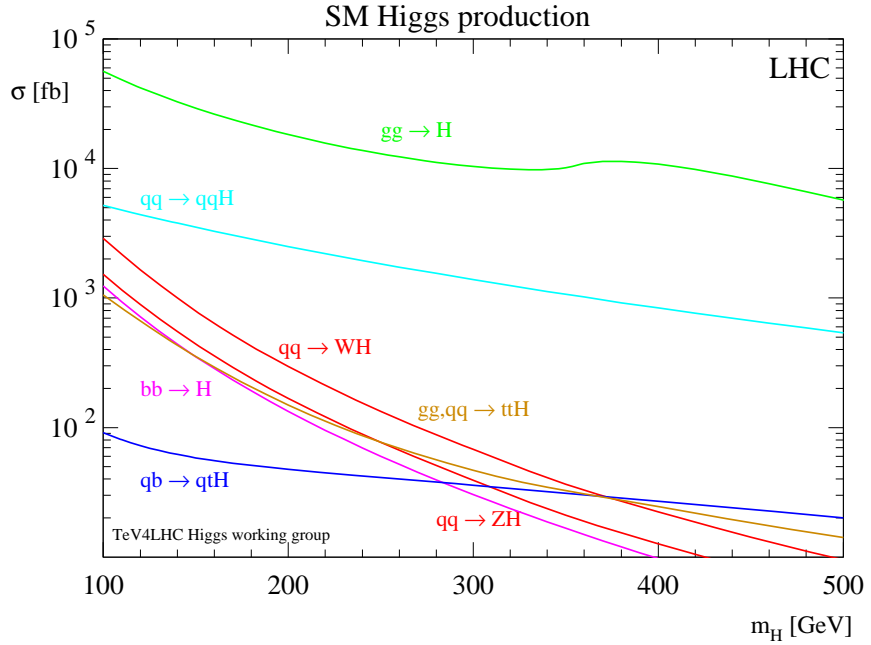


Figure 1.9: Cross section of the Standard Model Higgs boson versus the Higgs boson mass. The different curves give the contribution to the cross section from different production mechanisms. Source: [19].

(fig:LHCSMHiggsXsec)

570 decays to vector bosons ( $H \rightarrow W^\pm W^\mp$  and  $H \rightarrow ZZ$ ) dominate. The dependence of  
 571 branching fraction on  $M_H$  and the other rare decay modes are illustrated in Figure 1.10. For  
 572 low mass Higgs, the  $\tau^+\tau^-$  decay mode plays a particularly important role. The dominant  
 573 decay mode  $H \rightarrow b\bar{b}$ , suffers from enormous backgrounds from QCD jet production. It  
 574 is important to understand the magnitude of difference between expected Higgs boson  
 575 production and the rates of various backgrounds. Figure 1.11 illustrates the cross sections  
 576 for different SM processes at hadron colliders. The rate of Higgs production is many orders  
 577 of magnitude ( $\mathcal{O}(10^{-7})$ ) smaller than that of QCD production. It is important to therefore  
 578 design searches to use handles that can reject the vast majority of the uninteresting events  
 579 at hadron colliders.

### 580 §1.3.2 MSSM Higgs Phenomenology

(sec:MSSMHiggsPhenom)  
 581 The phenomenology of the Higgs sector of the MSSM is similar to the Standard Model in  
 582 some respects, but differs in some key aspects which have important implications for final  
 583 states involving  $\tau$  leptons and  $b$  quarks. When the parameter  $\tan\beta$  is large, the coupling

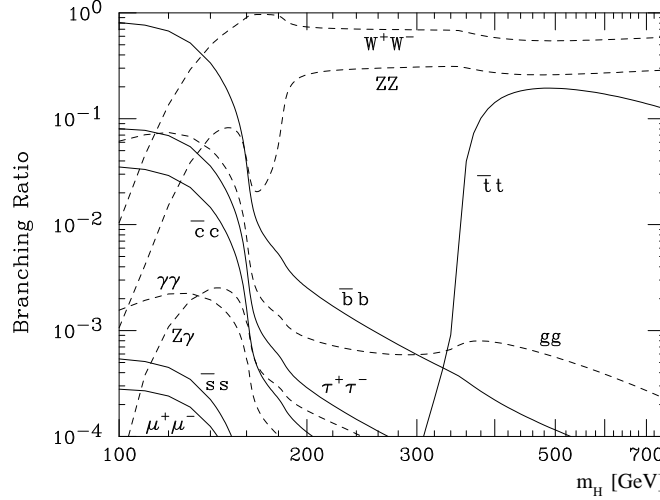


Figure 1.10: Branching fraction of the Standard Model Higgs bosons for different values of  $M_H$ . Source: [19].

`(fig:SMHiggsBR)`

584 factor between the Higgs and the down-type quarks and leptons (effectively the  $\tau$  and  $b$   
 585 quark) is enhanced by  $\tan \beta$ . The gluon–gluon cross section is therefore increased by  $\tan^2 \beta$ ,  
 586 where the top quark loop in Figure 1.3.1 is replaced by a ( $\tan \beta$  enhanced)  $b$  quark loop.  
 587 Additionally, MSSM Higgs production with associated  $b$ -quarks, illustrated in Figure 1.3.2,  
 588 becomes an important production mode. At tree-level, the MSSM can be defined by the  
 589 mass of the CP-odd Higgs  $m_{A^0}$  and  $\tan \beta$ . For a reasonably high  $\tan \beta$ , there is always one  
 590 CP-even Higgs ( $h^0$  or  $H^0$ ) which is mass-degenerate with the  $A^0$ . When  $\tan \beta$  and  $m_{A^0}$   
 591 are both large, associated  $b$  production dominates the total cross section [21]. The cross  
 592 sections of the different MSSM neutral Higgs bosons are shown in Figure 1.13. The  $\tan \beta$   
 593 enhancement of the MSSM Higgs coupling to the  $b$  quarks and  $\tau$  leptons cause the branching  
 594 fraction of all neutral MSSM Higgs to be  $H \rightarrow b\bar{b}$  (90%) and  $H \rightarrow \tau^+\tau^-$  (10%) across the  
 595 entire range of  $m_{A^0}$ . The enhanced production rate and the high branching fraction to  $\tau$   
 596 leptons make the MSSM Higgs decaying to  $\tau$  leptons an exciting and promising channel to  
 597 search for Higgses and Supersymmetric physics at colliders.

### 598 §1.3.3 Results from LEP and Tevatron

`(sec:lepAndTevatron)` The LEP and Tevatron experiments have both set limits on the existence of the Standard  
 599 Model and MSSM Higgs. Additionally, precision electroweak measurements give additional  
 600 hints on the prospects for both models.

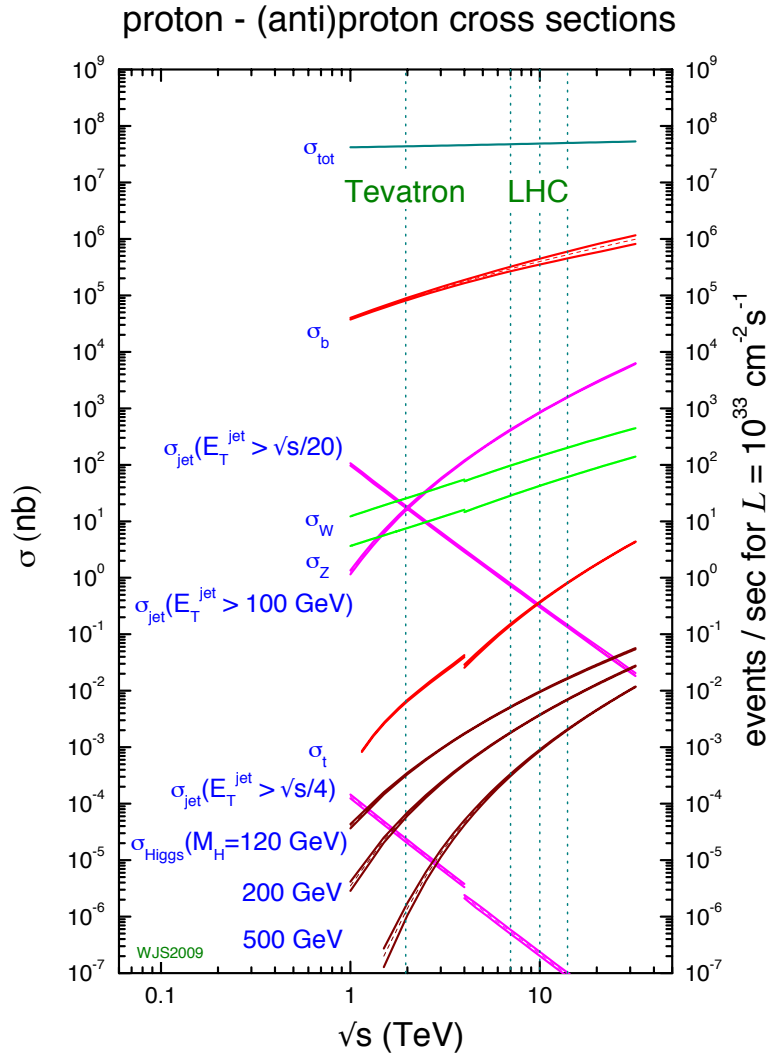
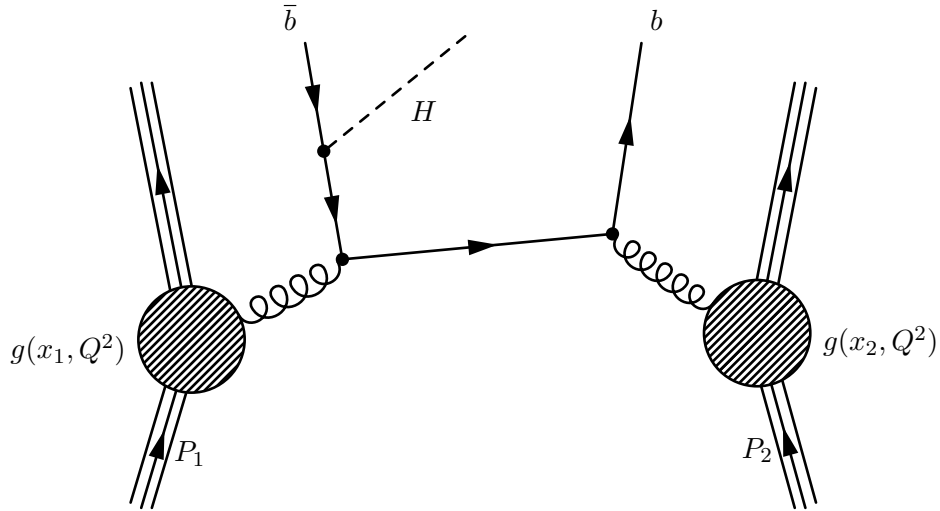


Figure 1.11: Cross sections of various processes at hadron colliders. The horizontal axis represents the center of mass energy of the collision. Of note is the vast difference in scales between Higgs production (maroon lines,  $\mathcal{O}(10^{-2})$  nb) and the QCD cross section to produce  $b\bar{b}$  pairs (red line,  $\mathcal{O}(10^4)$  nb). Source: [20].

hadronColliderCrossSections



g:AssociatedBProduction)

Figure 1.12: One possible diagram for an MSSM Higgs produced with associated  $b$ -quarks in a proton–proton collision.

Higgs Decay	$Z$ Decay
$b\bar{b}$	$q\bar{q}$
$\tau^+\tau^-$	$q\bar{q}$
$b\bar{b}$	$t\bar{t}$
$b\bar{b}$	$\nu\bar{\nu}$
$b\bar{b}$	$\mu^+\mu^-$
$b\bar{b}$	$e^+e^-$

(tab:LEPModes)

Table 1.3: Different channels used at LEP to search for Higgs bosons produced with the Higgstrahlung mechanism.

602        LEP was an  $e^+e^-$  collider at CERN and has effectively excluded the presence of a  
 603        low (less than 114  $GeVcc$ ) mass Higgs boson. The dominant SM Higgs production mode  
 604        at LEP is Higgstrahlung, where the Higgs is produced in association with a  $Z$  boson (see  
 605        Figure 1.3.1). The search at LEP utilized a number of different decay channels [19]. The  
 606        decay channels used in the LEP search are summarized in Table 1.3.3.

607        The results using all channels from the four LEP experiments<sup>10</sup> have been combined into  
 608        a single limit, shown in Figure 1.14. The analysis sets a limit on the ratio  $\xi^2 = (gh_{ZZ}/gh_{HZZ})^2$ ,  
 609        the upper limit on the  $HZZ$  coupling divided by the prediction of the Standard Model. For

<sup>10</sup>ALEPH, DELPHI, L3, and OPAL

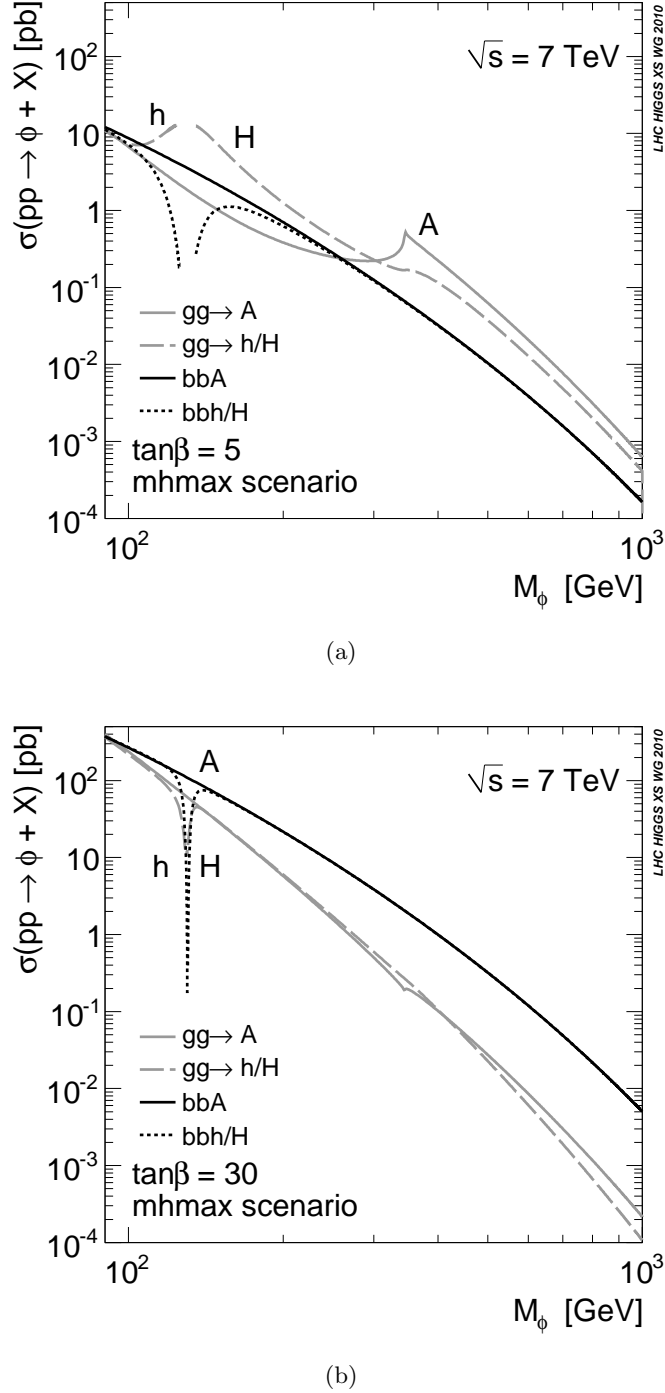


Figure 1.13: Cross sections for the different MSSM Higgs bosons versus  $m_{A^0}$  in the  $m_{hmax}$  benchmark scenario [22] scenario for  $\tan\beta = 5$  (a) and  $\tan\beta = 30$  (b). Source: [21]

MSSMXSectionsTanBeta

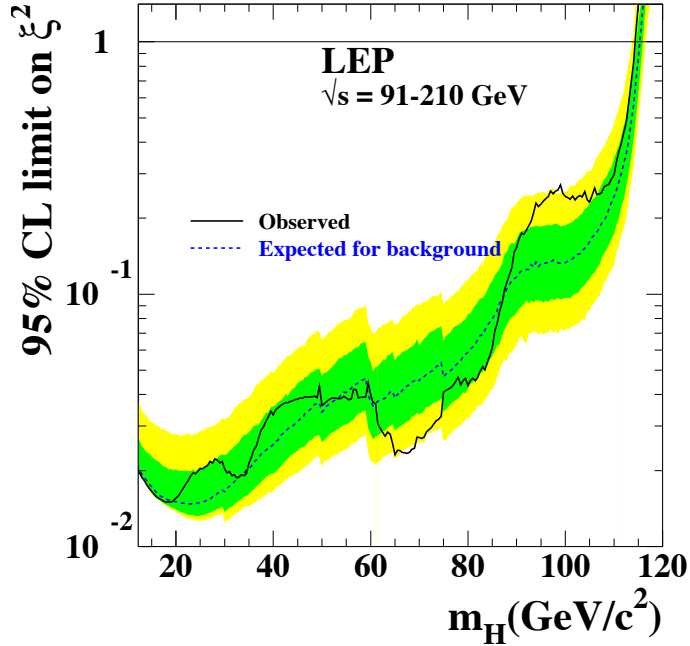


Figure 1.14: Combined LEP upper limit set on the quantity  $\xi^2 = (g_{HZZ}/g_{HZZ})^2$  at 95% confidence level. Regions where the observed ratio is less than one exclude the Standard Model. The dashed line gives the expected limit for the null (background only) hypothesis, with the green and yellow bands representing the expected variance at one and two sigma, respectively, of the limit. The solid line is the observed limit from the combined LEP data. Reference: [19]

(fig:LEPHiggsLimit)

610    Higgs masses below  $114 \text{ GeV}/c^2$ , the ratio is below unity at the 95% confidence level, ruling  
 611    out a Standard Model Higgs below that mass.

612    The Tevatron is a proton–antiproton collider with a center-of-mass energy of  $\sqrt{s} =$   
 613     $1.96 \text{ TeV}$ . There are two general purpose detectors at the Tevatron, CDF and DØ. The  
 614    dominant Higgs production modes at the Tevatron are Higgstrahlung and gluon fusion (see  
 615    Figure 1.3.1). For low mass ( $m_H < 135 \text{ GeV}/c^2$ ) Higgs bosons the dominant channel at  
 616    the Tevatron is the Higgstrahlung production mode and  $H \rightarrow b\bar{b}$  decays. Large multi-jet  
 617    backgrounds prevent the  $H \rightarrow b\bar{b}$  decay mode from being useful for searching for Higgs  
 618    bosons produced by gluon fusion. The  $H \rightarrow \tau^+\tau^-$  and  $H \rightarrow \gamma\gamma$  decays are additionally  
 619    used in an inclusive search at low mass, but do not dominate the search sensitivity. The  
 620    combined low-mass limit on the Standard Model Higgs from both Tevatron experiments is  
 621    shown in Figure 1.15. The Tevatron currently sets an upper limit on the SM Higgs cross

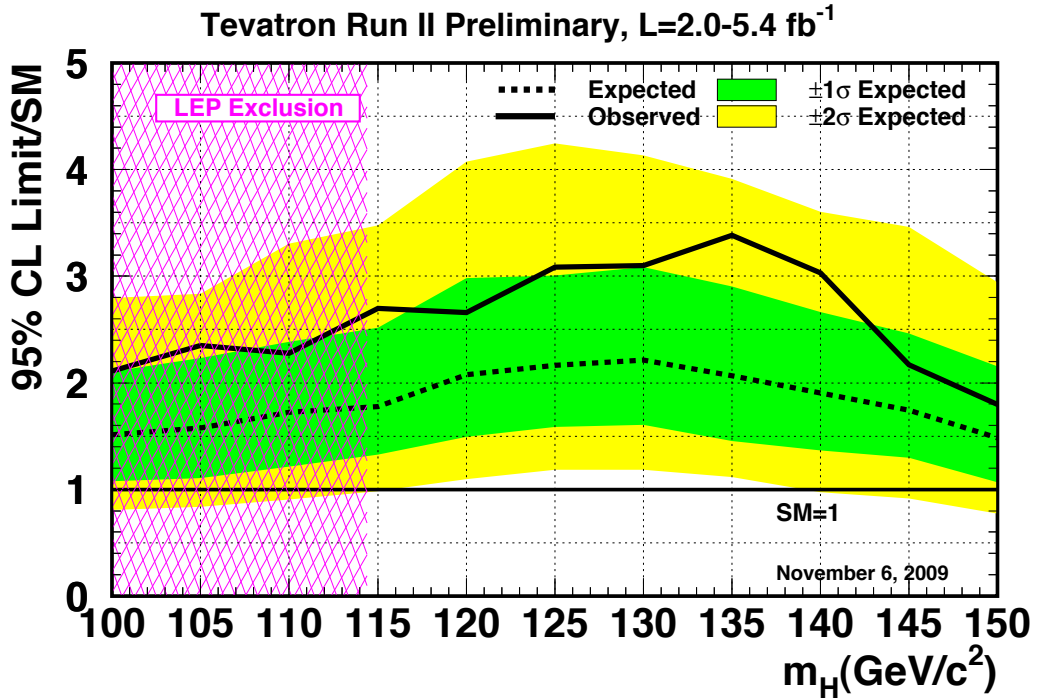


Figure 1.15: Combined CDF and D $\emptyset$  RunII upper limit on the cross section of a Standard Model-like Higgs boson. The LEP limit is shown in pink. Reference: [19]

atronLowMassHiggsLimit)

622 section of about 2.5 times the Standard Model expectation.

623 When ( $m_H < 135$  GeV/ $c^2$ ) the  $H \rightarrow W^+W^-$  decay mode becomes significant. Low  
 624 di–boson backgrounds allow this decay mode to probe both Higgstrahlung and gluon fusion  
 625 production modes. The combined results of the CDF and D $\emptyset$  searches using the  $W^+W^-$   
 626 have decay mode recently excluded (See Figure 1.16) a Standard Model Higgs with a mass  
 627 between 162 and 166 GeV/ $c^2$ . This is the first exclusion in Standard Model Higgs mass  
 628 parameter space since the LEP result.

629 Analyses at LEP and Tevatron have also addressed excluded regions of the MSSM. At  
 630 LEP, the dominant production modes of the MSSM Higgs bosons are Higgstrahlung and  
 631 pair production, where  $e^+e^- \rightarrow h^0A^0$  or  $H^0A^0$ . For the Higgstrahlung production mode,  
 632 the Standard Model search can be reinterpreted in terms of the MSSM. To address the pair  
 633 production mode, searches were performed in the  $e^+e^- \rightarrow h^0A^0 \rightarrow b\bar{b}b\bar{b}$  and  $\tau^+\tau^-q\bar{q}$  decay  
 634 modes. Finally, LEP is also sensitive to at low  $m_{A^0}$  and high  $\tan\beta$  to associated production,  
 635  $e^+e^- \rightarrow \{\bar{\phi}$ , where the associated fermions  $\{\$  are  $b$ –quarks or tau leptons. The combined

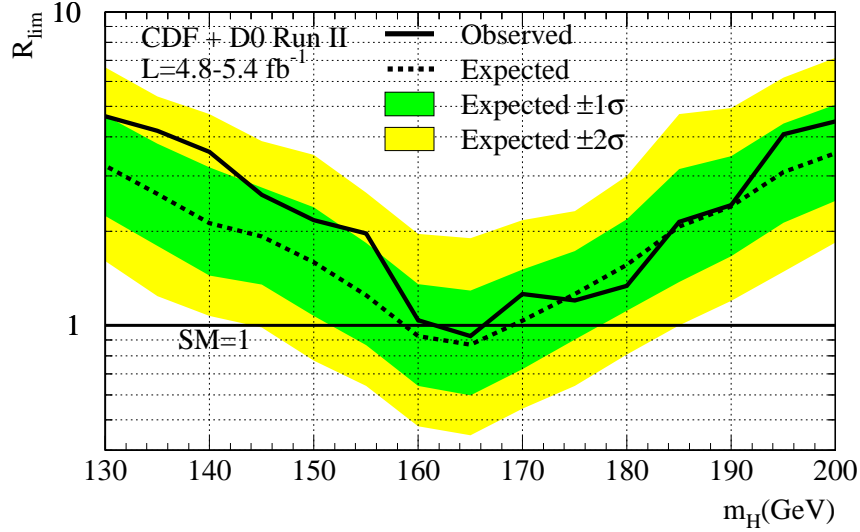


Figure 1.16: Combined CDF and DØ RunII upper limit on the cross section of a Standard Model-like Higgs boson using the  $H \rightarrow W^+W^-$  decay mode. The Standard Model is excluded for Higgs boson masses between 162 and 166  $\text{GeV}/c^2$ . Reference: [19]

tevatronHighMassHiggsLimit)

636 limits from LEP in the  $m_{A^0} - \tan \beta$  plane are shown in Figure 1.17.

637 At the Tevatron, CDF and DØ have set a combined limit on the MSSM using the  
 638 inclusive  $H \rightarrow \tau^+\tau^-$  channel. The analysis presented in this thesis is very similar to the  
 639 approaches used at the Tevatron. Results from the Tevatron have excluded the MSSM for  
 640  $\tan \beta$  greater than approximately 35 for MSSM Higgs mass  $m_{A^0} < 200$   $\text{GeV}/c^2$ . The full  
 641 exclusion plot for the  $m_h$ -max and “no mixing” MSSM benchmark scenarios are shown in  
 642 Figure 1.18.

## 643 §1.4 The Physics of the Tau Lepton

644 As discussed in sections 1.3.1 and 1.2.3, the  $\tau$  lepton is an important probe of Higgs physics.  
 645 The  $\tau$  lepton has some unusual properties which make it particularly challenging at hadron  
 646 colliders. With a mass of 1.78  $\text{GeV}/c^2$ , the  $\tau$  lepton is heaviest of the leptons. The nominal  
 647 decay distance  $c\tau$  of the  $\tau$  lepton is 87  $\mu\text{m}$ , which in practice means that the  $\tau$  will always  
 648 decay before reaching the first layer of the detector. Tau decays can be effectively classified  
 649 into two types. “Leptonic” decays consist of a  $\tau$  decaying to a light lepton ( $\ell = e, \mu$ ) and two  
 650 neutrinos  $\tau^+ \rightarrow \ell^+ \nu_\tau \bar{\nu}_\ell$ . “Hadronic” decays consist of a low-multiplicity collimated group of  
 651 hadrons, typically  $\pi^\pm$  and  $\pi^0$  mesons. The hadronic decays of the  $\tau$  lepton compose approx-

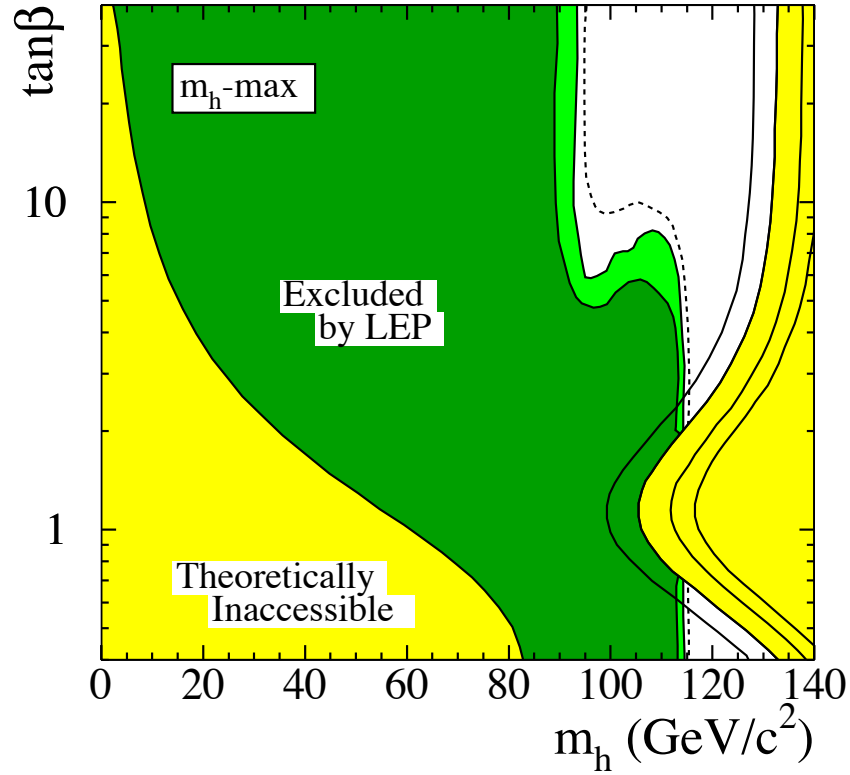


Figure 1.17: Combined LEP limits on the MSSM. The results are interpreted in the context of the  $m_h$ -max benchmark [22] scenario of the MSSM. Reference: [19]

(fig:LEPMSSMLimits)

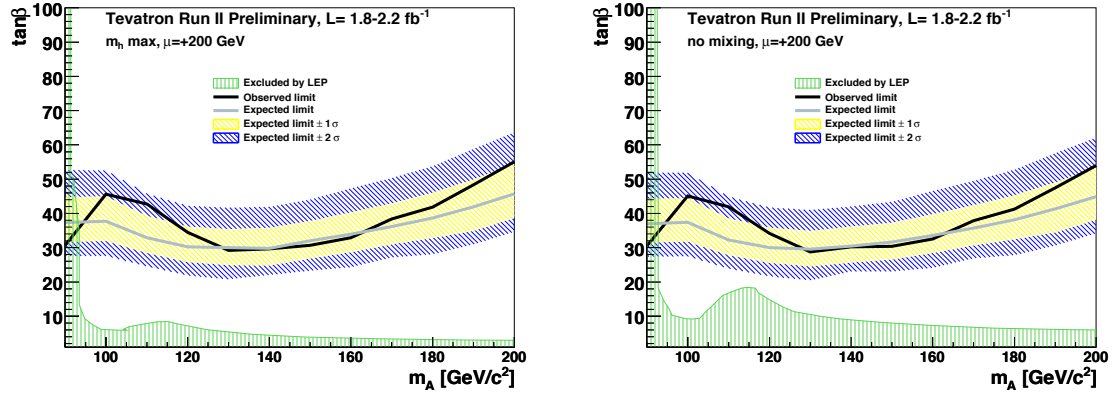


Figure 1.18: Combined Tevatron limits on the MSSM. The grey line and blue and yellow bands give the expected limit and its one and two sigma contours. The black line is the observed limit. The results are interpreted in the context of the  $m_h$ -max benchmark (left) and “no mixing” (right) MSSM scenarios. The limit from LEP is shown in green. Reference: [19]

(fig:TevMSSMLimits)

Visible Decay Products	Resonance	Mass ( MeV/ $c^2$ )	Fraction [19]
Leptonic modes			
$e^- \nu_\tau \bar{\nu}_e$	-	0.5	17.8%
$\mu^- \nu_\tau \bar{\nu}_\mu$	-	105	17.4%
Hadronic modes			
$\pi^- \nu_\tau$	-	135	10.9%
$\pi^- \pi^0 \nu_\tau$	$\rho$	770	25.5%
$\pi^- \pi^0 \pi^0 \nu_\tau$	$a1$	1200	9.3%
$\pi^- \pi^- \pi^+ \nu_\tau$	$a1$	1200	9.0%
$\pi^- \pi^- \pi^+ \pi^0 \nu_\tau$	$a1$	1200	4.5%
Total			94.4%

{tab:decay'modes}

Table 1.4: Resonances and branching ratios of the dominant decay modes of the  $\tau$  lepton. The decay products listed correspond to a negatively charged  $\tau$  lepton; the table is identical under charge conjugation.

652 imately 65% of the  $\tau$  lepton branching fraction, with the remainder shared approximately  
 653 equally by the leptonic decays. The branching fractions for the leptonic and most common  
 654 hadronic decays are shown in table 1.4.

655 The tau is also a challenging object in that the decay of the tau always includes neu-  
 656 trinos. The associated neutrinos are weakly interacting and do not create a signal in any  
 657 detector at CMS. The only sign that the neutrinos are there is an imbalance in the total  
 658 transverse<sup>11</sup> energy in the event. This thesis will describe a novel way to reconstruct the  
 659 neutrinos associated to tau decays in Chapter 4.

The lifetime of the tau is  $c\tau = 87$   $\mu\text{m}$ . In practice, this means that a tau with produced  
 with energy  $E$  travels on average

$$\gamma c\tau = \frac{E}{1.78 \text{ GeV}} 87 \text{ } \mu\text{m}$$

660 before decaying in the detector. These lengths are comparable to the resolution of the CMS  
 661 tracker, therefore it is possible to reconstruct a vertex corresponding to a tau decay that is  
 662 displaced with respect to the primary vertex. This can be used as an additional discriminant

---

<sup>11</sup>At proton colliders, the constituent quarks/gluons of the proton share the total proton momentum. As the total fraction of momentum carried by the parton involved in a hard collision is unknown, longitudinal momentum is not conserved.

663 against QCD, which is expected to decay promptly. Furthermore, in Chapter 4 we will see  
664 it may be possible to use it to reconstruct the associated neutrinos.

665

## Chapter 2

666

# The Compact Muon Solenoid Experiment

&lt;ch:detector&gt;

667 The Compact Muon Solenoid (CMS) Experiment is a “general purpose” particle detector  
 668 designed to measure collision events at the Large Hadron Collider (LHC), a proton–proton  
 669 synchrotron located at the CERN laboratory in Geneva, Switzerland. The design goals of  
 670 the CMS experiment are [23], in order of priority:

- 671     • Good muon identification and momentum resolution over a wide range of momenta  
       and angles, good dimuon mass resolution ( $\approx 1\%$  at 100 GeV/ $c^2$ ), and the ability to  
       determine unambiguously the charge of muons with  $p < 1$  TeV/ $c$ ;
- 674     • Good charged-particle momentum resolution and reconstruction efficiency in the in-  
       ner tracker. Efficient triggering and offline tagging of  $\tau$ ’s and  $b$ -jets, requiring pixel  
       detectors close to the interaction region;
- 677     • Good electromagnetic energy resolution, good diphoton and dielectron mass resolution  
       ( $\approx 1\%$  at 100 GeV/ $c^2$ ), wide geometric coverage,  $\pi^0$  rejection, and efficient photon and  
       lepton isolation at high luminosities;
- 680     • Good missing-transverse-energy and dijet-mass resolution, requiring hadron calorime-  
       ters with a large hermetic geometric coverage and with fine lateral segmentation.

682 The detector uses a hermetic design that maximizes the solid-angle of the fiducial region to  
 683 capture as much information about the collisions as possible. The general geometry of the  
 684 detector is cylindrical. A cutaway diagram of the detector is shown in Figure 2.1. Each of  
 685 the sub-detector components consists of “barrel” and “endcap” components. As its name  
 686 suggests, the detector is centered around a four Tesla superconducting solenoid magnet.  
 687 The individual sub-detectors of CMS are arranged in a manner that permits identification

688 of different species of particles. The central (closest to interaction point) sub-detector are  
 689 the charged particle tracking systems (the “tracker”). The tracker is designed to be a *non-*  
 690 *destructive* instrument, which means that ideally that the momentum of particles are un-  
 691 changed after passing through it. Outside of the tracker is the electromagnetic and hadronic  
 692 calorimeters, which are abbreviated ECAL and HCAL, respectively. The calorimeter is a  
 693 *destructive* detector, and is designed such that visible incident particles are completely ab-  
 694 sorbed. The outer layers of CMS are designed to measure muons, the one<sup>1</sup> species of particle  
 695 that is immune to the effects of the calorimeter. The arrangement of destructive and non-  
 696 destructive sub-detectors facilitates the identification of different types of particles. This  
 697 concept is illustrated in Figure 2.1(b). In this chapter we give an brief overview of the LHC  
 698 machine, and then describe the individual sub-detector systems of CMS.

## 699 §2.1 The Large Hadron Collider

700 The Large Hadron Collider is a proton–proton synchrotron, with a design collision energy  
 701 of 14 TeV. At the time of this writing (and for the foreseeable future), the LHC is the  
 702 world’s largest and highest energy particle accelerator. A synchrotron is a machine that  
 703 accelerates beams of charged particles by using magnets to steer them in a circle through  
 704 radio-frequency resonating cavities which accelerate the particles. As the LHC is a collider,  
 705 there are two beams that are accelerated in opposite directions. The maximum beam energy  
 706 of a synchrotron is determined by its radius and the maximum strength of the magnetic  
 707 fields used to bend the path of the beam. The dipole magnets used by the LHC to steer the  
 708 particles are superconducting niobium–titanium. To maintain them in a superconducting  
 709 state, they are cooled using superfluid liquid helium to 1.9 Kelvin. To store the beam at the  
 710 injection energy of 450 GeV, the magnetic dipole fields must be maintained at 1/2 Tesla. As  
 711 the energy of each beam energy is increased to its (design) maximum of 7 TeV, the dipole  
 712 fields are ramped to a maximum field of over 8 Tesla.

---

<sup>1</sup>Neutrinos of course fulfill this requirement as well, but are so weakly interacting that they are effectively invisible.

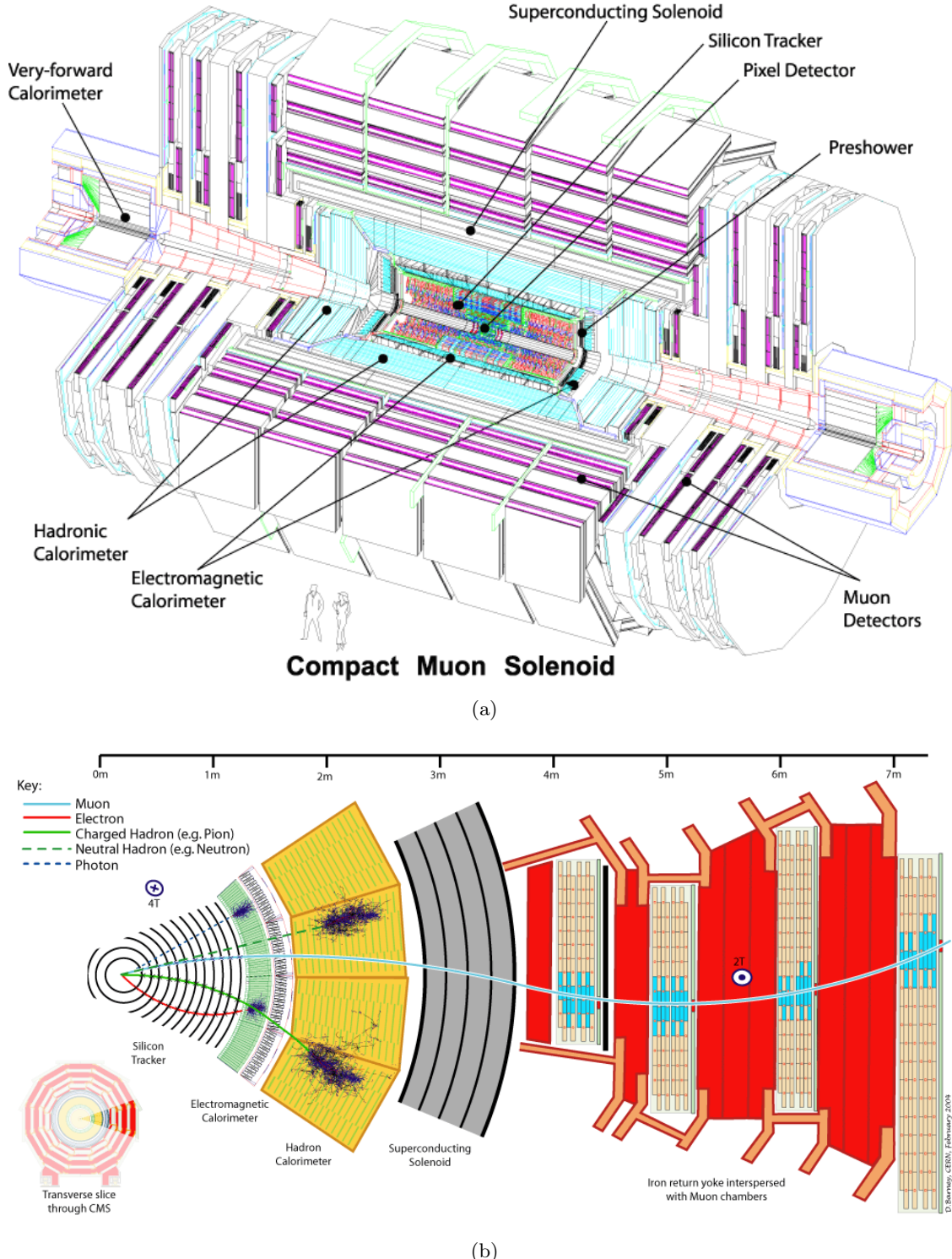


Figure 2.1: Figure (a), top, shows a schematic drawing of the CMS detector. The individual sub-detectors are labeled. Two humans are shown in the foreground for scale. Figure (b) shows a radial cross section of the detector and demonstrates how the (non-)destructiveness of different sub-detectors facilitates particle identification.

(fig:AllCMSCutaways)

## 713 §2.2 Solenoid Magnet

?<sec:Magnet>? The four Tesla field of the CMS solenoid magnet is a critical factor in ability of CMS to precisely measure collisions at the LHC. The momentum of charged particles is measured in the detector by examining the curvature of the particles path as it travels through the magnetic field. The radius of curvature  $r$  of a charged particle in a magnetic field is given by

$$r = \frac{p_{\perp}}{|qB|}, \quad (2.1) \boxed{\text{eq:LarmorRadius}}$$

714 where  $q$  is the charge of the particle,  $B$  is the magnetic field, and  $p_{\perp}$  is the component of the  
 715 particle's relativistic momentum perpendicular to the direction of the magnetic field. From  
 716 Equation 2.1, it is evident that the ability to measure high momentum charged particles (a  
 717 critical goal of CMS) requires a high magnetic field. Even at very high particle energies where  
 718 the resolution becomes poor, the strength of the magnetic field is still very important for  
 719 identifying the bending direction of the particle; the direction corresponds to the particle's  
 720 electric charge. Furthermore, the homogeneity of the magnetic field is important to minimize  
 721 systematic errors in the measurement of tracks.

722 The CMS solenoid is extremely large. The radial bore of the magnet is 6.3 meters; the  
 723 magnet is 12.5 meters in length and weighs 220 tons. The large bore of the magnet allows  
 724 the tracker and calorimeter systems to be located inside the solenoid. The internal windings  
 725 of solenoid is arranged in four layers to increase the total field strength and are cooled by  
 726 liquid helium to a temperature of 4.5 Kelvin. The windings are magnetically coupled to  
 727 the support superstructure. This coupling allows the magnetic to heat uniformly during a  
 728 “quench<sup>2</sup>” event, reducing localized stresses. The nominal current at full field of the solenoid  
 729 is 19.14 kA. The solenoid itself is surrounded by an iron return yoke with a total mass of  
 730 10,000 tons. The return yoke surrounding the solenoid minimizes the fringing field. The  
 731 muon detector system is interspersed inside the yoke, and takes advantage of the field in  
 732 the yoke to measure the momentum and charge of muons.

---

<sup>2</sup>A quench event occurs when some part of the magnet is suddenly no longer in a superconducting state. The coil becomes resistive and the large current in the magnet creates large amounts of heat.

## 733 §2.3 Charged Particle Tracking Systems

734 ?<sec:Tracker>? The charged particle tracking system measures the trajectories of charged particles emerging  
 735 from the event. The tracker measures the trajectory of a charged particle by measuring  
 736 “hits” along the trajectory. Each hit corresponds to the global position of the trajectory  
 737 on a given surface. The trajectory can then be reconstructed by a helix to the points.  
 738 The tracker is designed to have a resolution that permits the reconstruction of “secondary  
 739 vertices” in  $b$ –quark and  $\tau$  lepton decays. To accomplish this, there are two types of tracking  
 740 detectors in CMS. The “pixel detector” composes the inner layers (three in the barrel, two in  
 741 the endcaps). The pixel detector is situated as close as possible (4.4 cm) to the interaction  
 742 point and has a very high resolution. Outside of the pixel detector is the silicon strip tracker,  
 743 with ten layers in the barrel and 12 layers in the endcaps. A secondary vertex occurs when a  
 744 particle is semi-stable, traveling some non-negligible distance in the detector, but decaying  
 745 before the first layer of the tracking system. The pixel and strip tracking detectors have a  
 746 fiducial region which extends to a pseudorapidity of approximately  $|\eta| \approx 2.5$ .

747 Both the pixel and strip trackers are silicon based. The principle of operation is similar  
 748 to that of a charged-coupled discharge (CCD) in a modern digital camera. The sensitive  
 749 portion of the detector is a silicon chip that is arranged with diode junctions formed by  
 750 a  $p$ –doped layer and an  $n$ –doped layer<sup>3</sup>. Each  $p - n$  junction is electrically isolated from  
 751 adjacent layers. The size of each junction region determines<sup>4</sup> the spatial resolution of the  
 752 sensor. In the pixel detector, each sensor region “pixel” is  $100 \times 150 \mu\text{m}^2$ . In the strip  
 753 tracker, The rear side of the chip is mounted to read-out electronics. During operation, a  
 754 high-voltage reverse bias is applied to each  $p - n$  junction to achieve full depletion. When  
 755 a charged particle passes through the detector, the diode-junction breaks down and the  
 756 readout system registers the hit.

757 The tracking system has been specifically designed for the high radiation environment  
 758 around the interaction point. The detector is cooled to  $-27^\circ\text{C}$  during operation to minimize

---

<sup>3</sup>The pixel detector actually uses a more complicated multi-layered scheme to improve radiation hardness. For details, see Section 3.2.2 of [23].

<sup>4</sup>Additionally, the size of the sensitive area needs to be small enough such that the hit occupancy during a typically LHC event is not too large, which would cause overlaps and spoil the ability to reconstruct tracks. The expected occupancy depends on the distance  $r^2$  from the interaction. The expected occupancy in the pixel detector for LHC collisions is  $10^{-4}$ .

**Fixme:** right

acronym

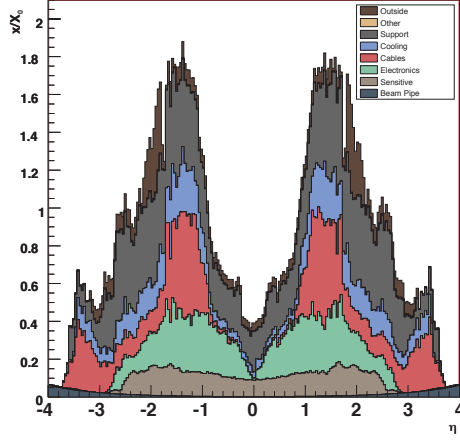


Figure 2.2: Material budget of the CMS tracker in units of radiation lengths  $X_0$ . The material budget is broken down into the contributions from the different components of the tracker. The amount of material is largest in the “transition region” between the barrel and endcap.

`fig:TrackerMaterialBudget`

759 damage. Radiation exposure produced in LHC collisions can change behavior of the tracking  
 760 detector in three ways. Over time, radiation can induce positive holes in oxide layers found  
 761 in the read-out electrons which increase the signal-to-noise ratio. In the sensor mass itself,  
 762 radiation damage changes the doping from  $n$  to  $p$  over time. The required voltage to deplete  
 763 the sensor will thus increase over time. The readout electronics, bias voltage supplies, and  
 764 cooling systems are designed to scale with the radiation damage and maintain a signal-to-  
 765 noise ration of 10:1 or greater for 10 years of LHC operation. The final radiation effect is not  
 766 an integrating effect. A “single event upset” is transient effect where an ionizing charged  
 767 particle passes through the readout electronics and changes the state of the digital circuitry.

768 In the ideal case, the tracker would be a non-destructive instrument. However, charged  
 769 particles can interact with the mass of the tracker (and its support infrastructure). These  
 770 interactions limit the resolution of the tracker. The amount of matter in the tracker is  
 771 referred to as the “material budget”. The material budget of the CMS tracker depends  
 772 heavily on the pseudorapidity  $\eta$  and is illustrated in Figure 2.2. The relatively large material  
 773 budget of the CMS tracker has two effects: charged particles can “multiple scattering,”  
 774 interacting with material in the tracker. This can cause “kinks” in the reconstructed track.  
 775 Hadronic particles (charged and neutral) can undergo “nuclear interactions,” which are

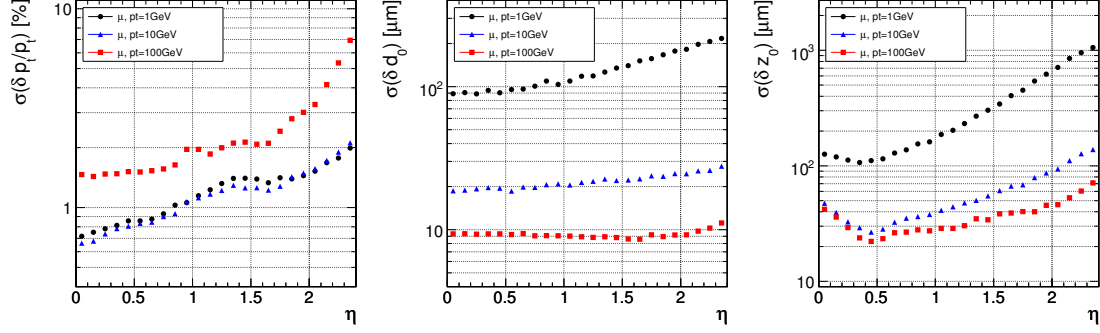


Figure 2.3: Expected resolutions of reconstructed transverse momentum (left), transverse impact parameter (center), and longitudinal impact parameter (right) versus absolute pseudorapidity  $|\eta|$ . The resolution is shown for three different cases of particle  $p_T$ , 1  $\text{GeV}/c$  (black), 10  $\text{GeV}/c$  (blue), and 100  $\text{GeV}/c$  (red).

(fig:ExpectedTrackerRes)

776 a hard collisions between the incident particle and the tracker material. This typically  
 777 produces a spray of hadrons from the point of interaction. Finally, the material budget can  
 778 cause “photon conversions.” A photon conversion occurs when a photon (which typically  
 779 does not interact with the tracker) converts into an electron–positron pair while passing  
 780 through matter in the tracker.

781 The expected (from simulation) impact parameter and transverse momentum resolu-  
 782 tion of the tracker is shown in Figure 2.3. The momentum scale of the tracker has been  
 783 measured [24] in 7 TeV 2010 CMS data using  $J/\psi \rightarrow \mu^+\mu^-$  decays and is found to agree  
 784 within 5% with the prediction from simulation. The impact parameter and vertex resolu-  
 785 tions have also been measured [25] in data and found to be in excellent agreement with the  
 786 simulation.

## 787 §2.4 Electromagnetic Calorimeter

788 The electromagnetic calorimeter (ECAL) of CMS is designed to measure the energy of par-  
 789 ticles which interact electromagnetically with high precision.<sup>5</sup> The ECAL is a *scintillation*  
 790 detector, and functions by counting the number of photons produced in an electromagnetic  
 791 shower inside a crystal. Upon entering the crystal, a charged particle or photon will inter-  
 792 act electromagnetically with the crystal, producing a shower of electrons and photons. The

---

<sup>5</sup>One of the design goals of the CMS experiment is to be able to conduct a search for Standard Higgs bosons decaying to pairs of photons. The branching fraction to photons is illustrated in Figure 1.10.

793 shower will expand until it consists entirely of photons. The crystal is optically clear, so  
 794 these photons travel to the rear face of the crystal where they are then counted by a pho-  
 795 tomultiplier. The number of detected photons can then be related to the energy that was  
 796 deposited in the crystal. At 18°C, about 4.5 photoelectrons will be produced per MeV of de-  
 797 posited energy. The ECAL has excellent solid angle coverage, extending to a pseudorapidity  
 798 of  $|\eta| = 3.0$ .

799 The ECAL uses lead tungstate ( $\text{PbWO}_4$ ) crystals as the scintillation medium. The  
 800 crystals have a very large density, which allows the calorimeter to be relatively compact.  
 801 To be able to correctly measure the energy of electrons and photons, an incident photon or  
 802 electron must be completely stopped by interactions with the calorimeter. The quantities  
 803 that determine if an electron or photon will be completely contained is the total depth of  
 804 the crystal, the crystal density, and the radiation length property  $X_0$  of the crystal. The  
 805 radiation length  $X_0$  is defined as the mean distance (normalized to material density) after  
 806 which an electron will have lost  $(1 - \frac{1}{e})$  of its energy. The  $\text{PbWO}_4$  crystals of the CMS  
 807 ECAL have a density of  $8.28 \text{ g/cm}^3$  and a depth of 230 mm. A single crystal thus has a  
 808 total radiation length of  $25.8 X_0$ , and will capture on average 99.9993% of the energy of an  
 809 incident electron. The front face of the crystal is  $22 \text{ mm} \times 22 \text{ mm}$ , which corresponds to an  
 810  $\eta - \phi$  area of  $0.00174 \times 0.00174$ . The Molière radius of a material is the average radial profile  
 811 size of an electromagnetic shower, and for  $\text{PbWO}_4$  is 2.2 cm. The fact that the Molière  
 812 radius is larger than the size of the individual crystals improves the spatial resolution of  
 813 the measurement. As the shower is shared between multiple crystals, the relative amounts  
 814 deposited in each crystal allows the true impact point to be determined with a resolution  
 815 smaller than the individual crystal size.

816 The transparency of the CMS ECAL crystals change as they are exposed to radia-  
 817 tion. However, at the working temperature of the ECAL (18°C), the crystal transparency  
 818 will naturally return to its nominal value. The transparency of the crystals thus decreases  
 819 during the course of a run of collisions, then increases during the following period collision-  
 820 less period. The changing transparency conditions need to be continuously monitored and  
 821 corrected for to ensure a stable detector response. The transparency of the crystals are  
 822 measured continuously using two lasers. One laser has wavelength  $\lambda = 400 \text{ nm}$  which cor-

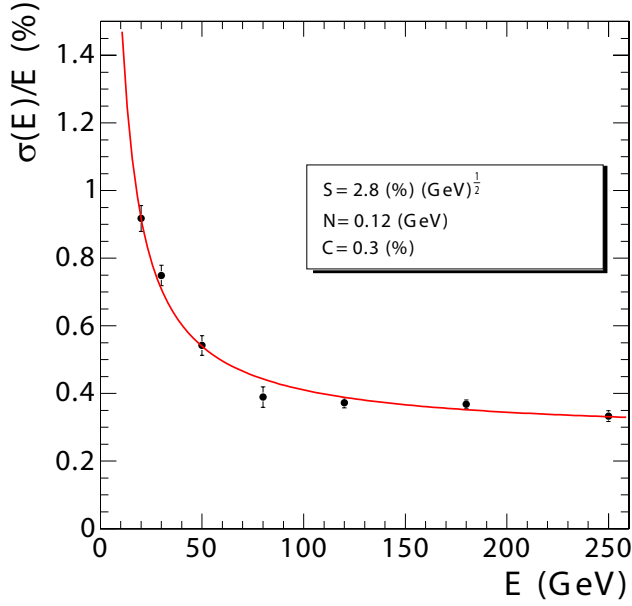


Figure 2.4: Energy resolution (in %) of the CMS ECAL measured at an electron test beam. The resolution depends on the incident energy of the electron. The points are fitted to function with the form given in Equation 2.2. The fitted parameters are given in the legend.

(fig:ECALResolution)

823 responds to the color of light produced in the scintillations and is sensitive to changes in  
 824 transparency. The other laser is in the near-infrared and is used to monitor the overall  
 825 stability of the crystal. The lasers synchronized to pulse between LHC bunch trains so the  
 826 transparency can be continuously monitored while collisions are occurring.

The energy resolution of the ECAL is given by

$$\left(\frac{\sigma}{E}\right)^2 = \left(\frac{S}{\sqrt{E}}\right)^2 + \left(\frac{N}{E}\right)^2 + C^2, \quad (2.2) \quad [\text{eq:ECALResolution}]$$

827 where  $S$  is a stochastic noise term (due to photon counting statistics),  $N$  is a noise term, and  
 828  $C$  is a constant term. The parameters of Equation 2.2 have been measured at an electron  
 829 test-beam (see Figure 2.4). The energy resolution is better than 1% for electron energies  
 830 greater than 20 GeV.

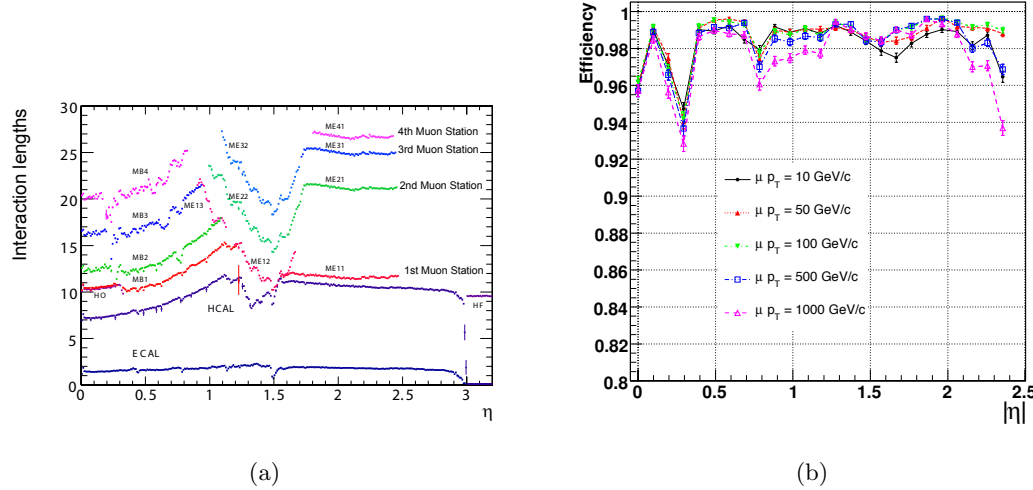
## 831 §2.5 Hadronic Calorimeter

?⟨sec:HCAL⟩?  
 832 The hadronic calorimeter (HCAL) surrounds the CMS ECAL and is located within the coil  
 833 of the CMS solenoid magnet. To ensure incident particles are completely contained within  
 834 the calorimeter volume, in the barrel region the HCAL employs a “tail-catcher”, an extra

835 layer of calorimetry outside of the magnet. The hadronic calorimeter measures the energy  
 836 of charged and neutral hadronic particles. The HCAL is a *sampling* calorimeter. Layers of  
 837 plastic scintillating tiles are interspersed between brass absorber plates. An incident hadron  
 838 produces a hadronic shower as it passes through the absorber. The particles in the shower  
 839 produce light as they pass through the scintillating tiles. Measuring the light produced in  
 840 each layer of tile allows the reconstruction of the radial profile of the shower which can be  
 841 related to the deposited energy. The response of the scintillator tiles are calibrated using a  
 842 radioactive source, either Cs<sup>137</sup> or Co<sup>60</sup>. Small stainless tubes permit the radioactive sources  
 843 to be moved into the center of the tile during calibration. The granularity of the HCAL is  
 844 0.087 × 0.087 and 0.17 × 0.17 in  $\eta - \phi$  in the barrel ( $|\eta| < 1.6$ ) and endcap ( $|\eta| > 1.6$ ),  
 845 respectively.

846 The outer HCAL (HO), or “tail catcher” is designed to capture showers which begin  
 847 late in the ECAL or HCAL and ensure they do not create spurious signals in the muon  
 848 system (“punch through”). The HO is installed outside of the solenoid magnet in the first  
 849 layer between the first two layers of the iron return yoke. The total depth of the HCAL,  
 850 including the HO is then 11.8 interaction lengths.

851 The HCAL includes a specially designed forward calorimeter (HF). The design of the  
 852 forward calorimeter is constrained by the extreme amount of radiation it is exposed to,  
 853 particularly at the highest rapidities. The active material of the HF are quartz fibers. The  
 854 fibers are installed inside grooves inside of a steel absorber. Charged particles created in  
 855 showers in the absorber create light in the fibers, provided they have energy greater than  
 856 the Cherenkov threshold. As Cherenkov light is created by  
 857 the passage of charged particles through matter, the HF design is not sensitive to neutrons  
 858 emitted by radionucleids that may be created in the absorber material during operation.  
 859 The fibers are grouped into two sets: one set of fibers are installed over the full depth of  
 860 the detector, the other only cover half the depth. A crude form of particle identification  
 861 is possible, as showers created by electrons and photons will deposit the majority of the  
 862 energy in the front of the detector.



detectorChapterMuonShit)?

Figure 2.5: The left figure, (a), illustrates the number of interaction lengths versus pseudorapidity  $\eta$  of material that must be traversed before reaching the different layers of the muon system. On the right, (b) shows the efficiency versus  $\eta$  to reconstruct a “global” muon for different transverse momenta.

## §2.6 Muon System

The ability to detect and measure muons is one of the most valuable tools an experimentalist has at a hadron collider experiment. Muons have particular properties that cause them to leave extremely signatures in the detectors.

- Muons are stable particles, for the typical energies and distances considered at a collider.

• Muons have non-zero charge, so their trajectories can be measured.

- Muons are heavy enough that they are “minimum ionizing particles,” in that they lose much less energy as they pass through material.

The approach to detecting muons is to build the detector to a thickness that typical particles (electrons, photons, hadrons) will not penetrate the outermost calorimeter. Any charged particle that is detected outside of this region can be identified as a muon. At CMS, the muon detection systems are built into the magnet return yoke outside of the CMS calorimeters and magnet, giving them excellent protection (illustrated in Figure 2.5(a)) against hadronic “punch-through.” The purity of particles that reach the muon system make it especially

878 effective as a “trigger” of interesting physics. The CMS muon system has the feature that  
 879 it additionally can trigger on the transverse momenta of muons. The CMS muon system  
 880 is composed of three types of detectors: drift tubes (DT), resistive plate chambers (RPC),  
 881 and cathode strip chambers (CSC).

882 A drift tube detector is of a tube filled with a mixture of argon (85%) and carbon  
 883 dioxide (15%) gas with a positively charged ( $V = +3.6$  kV) wire running through the  
 884 middle of the tube. When a charged particle passes through the tube, it ionizes some gas.  
 885 The free electrons are then drawn to the positively charged wire inside the tube, creating a  
 886 signal when reach it. The speed of the detector is limited by the “drift time,” the maximum  
 887 amount of time it may take for an electron to reach sensor wire. The precision of the spatial  
 888 measurement can be increased by recording the time at which each wire records a signal  
 889 and correlating the measurements across multiple tubes. The time resolution of the CMS  
 890 DTs is on the order of a few nanoseconds, allowing the DT to provide a trigger on a given  
 891 proton bunch crossing. The tubes in adjacent layers are offset by one half tube width to  
 892 take advantage of this effect and ensure there are no gaps in the fiducial region. In CMS, the  
 893 smallest unit of the DT system is the superlayer, which consists of four layers of tubes. A  
 894 DT chamber consists of three or two superlayers. The tubes in the two superlayers farthest  
 895 from the beam are oriented parallel to the beam and measured the bending of the muons in  
 896 the magnetic field. The inner superlayer is oriented orthogonally to the beam and measures  
 897 the longitudinal position of incident muons. There are four muon “stations” in the barrel  
 898 which contain DT chambers. The stations correspond to available areas in the magnetic  
 899 return yoke. In the barrel, the muon momentum resolution of the DTs is better than 95%.

900 Cathode strip chambers (CSCs) are used in the endcap muon system, providing cov-  
 901 erage in the pseudorapidity range  $0.9 < |\eta| < 2.4$ . A cathode strip chamber consists of a  
 902 chamber filled with inert gas that with a number of internal wires held at a high voltage. A  
 903 number of cathode strips are installed perpendicular<sup>6</sup> induced to the wires on the walls of  
 904 the chamber. When a muon passes through the CSC, it creates ionizes some of the gas. The  
 905 high voltage on a nearby wire causes this ionized gas to break down, forming a conductive

---

<sup>6</sup>The wires are actually placed at an angle to the perpendicular to compensate for a shifting effect caused by the magnetic field Lorentz force.

906 passage in the gas and an “avalanche” current between the wire and a number of the cathode strips. The spatial position of the hit in two dimensions is found taking one coordinate  
 907 from the wire and the other coordinate from the signal average of the cathode strips.  
 908

909 The CSCs in the CMS endcap are positioned such that a muon in the pseudorapidity  
 910 range  $1.2 < |\eta| < 2.4$  will cross three or four CSC detectors. The geometry of the CSC  
 911 strips and wires is designed to provide a spatial  $r - \phi$  resolution of 2 mm at the L1 trigger  
 912 level and a final offline reconstruction resolution of 75  $\mu\text{m}$  for the first layer and 150  $\mu\text{m}$  for  
 913 outer layers. The RMS of the response time for a CSC layer is about 11 ns, which is too  
 914 long to correctly associate a signal in the CSCs to an LHC bunch crossing (25 ns) with  
 915 high efficiency. By grouping the layers into chambers, and taking the shortest response, the  
 916 correct bunch crossing can be identified with 98–99% efficiency.

917 The Resistive Plate Chamber (RPC) muon detectors ensure that the muon system can  
 918 be used as a fast, first level trigger. The RPC detector consists of two gaps filled with gas  
 919 (up and down) with a common set of strips between the two gaps. The strips are oriented  
 920 parallel to the beam line to permit measurement of the transverse momentum of the muons.

## 921 §2.7 Trigger System

922 *(sec:Trigger)* At the LHC, proton bunch crossings (collisions) occur every 25 ns. This corresponds  
 923 to an interaction of 40 MHz. At this high rate, and with the huge number of channels  
 924 in the CMS detector, the front-end bandwidth readout from the detector is over 1 Pb/s.  
 925 Due to bandwidth and storage requirements, the rate at which events are permanently  
 926 recorded must be reduced by more than a factor of a million. This reduction is achieved  
 927 by CMS trigger system. As only a fraction of the total events can be stored, and the rate  
 928 of diffractive and common QCD multi-jet production is many orders of magnitude larger  
 929 than “interesting” new physics (see Figure 1.11). The trigger must therefore be designed to  
 930 select “interesting” events. A typical requirement applied at the trigger level might be the  
 931 presence of a high- $p_T$  muon, an isolated ECAL deposit, or a large deposit of energy in the  
 932 event.

933 The CMS trigger consists of two stages: a fast Level-1 (L1) trigger and a High-Level  
 934 Trigger (HLT). The L1 trigger system is built on custom, typically re-programmable elec-

tronics and interfaces directly to the detector subsystems. The L1 trigger has access to information from the muon and calorimeter systems. The L1 does not have access to the full granularity of the muon system and calorimeters but must make the decision based on coarse segments. The design acceptance rate of the L1 trigger is 100 kHz. The trigger typically operates at a nominal rate of 30 kHz. The maximum latency of the L1 is 3.2  $\mu$ s, requiring that the output from detector electronics be passed through memory pipelines to ensure that no bunch crossings go unanalyzed. The High-Level trigger runs on a farm of about 1000 commercial compute nodes and processes events that pass that are accepted by the L1 trigger. A High-Level trigger decision (“path”) has the ability to reconstruct tracks and do a full regional unpacking of the recorded hits in a regions of the calorimeter. Each HLT path has a strict rate budget, as the total rate of the HLT is required to be less than 100 Hz. The triggers used at CMS change as the conditions change. To limit the total rate to 100 Hz as the luminosity increases, trigger paths must either increase their thresholds, or apply a “prescale.” When a prescale is applied, a fraction of events passing the trigger are thrown away randomly.

The CMS trigger is a deep subject and a complete description is beyond the scope of this thesis. A detailed description can be found in [26]. The triggers used in the analysis presented in this thesis will be briefly described. Two types of trigger selections were applied to the 2010 datasets used in this analysis. During the initial period of low luminosity running, single muon triggers were used. As the luminosity increased, the  $p_T$  threshold of the trigger was increased. In some cases, an “isolated muon” HLT trigger was required, in which a veto was applied on muons with associated energy deposits in the calorimeter. In the final period of data taking, two “cross-triggers” were used. These required the presence of both a muon and a hadronic tau decay in the event. The triggers used in this analysis in the different 2010 run periods are enumerated in Table 5.1.

The muon component of all the triggers used in this analysis is based on the “L1 seed trigger” BLAH. The L1 muon trigger decision is determined by the Global Muon Trigger (GMT), which combines information from the DT, CSC, and RPC sub-detectors, and is able to trigger muons up to a pseudorapidity of  $|\eta| < 2.1$ . Each sub-detector has a “local trigger,” which can reconstruct tracks in the muon system. For the drift tubes,

965 the Bunch Track Identifiers (BTI), a custom integrated circuit, searches for aligned hits in  
966 the associated DT chamber. The CSCs and RPCs employ similar strategies to detect local  
967 muon tracks. The sub-detectors send the GMT the charge,  $p_T$ ,  $\eta$ ,  $\phi$ , and a quality code of  
968 up to four local muons. The measurements from the sub-detectors are combined and a final  
969 decision is made by the GMT.

---

## Chapter 3

---

# Tau Identification: The Tau Neural Classifier

970

971

972

973           High tau identification performance is important for the discovery potential of many possible new physics signals at the Compact Muon Solenoid (CMS). The Standard Model background rates from true tau leptons are typically the same order of magnitude as the expected signal rate in many searches for new physics. The challenge of doing physics with taus is driven by the rate at which objects are incorrectly tagged as taus. In particular, quark and gluon jets have a significantly higher production cross-section and events where these objects are incorrectly identified as tau leptons can dominate the backgrounds of searches for new physics using taus. Efficient identification of hadronic tau decays and low misidentification rate for quarks and gluons is thus essential to maximize the significance of searches for new physics at CMS.

983           Tau leptons are unique in that they are the only type of leptons which are heavy enough to decay to hadrons. The hadronic decays compose approximately 65% of all tau decays, the remainder being split nearly evenly between  $\tau^- \rightarrow \mu^- \bar{\nu}_\mu \nu_\tau$  and  $\tau^- \rightarrow e^- \bar{\nu}_e \nu_\tau$ . The hadronic decays are typically composed of one or three charged pions and zero to two neutral pions. The neutral pions decay almost instantaneously to pairs of photons.

988           In this chapter, we describe a technique to identify hadronic tau decays. Tau decays to electrons and muons are difficult to distinguish from prompt production of electrons and muons in  $pp$  collisions. Analyses that use exclusively use the leptonic ( $e, \mu$ ) decays of taus typically require that the decays be of opposite flavor. With the Tau Neural Classifier, we aim to improve the discrimination of true hadronic tau decays from quark and gluon jets using a neural network approach.

### 994 §3.1 Geometric Tau Identification Algorithms

995 ⟨sec:GeometricTauId⟩ The tau identification strategies used in previously published CMS analyses are fully de-  
 996 scribed in [27]. A summary of the basic methods and strategies is given here. There are  
 997 two primary methods for selecting objects used to reconstruct tau leptons. The CaloTau  
 998 algorithm uses tracks reconstructed by the tracker and clusters of hits in the electromag-  
 999 netic and hadronic calorimeter. The other method (PFTau) uses objects reconstructed by  
 1000 the CMS particle flow algorithm, which is described in [28]. The particle flow algorithm  
 1001 provides a global and unique description of every particle (charged hadron, photon, elec-  
 1002 tron, etc.) in the event; measurements from sub-detectors are combined according to their  
 1003 measured resolutions to improve energy and angular resolution and reduce double counting.  
 1004 All of the tau identification strategies described in this thesis use the particle flow objects.

1005 Both methods typically use an “leading object” and an isolation requirement to reject  
 1006 quark and gluon jet background. Quark and gluon jets are less collimated and have a higher  
 1007 constituent multiplicity and softer constituent  $p_T$  spectrum than a hadronic tau decay of  
 1008 the same transverse momentum. The “leading track” requirement is applied by requiring a  
 1009 relatively high momentum object near the center of the jet; typically a charged track with  
 1010 transverse momentum greater than 5 GeV/c within  $\Delta R < 0.1$  about the center of the jet  
 1011 axis. The isolation requirement exploits the collimation of true taus by defining an isolation  
 1012 annulus about the kinematic center of the jet and requiring no detector activity about a  
 1013 threshold in that annulus. This approach yields a misidentification rate of approximately 1%  
 1014 for QCD backgrounds and a hadronic tau identification efficiency of approximately 50% [27].

### 1015 §3.2 Decay Mode Tau Identification: Motivation

1016 The tau identification strategy described previously can be extended by looking at the dif-  
 1017 ferent hadronic decay modes of the tau individually. The dominant hadronic decays of taus  
 1018 consist of a one or three charged  $\pi^\pm$  mesons and up to two  $\pi^0$  mesons and are enumerated  
 1019 in Table 1.4. The majority of these decays proceed through intermediate resonances and  
 1020 each of these decay modes maps directly to a tau final state multiplicity. Each intermediate  
 1021 resonance has a different invariant mass (see Figure 3.1). This implies that the problem of

hadronic tau identification can be re-framed from a global search for collimated hadrons satisfying the tau mass constraint into a ensemble of searches for single production of the different hadronic tau decay resonances. The Tau Neural Classifier algorithm implements this approach using two complimentary techniques: a method to reconstruct the decay mode and an ensemble of neural network classifiers used to identify each decay mode resonance and reject quark and gluon jets with the same final state topology.

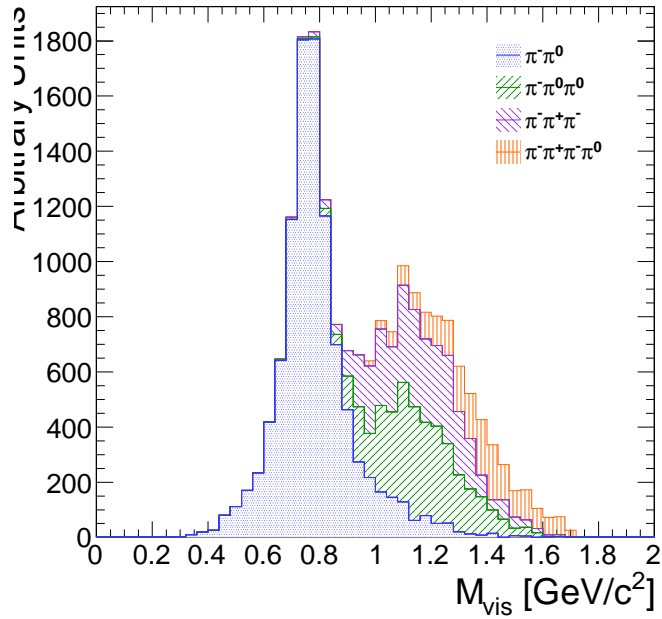


Figure 3.1: The invariant mass of the visible decay products in hadronic tau decays. The decay mode  $\tau^- \rightarrow \pi^- \nu_\tau$  is omitted. The different decay modes have different invariant masses corresponding to the intermediate resonance in the decay.

(fig:trueInvMass)

### §3.3 The Tau Neural Classifier

(sec:Tanc) The Tau Neural Classifier algorithm reconstructs the decay mode of the tau–candidate and then feeds the tau–candidate to a discriminator associated to that decay mode to make the classification decision. Each discriminator therefore maps to a reconstructed decay mode in a one-to-one fashion. To optimize the discrimination for each of the different decay modes, the TaNC uses an ensemble of neural nets. Each neural net corresponds to one of the dominant hadronic decay modes of the tau lepton. These selected hadronic decays constitute 95% of

1035 all hadronic tau decays. Tau–candidates with reconstructed decay modes not in the set of  
 1036 dominant hadronic modes are immediately tagged as background.

### 1037 §3.3.1 Decay mode reconstruction

`<sec:decay`mode`reco>` 1038 The major task in reconstructing the decay mode of the tau is determining the number of  
 1039  $\pi^0$  mesons produced in the decay. A  $\pi^0$  meson decays almost instantaneously to a pair of  
 1040 photons. The photon objects are reconstructed using the particle flow algorithm [28]. The  
 1041 initial collection of photon objects considered to be  $\pi^0$  candidates are the photons in the  
 1042 signal cone described by using the “shrinking–cone” tau algorithm, described in [27].

1043 The reconstruction of photons from  $\pi^0$  decays present in the signal cone is complicated  
 1044 by a number of factors. To suppress calorimeter noise and underlying event photons, all  
 1045 photons with minimum transverse energy less than 0.5 GeV are removed from the signal  
 1046 cone, which removes some signal photons. Photons produced in secondary interactions,  
 1047 pile-up events, and electromagnetic showers produced by signal photons that convert to  
 1048 electron–positron pairs can contaminate the signal cone with extra low transverse energy  
 1049 photons. Highly boosted  $\pi^0$  mesons may decay into a pair of photons with a small opening  
 1050 angle, resulting in two overlapping showers in the ECAL being reconstructed as one photon.  
 1051 The  $\pi^0$  meson content of the tau–candidate is reconstructed in two stages. First, photon  
 1052 pairs are merged together into candidate  $\pi^0$  mesons. The remaining un–merged photons are  
 1053 then subject to a quality requirement.

#### 1054 Photon merging

1055 Photons are merged into composite  $\pi^0$  candidates by examining the invariant mass of all  
 1056 possible pairs of photons in the signal region. Only  $\pi^0$  candidates (photon pairs) with a  
 1057 composite invariant mass less than 0.2 GeV/c are considered. The combination of the high  
 1058 granularity of the CMS ECAL and the particle flow algorithm provide excellent energy  
 1059 and angular resolution for photons; the  $\pi^0$  mass peak is readily visible in the invariant  
 1060 mass spectrum of signal photon pairs (see figure 3.3.1). The  $\pi^0$  candidates that satisfy the  
 1061 invariant mass requirement are ranked by the difference between the composite invariant  
 1062 mass of the photon pair and the invariant mass of the  $\pi^0$  meson given by the PDG [19]. The

1063 best pairs are then tagged as  $\pi^0$  mesons, removing lower-ranking candidate  $\pi^0$ s as necessary  
 1064 to ensure that no photon is included in more than one  $\pi^0$  meson.

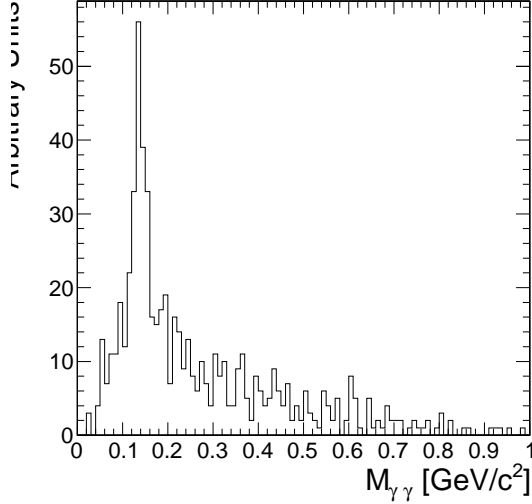


Figure 3.2: Invariant mass of the photon pair for reconstructed tau-candidates with two reconstructed photons in the signal region that are matched to generator level  $\tau^- \rightarrow \pi^- \pi^0 \nu_\tau$  decays.

mDiPhotonsForTrueDM1)

1065 Quality requirements

1066 Photons from the underlying event and other reconstruction effects cause the number of  
 1067 reconstructed photons to be greater than the true number of photons expected from a given  
 1068 hadronic tau decay. Photons that have not been merged into a  $\pi^0$  meson candidate are  
 1069 recursively filtered by requiring that the fraction of the transverse momentum carried by  
 1070 the lowest  $p_T$  photon be greater than 10% with respect to the entire (tracks,  $\pi^0$  candidates,  
 1071 and photons) tau-candidate. In the case that a photon is not merged but meets the minimum  
 1072 momentum fraction requirement, it is considered a  $\pi^0$  candidate. This requirement removes  
 1073 extraneous photons, while minimizing the removal of single photons that correspond to a  
 1074 true  $\pi^0$  meson (see 3.3). A mass hypothesis with the nominal [19] value of the  $\pi^0$  is applied to  
 1075 all  $\pi^0$  candidates. All objects that fail the filtering requirements are moved to the isolation  
 1076 collection.

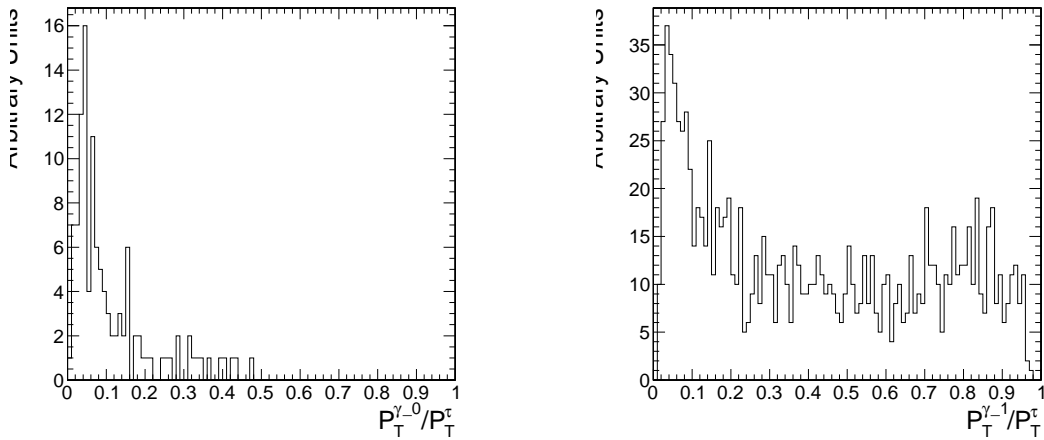


Figure 3.3: Fraction of total  $\tau$ -candidate transverse momenta carried by the photon for reconstructed taus containing a single photons for two benchmark cases. On the left, the reconstructed tau-candidate is matched to generator level  $\tau^- \rightarrow \pi^- \nu_\tau$  decays, for which no photon is expected. On the right, the reconstructed tau-candidate is matched to generator level  $\tau^- \rightarrow \pi^- \pi^0 \nu_\tau$  decays and the photon is expected to correspond to a true  $\pi^0$  meson. The requirement on the  $p_T$  fraction of the lowest  $p_T$  photon improves the purity of the decay mode reconstruction.

(fig:photonFiltering)

## 1077 Performance

1078 The performance of the decay mode reconstruction can be measured for tau-candidates that  
 1079 are matched to generator level hadronically decaying tau leptons by examining the correla-  
 1080 tion of the reconstructed decay mode to the true decay mode determined from the Monte  
 1081 Carlo generator level information. Figure 3.4 compares the decay mode reconstruction per-  
 1082 formance of a naive approach where the decay mode is determined by simply counting  
 1083 the number of photons to the performance of the photon merging and filtering approach  
 1084 described in section 3.3.1. The correlation for the merging and filtering algorithm is much  
 1085 more diagonal, indicating higher performance. The performance is additonally presented for  
 1086 comparison in tabular form in table 3.3.1 (merging and filtering approach) and table 3.3.1  
 1087 (naive approach).

1088 The performance of the decay mode reconstruction is dependent on the transverse  
 1089 momentum and  $\eta$  of the tau-candidate and is shown in figure 3.5. The  $p_T$  dependence  
 1090 is largely due to threshold effects; high multiplicity decay modes are suppressed at low  
 1091 transverse momentum as the constituents are below the minimum  $p_T$  quality requirements.

1092 In the forward region, nuclear interactions and conversions from the increased material  
1093 budget enhances modes containing  $\pi^0$  mesons.

True decay mode	Reconstructed Decay Mode					
	$\pi^- \nu_\tau$	$\pi^- \pi^0 \nu_\tau$	$\pi^- \pi^0 \pi^0 \nu_\tau$	$\pi^- \pi^+ \pi^- \nu_\tau$	$\pi^- \pi^+ \pi^- \pi^0 \nu_\tau$	Other
$\pi^- \nu_\tau$	14.8%	1.6%	0.4%	0.1%	0.0%	0.7%
$\pi^- \pi^0 \nu_\tau$	6.0%	17.1%	9.0%	0.1%	0.1%	5.5%
$\pi^- \pi^0 \pi^0 \nu_\tau$	0.9%	3.8%	4.2%	0.0%	0.1%	5.9%
$\pi^- \pi^+ \pi^- \nu_\tau$	0.8%	0.3%	0.1%	9.7%	1.6%	6.2%
$\pi^- \pi^+ \pi^- \pi^0 \nu_\tau$	0.1%	0.2%	0.1%	1.7%	2.7%	4.5%

:dmResolutionNoNothing

Table 3.1: Decay mode correlation table for the selected dominant decay modes for the naive approach. The percentage in a given row and column indicates the fraction of hadronic tau decays from  $Z \rightarrow \tau^+ \tau^-$  events that are matched to a generator level decay mode given by the row and are reconstructed with the decay mode given by the column. Entries in the "Other" column are immediately tagged as background.

True decay mode	Reconstructed Decay Mode					
	$\pi^- \nu_\tau$	$\pi^- \pi^0 \nu_\tau$	$\pi^- \pi^0 \pi^0 \nu_\tau$	$\pi^- \pi^+ \pi^- \nu_\tau$	$\pi^- \pi^+ \pi^- \pi^0 \nu_\tau$	Other
$\pi^- \nu_\tau$	16.2%	1.0%	0.1%	0.1%	0.0%	0.3%
$\pi^- \pi^0 \nu_\tau$	10.7%	21.4%	3.6%	0.2%	0.1%	1.9%
$\pi^- \pi^0 \pi^0 \nu_\tau$	1.8%	7.1%	4.4%	0.1%	0.0%	1.5%
$\pi^- \pi^+ \pi^- \nu_\tau$	0.9%	0.2%	0.0%	11.5%	0.6%	5.4%
$\pi^- \pi^+ \pi^- \pi^0 \nu_\tau$	0.1%	0.3%	0.0%	3.2%	2.9%	2.7%

:ab:dmResolutionStandard

Table 3.2: Decay mode correlation table for the selected dominant decay modes for the merging and filtering approach. The percentage in a given row and column indicates the fraction of hadronic tau decays from  $Z \rightarrow \tau^+ \tau^-$  events that are matched to a generator level decay mode given by the row and are reconstructed with the decay mode given by the column. Entries in the "Other" column are immediately tagged as background.

### 1094 §3.3.2 Neural network classification

#### 1095 Neural Network Training

sec:tanc'nn'training  
1096 The samples used to train the TaNC neural networks are typical of the signals and back-  
1097 grounds found in common physics analyses using taus. The signal-type training sample is

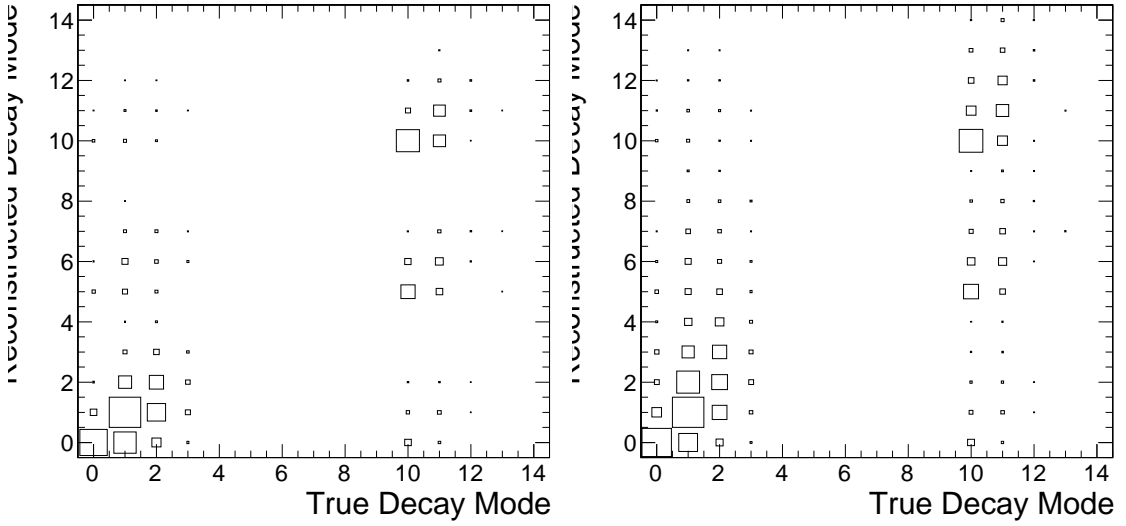


Figure 3.4: Correlations between reconstructed tau decay mode and true tau decay mode for hadronic tau decays in  $Z \rightarrow \tau^+\tau^-$  events. The correlation when no photon merging or filtering is applied is shown on the right, and the correlation for the algorithm described in section 3.3.1 is on the right. The horizontal and vertical axis are the decay mode indices of the true and reconstructed decay mode, respectively. The decay mode index  $N_{DM}$  is defined as  $N_{DM} = (N_{\pi^\pm} - 1) \cdot 5 + N_{\pi^0}$ . The area of the box in each cell is proportional to the fraction of tau-candidates that were reconstructed with the decay mode indicated on the vertical axis for the true tau decay on the horizontal axis. The performance of a decay mode reconstruction algorithm can be determined by the spread of the reconstructed number of  $\pi^0$  mesons about the true number (the diagonal entries) determined from the generator level Monte Carlo information. If the reconstruction was perfect, the correlation would be exactly diagonal.

(fig:dmResolution)

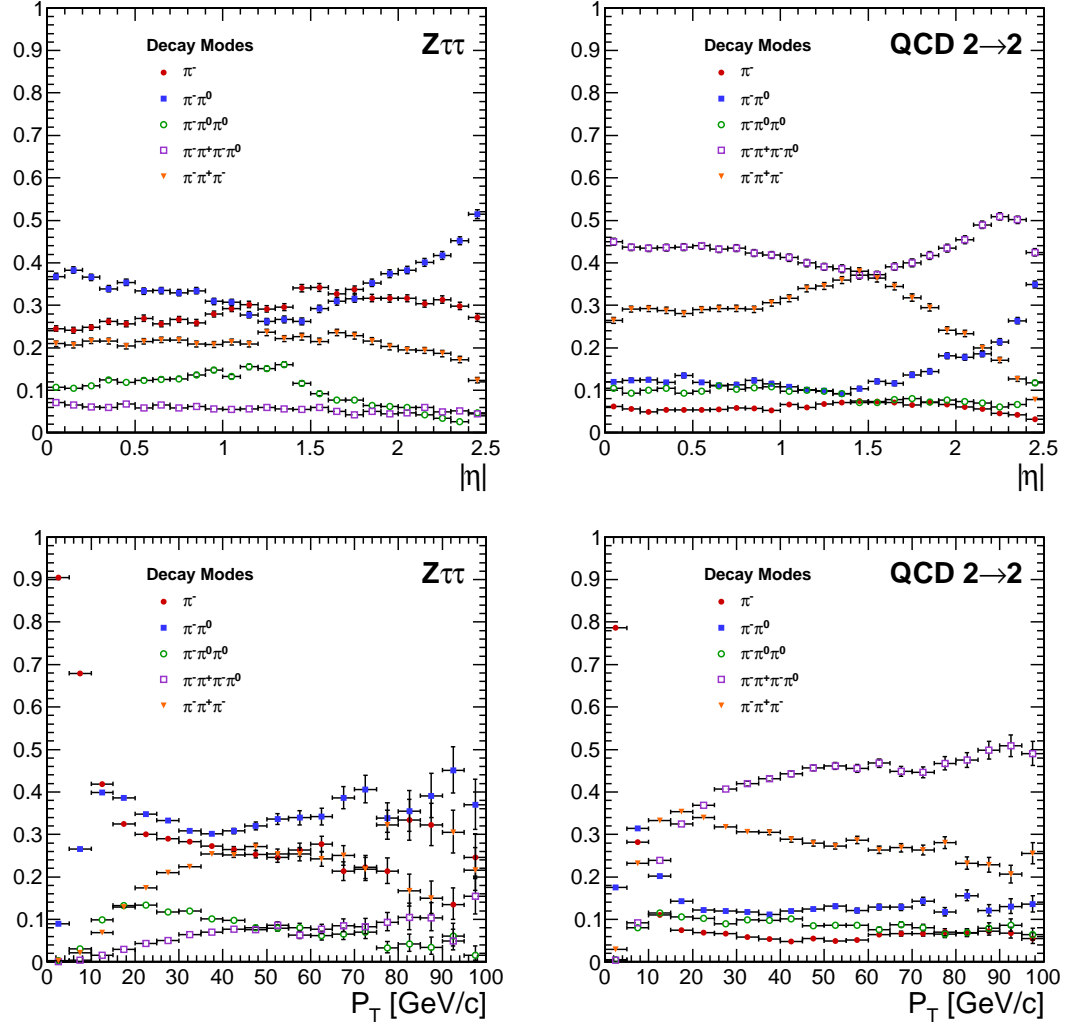


Figure 3.5: Kinematic dependence of reconstructed decay mode for tau-candidates from  $Z \rightarrow \tau^+\tau^-$  (left) and QCD di-jets (right) versus transverse momentum (top) and pseudo-rapidity (bottom). Each curve is the probability for a tau-candidate to be reconstructed with the associated decay mode after the leading pion and decay mode preselection has been applied.

(fig:dmKinematics)

1098 composed of reconstructed tau–candidates that are matched to generator level hadronic tau  
 1099 decays coming from simulated  $Z \rightarrow \tau^+ \tau^-$  events. The background training sample consists  
 1100 of reconstructed tau–candidates in simulated QCD  $2 \rightarrow 2$  hard scattering events. The QCD  
 1101  $p_T$  spectrum is steeply falling, and to obtain sufficient statistics across a broad range of  $p_T$   
 1102 the sample is split into different  $\hat{p}_T$  bins. Each binned QCD sample imposes a generator  
 1103 level cut on the transverse momentum of the hard interaction. During the evaluation of  
 1104 discrimination performance the QCD samples are weighted according to their respective  
 1105 integrated luminosities to remove any effect of the binning.

1106 The signal and background samples are split into five subsamples corresponding to  
 1107 each reconstructed decay mode. An additional selection is applied to each subsample by  
 1108 requiring a “leading pion”: either a charged hadron or gamma candidate with transverse  
 1109 momentum greater than  $5 \text{ GeV}/c$ . A large number of QCD training events is required as  
 1110 both the leading pion selection and the requirement that the decay mode match one of the  
 1111 dominant modes given in table 1.4 are effective discriminants. For each subsample, 80%  
 1112 of the signal and background tau–candidates are used for training the neural networks by  
 1113 the TMVA software, with half (40%) used as a validation sample used to ensure the neural  
 1114 network is not over-trained. The number of signal and background entries used for training  
 1115 and validation in each decay mode subsample is given in table 3.3.2.

1116 The remaining 20% of the signal and background samples are reserved as a statistically  
 1117 independent sample to evaluate the performance of the neural nets after the training is  
 1118 completed. The TaNC uses the “MLP” neural network implementation provided by the  
 1119 TMVA software package, described in [29]. The “MLP” classifier is a feed-forward artificial  
 1120 neural network. There are two layers of hidden nodes and a single node in the output layer.  
 1121 The hyperbolic tangent function is used for the neuron activation function.

The neural networks used in the TaNC have two hidden layers and single node in the output layers. The number of nodes in the first and second hidden layers are chosen to be  $N + 1$  and  $2N + 1$ , respectively, where  $N$  is the number of input observables for that neural network. According to the Kolmogorov’s theorem [30], any continuous function  $g(x)$  defined

	Signal	Background
Total number of tau-candidates	874266	9526176
Tau-candidates passing preselection	584895	644315
Tau-candidates with $W(p_T, \eta) > 0$	538792	488917
Decay Mode	Training Events	
$\pi^-$	300951	144204
$\pi^-\pi^0$	135464	137739
$\pi^-\pi^0\pi^0$	34780	51181
$\pi^-\pi^-\pi^+$	53247	155793
$\pi^-\pi^-\pi^+\pi^0$	13340	135871

{tab:trainingEvents}

Table 3.3: Number of events used for neural network training and validation for each selected decay mode.

on a vector space of dimension  $d$  spanned by  $x$  can be represented by

$$g(x) = \sum_{j=1}^{j=2d+1} \Phi_j \left( \sum_{i=1}^d \phi_i(x) \right) \quad (3.1) \quad \text{[eq:Kolmogorov]}$$

for suitably chosen functions for  $\Phi_j$  and  $\phi_i$ . As the form of equation 3.1 is similar to the topology of a two hidden-layer neural network, Kolmogorov's theorem suggests that *any* classification problem can be solved with a neural network with two hidden layers containing the appropriate number of nodes.

The neural network is trained for 500 epochs. At ten epoch intervals, the neural network error is computed using the validation sample to check for over-training (see figure 3.6).

The neural network error  $E$  is defined [29] as

$$E = \frac{1}{2} \sum_{i=1}^N (y_{ANN,i} - \hat{y}_i)^2 \quad (3.2) \quad \text{[eq:NNerrorFunc]}$$

where  $N$  is the number of training events,  $y_{ANN,i}$  is the neural network output for the  $i$ th training event, and  $y_i$  is the desired (-1 for background, 1 for signal) output the  $i$ th event.

No evidence of over-training is observed.

The neural networks use as input observables the transverse momentum and  $\eta$  of the tau-candidates. These observables are included as their correlations with other observables can increase the separation power of the ensemble of observables. For example, the opening angle in  $\Delta R$  for signal tau-candidates is inversely related to the transverse momentum,

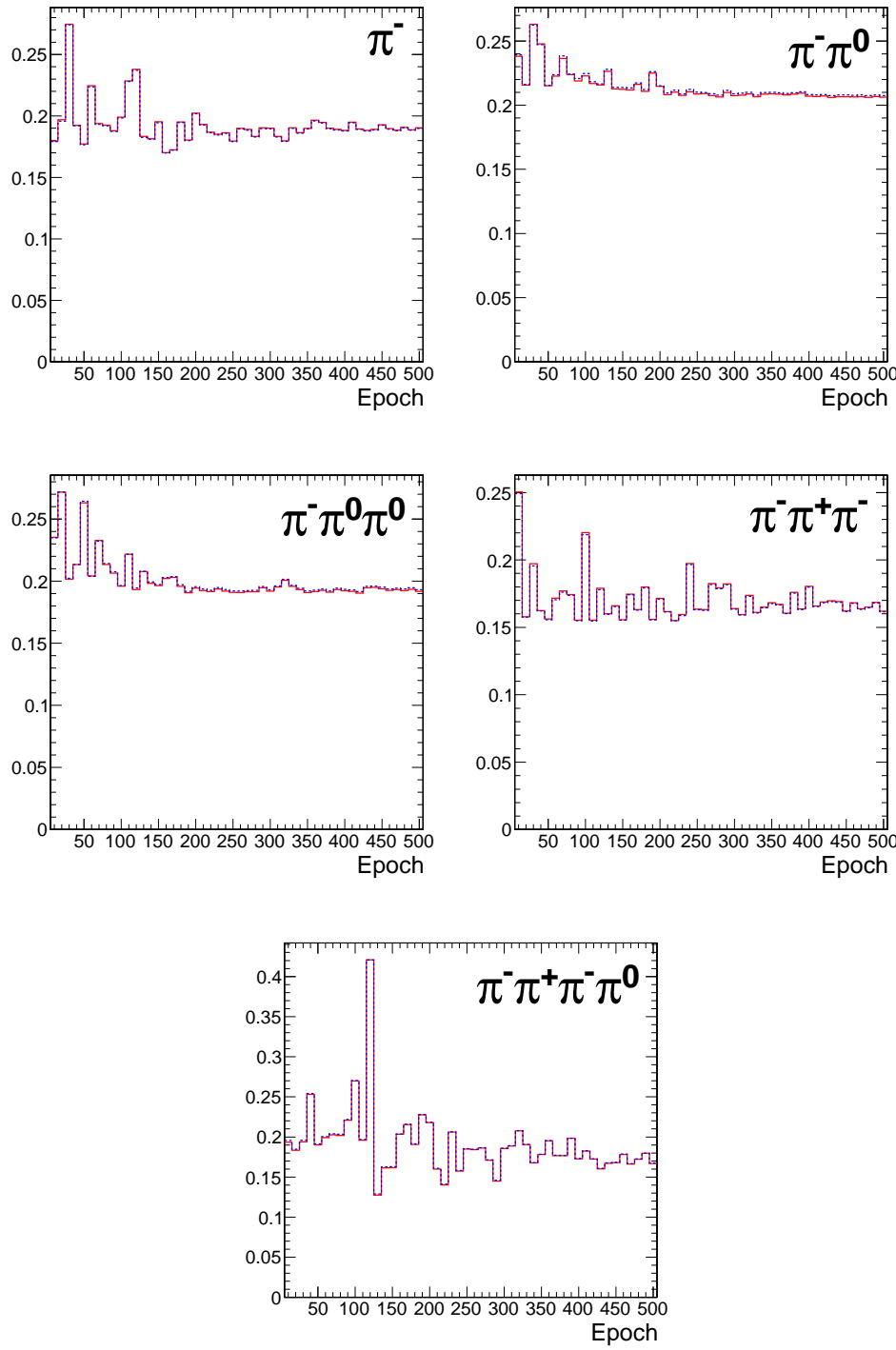


Figure 3.6: Neural network classification error for training (solid red) and testing (dashed blue) samples at ten epoch intervals over the 500 training epochs for each decay mode neural network. The vertical axis represents the classification error, defined by equation 3.2. N.B. that the choice of hyperbolic tangent for neuron activation functions results in the desired outputs for signal and background to be 1 and -1, respectively. This results in the computed neural network error being larger by a factor of four than the case where the desired outputs are (0, 1). Classifier over-training would be evidenced by divergence of the classification error of the training and testing samples, indicating that the neural net was optimizing about statistical fluctuations in the training sample.

{fig:overTrainCheck}

1133 while for background events the correlation is very small [31]. In the training signal and  
 1134 background samples, there is significant discrimination power in the  $p_T$  spectrum. However,  
 1135 it is desirable to eliminate any systematic dependence of the neural network output on  $p_T$   
 1136 and  $\eta$ , as in practice the TaNC will be presented with tau-candidates whose  $p_T - \eta$  spectrum  
 1137 will be analysis dependent. The dependence on  $p_T$  and  $\eta$  is removed by applying a  $p_T$  and  
 1138  $\eta$  dependent weight to the tau-candidates when training the neural nets.

The weights are defined such that in any region in the vector space spanned by  $p_T$  and  $\eta$  where the signal sample and background sample probability density functions are different, the sample with higher probability density is weighted such that the samples have identical  $p_T - \eta$  probability distributions. This removes regions of  $p_T - \eta$  space where the training sample is exclusively signal or background. The weights are computed according to

$$W(p_T, \eta) = \text{less}(p_{sig}(p_T, \eta), p_{bkg}(p_T, \eta))$$

$$w_{sig}(p_T, \eta) = W(p_T, \eta)/p_{sig}(p_T, \eta)$$

$$w_{bkg}(p_T, \eta) = W(p_T, \eta)/p_{bkg}(p_T, \eta)$$

1139 where  $p_{sig}(p_T, \eta)$  and  $p_{bkg}(p_T, \eta)$  are the probability densities of the signal and background  
 1140 samples after the “leading pion” and dominant decay mode selections. Figure 3.7 shows the  
 1141 signal and background training  $p_T$  distributions before and after the weighting is applied.

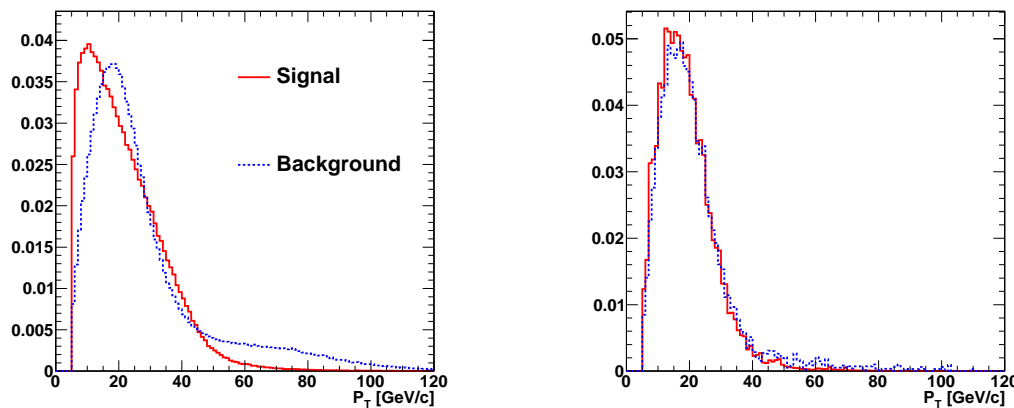


Figure 3.7: Transverse momentum spectrum of signal and background tau-candidates used in neural net training before (left) and after (right) the application of  $p_T - \eta$  dependent weight function. Application of the weights lowers the training significance of tau-candidates in regions of  $p_T - \eta$  phase space where either the signal or background samples has an excess of events.

(fig:nnTrainingWeights)

1142    **Discriminants**

1143    Each neural network corresponds to a different decay mode topology and as such each  
 1144    network uses different observables as inputs. However, many of the input observables are  
 1145    used in multiple neural nets. The superset of all observables is listed and defined below.  
 1146    Table 3.4 maps the input observables to their associated neural networks. In three prong  
 1147    decays, the definition of the “main track” is important. The main track corresponds to the  
 1148    track with charge opposite to that of the total charge of the three tracks. This distinction is  
 1149    made to facilitate the use of the “Dalitz” observables, allowing identification of intermediate  
 1150    resonances in three–body decays. This is motivated by the fact that the three prong decays  
 1151    of the tau generally proceed through  $\tau^- \rightarrow a1^- \nu_\tau \rightarrow \pi^- \rho^0 \nu_\tau \rightarrow \pi^- \pi^+ \pi^- \nu_\tau$ ; the oppositely  
 1152    charged track can always be identified with the  $\rho^0$  decay.

1153    **ChargedOutlierAngleN**

1154     $\Delta R$  between the Nth charged object (ordered by  $p_T$ ) in the isolation region and the  
 1155    tau–candidate momentum axis. If the number of isolation region objects is less than  
 1156    N, the input is set at one.

1157    **ChargedOutlierPtN**

1158    Transverse momentum of the Nth charged object in the isolation region. If the number  
 1159    of isolation region objects is less than N, the input is set at zero.

1160    **DalitzN**

1161    Invariant mass of four vector sum of the “main track” and the Nth signal region  
 1162    object.

1163    **Eta**

1164    Pseudo-rapidity of the signal region objects.

1165    **InvariantMassOfSignal**

1166    Invariant mass of the composite object formed by the signal region constituents.

1167 **MainTrackAngle**

1168      $\Delta R$  between the “main track” and the composite four–vector formed by the signal  
 1169     region constituents.

1170 **MainTrackPt**

1171     Transverse momentum of the “main track.”

1172 **OutlierNCharged**

1173     Number of charged objects in the isolation region.

1174 **OutlierSumPt**

1175     Sum of the transverse momentum of objects in the isolation region.

1176 **PiZeroAngleN**

1177      $\Delta R$  between the Nth  $\pi^0$  object in the signal region (ordered by  $p_T$ ) and the tau–  
 1178     candidate momentum axis.

1179 **PiZeroPtN**

1180     Transverse momentum of the Nth  $\pi^0$  object in the signal region.

1181 **TrackAngleN**

1182      $\Delta R$  between the Nth charged object in the signal region (ordered by  $p_T$ ) and the  
 1183     tau–candidate momentum axis, exclusive of the main track.

1184 **TrackPtN**

1185     Transverse momentum of the Nth charged object in the signal region, exclusive of the  
 1186     main track.

1187 Neural network performance

1188     The classification power of the neural networks is unique for each of the decay modes.  
 1189     The performance is determined by the relative separation of the signal and background  
 1190     distributions in the parameter space of the observables used as neural network inputs. A  
 1191     pathological example is the case of tau–candidates with the reconstructed decay mode of  
 1192      $\tau^- \rightarrow \pi^- \nu_\tau$ . If there is no isolation activity, the neural net has no handle with which it

1193 can separate the signal from the background. The neural net output for tau-candidates in  
 1194 the testing sample (independent of the training and validation samples) for each of the five  
 1195 decay mode classifications is shown in figure 3.8.

1196 When a single neural network is used for classification, choosing an operating point is  
 1197 relatively straightforward: the requirement on neural network output is tuned such that the  
 1198 desired purity is attained. However, in the case of the TaNC, multiple neural networks are  
 1199 used. Each network has a unique separation power (see figure 3.9) and each neural network  
 1200 is associated to a reconstructed decay mode that composes different relative fractions of the  
 1201 signal and background tau-candidates. Therefore, a set of five numbers is required to define  
 1202 an “operating point” (the signal efficiency and background misidentification rate) in the  
 1203 TaNC output. All points in this five dimensional cut-space map to an absolute background  
 1204 fake-rate and signal efficiency rate. Therefore there must exist a 5D “performance curve”  
 1205 which for any attainable signal efficiency gives the lowest fake-rate. A direct method to  
 1206 approximate the performance curve is possible using a Monte Carlo technique.

1207 The maximal performance curve can be approximated by iteratively sampling points in  
 1208 the five-dimensional cut space and selecting the highest performance points. The collection  
 1209 of points in the performance curve are ordered by expected fake rate. During each iteration,  
 1210 the sample point is compared to the point before the potential insertion position of the  
 1211 sample in the ordered collection. The sample point is inserted into the collection if it has  
 1212 a higher signal identification efficiency than the point before it. The sample point is then  
 1213 compared to all points in the collection after it (i.e. those with a larger fake rate); any point  
 1214 with a lower signal efficiency than the sample point is removed. After the performance curve  
 1215 has been determined, the set of cuts are evaluated on an independent validation sample  
 1216 to ensure that the measured performance curve is not influenced by favorable statistical  
 1217 fluctuations being selected by the Monte Carlo sampling. The performance curves for two  
 1218 different transverse momentum ranges are shown in figure 3.10.

The 5D performance curve can also be parameterized by using the probability for a tau-candidate to be identified for a given decay mode. An artificial neural network maps a point in the space of input observables to some value of neural network output  $x$ . The neural network training error is given by equation 3.2. A given point in the vector space

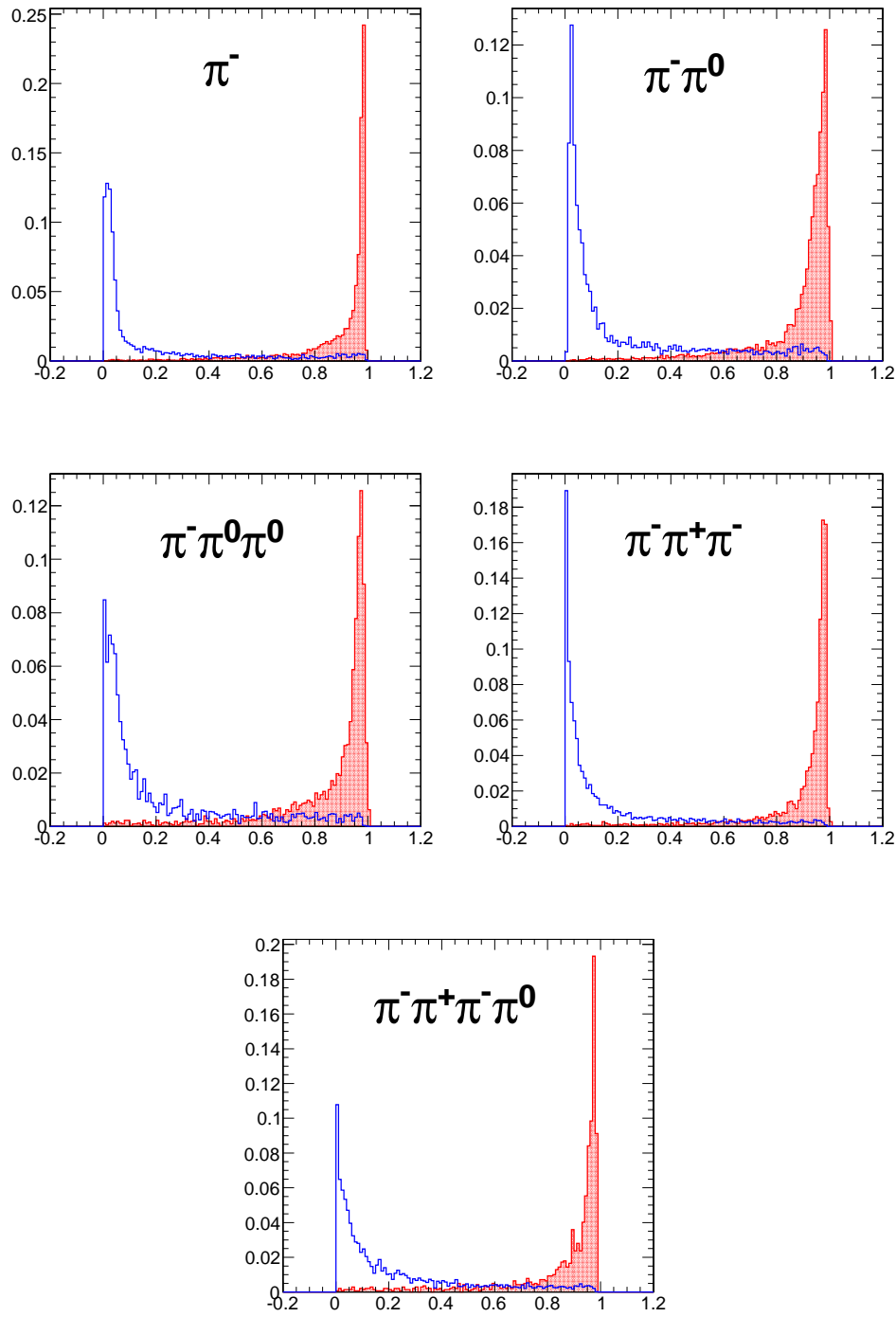


Figure 3.8: Neural network output distributions for the five reconstructed tau–candidate decay modes used in the TaNC for  $Z \rightarrow \tau^+\tau^-$  events (red) and QCD di-jet events (blue).

fig:NNoutputDistributions

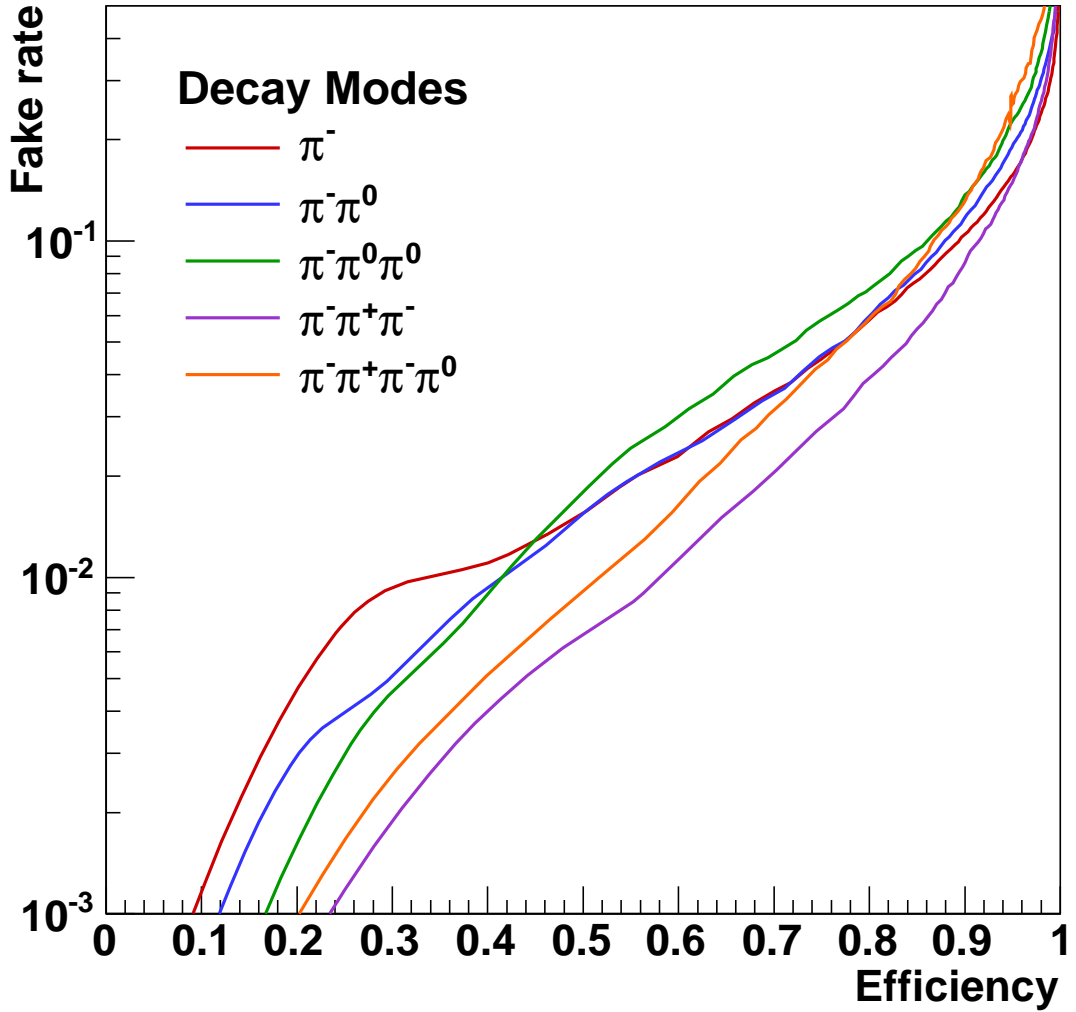


Figure 3.9: Performance curves for the five neural networks used by the TaNC for tau-candidates with transverse momentum greater than 20 GeV/c. Each curve represents the signal efficiency (on the horizontal axis) and background misidentification rate (vertical axis) for a scan of the neural network selection requirement for a single neural network. The efficiency (or misidentification rate) for each neural network performance curve is defined with respect to the preselected tau-candidates that have the reconstructed decay mode associated with that neural network. Each neural network has a different ability to separate signal and background as each classifier uses different observables as inputs.

(fig:nnPerfCurves)

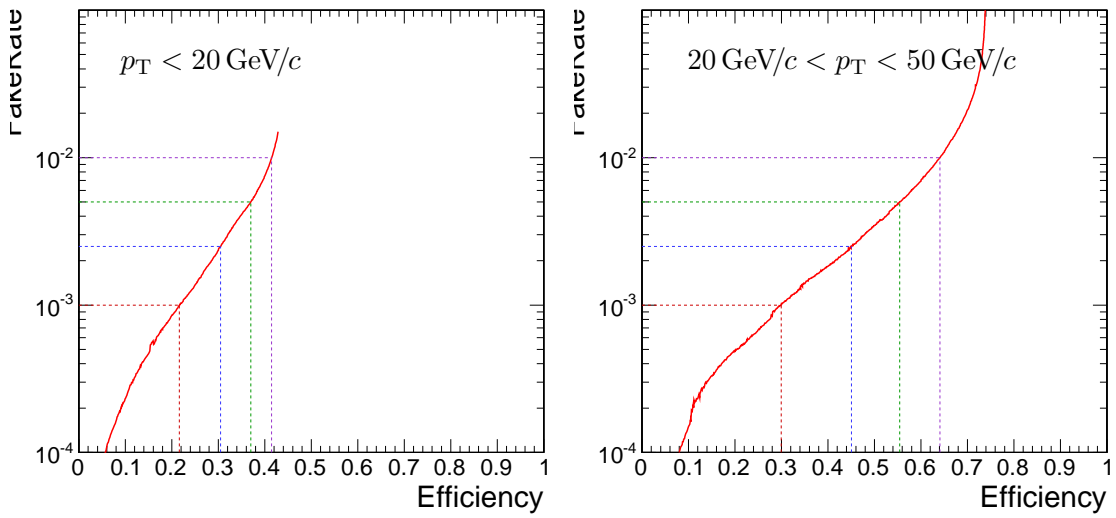


Figure 3.10: Tau Neural Classifier performance curves for tau-candidates with  $p_T < 20 \text{ GeV}/c$  (left) and  $20 \text{ GeV}/c < p_T < 50 \text{ GeV}/c$  (right). The vertical axis represents the expected fake-rate of QCD jets and the horizontal axis the expected signal efficiency for hadronic tau decays. The performance curve for the low transverse momentum range is worse due to leading pion selection. While both true taus and QCD are removed by this cut, the selection preferentially keeps the QCD tau-candidates with low multiplicities, which increases the number of QCD tau-candidates passing the decay mode selection.  
(fig:mcPerfCurves)

spanned by the neural network input observables (denoted as “feature space”) contributes to the neural network training error  $E$  by

$$E' = (1 - x)^2 \cdot \rho^\tau + x^2 \cdot \rho^{QCD} \quad (3.3) \{?\}$$

1219 where  $\rho^\tau(\rho^{QCD})$  denotes the training sample density of the  $\tau$  signal and QCD–jet back-  
1220 ground at that point in feature space.

The value  $x$  assigned by the neural network to this region in feature space should satisfy the requirement of minimal error:

$$\begin{aligned} \frac{\partial E'}{\partial x} &= 0 \\ 0 &= -2(1 - x) \cdot \rho^\tau + 2x \cdot \rho^{QCD} \\ x &= \frac{\rho^\tau}{\rho^\tau + \rho^{QCD}} \quad (3.4) \boxed{\text{eq:probFracToX}} \\ \rho^\tau &= x(\rho^\tau + \rho^{QCD}) \\ \frac{\rho^{QCD}}{\rho^\tau} &= \frac{1}{x} - 1 \quad (3.5) \boxed{\text{eq:rawTransform}} \end{aligned}$$

1221 The ratio  $\frac{\rho^{QCD}}{\rho^\tau}$  corresponds to the ratio of the normalized probability density functions of  
1222 signal and background input observable distributions, i.e.  $\int \rho^\tau d\vec{x} = 1$ .

In the case of multiple neural networks, one can derive a formula that maps the output  $x_j$  of the neural network corresponding to decay mode  $j$  according to the “prior probabilities”  $p_j^\tau(p_j^{QCD})$  for true  $\tau$  lepton hadronic decays (quark and gluon jets) to pass the preselection criteria and be reconstructed with decay mode  $j$ . By substituting  $\rho^s \rightarrow \rho^s p_j^s$  for  $s \in \{\tau, QCD\}$  in equation 3.4, the output  $x_j$  can be related to  $p_j^\tau(p_j^{QCD})$  by

$$x'_j = \frac{\rho^\tau \cdot p_j^\tau}{\rho^\tau \cdot p_j^\tau + \rho^{QCD} \cdot p_j^{QCD}} = \frac{p_j^\tau}{p_j^\tau + \frac{\rho^{QCD}}{\rho^\tau} \cdot p_j^{QCD}} \quad (3.6) \boxed{\text{eq:probFracToX}}$$

Substituting equation 3.5 into equation 3.6 yields the transformation of the output  $x_j$  of the neural neural network corresponding to any selected decay mode  $j$  to a single discriminator output  $x'_j$  which for a given point on the optimal performance curve should be independent of  $j$ .

$$x'_j = \frac{p_j^\tau}{p_j^\tau + \left(\frac{1}{x_j} - 1\right) \cdot p_j^{QCD}} \quad (3.7) \boxed{\text{eq:TransformCut}}$$

1223 In this manner a single number (the “transform cut”) given by Equation 3.7 can be used  
1224 to specify any point on the performance curve. The training sample neural network output  
1225 after the transformation has been applied is shown in figure 3.12. The performance curve

1226 for the cut on the transformed output is nearly identical to the optimal performance curve  
 1227 determined by the Monte Carlo sampling technique.

1228 The discriminator output of the TaNC algorithm is a continuous quantity, enabling  
 1229 analysis specific optimization of the selection to maximize sensitivity. For the convenience  
 1230 of the user, four operating point benchmark selections are provided in addition to the  
 1231 continuous output. The four operating points are chosen such that for tau-candidates with  
 1232 transverse momentum between 20 and 50 GeV/c, the expected QCD di-jet fake rate will be  
 1233 0.1%, 0.25%, 0.50% and 1.0%, respectively.

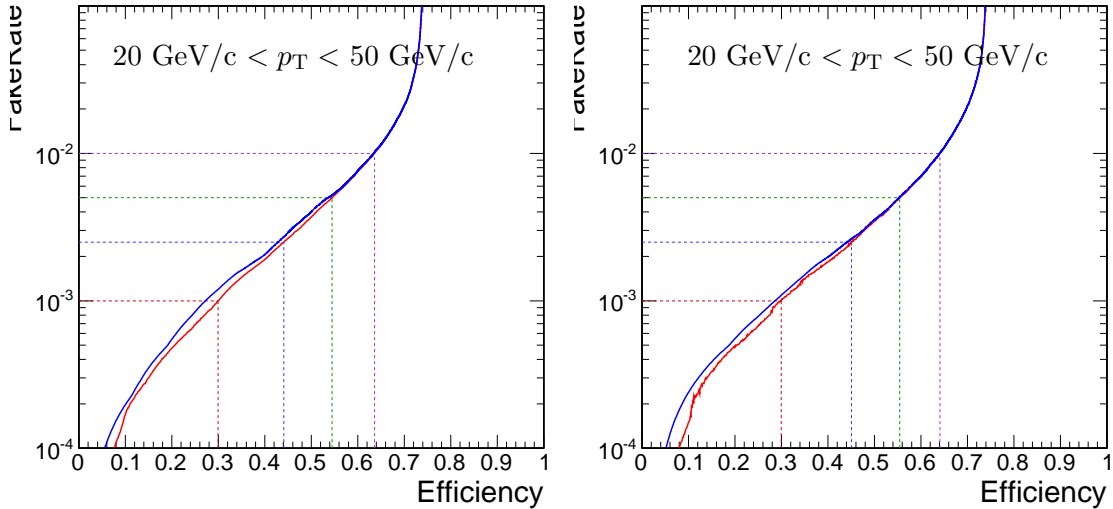


Figure 3.11: Tau Neural Classifier performance curves for tau-candidates with  $20 \text{ GeV}/c < p_T < 50 \text{ GeV}/c$ . The figure on the left compares the optimal performance curve determined by the Monte Carlo sampling method (red) to the performance curve obtained by scanning the “transform cut” (blue) defined in equation 3.7 from zero to one. The figure on the right is the same set of cuts (and cut transformation values) applied on an independent sample to remove any biases introduced by the Monte Carlo sampling. The four dashed lines indicate the performance for the four benchmark points.

### 1234 §3.4 Summary

1235 The Tau Neural classifier introduces two complimentary new techniques for tau lepton  
 1236 physics at CMS: reconstruction of the hadronic tau decay mode and discrimination from  
 1237 quark and gluon jets using neural networks. The decay mode reconstruction strategy pre-  
 1238 sented in section 3.3.1 significantly improves the determination of the decay mode. This

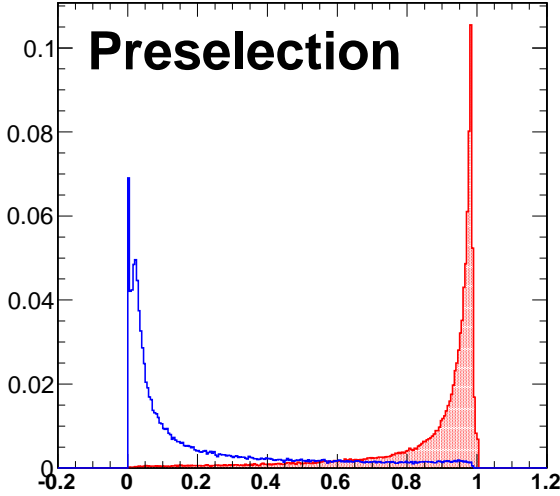


Figure 3.12: Transformed TaNC neural network output for tau-candidates with transverse momentum between 20 and 50  $\text{GeV}/c$  that pass the pre-selection criteria. The neural network output for each tau-candidate has been transformation according to equation 3.7. The decay mode probabilities  $\rho_i^{bkg}$ ,  $\rho_i^{signal}$  are computed using the entire transverse momentum range of the sample.

`fig:transformedNNOutput`

1239 information has the potential to be useful in studies of tau polarization and background  
 1240 estimation.

1241 The Tau Neural classifier tau identification algorithm significantly improves tau dis-  
 1242 crimination performance compared to isolation-based approaches [27] used in previous CMS  
 1243 analyses. Figure 3.13 compares the performance of the “shrinking cone” isolation tau-  
 1244 identification algorithm [27] to the performance of the TaNC for a scan of requirements  
 1245 on the transformed neural network output. The signal efficiency and QCD di-jet fake rate  
 1246 versus tau-candidate transverse momentum and pseudo-rapidity for the four benchmark  
 1247 points and the isolation based tau identification are show in figure 3.14. For tau-candidates  
 1248 with transverse momentum between 20 and 50  $\text{GeV}/c$ , the TaNC operating cut can be  
 1249 chosen such that the two methods have identical signal efficiency; at this point the TaNC  
 1250 algorithm reduces the background fake rate by an additional factor of 3.9. This reduction  
 1251 in background will directly improve the significance of searches for new physics using tau  
 1252 leptons at CMS.

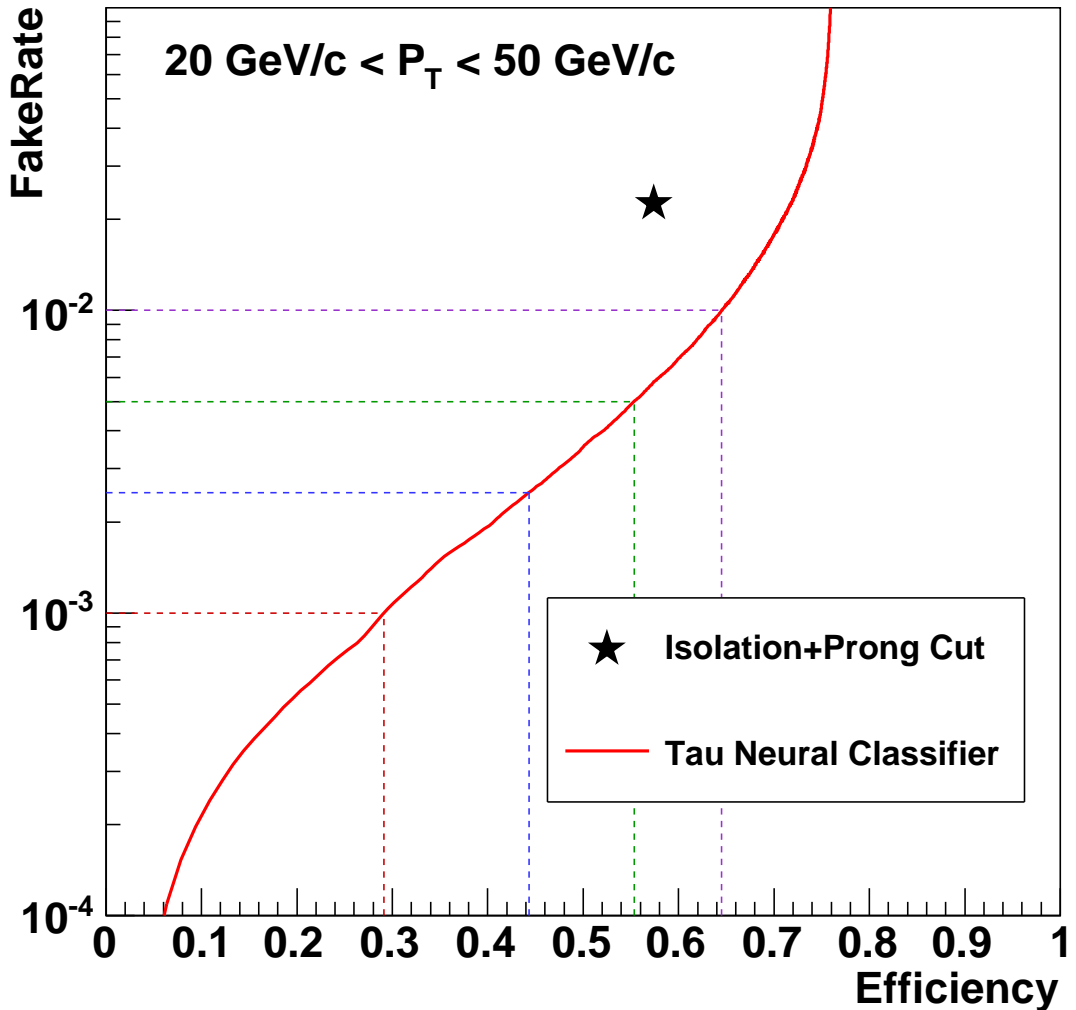


Figure 3.13: Performance curve (red) of the TaNC tau identification for various requirements on the output transformed according to equation 3.7. The horizontal axis is the efficiency for true taus with transverse momentum between 20 and 50 GeV/c to satisfy the tau identification requirements. The vertical axis gives the rate at which QCD dijets with generator-level transverse momentum between 20 and 50 GeV/c are incorrectly identified as taus. The performance point for the same tau-candidates using the isolation based tau-identification [27] used in many previous CMS analyses is indicated by the black star in the figure. An additional requirement that the signal cone contain one or three charged hadrons (typical in a final physics analysis) has been applied to the isolation based tau-identification to ensure a conservative comparison.

{fig:finalPerfCurve}

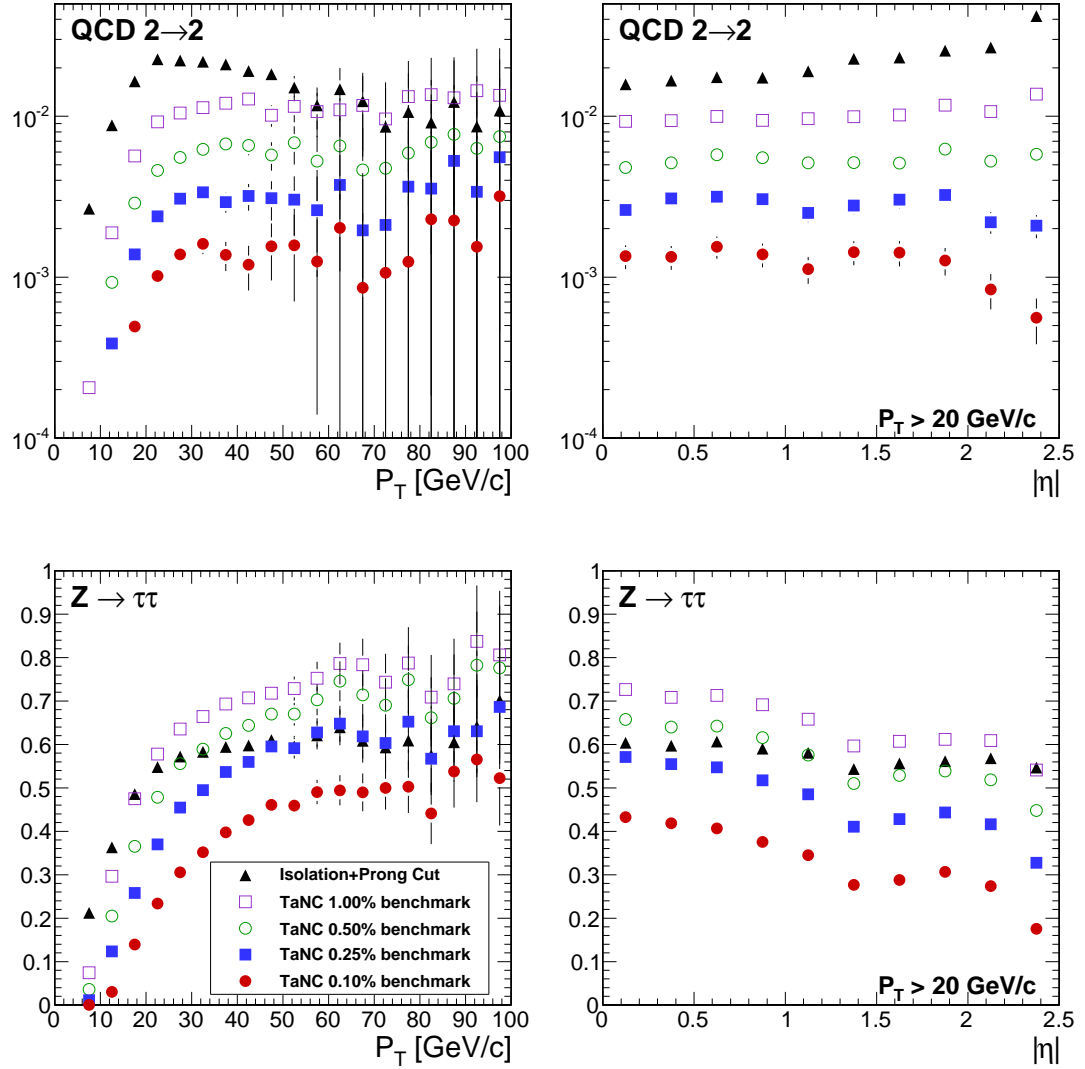


Figure 3.14: Comparison of the identification efficiency for hadronic tau decays from  $Z \rightarrow \tau^+\tau^-$  decays (bottom row) and the misidentification rate for QCD di-jets (top row) versus tau-candidate transverse momentum (left) and pseudo-rapidity (right) for different tau identification algorithms. The efficiency (fake-rate) in a given bin is defined as the quotient of the number of true tau hadronic decays (generator level jets) in that bin that are matched to a reconstructed tau-candidate that passes the identification algorithm divided by the number of true tau hadronic decays (generator level jets) in that bin. In the low transverse momentum region both the number of tau-candidates in the denominator and the algorithm acceptance vary rapidly with respect to  $p_T$  for both signal and background; a minimum transverse momentum requirement of 20 GeV/c is applied to the pseudorapidity plots to facilitate interpretation of the plots.

fig:kinematicPerformance)

## 1253 §3.5 HPS+TaNC: A Hybrid Algorithm

1253 `<sec:TauId>` The techniques used in the TaNC have been hybridized with techniques used by the “Hadrons plus Strips” (HPS) algorithm [32]. The combined algorithm is referred to “Hadrons plus Strips and Tau Neural Classifier” (HPS + TaNC) identification algorithm. The algorithm combines the HPS methods of constructing the signal components of the tau candidate and the discrimination methods of the TaNC algorithm. Both algorithms are based on reconstructing individual tau lepton hadronic decay modes, which has been demonstrated to improve the tau identification performance significantly with respect to previously used cone isolation based algorithms [33]. The HPS + TaNC algorithm first reconstructs the hadronic decay mode of the tau, and applies different discriminants based on the reconstructed decay mode. Identification of hadronic tau decays by the HPS + TaNC algorithm proceeds in two stages: first, the hadronic decay mode of the tau is reconstructed and then different discriminators are applied, based on the reconstructed decay mode. In the decay mode reconstruction particular attention is paid to the reconstruction of neutral pions, which are expected for the majority of hadronic decay modes.

### 1268 §3.5.1 Decay mode reconstruction

1269 The decay mode reconstruction algorithm is seeded by particle-flow jets reconstructed by  
 1270 the anti- $k_T$  algorithm [34]. In order to reconstruct the decay mode, the algorithm needs to  
 1271 merge photon candidates into candidate  $\pi^0$  mesons. The  $\pi^0$  candidates are reconstructed by  
 1272 two algorithms which are executed concurrently. The “combinatorial”  $\pi^0$  algorithm produces  
 1273 a  $\pi^0$  candidate for every possible pair of photons within the jet. The “strips” algorithm clus-  
 1274 ters photons strips in  $\eta - \phi$ . The results of both algorithms are combined and then “cleaned”,  
 1275 resolving multiple hypotheses. The quality of a  $\pi^0$  candidate is determined according to the  
 1276 following categorical rankings:

- 1277     • The  $\pi^0$  candidate is in the ECAL barrel region ( $|\eta| < 1.5$ ) and has invariant mass  
     1278        $|m_{\gamma\gamma} - m_{\pi^0}| < 0.05 \text{ GeV}/c^2$ .
- 1279     • The  $\pi^0$  candidate is in the ECAL endcap region ( $|\eta| > 1.5$ ) and has invariant mass  
     1280        $m_{\gamma\gamma} < 0.2 \text{ GeV}/c^2$ .

- 1281     • The  $\pi^0$  candidate contains two or more photons within an  $\eta - \phi$  strip of size  $0.05 \times 0.20$ .
- 1282     • Photons not satisfying any of the other categories are considered as unresolved  $\pi^0$
- 1283           candidates in case they have  $p_T > 1.0$  GeV/c.

1284     The symbol  $m_{\pi^0}$  denotes the nominal neutral pion mass [19]. The size of the invariant mass

1285     windows in the ECAL endcap and barrel regions is motivated by the resolution on the  $\pi^0$

1286     mass (illustrated in Figure 3.15) during the commissioning of the particle-flow algorithm

1287     in early CMS data [35]. Multiple  $\pi^0$  candidates in the same category are ranked in quality

1288     according to the difference of the reconstructed photon pair mass to the nominal  $\pi^0$  mass.

1289     After the  $\pi^0$  candidates are ranked, the highest ranked candidate is selected for the final

1290     collection. The photon constituents of the highest ranked candidate are removed from re-

1291     maining  $\pi^0$  candidates not yet selected for the final collection in order to prevent photons

1292     from entering more than one  $\pi^0$  candidate. The rank of remaining  $\pi^0$  candidates is reevalu-

1293     ated and the  $\pi^0$  candidate with the next highest rank is selected for the output collection.

The process is repeated until no more  $\pi^0$  candidates are remaining.

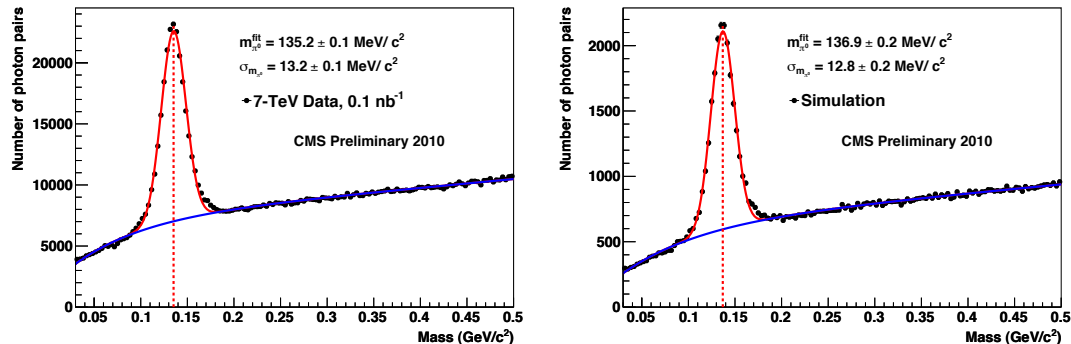


Figure 3.15: Invariant mass distribution of photon pairs reconstructed by the particle-flow in 2010 CMS minimum bias events (left), and predicted by the simulation (right). A clear resonant pick corresponding to the  $\pi_0$  meson is visible above the combinatoric background. Reference: [35]

(fig:PFPiZeroRes)  
1294

1295     Once the final collection of  $\pi^0$  candidates is determined, tau reconstruction in the

1296     HPS + TaNC algorithm proceeds by building tau candidates from reconstructed  $\pi^0$  candi-

1297     dates and charged hadrons reconstructed by the particle-flow algorithm. A combinatoric

1298     approach is again employed for the tau candidate building. A tau candidate hypothesis is

1299 built for every combination of jet constituents ( $\pi^0$  candidates plus charged hadrons) which  
 1300 has a multiplicity consistent with a hadronic tau decay. The tau candidates are ranked anal-  
 1301 ogous to the ranking utilized for the  $\pi^0$  reconstruction, but with the following categorical  
 1302 rankings:

- 1303     • In each decay mode category, the tau candidate with the highest neural network  
     1304       output is selected.
  - 1305     • The tau candidate has unit charge.
  - 1306     • The tau candidate passes the “lead pion” criteria, requiring that there is a photon or  
     1307       charged pion candidate with  $p_T > 5$  GeV/c.
  - 1308     • The tau candidate passes the HPS invariant mass and collimation<sup>1</sup> requirements.
- 1309 In case multiple tau candidates satisfy all four categorical requirements, the tau candidate  
 1310 with the highest energy sum of charged and neutral pions is selected as the highest ranking  
 1311 one.

### 1312 §3.5.2 Hadronic tau discrimination

1313 The final level of discrimination is performed by an ensemble of neural networks, with each  
 1314 neural network corresponding to a specific decay mode, analogously to the method used  
 1315 original TaNC algorithm (Section 3.3.2). The inputs of each neural network are different  
 1316 and correspond to the observables (invariant mass, Dalitz masses) available for its associ-  
 1317 ated decay mode. The neural networks are trained on samples simulated  $Z \rightarrow \tau^+\tau^-$  events  
 1318 (“signal”) and QCD di-jet events selected in the 7 TeV data collected by CMS in 2010  
 1319 (“background”). All of the tau hypothesis from a given jet reconstructed in data are used  
 1320 for training. The  $Z \rightarrow \tau^+\tau^-$  signal sample is generated by PYTHIA [36] which has been  
 1321 interfaced TAUOLA [37] for the purpose of generating the tau decays and simulated passed  
 1322 through the “full” GEANT [38] based simulation of the CMS detector. Only tau candidates  
 1323 which have been reconstructed in a decay mode matching the true decay mode of the tau

---

<sup>1</sup>The invariant mass of the signal candidates is required to be compatible with the resolution for that decay mode. The collimation selection requires the maximum  $\Delta R$  between any two signal candidates to be less than  $2.8/E_T$ , where  $E_T$  is the total transverse energy of the signal candidates. A full description is available in [32].

1324 on generator level enter the signal training sample. The neural network implementation,  
 1325 network layout, and training strategies are the same as in the original TaNC algorithm de-  
 1326 scribed in this chapter. To account for differences in the input signal purity and separation  
 1327 power of the neural networks between decay modes, the outputs of each neural network  
 1328 are transformed according to the method described in [39]. Multiple working-points corre-  
 1329 sponding to different purities are provided. The “loose” working point corresponds to an  
 1330 approximate fake-rate of 1%, and has slightly higher signal efficiency performance at high  
 1331  $p_T$  than the corresponding HPS-only working point.

### 1332 §3.6 Electron and Muon Rejection

sec:LightLeptonRejection) Additional discriminators must be applied to prevent electrons and muons from being iden-  
 1333 tified as hadronic tau decays. This is especially important for removing  $Z \rightarrow e^+e^-$  and  
 1334  $Z \rightarrow \mu^+\mu^-$  contributions when selecting events with two taus and requiring one of them to  
 1335 decay leptonically and the other hadronically. The electron and muon discrimination algo-  
 1336 rithms and performance are described in detail in [27]. A cursory overview of the techniques  
 1337 used are given here. Muon removal is achieved with high purity by requiring that no track in  
 1338 the signal collection of the tau candidate is matched to a segment<sup>2</sup> in the muon system. The  
 1339 rejections of true electrons is more difficult. Electrons leave no signal in the muon system  
 1340 and produce Bremsstrahlung photons as they travel through the magnetic field. The most  
 1341 significant difference from a true hadronic tau is that an electron is not expected to deposit  
 1342 any energy in the hadronic calorimeter. Electrons are thus rejected by requiring that there  
 1343 is a HCAL energy deposit with a magnitude that is greater than 10% of the momentum of  
 1344 the leading track in the tau.

---

<sup>2</sup>A track reconstructed in the DT or CSC sub-detectors.

Input observable	Neural network				
	$\pi^- \nu_\tau$	$\pi^- \pi^0 \nu_\tau$	$\pi^- \pi^0 \pi^0 \nu_\tau$	$\pi^- \pi^+ \pi^- \nu_\tau$	$\pi^- \pi^+ \pi^- \pi^0 \nu_\tau$
ChargedOutlierAngle1	•	•	•	•	•
ChargedOutlierAngle2	•	•	•	•	•
ChargedOutlierPt1	•	•	•	•	•
ChargedOutlierPt2	•	•	•	•	•
ChargedOutlierPt3	•	•	•	•	•
ChargedOutlierPt4	•	•	•	•	•
Dalitz1			•	•	•
Dalitz2			•	•	•
Eta	•	•	•	•	•
InvariantMassOfSignal		•	•	•	•
MainTrackAngle		•	•	•	•
MainTrackPt	•	•	•	•	•
OutlierNCharged	•	•	•	•	•
OutlierSumPt	•	•	•	•	•
PiZeroAngle1		•	•		•
PiZeroAngle2			•		
PiZeroPt1		•	•		•
PiZeroPt2			•		
TrackAngle1				•	•
TrackAngle2				•	•
TrackPt1				•	•
TrackPt2				•	•

Table 3.4: Input observables used for each of the neural networks implemented by the Tau Neural Classifier. The columns represents the neural networks associated to various decay modes and the rows represent the superset of input observables (see section 3.3.2) used in the neural networks. A dot in a given row and column indicates that the observable in that row is used in the neural network corresponding to that column.

(tab:nn`var`table)

## 1346 Chapter 4

# 1347 Mass Reconstruction: The Secondary Ver- 1348 tex Fit

1349  $\langle\text{ch:svfit}\rangle$  The dominant background in the search for a Higgs decaying to a  $\tau^+\tau^-$  pair is Standard  
 1350 Model  $Z \rightarrow \tau^+\tau^-$  events. The most “natural” observable to discriminate between Higgs  
 1351 signal and  $Z$  background would be the invariant mass of the di-tau system, utilizing the  
 1352 fact that the  $Z$  resonance is well known ( $m_Z = 91.1876 \pm 0.0021$  GeV/c<sup>2</sup>) and has a narrow  
 1353 width ( $\Gamma_Z = 2.4952 \pm 0.0023$  GeV) [19]. The experimental complication in this approach  
 1354 is due to the neutrinos produced in the tau lepton decays, which escape detection and  
 1355 carry away an unmeasured amount of energy, and making it difficult to reconstruct the  
 1356 tau lepton four-vectors. In this chapter we give an overview of techniques used in previous  
 1357 literature [18, 40, 41] to construct an observable related to the tau pair mass. We then  
 1358 introduce a new algorithm, called the Secondary Vertex (SV) fit. The SVfit reconstructs  
 1359 the “full” tau pair mass, and provides increased performance with respect to techniques  
 1360 previously used in the literature.

### 1361 §4.1 Existing mass reconstruction algorithms

1362 The simplest observable related to the  $\tau^+\tau^-$  mass is one can construct that is sensitive to  
 1363 new particle content is the invariant mass of the visible (reconstructible) decay products  
 1364 associated with each tau decays. This quantity, referred in this document as the “Visible  
 1365 Mass,” has the advantages of simplicity and lack of exposure to systematic errors associ-  
 1366 ated with the reconstruction of the  $E_T^{\text{miss}}$ . However, no attempt is made to reconstruct the  
 1367 neutrinos in the event. The reconstructed mass is thus systematically smaller than mass of  
 1368 the resonance which produced the tau leptons. The visible mass is typically on the order of

<sup>1369</sup> 1/2 of the resonance mass, depending on the kinematic requirements applied to the visible  
<sup>1370</sup> products of the tau decays.

The Collinear Approximation is a technique previously used [18] to reconstruct the *full*  $\tau^+\tau^-$  mass. In an event with two tau decays, there are a total of six unknowns associated with the missing energy: the three components of the momentum of each neutrino. The Collinear Approximation makes the assumption that the neutrinos have the same direction as their associated visible decay products. This assumption reduces the number of unknown quantities to two, corresponding to the total energy of each neutrino. These two unknowns can be solved for by using the two components of the reconstructed missing transverse energy, which in the ideal case corresponds to the transverse component of the vector sum of the two neutrino's four momentum. The characteristic equation of the Collinear Approximation is

$$\begin{pmatrix} E_x^{\text{miss}} \\ E_y^{\text{miss}} \end{pmatrix} = \begin{pmatrix} \cos \phi_1 & \cos \phi_2 \\ \sin \phi_1 & \sin \phi_2 \end{pmatrix} \begin{pmatrix} E_1 \\ E_2 \end{pmatrix} \quad (4.1) \quad [\text{eq:CollinearAppr}]$$

where  $(E_x^{\text{miss}}, E_y^{\text{miss}})$  are the two components of the reconstructed missing transverse energy,  $\phi_{1(2)}$  is the azimuthal angle of the visible component of the first (second) tau decay, and  $E_{1(2)}$  is the reconstructed energy of neutrino of the first (second) tau decay.  $E_1$  and  $E_2$  can be extracted by inverting the matrix on the right hand side of Equation 4.1.

$$\begin{pmatrix} E_1 \\ E_2 \end{pmatrix} = \frac{1}{\sin(\phi_2 - \phi_1)} \begin{pmatrix} \sin \phi_2 & -\cos \phi_2 \\ -\sin \phi_1 & \cos \phi_1 \end{pmatrix} \begin{pmatrix} E_x^{\text{miss}} \\ E_y^{\text{miss}} \end{pmatrix} \quad (4.2) \quad [\text{eq:CollinearAppr}]$$

<sup>1371</sup> The Collinear Approximation suffers from two problems. The approximation can fail  
<sup>1372</sup> (yielding unphysical negative energies for the reconstructed neutrinos) when the missing  
<sup>1373</sup> transverse energy is mis-measured. The events with unphysical solutions must be removed  
<sup>1374</sup> from the analysis, leading to a dramatic reduction in acceptance (on the order of 50% in  
<sup>1375</sup> this analysis). Improvements to the collinear approximation algorithm have recently been  
<sup>1376</sup> made which aim to recover part of the events with unphysical solutions [42]. But even with  
<sup>1377</sup> these improvements, no physical solution is still found for a large fraction of signal events.  
<sup>1378</sup> Additionally, the method is numerically sensitive when the two  $\tau$  lepton are nearly back-

1379 to-back in azimuth. In these cases the  $\sin(\phi_2 - \phi_1)^{-1}$  term in Equation 4.2 is very large  
 1380 and small mis-measurements of the missing transverse energy can produce a large tail on  
 1381 the reconstructed mass. This tail is particularly large for low-mass resonances. The large  
 1382 tail for low mass is predominantly due to the fact (discussed in subsection 4.4.2) that the  
 1383 kinematic requirements<sup>1</sup> applied on the visible decay products preferentially selects events  
 1384 where the visible decay products carry the majority of the energy of the original  $\tau$  lepton,  
 1385 reducing the amount of true missing energy in the event.

## 1386 §4.2 The Secondary Vertex fit

1387 A novel algorithm is presented in the following, which succeeds in finding a physical solution  
 1388 for every event. As an additional benefit, the new algorithm is found to improve the di-tau  
 1389 invariant mass resolution, making it easier to separate the Higgs signal from the  $Z \rightarrow \tau^+\tau^-$   
 1390 background.

1391 The novel Secondary Vertex fit (SVfit) algorithm for di-tau invariant mass reconstruc-  
 1392 tion that we present in the following utilizes a likelihood maximization to fit a  $\tau^+\tau^-$  in-  
 1393 variant mass hypothesis for each event. The likelihood is composed of separate terms which  
 1394 represent probability densities of:

- 1395     • tau decay kinematics
- 1396     • matching between the momenta of neutrinos produced in the tau decays and the  
     1397        reconstructed missing transverse momentum
- 1398     • a regularization “ $p_T$ -balance” term which accounts for the effects on the di-tau in-  
     1399        variant mass of acceptance cuts on the visible tau decay products
- 1400     • the compatibility of tau decay parameters with the position of reconstructed tracks  
     1401        and the known tau lifetime of  $c\tau = 87 \mu\text{m}$  [19].

1402 The likelihood is maximized as function of a set of parameters which fully describe the tau  
 1403 decay.

---

<sup>1</sup>The kinematic requirements on the visible decay products are necessary to reduce backgrounds and maintain compatibility with un-prescaled event triggers. This topic is discussed in detail in Chapter 5.

### 1404 §4.3 Parametrization of tau decays

1405 <sec:svParameterization> The decay of a tau of visible four-momentum  $p_{vis}$  measured in the CMS detector (“laboratory”)  
 1406 frame can be parametrized by three variables. The invisible (neutrino) momentum  
 1407 is fully determined by these parameters.

1408       The “opening-angle”  $\theta$  is defined as the angle between the boost direction of the tau  
 1409 lepton and the momentum vector of the visible decay products in the rest frame of the  
 1410 tau. The azimuthal angle of the tau in the lab frame is denoted as  $\bar{\phi}$  (we denote quantities  
 1411 defined in the laboratory frame by a overline). A local coordinate system is defined such  
 1412 that the  $\bar{z}$ -direction lies along the visible momentum and  $\bar{\phi} = 0$  lies in the plane spanned  
 1413 by the momentum vector of the visible decay products and the proton beam direction. The  
 1414 third parameter,  $m_{\nu\nu}$ , denotes the invariant mass of the invisible momentum system.

Given  $\theta$ ,  $\bar{\phi}$  and  $m_{\nu\nu}$ , the energy and direction of the tau lepton can be computed by means of the following equations: The energy of the visible decay products in the rest frame of the tau lepton is related to the invariant mass of the neutrino system by:

$$E^{vis} = \frac{m_\tau^2 + m_{vis}^2 - m_{\nu\nu}^2}{2m_\tau} \quad (4.3) \quad \text{[eq:restFrameM...]$$

1415 Note that for hadronic decays,  $m_{\nu\nu}$  is a constant of value zero, as only a single neutrino is  
 1416 produced. Consequently, the magnitude of  $P^{vis}$  depends on the reconstructed mass of the  
 1417 visible decay products only and is a constant during the SVfit.

The opening angle  $\bar{\theta}$  between the tau lepton direction and the visible momentum vector in the laboratory frame is determined by the rest frame quantities via the (Lorentz invariant) component of the visible momentum perpendicular to the tau lepton direction:

$$\begin{aligned} p_{\perp}^{vis} &= \bar{p}_{\perp}^{vis} \\ \Rightarrow \sin \bar{\theta} &= \frac{p^{vis} \sin \theta}{\bar{p}^{vis}} \end{aligned} \quad (4.4) \quad \text{[eq:labFrameOpen...]$$

Substituting the parameters  $m_{\nu\nu}$  and  $\theta$  into equations 4.3 and 4.4, the energy of the tau is obtained by solving for the boost factor  $\gamma$  in the Lorentz transformation between tau rest frame and laboratory frame of the visible momentum component parallel to the tau

direction:

$$\bar{p}^{vis} \cos \bar{\theta} = \gamma \beta E^{vis} + \gamma p^{vis} \cos \theta$$

$$\Rightarrow \gamma = \frac{E^{vis}[(E^{vis})^2 + (\bar{p}^{vis} \cos \bar{\theta})^2 - (p^{vis} \cos \theta)^2]^{1/2} - p^{vis} \cos \theta \bar{p}^{vis} \cos \bar{\theta}}{(E^{vis})^2 - (p^{vis} \cos \theta)^2},$$

$$E^\tau = \gamma m_\tau$$

1418     The energy of the tau lepton in the laboratory frame as function of the measured visible  
 1419   momentum depends on two of the three parameters only - the rest frame opening angle  $\theta$  and  
 1420   the invariant mass  $m_{\nu\nu}$  of the neutrino system. The direction of the tau lepton momentum  
 1421   vector is not fully determined by  $\theta$  and  $m_{\nu\nu}$ , but is constrained to lie on the surface of a  
 1422   cone of opening angle  $\bar{\theta}$  (given by equation 4.4), the axis of which is given by the visible  
 1423   momentum vector. The tau lepton four-vector is fully determined by the addition of the  
 1424   third parameter  $\bar{\phi}$ , which describes the azimuthal angle of the tau lepton with respect to the  
 1425   visible momentum vector. The spatial coordinate system used is illustrated in Figure 4.1.

## 1426   §4.4 Likelihood for tau decay

The probability density functions for the tau decay kinematics are taken from the kinematics review of the PDG [19]. The likelihood is proportional to the phase-space volume for two-body ( $\tau \rightarrow \tau_{had}\nu$ ) and three-body ( $\tau \rightarrow e\nu\nu$  and  $\tau \rightarrow \mu\nu\nu$ ) decays. For two-body decays the likelihood depends on the decay angle  $\theta$  only:

$$d\Gamma \propto |\mathcal{M}|^2 \sin \theta d\theta$$

For three-body decays, the likelihood depends on the invariant mass of the neutrino system also:

$$d\Gamma \propto |\mathcal{M}|^2 \frac{((m_\tau^2 - (m_{\nu\nu} + m_{vis})^2)(m_\tau^2 - (m_{\nu\nu} - m_{vis})^2))^{1/2}}{2m_\tau} m_{\nu\nu} dm_{\nu\nu} \sin \theta d\theta \quad (4.5) \quad \text{[eq:pdfKineLepto]}$$

1427   In the present implementation of the SVfit algorithm, the matrix element is assumed to be  
 1428   constant, so that the likelihood depends on the phase-space volume of the decay only <sup>2</sup>.

### 1429   §4.4.1 Likelihood for reconstructed missing transverse momentum

1430   Momentum conservation in the plane perpendicular to the beam axis implies that the  
 1431   vectorial sum of the momenta of all neutrinos produced in the decay of the tau lepton pair

---

<sup>2</sup>The full matrix elements for tau decays may be added in the future, including terms for the polarization of the tau lepton pair, which is different in Higgs and  $Z$  decays [43].

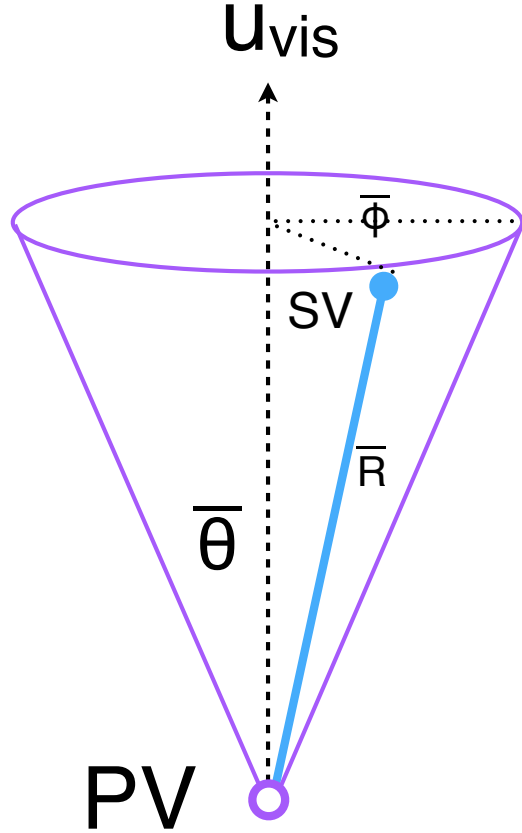


Figure 4.1: Illustration of the coordinate system used by the SVfit to describe the decays of tau leptons.

ig:svFitDecayParDiagram)

- <sup>1432</sup> matches the reconstructed missing transverse momentum. Differences are possible due to
- <sup>1433</sup> the experimental resolution and finite  $p_T$  of particles escaping detection in beam direction
- <sup>1434</sup> at high  $|\eta|$ .

The  $E_T^{\text{miss}}$  resolution is measured in  $Z \rightarrow \mu^+\mu^-$  events selected in the 7 TeV data collected by CMS in 2010. Corrections are applied to the distribution of  $E_T^{\text{miss}}$  in the Monte Carlo simulated events to match the resolution measured in data. The uncertainty on this correction factor is taken as a “shape systematic.” The treatment of this correction and its corresponding uncertainty are described in Chapters 7 and 8. The momentum vectors of reconstructed  $E_T^{\text{miss}}$  and neutrino momenta given by the fit parameters are projected in direction parallel and perpendicular to the direction of the  $\tau^+\tau^-$  momentum vector. For both components, a Gaussian probability function is assumed. The width and mean values

of the Gaussian in parallel (“||”) and perpendicular (“ $\perp$ ”) direction are:

$$\sigma_{\parallel} = \max(7.54(1 - 0.00542 \cdot q_T), 5.)$$

$$\mu_{\parallel} = -0.96$$

$$\sigma_{\perp} = \max(6.85(1 - 0.00547 \cdot q_T), 5.)$$

$$\mu_{\perp} = 0.0,$$

1435 where  $q_T$  denotes the transverse momentum of the tau lepton pair.

#### 1436 §4.4.2 Likelihood for tau lepton transverse momentum balance

(sec:ptBalance) The tau lepton transverse momentum balance likelihood term represents the probability  $p(p_T^{\tau}|M_{\tau\tau})$  for a tau to have a certain  $p_T$ , given that the tau is produced in the decay of a resonance of mass  $M_{\tau\tau}$ . The likelihood is constructed by parametrizing the shape of the tau lepton  $p_T$  distribution in simulated Higgs  $\rightarrow \tau^+\tau^-$  events as a function of the Higgs mass. The functional form of the parametrization is taken to be the sum of two terms. The first term, denoted by  $p^*(p_T|M)$ , is derived by assuming an isotropic two-body decay, that is

$$dp^* \propto \sin \theta d\theta.$$

Performing a variable transformation from  $\theta$  to  $p_T \sim \frac{M}{2} \sin \theta$ , we obtain

$$\begin{aligned} p^*(p_T|M) &= \frac{dp}{dp_T} = \frac{dp}{d \cos \theta} \left| \frac{d \cos \theta}{dp_T} \right| \\ &\propto \left| \frac{d}{dp_T} \sqrt{1 - \left(2 \frac{p_T}{M}\right)^2} \right| \\ &= \frac{1}{\sqrt{\left(\frac{M}{2p_T}\right)^2 - 1}}. \end{aligned} \tag{4.6} \quad \boxed{\text{eq:ptBalanceTerm}}$$

The first term of the  $p_T$ -balance likelihood is taken as the convolution of equation 4.6 with a Gaussian of width  $s$ . The second term is taken to be a Gamma distribution of scale parameter  $\theta$  and shape parameter  $k$ , in order to account for tails in the  $p_T$  distribution of the tau lepton pair. The complete functional form is thus given by

$$p(p_T|M) \propto \int_0^{\frac{M}{2}} p^*(p'_T|M) e^{-\frac{(p_T-p'_T)^2}{2s^2}} dp'_T + a\Gamma(p_T, k, \theta). \tag{4.7} \quad \boxed{\text{eq:ptBalanceLike}}$$

Numerical values of the parameters  $s$ ,  $\theta$  and  $k$  are determined by fitting function 4.7 to the tau lepton  $p_T$  distribution in simulated Higgs  $\rightarrow \tau^+\tau^-$  events. The relative weight  $a$  of the two terms is also determined in the fit. Replacing the integrand in equation 4.7 by its Taylor

expansion, so that the integration can be carried out analytically, keeping polynomial terms up to fifth order, and assuming the fit parameters to depend at most linearly on the Higgs mass, we obtain the following numerical values for the parameters:

$$\begin{aligned}s &= 1.8 + 0.018 \cdot M_{\tau\tau} \\k &= 2.2 + 0.0364 \cdot M_{\tau\tau} \\ \theta &= 6.74 + 0.02 \cdot M_{\tau\tau} \\a &= 0.48 - 0.0007 \cdot M_{\tau\tau}.\end{aligned}$$

1437        The motivation to add the  $p_T$ –balance likelihood to the SVfit is to add a “regulariza-  
 1438        tion” term which compensates for the effect of  $p_T$  cuts applied on the visible decay products  
 1439        of the two tau leptons. In particular for tau lepton pairs produced in decays of resonances  
 1440        of low mass, the visible  $p_T$  cuts significantly affect the distribution of the visible momentum  
 1441        fraction  $x = \frac{E_{vis}}{E_\tau}$ . The effect is illustrated in figures 4.3 and 4.4. If no attempt would be  
 1442        made to compensate for this effect, equations 4.4, 4.5 would yield likelihood values that  
 1443        are too high at low  $x$ , resulting in the SVfit to underestimate the energy of visible decay  
 1444        products (overestimate the energy of neutrinos) produced in the tau decay, resulting in a  
 1445        significant tail of the reconstructed mass distribution in the high mass region. The  $\tau^+\tau^-$   
 1446        invariant mass distribution reconstructed with and without the  $p_T$ –balance likelihood term  
 1447        is shown in figure 4.2. A significant improvement in resolution and in particular a significant  
 1448        reduction of the non–Gaussian tail in the region of high masses is seen.

#### 1449        §4.4.3 Secondary vertex information

1450        The parametrization of the tau decay kinematics described in section 4.3 can be extended  
 1451        to describe the production and decay of the tau. As the flight direction of the tau is already  
 1452        fully determined by the parameters  $\theta$ ,  $\bar{\phi}$  and  $m_{\nu\nu}$ , the position of the secondary (decay)  
 1453        vertex is hence fully determined by addition of a single parameter for the flight distance,  
 1454         $r$ . The tau lifetime  $c\tau = 87 \mu\text{m}$  is large enough to allow the displacement of the tau decay  
 1455        vertex from the primary event vertex to be resolved by the CMS tracking detector. The  
 1456        resolution provided by the CMS tracking detector is utilized to improve the resolution on  
 1457        the  $\tau^+\tau^-$  invariant mass reconstructed by the SVfit algorithm. The likelihood term based on  
 1458        the secondary vertex information is based on the compatibility of the decay vertex position

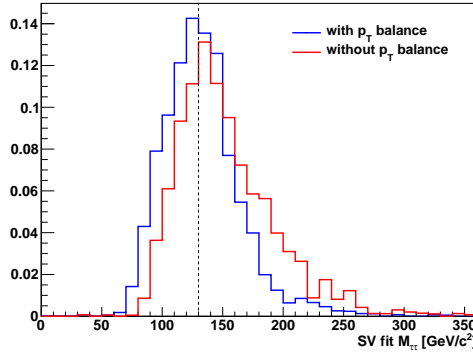


Figure 4.2: Distribution of di-tau invariant mass reconstructed by the SVfit algorithm in simulated Higgs events with  $m_{A^0} = 130 \text{ GeV}/c^2$ . The SVfit algorithm is run in two configurations, with (blue) and without (red) the  $p_T$ -balance likelihood term included in the fit.

with the reconstructed tracks of charged tau decay products. Perhaps surprisingly, it turns out that the flight distance parameter  $R$  is sufficiently constrained even for tau decays into a single charged hadron, electron or muon.

The parameter  $R$  can be constrained further by a term which represents the probability for a tau lepton of momentum  $P$  to travel a distance  $d$  before decaying:

$$p(d|P) = \frac{m_\tau}{P c \tau} e^{-\frac{m_\tau d}{P c \tau}}$$

The likelihood terms for the secondary vertex fit have been implemented in the SVfit algorithm. In the analysis presented in this note, the decay vertex information is not used, however, because of systematic effects arising from tracker (mis-)alignment which are not yet fully understood.

## §4.5 Performance

The tau pair mass reconstructed by the Secondary Vertex fit (“SVfit mass”) provides the observable with the largest separation between signal Higgs events and the dominant  $Z \rightarrow \tau^+ \tau^-$  background. The mean of the SVfit mass is located at the true mass of the di-tau pair. The SVfit algorithm has a higher acceptance and better resolution than the Collinear Approximation algorithm. The SVfit always finds a physical solution, improving the efficiency of the collinear approximation by a factor of two. Additionally, it has a much better resolution. The collinear approximation reconstructed mass distribution has a large

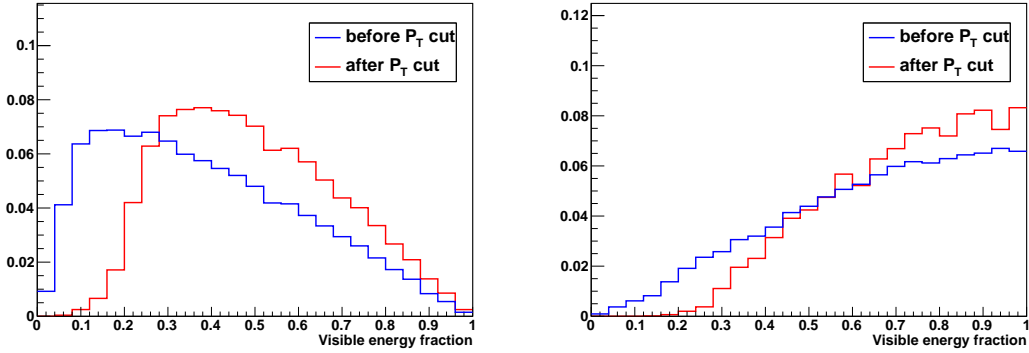


Figure 4.3: Normalized distributions of the fraction of total tau decay energy carried by the muon (left) and hadronic constituents (right) in simulated Higgs events with  $m_{A^0} = 130 \text{ GeV}/c^2$ . The distribution is shown before (blue) and after (red) the requirement on the  $p_T$  of the visible decay products described in Chapter 5.

(fig:ptBalancePtVisCuts)

tail at high mass due to events with poorly measured  $E_T^{\text{miss}}$ . The shape of the SVfit distribution is nearly Gaussian. The comparison is illustrated in Figure 4.5. Previous searches for Higgs bosons decaying to tau leptons [40] have in general used the “visible mass” as the observable used to search for new resonances. The SVfit method has the obvious difference that it reconstructs the “full” tau pair mass, which is the most natural observable corresponding to a particle decaying to tau leptons. In addition, the relative resolution<sup>3</sup> of the SV fit is superior to that of the visible mass. This feature is illustrated in Figure 4.6. In Figure 4.6, the visible mass distribution is scaled by an arbitrary number such that the scaled mean of the distribution matches the true mass of the tau pair (and the SVfit mass). The width of the SVfit distribution is smaller than that of the scaled visible mass distribution, indicating better performance. The increase in relative resolution allows a “bump,” due to the presence of signal events, to be more easily distinguished from the  $Z \rightarrow \tau^+\tau^-$  background. This increases the power of the search for the new signal.

---

<sup>3</sup>We define this metric of performance as the variance of a distribution divided by its mean.

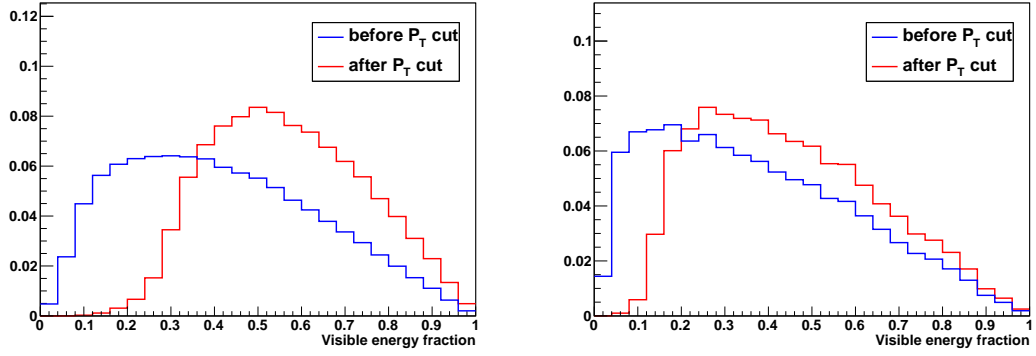


Figure 4.4: Normalized distributions of the fraction of total tau decay energy carried by the muon in simulated  $Z \rightarrow \tau^+\tau^-$  (left) and Higgs events with  $m_{A^0} = 200 \text{ GeV}/c^2$  (right). The distribution is shown before (blue) and after (red) the requirement that the  $p_T$  of the muon be greater than  $15 \text{ GeV}/c$ .

PtVisCutsCompareMasses

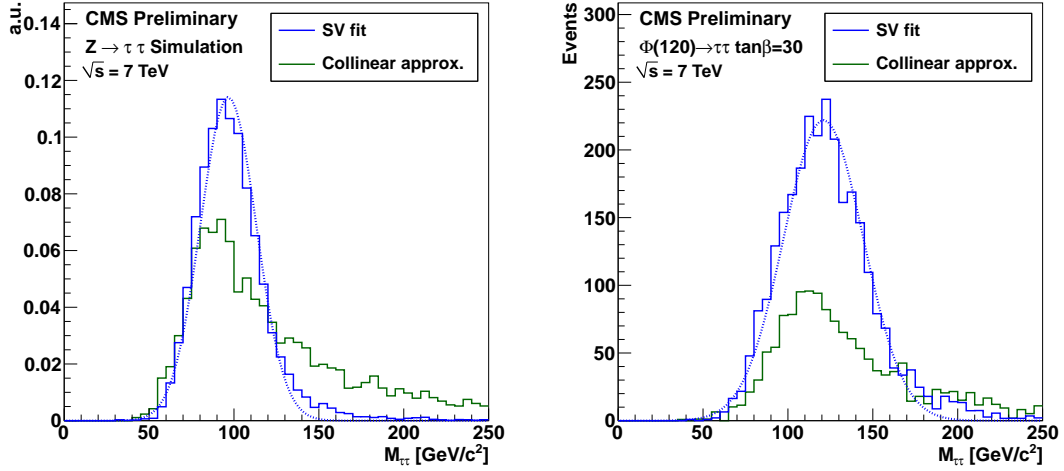


Figure 4.5: Comparison of the reconstructed tau pair mass spectrum in  $Z \rightarrow \tau^+\tau^-$  (left) and MSSM  $H(120) \rightarrow \tau^+\tau^-$  (right) events after the selections described in chapter 5. The mass spectrum reconstructed by the Secondary Vertex fit is shown in blue, the result of the collinear approximation algorithm is given in green. In the left plot, both distributions are normalized to unity, illustrating the improvement in resolution (shape) provided by the SVfit. In the right plot, the distributions are normalized to an (arbitrary) luminosity, illustrating the loss of events that occurs due to unphysical solutions in the application of the collinear approximation.

(fig:SVversusCollinear)

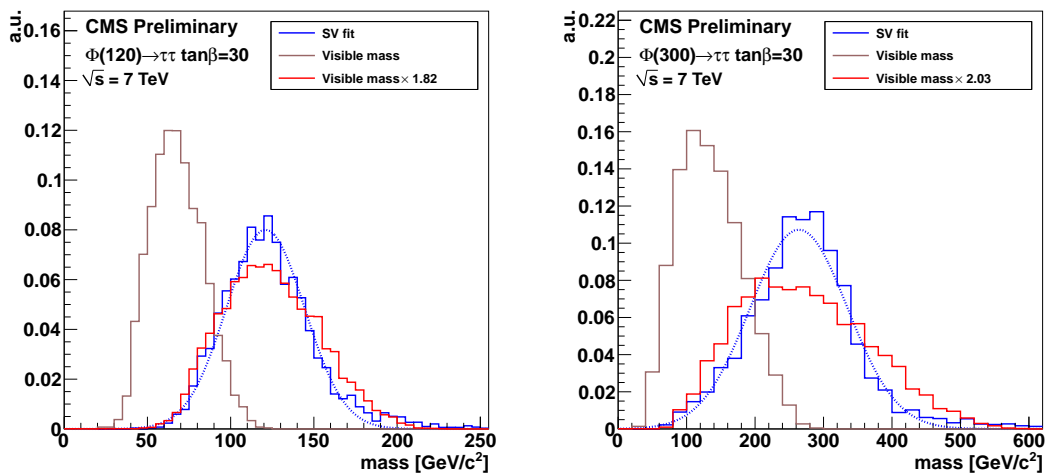


Figure 4.6: Comparison of the invariant mass of the muon and  $\tau_{\text{jet}}$  (the “visible mass”) with the full  $\tau^+\tau^-$  mass reconstructed by the SVfit. The spectrum is shown for two simulated MSSM Higgs samples, with  $m_{A^0} = 120 \text{ GeV}/c^2$  (left), and  $m_{A^0} = 200 \text{ GeV}/c^2$  (right). To illustrate that relative resolution of the SVfit is superior to that of the visible mass, the visible mass is also shown scaled up such that the mean of the two distributions are identical.

(fig:SVversusVis)

1487

## Chapter 5

---

1488

# Analysis Selections

&lt;ch:selections&gt;

1489 The selections applied to data in this analysis are designed to maximize the significance of  
 1490 Higgs signal events in the final set of selected events. This analysis presented in this thesis  
 1491 is an inclusive analysis, meaning that no preference is given to any single Higgs production  
 1492 mechanism. The analysis looks specifically at the channel in which one tau decays to a  
 1493 muon and the other decays to hadrons. Therefore the first step in the analysis selection is  
 1494 to find High Level Trigger selection that is highly efficiency for our signal and is not highly  
 1495 prescaled<sup>1</sup>. After the trigger selection, events are required to contain at least a good muon  
 1496 and a good tau. Vetoos on extra leptons are applied to reduce backgrounds from di-muon  
 1497 events. Finally, kinematic and charge selections on the are applied to the event to reduce  
 1498  $W + \text{jets}$  and QCD backgrounds.

1499

## §5.1 High Level Trigger

1500 As only data which passes the HLT is recorded, it is thus critical that an appropriate trigger  
 1501 path is found. The events in this analysis are triggered by a combination of muon and muon  
 1502 + tau-jet “cross-channel” triggers. For the muon triggers, paths with lowest  $p_T$  thresholds  
 1503 are used as long as the path remained unprescaled (see Table 5.1). The muon + tau-jet  
 1504 “cross-channel” trigger paths increase the trigger efficiency for events containing muons of  
 1505 transverse momenta close to the  $p_T^\mu > 15$  GeV/c cut threshold. The trigger efficiency is  
 1506 measured in data via the tag-and-probe technique. Details of the muon trigger efficiency  
 1507 measurement are given in Section 7.1. Monte Carlo simulated events are required to pass

---

<sup>1</sup>If a trigger has high background rates, it may exceed its rate budget with increasing luminosity. When this happens, it is generally “prescaled,” and some fraction of the events that pass this trigger are randomly thrown it away to reduce the rate. In general, it is better to use an unprescaled trigger with lower efficiency than a prescaled trigger.

Trigger path	run-range
HLT_Mu9	132440 - 147116
HLT_IsoMu9	147196 - 148058
HLT_Mu11	147196 - 148058
HLT_Mu15	147196 - 149442
HLT_IsoMu13	148822 - 149182
HLT_IsoMu9_PFTau15	148822 - 149182
HLT_Mu11_PFTau15	148822 - 149182

Table 5.1: Muon and muon + tau–jet “cross–channel” trigger paths utilized to trigger events in different data–taking periods.

{tab:AHToMuTauTriggers}

1508 the HLT\_Mu9 trigger path. Weights are applied to simulated events to account for the  
 1509 difference between the simulated HLT\_Mu9 efficiency and the combined efficiency of the set  
 1510 HLT\_Mu9, HLT\_IsoMu9, HLT\_Mu11, HLT\_IsoMu13, HLT\_Mu15, HLT\_IsoMu9\_PFTau15  
 1511 and HLT\_Mu11\_PFTau15 used to trigger the data.

## 1512 §5.2 Particle Identification

### 1513 §5.2.1 Muons

1514 {sec:MuonId} Muon candidates are required to be reconstructed as global and as tracker muons, meaning  
 1515 that a full track is reconstructed in the muon system and is well matched to a track in the  
 1516 silicon strip and pixel trackers. Additionally, they are required to pass the “Vector Boson  
 1517 Task Force” (VBTF) muon identification criteria developed for the  $Z \rightarrow \mu^+ \mu^-$  cross–section  
 1518 measurement [44]:

- 1519     •  $\geq 1$  Pixel hits
- 1520     •  $\geq 10$  hits in silicon Pixel + Strip detectors
- 1521     •  $\geq 1$  hit(s) in muon system
- 1522     •  $\geq 2$  matched segments

- 1523     •  $\chi^2/DoF < 10$  for global track fit
- 1524     • transverse impact parameter of “inner” track  $d_{\text{IP}} < 2$  mm with respect to beam-spot

1525       In order to reduce background contributions from muons originating from heavy quark  
 1526       decays in QCD multi-jet events, muons are required to be isolated. Isolation is computed  
 1527       as the  $p_{\text{T}}$  sum of charged and neutral hadrons plus photons reconstructed by the CMS  
 1528       particle-flow algorithm [28] within a cone of size  $\Delta R_{iso} = 0.4$  around the muon direction.  
 1529       The innermost region of size  $\Delta R_{veto} = 0.08$  (0.05) is excluded from the computation of  
 1530       the isolation  $p_{\text{T}}$  sum with respect to neutral hadrons (photons), in order to avoid energy  
 1531       deposits in the electromagnetic and hadronic calorimeters which are due to the muon to  
 1532       enter the sum. In order to reduce pile-up effects, particles entering the isolation  $p_{\text{T}}$  sum are  
 1533       required to have transverse momenta  $p_{\text{T}} > 1.0$  GeV/c. Charged particles are additionally  
 1534       required to originate from the same vertex as the muon. The muons are required to be  
 1535       isolated with respect to charged hadrons of  $p_{\text{T}} > 1.0$  GeV/c and photons of  $p_{\text{T}} > 1.5$  GeV/c  
 1536       as reconstructed by the particle-flow algorithm [28] in a cone of size  $\Delta R = 0.4$  around the  
 1537       direction of the muon.

1538     §5.2.2 Hadronic Taus

1539       Hadronic decays of taus are identified by the HPS + TaNC hybrid algorithm described in  
 1540       Section 3.5. The “medium” working point is used, corresponding to an expected QCD fake-  
 1541       rate of about 1%.  $Z \rightarrow \mu^+\mu^-$  background contributions are largely due to muons which  
 1542       failed to get reconstructed as global muons (thus failing the muon identification requirement)  
 1543       and are misidentified as tau-jet candidates. These muons are typically isolated and have a  
 1544       large chance to pass the hadronic tau ID discriminators. To reject these events, hadronic  
 1545       taus are additionally required to pass an anti-muon veto described in Section 3.6.

1546     §5.2.3 Missing Transverse Energy

1547       The missing transverse energy  $E_{\text{T}}^{\text{miss}}$ , in the event is reconstructed based on the vectorial  
 1548       momentum sum of particle candidates reconstructed by the particle-flow algorithm [28, 45].  
 1549       In the ideal case, the  $E_{\text{T}}^{\text{miss}}$  corresponds to the vector sum of the transverse components of  
 1550       all neutrinos in the event. The  $E_{\text{T}}^{\text{miss}}$  resolution in simulated  $Z \rightarrow \mu^+\mu^-$  events is found

Background	Cross Section ( pb)
QCD Heavy Flavor	84679 <sup>3</sup>
$W \rightarrow \mu\nu + \text{jets}$	10435
$Z \rightarrow \mu\mu + \text{jets}$	1666
$t\bar{t} + \text{jets}$	158

Table 5.2: The different backgrounds to the analysis presented in this thesis that include misidentified hadronic taus.

(tab:FakeBackgrounds)

1551 to be smaller (better) than in the data. The reconstructed  $E_T^{\text{miss}}$  in the simulated events is  
 1552 “smeared” by a correction factor such that the data and simulation are in agreement. The  
 1553 “Z-recoil”  $E_T^{\text{miss}}$  correction procedure is described in Section 7.4.

### 1554 §5.3 Event Selections

1555 The selections applied to the analysis are designed to reject large fractions of the background  
 1556 while maintaining a high efficiency for identifying signal (Higgs) events. The backgrounds  
 1557 can be divided into two classifications: “fake” backgrounds, in which there is at least one  
 1558 misidentified hadronic tau decay, and the irreducible  $Z \rightarrow \tau^+\tau^-$  background, which cannot<sup>2</sup>  
 1559 be distinguished from the potential presence of a Higgs boson of the same mass. Strategies  
 1560 for dealing with the irreducible  $Z$  background will be discussed in the Chapter 9. The  
 1561 different fake backgrounds, their cross section, and the basic removal strategies are outlined  
 1562 in Table 5.2.

1563 Events are selected by requiring a muon of  $p_T^\mu > 15$  GeV/c within  $|\eta_\mu| < 2.1$  and a tau-  
 1564 jet candidate of  $p_T^{\tau-\text{jet}} > 20$  GeV/c within  $|\eta_{\tau-\text{jet}}| < 2.3$ . The  $\eta$  requirement on the muon  
 1565 ensures that it is within the fiducial region of the muon trigger system. The  $\eta$  requirement  
 1566 on the hadronic tau ensures it is well within the fiducial region of the tracker ( $|\eta| < 2.5$ )  
 1567 and minimizes exposure to large QCD backgrounds in the very forward region.

---

<sup>2</sup>Due to the differences in spin between the  $Z$  (spin 1) and the Higgs (spin 0), it maybe be possible to separate the two using spin correlations of the two tau decays.

1568        The muon and tau–jet candidate are required to be of opposite charge, as the Higgs is  
 1569        neutral and charge is conserved. The muon is required to be pass the identification criteria  
 1570        described in Section 5.2.1. The tau-jet candidate is required to pass the “loose” TaNC tau  
 1571        identification discriminator.

1572        Additional event selection criteria are applied to reduce contributions of specific back-  
 1573        ground processes. In order to reject this background, a dedicated discriminator against  
 1574        muons is applied [27]. Remaining muon background is suppressed by rejecting events which  
 1575        have a track of  $p_T > 15 \text{ GeV}/c$  and for which the sum of energy deposits in ECAL plus  
 1576        HCAL is below  $0.25 \cdot P$  within a cylinder of radius 15 cm(ECAL) and 25 cm(HCAL),  
 1577        respectively. Contamination from  $Z \rightarrow \tau^+\tau^-$  events in which the reconstructed tau–jet can-  
 1578        didate is due to a  $\tau \rightarrow e\nu\nu$  decay is reduced by applying a dedicated tau ID discriminator  
 1579        against electrons.

The  $t\bar{t}$  and  $W + \text{jets}$  backgrounds are suppressed by cuts on the transverse mass of the  $\mu - -E_T^{\text{miss}}$  system and the  $P_\zeta$  variable. The transverse mass ( $M_T$ ) cut is defined as the quantity

$$M_T = p_T^\mu E_T^{\text{miss}} \sqrt{1 - \cos \Delta\phi}, \quad (5.1) \{?\}$$

1580        where  $\Delta\phi$  is the angle between the muon and the reconstructed  $E_T^{\text{miss}}$  in the transverse  
 1581        plane. The  $M_T$  quantity is much higher in events  $W \rightarrow \mu\nu$  decays than in signal Higgs  
 1582        events. In  $W \rightarrow \mu\nu$  decays, the neutrino expected to be produced in the opposite to the  
 1583        muon in azimuth. In signal events, there are three neutrinos produced, with the majority  
 1584        (two) of the neutrinos being associated to the  $\tau \rightarrow \mu\nu\nu$  decay. Accordingly, we expect that  
 1585        the  $E_T^{\text{miss}}$  is on average collinear with the muon in signal events. The  $M_T$  distribution before  
 1586        the  $M_T$  cut is applied is illustrated in Figure 5.1(b) for the different background sources  
 1587        and 2010 data.

1588        The  $P_\zeta$  variable is another quantity with discriminant power against  $W + \text{jets}$  and  
 1589         $t\bar{t}$  backgrounds. The observable has been introduced in the search for  $H \rightarrow \tau^+\tau^-$  events  
 1590        performed by the CDF collaboration [?]. The observable is motivated by the fact that in  
 1591         $\tau^+\tau^-$  signal events all neutrinos are produced in direction very close of the visible decay  
 1592        products of one of the two tau leptons. It is therefore expected that the direction of the  
 1593        missing transverse energy vector in these events point in a direction somewhere between

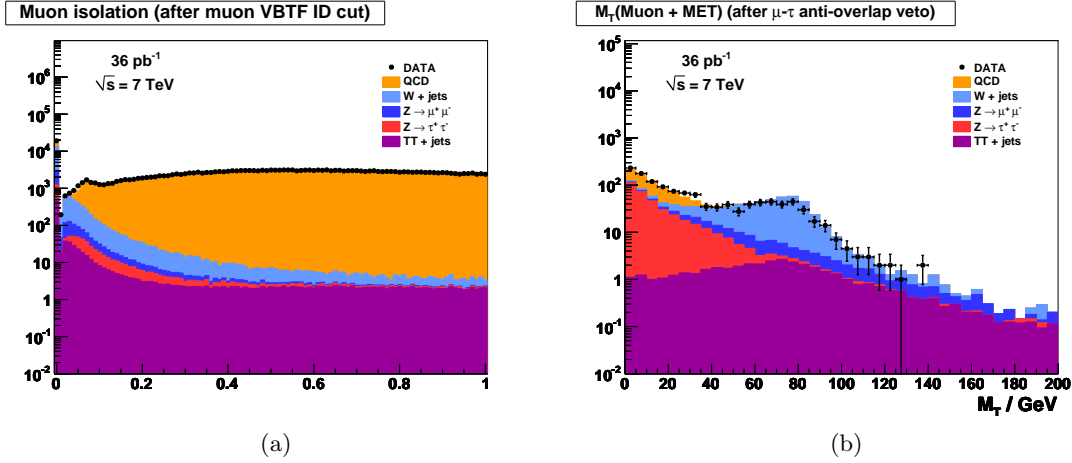


Figure 5.1: Distributions of the muon isolation (a) and  $M_T$  (b) discriminant variables. The muon isolation discriminant rejects the QCD background at a high rate. The  $M_T$  cut is designed to reject  $W + \text{jets}$  and  $t\bar{t} + \text{jets}$  backgrounds. The distributions shown are computed immediately before the corresponding selection is applied.

fig:CutFlowControlPlots)?

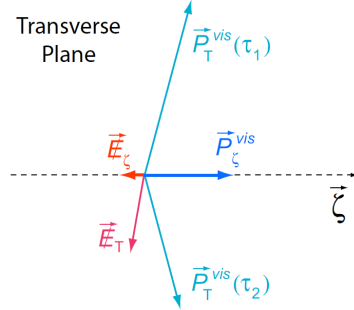


Figure 5.2: Reconstruction of the quantity  $P_\zeta - 1.5 \cdot P_\zeta^{\text{vis}}$  Image credit: [?] (fig:PzetaDefinition)

the visible  $\tau$ -lepton decay products. This event topology is not preferred in  $W + \text{jets}$ ,  $t\bar{t}$  and QCD background events. The observable is computed as difference of the projections:

$$\begin{aligned} P_\zeta &= \vec{P}_T^{\text{vis}1} + \vec{P}_T^{\text{vis}2} + E_{\text{T}}^{\text{miss}} \\ P_\zeta^{\text{vis}} &= \vec{P}_T^{\text{vis}1} + \vec{P}_T^{\text{vis}2} \end{aligned} \quad (5.2) ?_{\text{eq:PZetaEq?}}$$

on the axis  $\zeta$  bisecting the directions  $\vec{P}_T^{\text{vis}1}$  and  $\vec{P}_T^{\text{vis}2}$  of the visible  $\tau$  lepton decay products in the transverse plane (see Figure 5.2 for illustration). The complete set of event selection criteria applied are summarized in Table 5.3.

Requirement	
Trigger	HLT_Mu9 for MC <i>cf.</i> table 5.1 for Data
Vertex	reconstructed with beam-spot constraint: $-24 < z_{vtx} < +24$ cm, $ \rho  < 2$ cm, $N_{\text{DOF}} > 4$
Muon	reconstructed as global Muon with: $p_T > 15$ GeV/c, $ \eta  < 2.1$ , VBTF Muon ID passed, isolated within $\Delta R = 0.4$ cone with respect to charged hadrons of $p_T > 1.0$ GeV/c and neutral electromagnetic objects of $E_T > 1.5$ GeV
Tau-jet Candidate	reconstructed by HPS + TaNC combined Tau ID algorithm TaNC “medium” Tau ID discriminator and discriminators against electrons and muons passed, calorimeter muon rejection passed
Muon + Tau-jet	$\text{charge}(\text{Muon}) + \text{charge}(\text{Tau-jet}) = 0$ , $\Delta R(\text{Muon}, \text{Tau-jet}) > 0.5$
Kinematics	$M_T(\text{Muon-MET}) < 40$ GeV $P_\zeta - 1.5 \cdot P_\zeta^{\text{vis}} > -20$ GeV

Table 5.3: Event selection criteria applied to select  $H \rightarrow \tau^+ \tau^- \rightarrow \mu \tau_{\text{had}}$  events.

HtoMuTauEventSelection)

1599

## Chapter 6

1600

# Data–Driven Background Estimation

&lt;ch:backgrounds&gt;

1601 For the result of this analysis to be reliable, it is of paramount importance that the back-  
 1602 grounds be well understood. The CMS experiment has adopted a policy that if possible, all  
 1603 background processes should be measured in a “data–driven” way. By requiring that the  
 1604 background comes from data, biases due to incorrectly modeling the background processes  
 1605 in simulation can be minimized or eliminated. In general, the data–driven methods also have  
 1606 the advantage that they are independent of the uncertainty on the integrated luminosity.  
 1607 This analysis measures the backgrounds using two complementary methods, the “Template  
 1608 Method” and the “Fake–rate method.” In both cases, predictions are made about back-  
 1609 grounds in the signal region using measurements obtained in background enriched control  
 1610 regions of the data. The Template Method fits the sum of background shape templates to  
 1611 the  $M_{vis}$  spectrum of events selected in the final analysis and is described in Section 6.3.  
 1612 The Fake–rate Method is based on applying probabilities for quark and gluon jets to be  
 1613 misidentified as hadronic tau decays to events passing all event selection criteria except  
 1614 the tau identification requirements. The probabilities with which jets fake hadronic tau sig-  
 1615 natures are measured in data. Contrary to the Template Method, The Fake–rate Method  
 1616 estimates the sum of the contributions of backgrounds that contain incorrectly identified  
 1617 taus. The Fake–rate method is detailed in Section 6.2. The two methods are complementary  
 1618 as the Template Method uses only information about the different visible mass distribution  
 1619 shapes of the backgrounds, while the Fake–rate method uses only information about the  
 1620 hadronic tau fake–rate.

## 1621 §6.1 Background Enriched Control Regions

?<sec:controlregions>? The criteria applied to select events in the background enriched control regions for the  
 1622 Template Method is based on the work described in [46]. With respect to that work, the  
 1623 muon isolation criteria applied to select  $Z \rightarrow \mu^+ \mu^-$ ,  $W + \text{jets}$ ,  $t\bar{t} + \text{jets}$  and QCD background  
 1624 enriched control samples has been changed to relative isolation with respect to charged  
 1625 hadrons and neutral electromagnetic objects reconstructed by the particle-flow algorithm.  
 1626 The selection of the enriched backgrounds is accomplished by disabling or inverting specific  
 1627 selections of Chapter 5 that were implemented to reject the given background. The selection  
 1628 of control regions used to measure the fake–rates for different types of background processes  
 1629 are very similar to the selections used for the Template Method. The details of the fake–rate  
 1630 measurement selections may be found in [47].

1632 All control regions are selected from the 2010 CMS muon primary datasets using single  
 1633 muon HLT trigger paths. The set of triggers and run–ranges used to select events in the  
 1634 background enriched control samples is the same as for the analysis (see Table 5.1). The  
 1635 Monte Carlo simulated events used for comparison with the control region selections are  
 1636 required to pass the HLT\_Mu9 trigger path and are weighted according to the description  
 1637 in Chapter 7 to account for the difference in efficiency between HLT\_Mu9 and the trigger  
 1638 paths required to have passed in the data.

1639 QCD di–jet events containing a muon (originating from the leptonic decay of a  $b$  or  $c$   
 1640 quark) are selected by applying an *anti*–isolation requirement on the jet containing a muon.  
 1641  $W + \text{jets}$  and  $t\bar{t} + \text{jets}$  are selected by requiring an isolated muon, and inverting the transverse  
 1642 mass ( $M_T$ ) and  $P_\zeta$  selections. Tau–jet candidates considered in the  $Z \rightarrow \mu^+ \mu^-$  sample where  
 1643 the reconstructed tau–jet candidate is faked by a misidentified muon and in the  $t\bar{t} + \text{jets}$   
 1644 control sample are required to pass the “loose” TaNC discriminator. For the Template  
 1645 Method, the  $Z \rightarrow \mu^+ \mu^-$  sample where the reconstructed tau–jet candidate is faked by a  
 1646 misidentified quark or gluon jet, the  $W + \text{jets}$  and the QCD enriched control samples have a  
 1647 loose hadronic tau “preselection” applied. The tau–jet candidates are required to pass the  
 1648 “very loose”, but fail the “loose” TaNC discriminator. The criteria applied to select events  
 1649 in the different background enriched control samples are summarized in Table 6.1. The goal

Requirement	Enriched background process				
	$Z \rightarrow \mu^+ \mu^-$		$W + \text{jets}$	$t\bar{t} + \text{jets}$	QCD
	Muon fake	Jet fake			
Muon rel. iso.	< 0.15	< 0.1	< 0.1	< 0.1	> 0.10 && < 0.30
Muon Track IP	-	-	-	-	-
Tau TaNC discr.	-	1	1	medium passed	1
Tau 1  3-Prong	-	-	-	-	-
Charge(Tau) = $\pm 1$	-	-	-	-	-
Tau $\mu$ -Veto	inverted	applied	applied	applied	applied
Charge(Muon+Tau)	applied	-	-	applied	-
$M_T$ (Muon-MET)	-	< 40 GeV	-	-	< 40 GeV
$P_\zeta - 1.5 \cdot P_\zeta^{vis}$	> -20 GeV	-	-	-	> -20 GeV
global Muons	< 2	-	< 2	< 2	< 2
central Jet Veto	-	-	2	-	-
b-Tagging	-	-	-	3	-

<sup>1</sup> vloose passed && loose failed <sup>2</sup> no Jets of  $E_T > 20$  GeV within  $|\eta| < 2.1$  (other than the  $\tau$ -jet candidate)

<sup>3</sup> min. two Jets of  $E_T > 40$  GeV, at least one of which with  $E_T > 60$  GeV and at least of which with “TrackCountingHighEff” discriminator  $> 2.5$

Table 6.1: Criteria to select events in different background enriched control samples.  
Hyphens indicate event selection criteria which are not applied.

MuTauBgControlRegions

1650 of the background enriched selection process is to select different background processes with  
 1651 high purity. A highly pure background control sample improves the stability of inferences  
 1652 about the signal region made using information in the enriched control region. The purity  
 1653 of the control regions (estimated using simulation) are summarized in Table 6.2.

1654 The number of events observed in the different control samples is compared to the  
 1655 Monte Carlo expectation in table 6.2. Except for the contribution of  $Z \rightarrow \mu^+ \mu^-$  events  
 1656 in which the reconstructed tau-jet candidate is due to a misidentified quark or gluon jet,  
 1657 good agreement between data and Monte Carlo simulation is observed. Differences observed  
 1658 between data and simulation will be accounted for as systematic uncertainties.

1659 The distributions of visible and “full”  $\tau^+ \tau^-$  invariant mass reconstructed by the SVfit  
 1660 algorithm (see Chapter 4) observed in the background enriched control regions is compared

Enriched Selection	Data	Contribution from						Purity
		$\Sigma$ SM	$Z \rightarrow \tau^+\tau^-$	$Z \rightarrow \mu^+\mu^-$	$W + \text{jets}$	$t\bar{t} + \text{jets}$	QCD	
$Z \rightarrow \mu^+\mu^-$								
Muon fake	15156	17109.8	331.6	16586.6	55.1	80.4	35.0	96.9%
Jet fake	85	62.7	2.5	55.5	0.5	1.4	2.4	88.5%
$W + \text{jets}$	514	642.4	17.9	22.9	581.7	0.8	16.7	90.6%
$t\bar{t} + \text{jets}$	26	39.7	0.7	< 0.1	0.6	38.4	< 1.0	96.7%
QCD	2510	2571.8	16.6	0.8	9.3	1.6	2543.4	98.9%

Table 6.2: Number of events observed in the different background enriched control samples compared to Monte Carlo expectations.  $\Sigma$  SM denotes the sum of  $Z \rightarrow \tau^+\tau^-$ ,  $Z \rightarrow \mu^+\mu^-$ ,  $W + \text{jets}$ ,  $t\bar{t} + \text{jets}$  and QCD processes. The expected purity of each control sample is computed as the ratio of contribution of the enriched process to  $\Sigma$  SM.

MuTauBgControlRegions)

to the Monte Carlo simulation in Figures 6.1 and 6.2. The template for the  $W + \text{jets}$  background has been corrected for the bias on the  $M_{vis}^{\mu\tau_{had}}$  shape caused by the  $M_T^{\mu E_T^{\text{miss}}} < 50 \text{ GeV}/c^2$  and  $P_\zeta - 1.5 \cdot P_\zeta^{vis} > -20 \text{ GeV}$  requirements applied in the final analysis via the reweighting procedure described in [46]. In the  $t\bar{t} + \text{jets}$  enriched control region a peak at the  $Z$  mass is observed in data, which is not modeled by the Monte Carlo samples considered. The peak could be due to  $Z \rightarrow \mu^+\mu^-$  events produced in association with  $b$  quarks. On the other hand, the contribution from  $t\bar{t} + \text{jets}$  events to that sample seems to be overestimated. The origin of the  $Z$  mass peak merits further investigation, but overall the  $t\bar{t} + \text{jets}$  is a negligible background contribution.

## §6.2 The Fake-rate Method

The probabilities with which quark and gluon jets get misidentified as tau-jets may be utilized to obtain an estimate of background contributions in physics analyses. As an illustrative example and in order to demonstrate the precision achievable with the method, we introduce the method in the context of a “closure test,” using a simulated samples, a simple method of computing the fake-rate, and a simpler<sup>1</sup> hadronic tau identification algorithm. The closure test demonstrates that the method is self-consistent, and that the

<sup>1</sup>The closure test uses the “shrinking cone” tau identification algorithm, which is described briefly in Section 3.1. A full description can be found in [27].

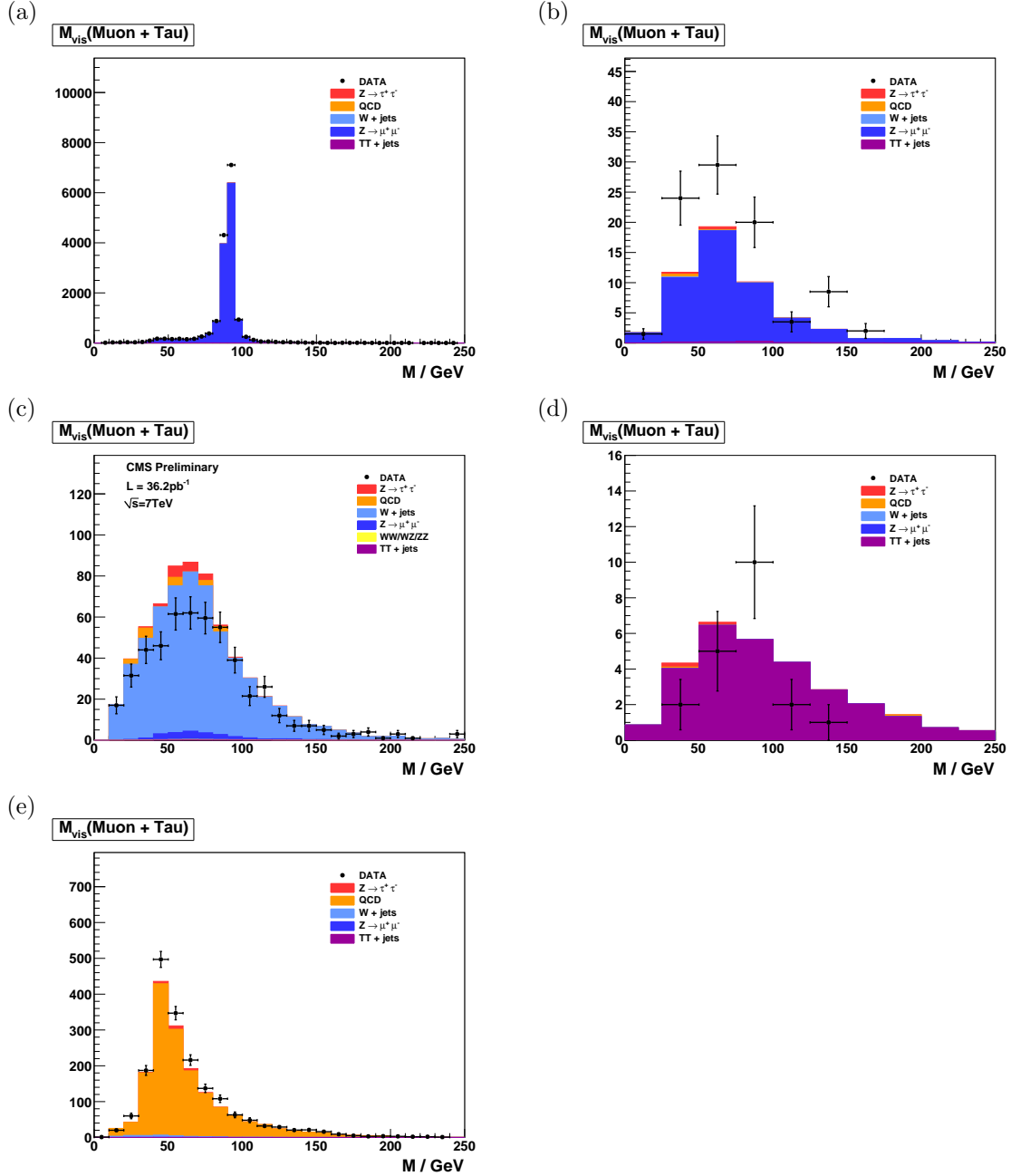


Figure 6.1: Distribution of visible mass of muon plus the tau–jet candidate reconstructed in the background enriched control samples for  $Z \rightarrow \mu^+ \mu^-$  (a) and (b),  $W + \text{jets}$  (c),  $t\bar{t} + \text{jets}$  (d) and QCD multi-jet (e) backgrounds. In (a) reconstructed tau–jet candidates are expected to be dominantly due to misidentified muons, while in (b) they are expected to be mostly due to misidentified misidentified quark or gluon jets.

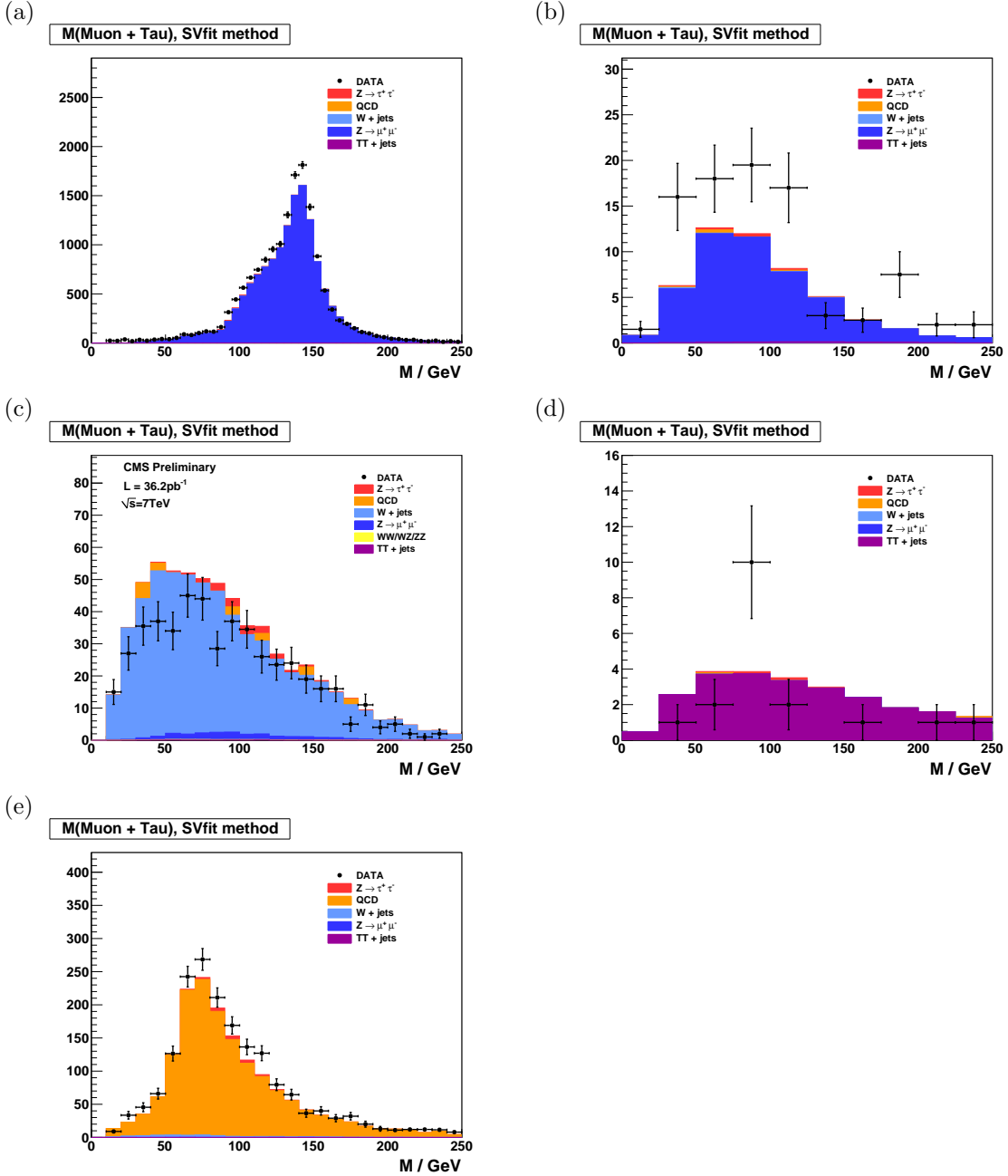


Figure 6.2: Distribution of “full” invariant mass reconstructed by the SVfit algorithm in the background enriched control samples for  $Z \rightarrow \mu^+\mu^-$  (a) and (b),  $W + \text{jets}$  (c),  $t\bar{t} + \text{jets}$  (d) and QCD multi-jet (e) backgrounds. In (a) reconstructed tau-jet candidates are expected to be dominantly due to misidentified muons, while in (b) they are expected to be mostly due to misidentified misidentified quark or gluon jets.

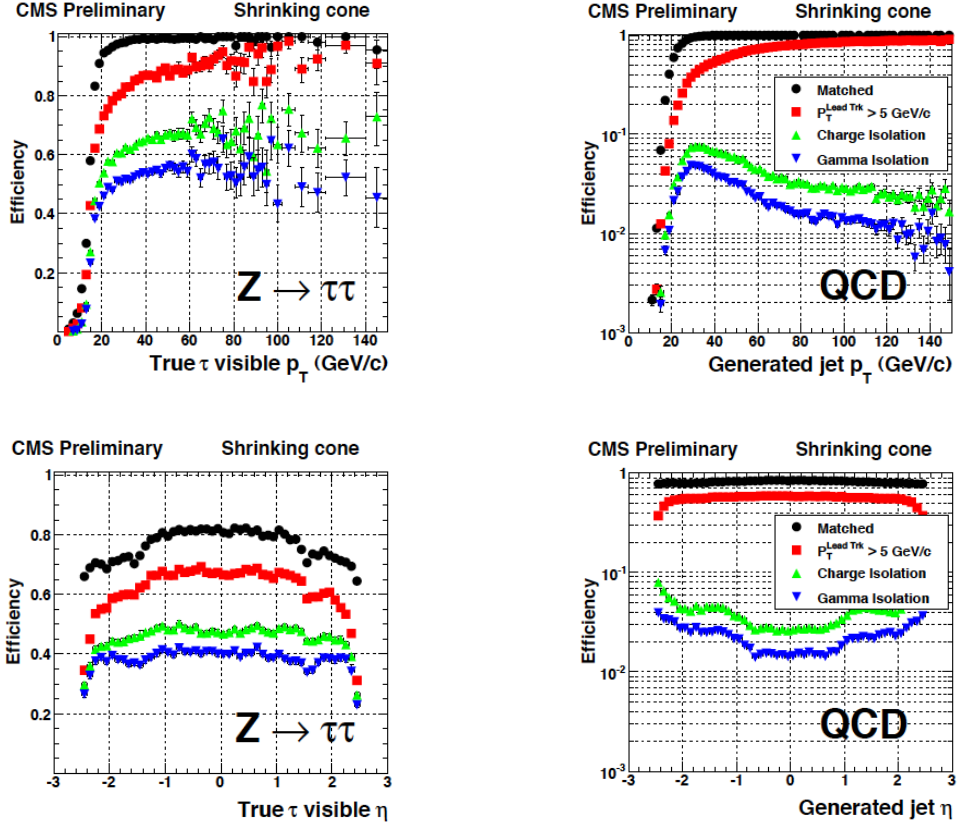


Figure 6.3: Cumulative efficiencies (left) and fake-rates (right) of successively applied tau identification cuts of the “shrinking signal cone” particle-flow based tau identification algorithm described in [27] as function of  $p_T^{\text{jet}}$  (top) and  $\eta^{\text{jet}}$  (bottom) of tau-jet candidates. The efficiencies/fake-rates for the complete set of tau identification criteria are represented by the blue (downwards facing) triangles.

EfficienciesAndFakeRates)

1677 fake-rate technique can be used to estimate the contributions of QCD,  $W + \text{jets}$ ,  $t\bar{t} + \text{jets}$   
 1678 and  $Z \rightarrow \mu^+\mu^-$  backgrounds. The analysis selections used in the closure test are almost  
 1679 identical to the selections used in this analysis. Exact details of the selections can be found  
 1680 in reference analysis [44]. The method is then extended to use fake-rates measured in data,  
 1681 a multivariate method of computing the fake-rates, and the HPS + TaNC tau identification  
 1682 algorithm used in this analysis.

### 1683 §6.2.1 Parameterization of Fake-rates

FakeRateParametrization)  
 1684 Efficiencies and fake-rates of the tau identification algorithm based on requiring no tracks  
 1685 of  $p_T > 1 \text{ GeV}/c$  and ECAL energy deposits of  $p_T > 1.5 \text{ GeV}/c$  reconstructed within

1686 an “isolation cone” of size  $\Delta R_{iso} = 0.5$  and outside of a “shrinking signal cone” of size  
 1687  $\Delta R_{sig} = 5.0/E_T$  as it is used in the  $Z \rightarrow \tau^+\tau^- \rightarrow \mu + \tau$ -jet analysis [44] are displayed  
 1688 in Figure 6.3. In order to account for the visible  $p_T$  and  $\eta$  dependence, we parametrize  
 1689 the fake-rates in bins of transverse momentum and pseudo-rapidity. As we will show in  
 1690 section 6.2.3, the parametrization of the fake-rates by  $p_T$  and  $\eta$  makes it possible to not  
 1691 only estimate the total number of background events contributing to physics analyses, but  
 1692 to model the distributions of kinematic observables with a precision that is sufficient to  
 1693 extract information on the background shape.

We add a third quantity, the  $E_T$ -weighted jet-width  $R_{jet}$ , to the parametrization in order to account for differences between the fake-rates of quark and gluon jets, which on average have differing widths and different fake-rates. The jet width quantity  $R_{jet}$  is defined as

$$R_{jet} = \sqrt{E(\eta^2) + E(\phi^2)}$$

1694 where  $E(\eta^2)$ ,  $E(\phi^2)$  is the second  $\eta$ ,  $\phi$  moment of the jet constituents, weighted by constituent transverse energy. Analyses performed by the CDF collaboration [40, 48, 49] found  
 1695 that systematic uncertainties on background estimates obtained from the fake-rate method  
 1696 are reduced in case differences between quark and gluon jets are accounted for in this way.  
 1697

### 1698 §6.2.2 Measurement of Fake-rates

Efficiencies and fake-rates are obtained by counting the fraction of tau-jet candidates passing all tau identification cuts and discriminators in a given bin<sup>2</sup> of  $p_T^{jet}$ ,  $\eta_{jet}$  and  $R_{jet}$ :

$$P_{fr}(p_T^{jet}, \eta_{jet}, R_{jet}) := \frac{N_{jets}(p_T^{jet}, \eta_{jet}, R_{jet} | \text{tau ID passed})}{N_{jets}(p_T^{jet}, \eta_{jet}, R_{jet} | \text{preselection passed})} \quad (6.1) \quad [\text{eqBgEstFakeRate}]$$

1699 The pre-selection in the denominator of equation 6.1 in general refers to  $p_T$  and  $\eta$  cuts,  
 1700 which are applied with thresholds matching those applied on the final analysis level, but  
 1701 may include loose tau identification criteria (which may be applied e.g. already during event  
 1702 skimming). It is critical that the selection used in the denominator be identical to that of  
 1703 the final analysis to ensure the fake-rates are not biased by different selections.

---

<sup>2</sup>The example presented in the closure tests bins the fake-rate calculation in bins of the parameterization variables. In Section 6.2.6 we describe a more robust multivariate method to compute the fake-rates.

1704        Different sets of fake–rates are determined for the highest  $p_T$  and for the second highest  
 1705         $p_T$  jet in QCD di–jet events, for jets in a QCD event sample enriched by the contribution  
 1706        of heavy quarks and gluons by requiring the presence of a muon reconstructed in the final  
 1707        state, and for jets in “electroweak” events selected by requiring a  $W$  boson in the final state.

### 1708        §6.2.3 Application of Fake–rates

⟨sec:FakeRateApplication⟩  
 1709        Knowledge of the tau identification efficiencies and fake–rates as function of the parameters  
 1710         $p_T^{jet}$ ,  $\eta_{jet}$  and  $R_{jet}$  as defined by equation 6.1 is utilized to obtain an estimate for the contri-  
 1711        butions of background processes to physics analyses involving tau lepton hadronic decays  
 1712        in the final state. The basic idea is to replace tau identification cuts and discriminators by  
 1713        appropriately chosen weights.

1714        Application of the fake–rate technique consists of two stages. The first stage consists of  
 1715        loosening the tau identification cuts and discriminators and applying only the preselection  
 1716        requirements defined by the denominator of Equation 6.1, in order to obtain an event  
 1717        sample dominated by contributions of background processes. After disabling the selections  
 1718        on hadronic tau identification, the relative contributions of the backgrounds are expected  
 1719        to increase by the inverse of the (average) fake–rate, typically by a factor  $\mathcal{O}(100)$ . In the  
 1720        second stage, weights are applied to all events in the background dominated control sample,  
 1721        according to the probabilities  $P_{fr}(p_T^{jet}, \eta_{jet}, R_{jet})$  for jets to fake the signature of a hadronic  
 1722        tau decay. After application of the weights, an estimate for the total number of background  
 1723        events passing the tau identification cuts and discriminators and thus contributing to the  
 1724        final analysis sample is obtained.

1725        The fake–rate technique works best if all background contributions to the analysis arise  
 1726        from misidentification of quark and gluon jets as hadronic tau decays. Corrections to the  
 1727        estimate obtained from the fake–rate technique are needed in case of background processes  
 1728        contributing to the final analysis sample which either produce genuine tau leptons in the  
 1729        final state (e.g.  $t\bar{t} + \text{jets}$ ) or in which tau–jet candidates are due to misidentified electrons  
 1730        or muons (e.g.  $Z \rightarrow \mu^+\mu^-$ ,  $Z \rightarrow e^+e^-$ ), as the latter may fake signatures of hadronic tau  
 1731        decays with very different probabilities than quark and gluon jets.

1732 In the “simple” fake–rate method described in detail in the next section, the correc-  
 1733 tions are taken from Monte Carlo simulations. Corrections based on Monte Carlo are needed  
 1734 also to compensate for signal contributions to the background dominated control sample.  
 1735 An alternative to Monte Carlo based corrections is to utilize additional information con-  
 1736 tained in the background dominated control sample. The modified version is described in  
 1737 section 6.2.5. It has been used to estimate background contributions in searches for Higgs  
 1738 boson production with subsequent decays into tau lepton pairs performed by the CDF col-  
 1739 laboration in TeVatron Run II data [40, 48, 49]. We will refer to the modified version as  
 1740 “CDF–type” method in the following.

#### 1741 §6.2.4 “Simple” weight method

In the “simple” method all tau–jet candidates within the background dominated event  
 sample are weighted by the probabilities of quark and gluon jets to fake the signature of a  
 hadronic tau decay:

$$w_{jet}^{simple} \left( p_T^{jet}, \eta_{jet}, R_{jet} \right) := P_{fr} \left( p_T^{jet}, \eta_{jet}, R_{jet} \right) \quad (6.2) \boxed{\text{eqBgEstFakeRate}}$$

1742 These weights are applied to all jets in the background dominated control sample which  
 1743 pass the preselection defined by the denominator of Equation 6.1. Note that the weights  
 1744 defined by Equation 6.2 can be used to estimate the contributions of background processes  
 1745 to distributions of tau–jet related observables. They cannot be used as event weights.

In order to compare distributions of event level quantities or per–particle quantities  
 for particles of types different from tau leptons decaying hadronically, event weights need  
 to be defined. Neglecting the small fraction of background events in which multiple tau–jet  
 candidates pass the complete set of all tau identification cuts and discriminators, event  
 weights can be computed by summing up the per–jet weights defined by Equation 6.2 over  
 all tau–jet candidates in the event which pass the preselection:

$$W_{event}^{simple} := \sum w_{jet}^{simple} \quad (6.3) \boxed{\text{eqBgEstFakeRate}}$$

A bit of care is needed in case one wants to compare distributions of observables  
 related to “composite particles” the multiplicity of which depends on the multiplicity of  
 tau–jet candidates in the event (e.g. combinations of muon + tau–jet pairs in case of the  
 $Z \rightarrow \tau^+\tau^- \rightarrow \mu + \tau\text{-jet}$  analysis). Per–particle weights need to be computed for such

Background Process	Expectation	Estimate obtained by applying weights of type:				Average fake-rate estimate
		QCD lead jet	QCD second jet	QCD $\mu$ -enriched	$W + \text{jets}$	
$W + \text{jets}$	$163.0 \pm 7.1$	$157.2 \pm 2.8$	$140.9 \pm 2.7$	$129.9 \pm 2.5$	$177.9 \pm 3.2$	$151.5^{+26.6}_{-21.8}$
QCD	$246.4 \pm 31.8$	$269.2 \pm 14.0$	$246.5 \pm 14.3$	$219.7 \pm 11.8$	$300.8 \pm 15.2$	$259.1^{+44.9}_{-41.7}$
$t\bar{t} + \text{jets}$	$12.2 \pm 0.6$	$14.3 \pm 0.3$	$12.6 \pm 0.3$	$11.6 \pm 0.3$	$16.5 \pm 0.3$	$13.8^{+2.7}_{-2.2}$
$Z \rightarrow \mu^+ \mu^-$	$68.6 \pm 2.9$	$58.2 \pm 1.3$	$51.2 \pm 1.2$	$48.5 \pm 1.1$	$65.8 \pm 1.4$	$55.9^{+10.0}_{-7.5}$
$\Sigma$ Background	$490.4 \pm 32.7$	$499.9 \pm 14.4$	$451.2 \pm 14.6$	$409.7 \pm 12.1$	$561.1 \pm 15.6$	$480.2^{+82.7}_{-71.9}$
$Z \rightarrow \tau^+ \tau^-$	—	$284.3 \pm 3.7$	$269.0 \pm 3.9$	$256.5 \pm 3.3$	$325.3 \pm 4.2$	$283.3^{+42.2}_{-27.1}$

Table 6.3: Number of events from  $W + \text{jets}$ , QCD,  $t\bar{t} + \text{jets}$  and  $Z \rightarrow \mu^+ \mu^-$  background processes expected to pass all selection criteria of the  $Z \rightarrow \tau^+ \tau^- \rightarrow \mu + \tau$ -jet cross-section analysis compared to the estimates obtained by weighting events in the background dominated control sample with the “simple” fake-rate weights defined by Equation 6.3.

FakeRate'frSimpleResults`

“composite particles”, depending on  $p_T^{jet}$ ,  $\eta_{jet}$ ,  $R_{jet}$  of its tau-jet candidate constituent, according to:

$$w_{\text{comp-part}}^{\text{simple}}(p_T^{jet}, \eta_{jet}, R_{jet}) := w_{jet}^{\text{simple}}(p_T^{jet}, \eta_{jet}, R_{jet}) \quad (6.4) \quad \text{eqBgEstFakeRate}$$

Different estimates are obtained for the fake-rate probabilities determined for the highest and second highest  $p_T$  jet in QCD di-jet events, jets in a muon enriched QCD sample and jets in  $W + \text{jets}$  events. The arithmetic average of the four estimates of the closure test together with the difference between the computed average and the minimum/maximum value is given in Table 6.3.

We take the average value as “best” estimate of the background contribution and the difference between the average and the minimum/maximum estimate as its systematic uncertainty. We obtain a value of  $\mathcal{O}(15\%)$  for the systematic uncertainty and find that the true sum of QCD,  $W + \text{jets}$ ,  $t\bar{t} + \text{jets}$  and  $Z \rightarrow \mu^+ \mu^-$  background contributions agrees well with the “best” estimate obtained by the fake-rate method within the systematic uncertainty.

Note that the estimate for the sum of background contributions which one obtains

1746  
1747  
1748  
1749  
1750  
1751  
1752  
1753  
1754  
1755  
1756  
1757

in case one applies the “simple” fake–rate weights defined by Equation 6.3 to a background dominated control sample selected in data is likely to overestimate the true value of background contributions by a significant amount. The reason is that contributions of  $Z \rightarrow \tau^+\tau^-$  events with true taus are non–negligible. In fact, genuine tau contributions to the background dominated control sample are expected to be 14.9% and since the per–jet weights computed by Equation 6.2 are larger on average in signal than in background events, the signal contribution increases by the weighting and amounts to 37.1% of the sum of event weights computed by Equation 6.3 and given in Table 6.3.

The contribution of the  $Z \rightarrow \tau^+\tau^-$  signal needs to be determined by Monte Carlo simulation and subtracted from the estimate obtained by applying the “simple” fake–rate method to data, in order to get an unbiased estimate of the true background contributions.

### §6.2.5 “CDF–type” weights

Instead of subtracting from the estimate obtained for the sum of background contributions a correction determined by Monte Carlo simulation, the genuine tau contribution contribution to the background dominated event sample selected in data can be corrected for by adjusting the weights, based solely on information contained in the analyzed data sample, avoiding the need to rely on Monte Carlo based corrections.

In the “CDF–type” method, additional information, namely whether or not tau–jet candidates pass or fail the tau identification cuts and discriminators, is drawn from the data. The desired cancellation of signal contributions is achieved by assigning negative weights to those tau–jet candidates which pass all tau identification cuts and discriminators, i.e. to a fair fraction of genuine hadronic tau decays, but to a small fraction of quark and gluon jets only. The small reduction of the background estimate by negative weights assigned to quark and gluon jets is accounted for by a small increase of the positive weights assigned to those tau–jet candidates for which at least one of the tau identification cuts or discriminators fails. In this way, an unbiased estimate of the background contribution is maintained.

To be specific, the “CDF–type” weights assigned to tau–jet candidates are computed

as:

$$w_{jet}^{CDF} (p_T^{jet}, \eta_{jet}, R_{jet}) := \begin{cases} \frac{P_{fr}(p_T^{jet}, \eta_{jet}, R_{jet}) \cdot \varepsilon(p_T^{jet}, \eta_{jet}, R_{jet})}{\varepsilon(p_T^{jet}, \eta_{jet}, R_{jet}) - P_{fr}(p_T^{jet}, \eta_{jet}, R_{jet})} & \text{all tau ID passed} \\ \frac{P_{fr}(p_T^{jet}, \eta_{jet}, R_{jet}) \cdot (1 - \varepsilon(p_T^{jet}, \eta_{jet}, R_{jet}))}{\varepsilon(p_T^{jet}, \eta_{jet}, R_{jet}) - P_{fr}(p_T^{jet}, \eta_{jet}, R_{jet})} & \text{otherwise} \end{cases} \quad (6.5) \boxed{\text{eqBgEstFakeRate}}$$

1784 For the derivation of equation 6.5 for the “CDF–type” weights assigned to tau–jet candi-  
 1785 dates, we will use the following notation: Let  $n_\tau$  ( $n_{QCD}$ ) denote the total number of tau–jets  
 1786 (quark and gluon jets) in a certain bin of transverse momentum  $p_T^{jet}$ , pseudo–rapidity  $\eta_{jet}$   
 1787 and jet–width  $R_{jet}$  and  $n_\tau^{sel}$  ( $n_{QCD}^{sel}$ ) denote the number of tau–jets (quark and gluon jets)  
 1788 in that bin which pass all tau identification cuts and discriminators. By definition of the  
 1789 tau identification efficiency  $\varepsilon := \varepsilon(p_T^{jet}, \eta_{jet}, R_{jet})$  and fake–rate  $f := f(p_T^{jet}, \eta_{jet}, R_{jet})$ :

$$n_\tau^{sel} = \varepsilon \cdot n_\tau$$

$$n_{QCD}^{sel} = f \cdot n_{QCD}. \quad (6.6) \boxed{\text{eqBgEstFakeRate}}$$

Depending on whether or not a given tau–jet candidate passes all tau identification cuts and discriminators or not, we will assign a weight of value  $w_{passed}$  or  $w_{failed}$  to it. The values of the weights  $w_{passed}$  and  $w_{failed}$  shall be adjusted such that they provide an unbiased estimate of the background contribution:

$$w_{passed} \cdot f \cdot n_{QCD} + w_{failed} \cdot (1 - f) \cdot n_{QCD} \equiv n_{QCD}^{sel} = f \cdot n_{QCD} \quad (6.7) \boxed{\text{eqBgEstFakeRate}}$$

while averaging to zero for genuine hadronic tau decays:

$$w_{passed} \cdot \varepsilon \cdot n_\tau + w_{failed} \cdot (1 - \varepsilon) \cdot n_\tau \equiv 0.$$

The latter equation yields the relation:

$$w_{passed} = -\frac{1 - \varepsilon}{\varepsilon} \cdot w_{failed}, \quad (6.8) \boxed{\text{eqBgEstFakeRate}}$$

1790 associating the two types of weights. By inserting relation 6.8 into equation 6.7 we obtain:

$$\begin{aligned} & -\frac{1 - \varepsilon}{\varepsilon} \cdot w_{failed} \cdot f \cdot n_{QCD} + w_{failed} \cdot (1 - f) \cdot n_{QCD} = f \cdot n_{QCD} \\ \Rightarrow & \left( \frac{-f + \varepsilon \cdot f + \varepsilon - f \cdot \varepsilon}{\varepsilon} \right) \cdot w_{failed} = f \\ \Rightarrow & w_{failed} = \frac{f \cdot \varepsilon}{\varepsilon - f} \end{aligned}$$

and

$$w_{passed} = -\frac{f \cdot (1 - \varepsilon)}{\varepsilon - f} \quad (6.9) \{?\}$$

1791 which matches exactly equation 6.5 for the “CDF–type” weights applied to tau–jet candi-  
 1792 dates given in section 6.2.5.

1793 Event weights and the weights assigned to “composite particles” are computed in the

Background Process	Expectation	Estimate obtained by applying weights of type:				Average fake-rate estimate
		QCD lead jet	QCD second jet	QCD $\mu$ -enriched	$W + \text{jets}$	
$W + \text{jets}$	$163.0 \pm 7.1$	$163.2 \pm 3.8$	$140.6 \pm 3.4$	$128.0 \pm 3.1$	$188.3 \pm 4.2$	$155.0^{+33.6}_{-27.3}$
QCD	$246.4 \pm 31.8$	$300.5 \pm 19.5$	$266.1 \pm 19.0$	$236.0 \pm 16.4$	$335.1 \pm 20.4$	$284.4^{+55.5}_{-52.0}$
$t\bar{t} + \text{jets}$	$12.2 \pm 0.6$	$13.1 \pm 0.3$	$11.5 \pm 0.3$	$10.2 \pm 0.3$	$15.4 \pm 0.4$	$12.6^{+2.8}_{-2.4}$
$Z \rightarrow \mu^+\mu^-$	$68.6 \pm 2.9$	$52.7 \pm 1.4$	$46.7 \pm 1.4$	$41.9 \pm 1.2$	$60.3 \pm 1.6$	$50.4^{+10.1}_{-8.6}$
$\Sigma$ Background	$490.4 \pm 32.7$	$529.5 \pm 19.9$	$464.9 \pm 19.3$	$416.1 \pm 16.8$	$599.1 \pm 20.9$	$502.4^{+99.4}_{-88.4}$
$Z \rightarrow \tau^+\tau^-$	–	$0.3 \pm 2.4$	$-10.6 \pm 2.5$	$3.8 \pm 2.0$	$-10.8 \pm 2.8$	$-4.3^{+8.4}_{-7.2}$

Table 6.4: Number of events from  $W + \text{jets}$ , QCD,  $t\bar{t} + \text{jets}$  and  $Z \rightarrow \mu^+\mu^-$  background processes expected to pass all selection criteria of the closure test compared to the estimates obtained by weighting events in the background dominated control sample with the “CDF-type” fake-rate weights defined by equation 6.10.

keRate'frCDFtypeResults)

1794 same way as for the “simple” weights, based on the weights assigned to the tau-jet candi-

1795 dates:

$$W_{\text{event}}^{\text{CDF}} := \sum w_{\text{jet}}^{\text{CDF}}$$

$$w_{\text{comp-part}}^{\text{CDF}}(p_{\text{T}}^{\text{jet}}, \eta_{\text{jet}}, R_{\text{jet}}) := w_{\text{jet}}^{\text{CDF}}(p_{\text{T}}^{\text{jet}}, \eta_{\text{jet}}, R_{\text{jet}}), \quad (6.10) \boxed{\text{eqBgEstFakeRate}}$$

1796 where the sums extend over all jets in the background dominated control sample which pass

1797 the preselection defined by the denominator of equation 6.1.

1798 The effect of the negative weights to compensate the positive weights in case the “CDF-  
 1799 type” fake-rate method is applied to signal events containing genuine hadronic tau decays is  
 1800 shown in Table 6.4 and illustrated in Figure 6.4. As expected, positive and negative weights  
 1801 do indeed cancel in the statistical average.

1802 Figures 6.5, 6.6 and 6.7 demonstrate that an unbiased estimate of the background  
 1803 contribution by the “CDF-type” weights is maintained. Overall, the estimates obtained  
 1804 are in good agreement with the contributions expected for different background processes,  
 1805 indicating that the adjustment of negative and positive weights works as expected for the  
 1806 background as well.

1807 Results obtained by the “CDF-type” fake-rate method are summarized in table 6.4,

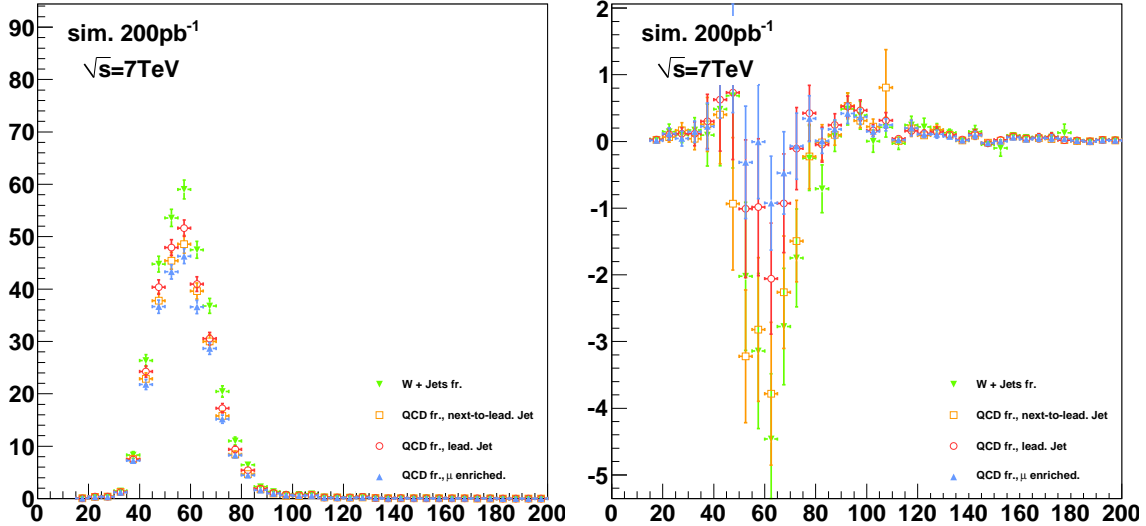


Figure 6.4: Distributions of visible invariant mass of muon plus tau–jet in  $Z \rightarrow \tau^+\tau^-$  signal events weighted by “simple” weights computed according to Equation 6.4 (left) and “CDF–type” weights computed according to Equation 6.10 (right). The signal contribution to the background estimate computed by the “simple” method is non–negligible and needs to be corrected for. The “CDF–type” weights achieve a statistical cancellation of positive and negative weights, such that the total signal contribution averages to zero, avoiding the need for Monte Carlo based corrections.

peResults.mVisibleSignal)

in which the total number of background events estimated by Equation 6.10 is compared to the true background contributions. The “best” estimate of the background contribution obtained from the “CDF–type” method is again taken as the arithmetic average of the estimates obtained by applying the fake–rate probabilities for the highest and second highest  $p_T$  jet in QCD di–jet events, jets in a muon enriched QCD sample and jets in  $W$ +jets events. Systematic uncertainties are taken from the difference between the computed average value and the minimum/maximum estimate. We obtain a value of  $\mathcal{O}(15\text{--}20\%)$  for the systematic uncertainty of the “CDF–type” method, slightly higher than the systematic uncertainty obtained for the “simple” method. The small increase of systematic uncertainties is in agreement with our expectation for fluctuations of the jet–weights in case weights of negative and positive sign are used.

1819    §6.2.6 k-Nearest Neighbor Fake-rate Calculation

1820     $\langle \text{sec:KNN} \rangle$  For the fake-rate method to give correct results, care must be taken that the measured  
 1821    fake-rate is well defined in all of the regions of phase space where it will be used. In the  
 1822    closure test described above, the computation of the fake-rate was accomplished by binning  
 1823    the numerator (tau ID passed) and denominator (tau ID passed and failed) distributions  
 1824    in the three dimensions of the parameterizations. This method has the disadvantage that  
 1825    the determination of the optimal binning is extremely difficult to determine, and that any  
 1826    bins with no entries in the denominator distribution caused the fake-rate to be undefined  
 1827    in those regions.

To overcome these problems, the fake-rate parameterization is implemented by adapting a multivariate technique known as a  $k$ -Nearest Neighbor classifier ( $k$ NN). A  $k$ NN classifier is typically used to classify events operates by populating (“training”) an  $n$ -dimensional space with signal and background events. The probability for a given point  $x$  in the space to be “signal-like” is determined by finding the  $k$  nearest neighbors and computing the ratio

$$p_{\text{sig}} = \frac{n_{\text{sig}}}{n_{\text{sig}} + n_{\text{bkg}}}, \quad (6.11) \quad \boxed{\text{eq:KNNEquation}}$$

1828    where  $n_{\text{sig}}, n_{\text{bkg}}$  are the observed number of signal and background events, respectively. By  
 1829    construction,  $k = n_{\text{sig}} + n_{\text{bkg}}$ . The principle of operation is illustrated in Figure 6.8

1830    The classification feature of a  $k$ NN can be trivially adapted to parameterize a fake-rate  
 1831    such that it is defined everywhere. Examining the form of Equation 6.11, it is clear that  
 1832    by replacing  $n_{\text{sig}}$  with  $n_{\text{passed}}$  and  $n_{\text{bkg}}$  with  $n_{\text{failed}}$ , the equation is equivalent to the tau-  
 1833    fake rate. We thus “train” the  $k$ NN with tau-candidates which pass the tau identification as  
 1834    signal events and those which fail as background events. The resulting classifier is a function  
 1835    which returns the expected fake-rate for any point in the space of the parameterization.  
 1836    The choice of  $k$  must be optimized. When  $k$  is low, the small number of neighbors causes  
 1837    large counting fluctuations in the fake rate. If  $k$  is too large, the  $k$ NN effectively averages  
 1838    over a large area of the space of the variables<sup>3</sup>. For the training statistics available in the  
 1839    2010 data,  $k = 20$  is found to be the optimal choice.

---

<sup>3</sup>In the limit  $k \rightarrow \inf$ , the  $k$ NN output reduces to a single number. In this extreme case, all information about the dependence of the fake-rate on the variables is lost.

1840    §6.2.7 Results of Background Estimation

1841    An independent estimate of the background contributions to the analysis presented in this  
 1842    thesis is obtained by applying the fake-rate method in a manner analogous to the closure  
 1843    test. Fake-rates in QCD multi-jet events (light quark enriched sample), QCD events con-  
 1844    taining muons (heavy quark and gluon enriched sample) and  $W + \text{jets}$  events are measured  
 1845    in data [33, 47] and applied to events which pass all the event selection criteria listed in  
 1846    table 5.3, with the exceptions of

- 1847         • the “medium” HPS + TaNC discriminator, and  
 1848         • the requirement that the tau have unit charge.

1849         No assumption is made on the composition of  $Z \rightarrow \mu^+ \mu^-$ ,  $W + \text{jets}$ ,  $t\bar{t} + \text{jets}$  and QCD  
 1850    backgrounds contributing to the event sample selected by the analysis. Differences between  
 1851    fake-rates obtained for QCD multi-jet, QCD muon enriched and  $W + \text{jets}$  background events  
 1852    are attributed as systematic uncertainties of the fake-rate method. Per jet and per event  
 1853    weights have been computed by the “simple” and “CDF-type” weights as described in the  
 1854    closure test and the results are found to be compatible within statistical and systematic  
 1855    uncertainties. In the following, we present results for “CDF-type” weights. The “CDF-type”  
 1856    weights have the advantage that the background estimate obtained does not change, whether  
 1857    there is MSSM Higgs  $\rightarrow \tau^+ \tau^-$  signal present in the data or not.

1858         Tau identification efficiencies need to be known when using “CDF-type” weights. Ded-  
 1859    icated studies have checked the tau identification efficiencies in data [47]. Statistical and  
 1860    systematic uncertainties of these studies are still sizeable at present, in the order to 20–30%.  
 1861    No indication has been found, however, that the Monte Carlo simulation does not correctly  
 1862    model hadronic tau decays in data. For the purpose of computing fake-rate weights via  
 1863    the “CDF-type” method, tau identification efficiencies are taken from the Monte Carlo  
 1864    simulation of hadronic tau decays in  $Z \rightarrow \tau^+ \tau^-$  events. Systematic uncertainties on the  
 1865    background estimate obtained by the fake-rate method are determined by varying the tau  
 1866    identification efficiencies by  $\pm 30\%$  relative to the value obtained from the Monte Carlo  
 1867    simulation.

Events weighted by:	Estimate
QCD lead jet	$202.1^{+14.9}_{-74.8}$
QCD second jet	$198.0^{+22.8}_{-79.3}$
QCD $\mu$ -enriched	$213.3^{+17.7}_{-82.6}$
$W + \text{jets}$	$232.8^{+21.1}_{-95.0}$
$N_{bgr}$ estimate	$236.1^{+24.1}_{-65.9}$

Table 6.5: Estimate for background contributions obtained by weighting events passing all selection criteria listed in Table 5.3 except for the requirement for tau-jet candidates to pass the “medium” tight TaNC discriminator and have unit charge by fake-rates measured in QCD multi-jet, QCD muon enriched and  $W + \text{jets}$  data samples.

IuTauFakeRateResultsOS)

1868        The results of applying the fake-rate method to the mu + tau channel are summarized  
 1869        in Table 6.5. The background prediction has been corrected for the expected<sup>4</sup> contribution  
 1870        of  $13.1^{+2.8}_{-0.6}$  events from  $Z \rightarrow \mu^+ \mu^-$  background events in which the reconstructed tau-jet is  
 1871        due to a misidentified muon. The obtained estimate is in good agreement with the Monte  
 1872        Carlo expectation.

1873        As an additional cross-check of the method, a sample of events containing a muon  
 1874        plus a tau-jet of like-sign charge is selected in data and compared to the background  
 1875        prediction obtained by applying the fake-rate method to the like-sign sample. The like-sign  
 1876        sample is expected to be dominated by the contributions of  $W + \text{jets}$  and QCD background  
 1877        processes and allows to verify the fake-rate method in a practically signal free event sample.  
 1878        The background estimate obtained by the fake-rate method is compared to the number of  
 1879        events observed in the like-sign data sample in Table 6.6. The number of events expected  
 1880        in the like-sign control sample from Monte Carlo simulation is indicated in the caption. All  
 1881        numbers are in good agreement.

1882        The fake-rate method does not only allow to estimate the total number of background  
 1883        events, but allows to model the distributions of background processes as well. The capability  
 1884        to model distributions is illustrated in Figure 6.9, which shows good agreement between the  
 1885        distributions observed in the like-sign data sample and the predictions obtained by the

---

<sup>4</sup>The contribution of  $Z \rightarrow \mu^+ \mu^-$  is estimated using a simulated sample.

Events weighted by:	Estimate
QCD lead jet	$191.7^{+2.3}_{-17.9}$
QCD second jet	$185.1^{+6.0}_{-21.1}$
QCD $\mu$ -enriched	$194.7^{+2.0}_{-20.5}$
$W + \text{jets}$	$208.9^{+0.5}_{-14.4}$
Fake-rate estimate	$201.8^{+14.2}_{-18.9}$
Observed	216

Table 6.6: Number of events observed in like-sign control region compared to estimate obtained by fake-rate method.

MuTauFakeRateResultsSS)

1886 fake-rate method for the distributions of muon plus tau-jet visible mass and of the “full”  
 1887 invariant mass reconstructed by the SVfit algorithm.

**Fixme:** THIS  
*IS FROM  
 THE HPS  
 NOTE!*

### 1888 §6.3 Template method

⟨sec:template⟩ 1889 Shape templates for the  $\mu + \tau_{had}$  visible mass  $M_{vis}$  are obtained from data, using a set of  
 1890 dedicated control regions which are chosen to select a high purity sample of one particular  
 1891 background process each. The number of events selected in each control region and com-  
 1892 parisons to the predictions from Monte Carlo simulations are summarized in Table 6.2. The  
 1893 template  $M_{vis}$  shapes obtained from data in the background enriched control regions are  
 1894 compared to the signal region shapes obtained by Monte Carlo simulation in figure 6.10.  
 1895 The  $M_{vis}$  spectrum observed in the final analysis is fitted to the sum of these templates. Es-  
 1896 timates for background yields are obtained from the normalization factor of each template,  
 1897 determined by the fit. Further details of the method can be found in [46] and [50].

1898 The TaNC (Section 3.3, [39]) discriminators used in [50] are replaced by the correspond-  
 1899 ing discriminators of the HPS + TaNC algorithm (Section 3.5, [32]). The  $Z/\gamma^* \rightarrow \tau^+\tau^-$  sig-  
 1900 nal shape is obtained via the  $Z/\gamma^* \rightarrow \mu^+\mu^-$  embedding technique [51]. The  $\mu + \tau_{had}$  visible  
 1901 mass spectrum observed in the final analysis is compared to the sum of template shapes  
 1902 scaled by the normalization factors determined by the fit in Figure 6.11. The corresponding  
 1903 estimates for background contributions are summarized in Table 6.7.

Process	Estimate
$Z \rightarrow \mu^+ \mu^-$	
Muon fake	$5.7 \pm 6.0$
Jet fake	$< 14.5$
$W + \text{jets } t\bar{t} + \text{jets}$	$7.6 \pm 6.9$
QCD	$141.3 \pm 40.4$
$N_{bgr}$ estimate	$226.5 \pm 33.1$

Table 6.7: Estimated contributions of individual background processes to the signal region, obtained via the template method. As the shapes are very similar, the normalization factors for QCD and  $W + \text{jets}$  background processes are anti-correlated. As a consequence, the sum of background contributions is determined by the fit more precisely than the individual contributions.

ab:BgEstTemplateMethod

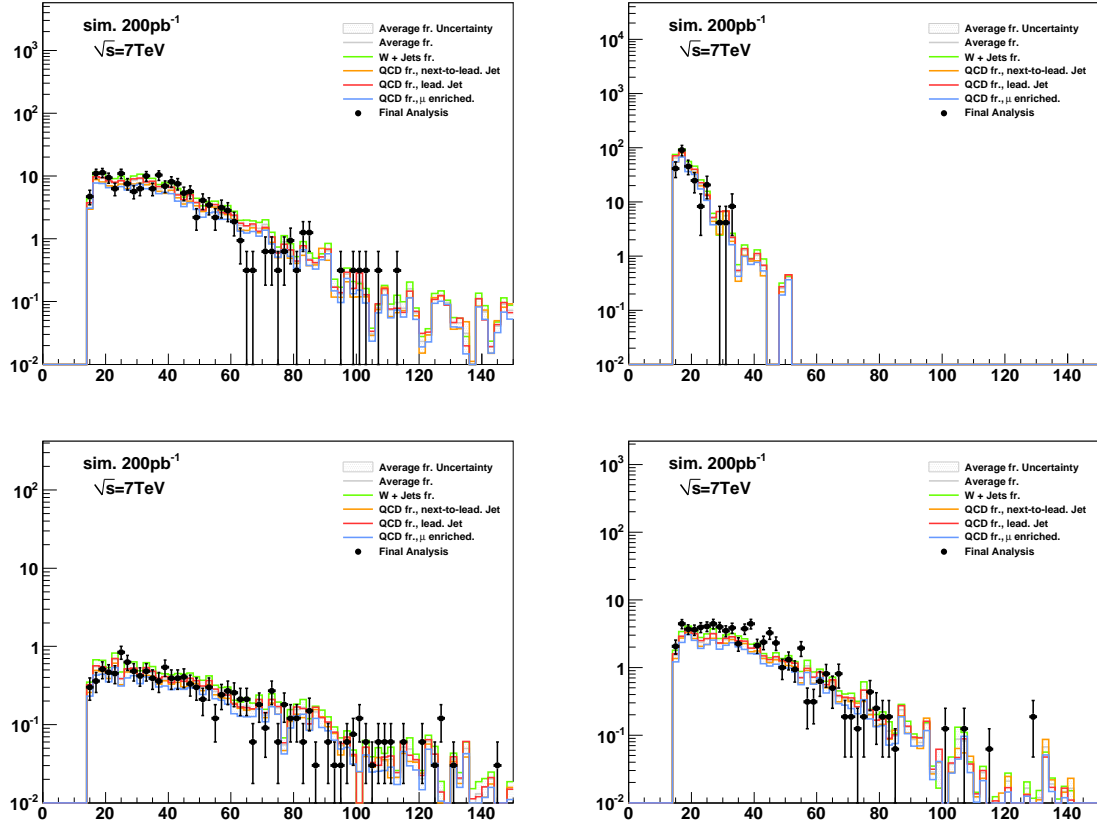


Figure 6.5: Distributions of muon transverse momentum in  $W + \text{jets}$  (top left), QCD (top right),  $t\bar{t} + \text{jets}$  (bottom left) and  $Z \rightarrow \mu^+ \mu^-$  (bottom right) background events which pass all selection criteria of the  $Z \rightarrow \tau^+ \tau^- \rightarrow \mu + \tau$ -jet cross-section analysis [44] compared to the estimate obtained from the “CDF method” fake-rate technique, computed according to equation 6.10. The expected contribution of background processes is indicated by points. Lines of different colors represent the estimates obtained by applying fake-rate weights determined for different compositions of light quark, heavy quark and gluon jets, as described in section 6.2.1. The maximum (minimum) estimate is interpreted as upper (lower) bound. The difference between the bounds is taken as systematic uncertainty on the estimate obtained from the “CDF-type” fake-rate method and is represented by the gray shaded area.

CDFtypeResults['muonPt']

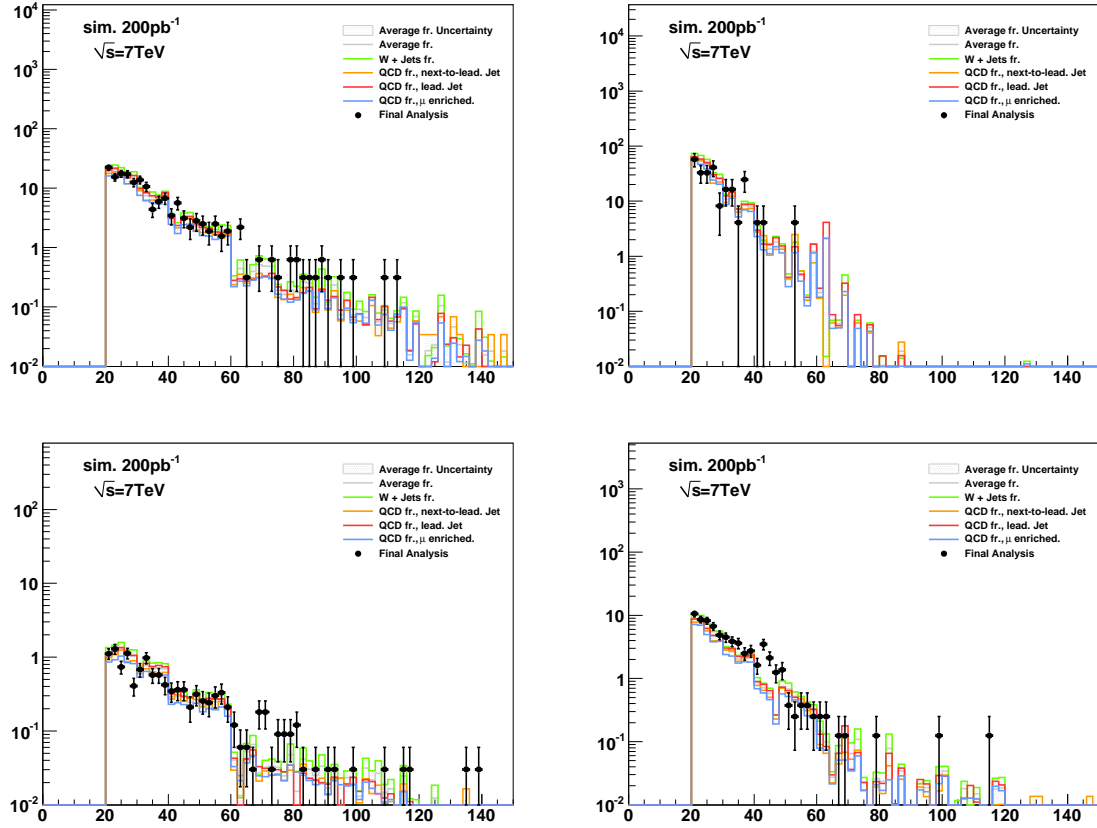


Figure 6.6: Distributions of transverse momenta of the tau-jet candidates in  $W + \text{jets}$  (top left), QCD (top right),  $t\bar{t} + \text{jets}$  (bottom left) and  $Z \rightarrow \mu^+\mu^-$  (bottom right) background events which pass all selection criteria of the  $Z \rightarrow \tau^+\tau^- \rightarrow \mu + \tau$ -jet cross-section analysis compared to the estimate obtained from the fake-rate technique, computed according to equation 6.5. The expected contribution of background processes is indicated by points. Lines of different colors represent the estimates obtained by applying fake-rate weights determined for different compositions of light quark, heavy quark and gluon jets, as described in section 6.2.1. The maximum (minimum) estimate is interpreted as upper (lower) bound. The difference between the bounds is taken as systematic uncertainty on the estimate obtained from the ‘‘CDF-type’’ fake-rate method and is represented by the gray shaded area.

CDFtypeResults'tauJetPt)

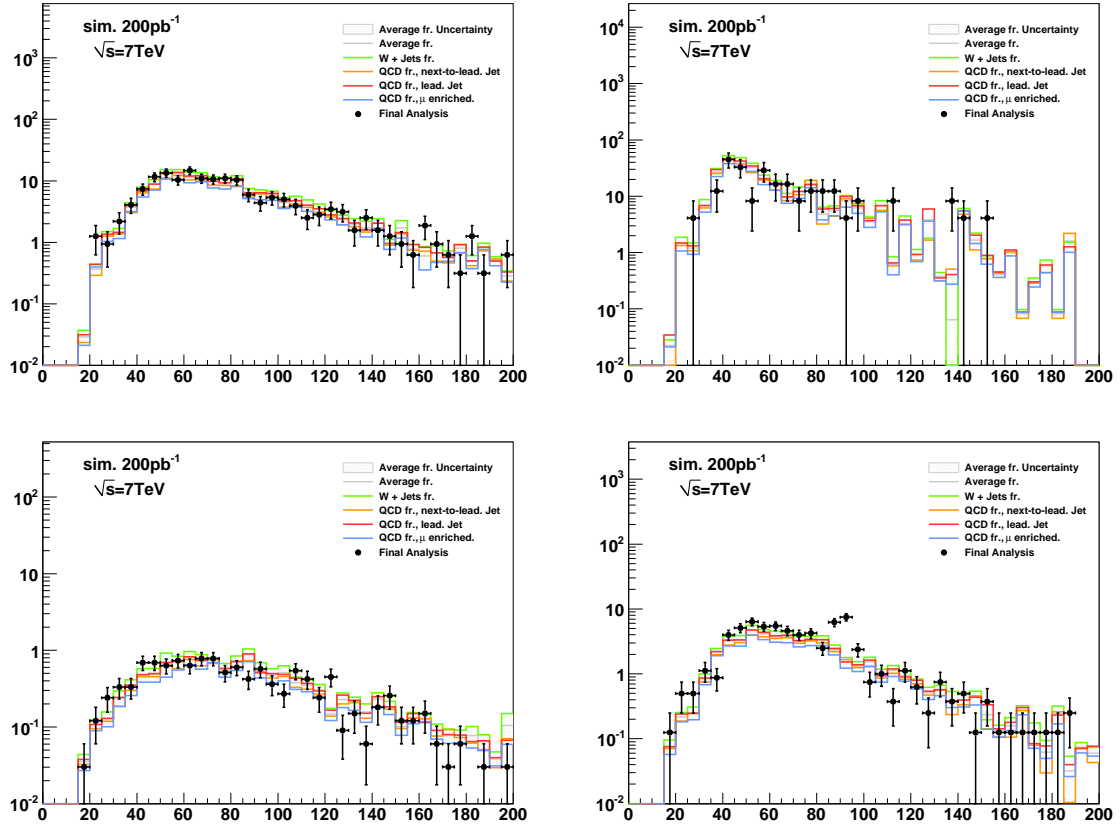


Figure 6.7: Distributions of the visible invariant mass of muon plus tau-jet in  $W + \text{jets}$  (top left), QCD (top right),  $t\bar{t} + \text{jets}$  (bottom left) and  $Z \rightarrow \mu^+\mu^-$  (bottom right) background events which pass all selection criteria of the closure test analysis compared to the estimate obtained from the fake-rate technique, computed according to Equation 6.10. The expected contribution of background processes is indicated by points. Lines of different colors represent the estimates obtained by applying fake-rate weights determined for different compositions of light quark, heavy quark and gluon jets, as described in Section 6.2.1. The maximum (minimum) estimate is interpreted as upper (lower) bound. The difference between the bounds is taken as systematic uncertainty on the estimate obtained from the “CDF-type” fake-rate method and is represented by the gray shaded area.

CDFtypeResults'mVisible)

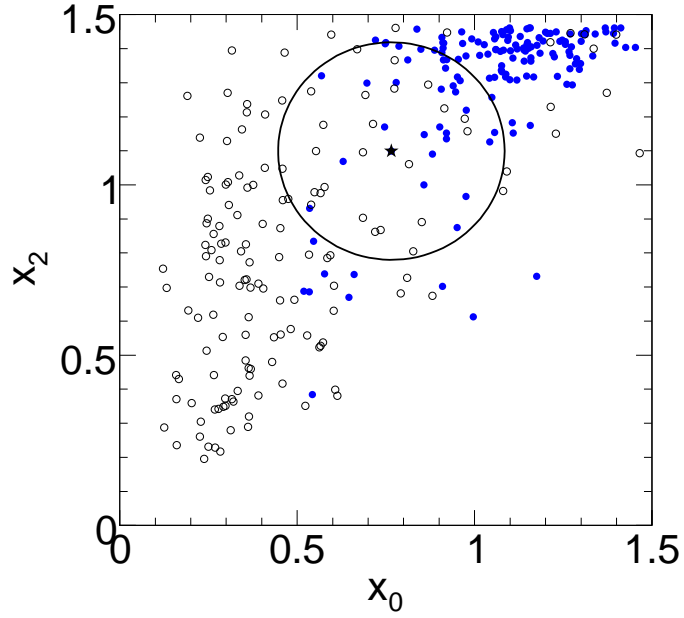


Figure 6.8: Example of the operation of a  $k$ NN classifier. The closest  $k = 50$  neighbors (those inside the circle) to a test point (indicated by the star marker) are selected. The probability that the star marker is a signal event is given the number of signal neighbors (blue markers) in the circle divided by  $k$ . Image credit: [29]

(fig:KNN)

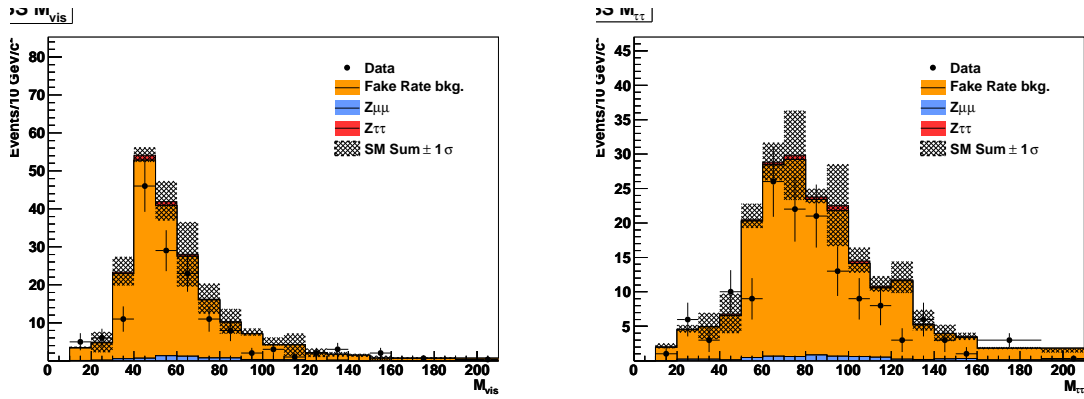


Figure 6.9: Distribution of visible mass (left) and “full” invariant mass reconstructed by the SVfit algorithm (right) observed in the like-sign charge control region compared to the background estimate obtained by the fake-rate method.

MuTauFakeRateResultsSS

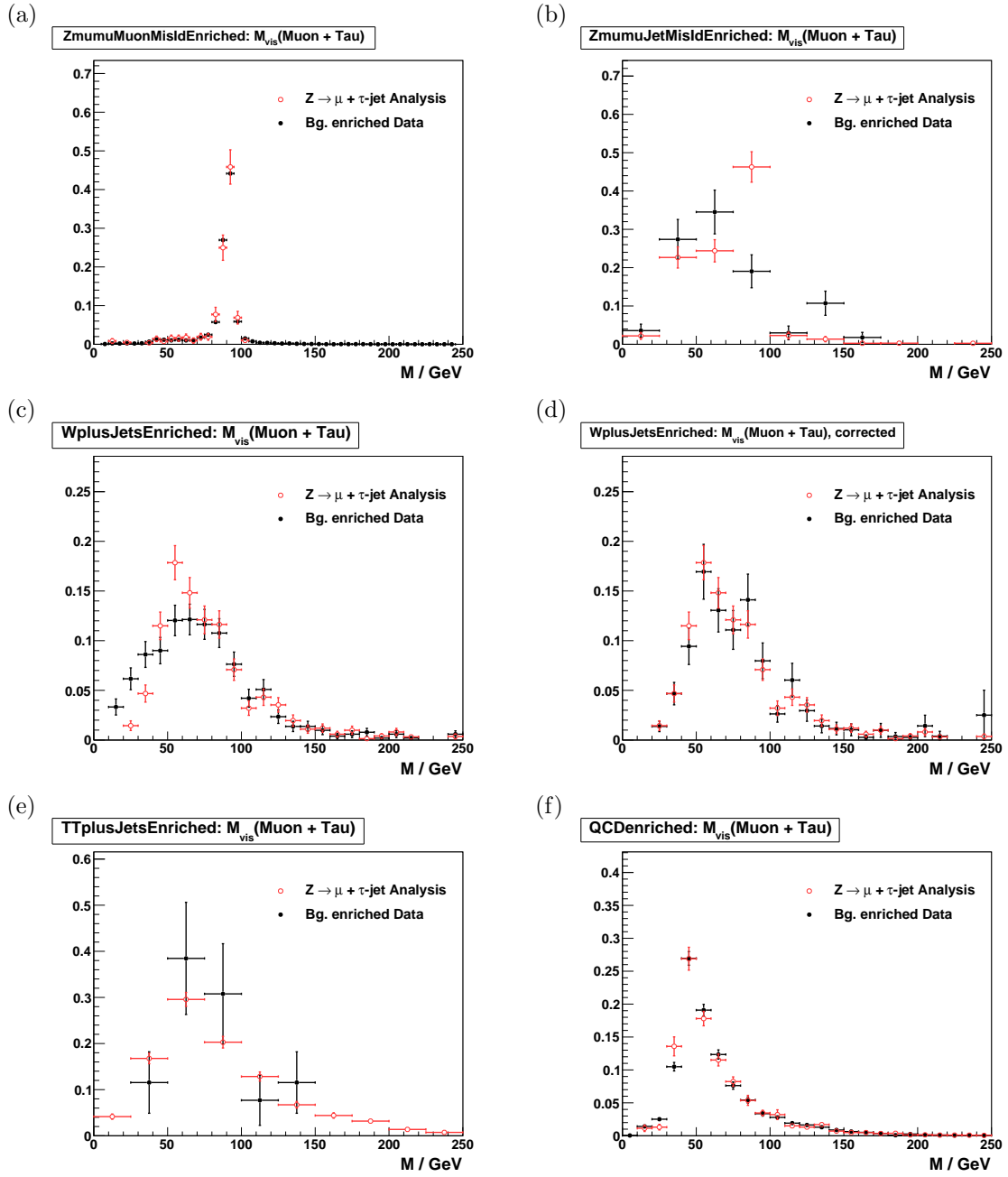


Figure 6.10:  $\mu + \tau_{had}$  shape templates obtained from  $Z \rightarrow \mu^+ \mu^-$  (a) and (b),  $W + \text{jets}$  before (c) and after (d) the bias correction explained in Section 6.3,  $t\bar{t} + \text{jets}$  (e) and QCD multi-jet (f) backgrounds enriched control regions compared to the expected distribution of the enriched background process to the signal region, predicted by Monte Carlo simulations. In (a) reconstructed tau-jet candidates are expected to be dominantly due to misidentified muons, while in (b) they are expected to be mostly due to misidentified quark or gluon jets.

`{fig:VisMassTemplates}`

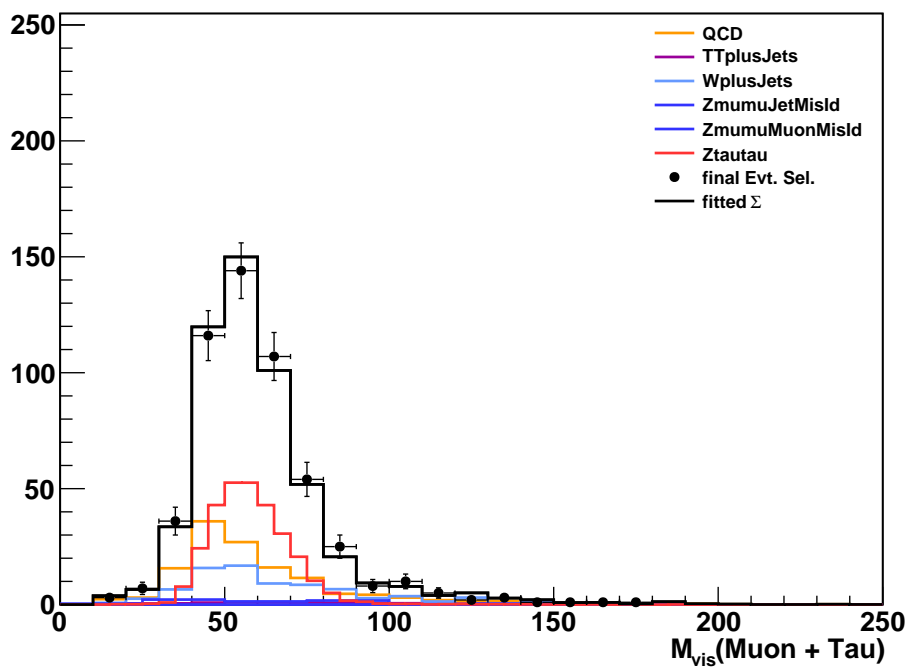


Figure 6.11:  $M_{vis}$  distribution of events selected by the  $Z/\gamma^* \rightarrow \tau^+\tau^- \rightarrow \mu + \tau_{had}$  cross-section analysis compared to the sum of shape templates for signal and background processes scaled by the normalization factors determined by the fit.

g:TemplateFitControlPlot)

1904

## Chapter 7

1905

# Monte Carlo Corrections

&lt;ch:corrections&gt;

1906 One of the most important goals of the analysis is to minimize the effect of potentially  
 1907 incorrect simulation effects on the final result. While the simulated CMS events have been  
 1908 observed to match the 2010 data with surprising results, it is nonetheless critical to measure  
 1909 in real data phenomenon which can have significant effects on the analysis whenever possible.  
 1910 In practice, these measurements are used to apply a correction factor to the corresponding  
 1911 measurement obtained from Monte Carlo. This measured correction factor has an associ-  
 1912 ated uncertainty, and is taken into account as a systematic uncertainty. The application of  
 1913 systematic uncertainties is described in the next chapter.

1914 The corrections measured and used in this analysis can be divided into two categories,  
 1915 efficiency corrections and scale corrections. Identification efficiency corrections scale the  
 1916 expected yield (due to a given identification selection) up or down. Scale corrections sys-  
 1917 tematically scale the energy of a particle (or  $E_T^{\text{miss}}$ ) up or down. In this analysis we apply  
 1918 efficiency corrections for the High Level Trigger muon requirement, all stages of muon iden-  
 1919 tification, and the hadronic tau identification. We apply a momentum scale correction to  
 1920 the muon and tau legs, and to the resolution of the  $E_T^{\text{miss}}$ . Finally, events are simulated with  
 1921 overlapping “pile-up”<sup>1</sup> events. The simulated events are weighted such that the number of  
 1922 pile-up events in the simulation matches that observed in the data.

1923

## §7.1 Muon Identification Efficiency

&lt;sec&gt;ZmumuTagAndProbe&gt;

1924 The identification efficiencies associated with the muon are measured in  $Z \rightarrow \mu^+ \mu^-$  events  
 1925 using the “tag and probe” technique [44].  $Z \rightarrow \mu^+ \mu^-$  events are selected from the Muon

---

<sup>1</sup>A pile-up event occurs when there are multiple interactions in one bunch proton bunch crossing. Pile-up increases with the instantaneous luminosity provided by the collider.

1926 7 TeV CMS 2010 datasets<sup>2</sup> by requiring that the events pass the “loose” Vector Boson Task  
 1927 Force (VBTF) event selections [44]. In the selected events, we define the “tag” muons as  
 1928 those that have transverse momentum greater than 15 GeV/c and pass the VBTF muon  
 1929 selection. The tag muons are further required to pass the “combined relative isolation” de-  
 1930 scribed in the VBTF paper. We finally require that the tag muon be matched to an HLT  
 1931 object corresponding to the run-dependent requirements listed in table 5.1. The trigger  
 1932 match requirement ensures that the event would be recorded independently of the probe  
 1933 muon. After the tag and probe muon pairs have been collected, we compare the muon iden-  
 1934 tification performance in the probe collection in events selected in data to the performance  
 1935 in simulated  $Z \rightarrow \mu^+ \mu^-$  events. The selection of events and tag muon in the simulated  
 1936 sample is the same as the data sample, with the notable exception that the only HLT re-  
 1937 quirement applied in MC is that the tag muon is matched to an HLT\_Mu9 object. Any  
 1938 difference in efficiency between the HLT\_Mu9 path and the paths used to select the data  
 1939 (in the tag–probe measurement and in the analysis) will be considered implicitly in the  
 1940 correction factor.

1941 The efficiencies for the muon selections applied in this analysis are measured using  
 1942 the “probe” objects. We measure the following marginal efficiencies, each relative to the  
 1943 previous requirement:

- 1944 • Efficiency of global probe muons to satisfy VBTF muon identification selections.
- 1945 • Efficiency of global probe muons passing the VBTF muon identification selection to  
1946 satisfy the isolation criteria described in Section 5.2.1.
- 1947 • Efficiency of probe muons passing the offline analysis selection defined in Chapter 5  
1948 to pass the HLT selection.

1949 In each case, the invariant mass spectrum of the tag–probe pair is fitted with a Crystal  
 1950 Ball function for the signal ( $Z \rightarrow \mu^+ \mu^-$ ) events and an exponential for the background.  
 1951 The fit is done for two cases; where the probe fails the selection and the where it passes.  
 1952 The method is illustrated in Figure 7.1. The signal yield  $N$  is extracted from each fit and

---

<sup>2</sup>/Mu/Run2010A-Sep17ReReco<sup>2</sup>/RECO and /Mu/Run2010B-PromptReco-v2/RECO

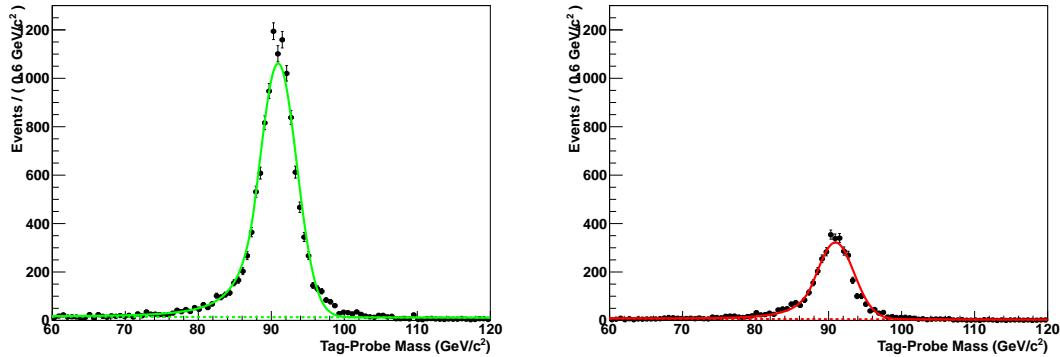


Figure 7.1: The tag–probe dimuon invariant mass spectrum in events in which the probe muon passed (left) and failed (right) the muon isolation requirement. The solid gives the result of the simultaneous fit of the signal (real  $Z \rightarrow \mu^+\mu^-$  events) and background. The fitted background contribution is shown as the dotted line. The muon isolation efficiency is then extracted from the number of signal events in the passing and failing bins.

(fig:TagAndProbeFits)

1953 the efficiency is computed as  $N_{pass}/(N_{pass} + N_{fail})$ . Each efficiency is measured in both the  
 1954 data and the simulation. The results of the measurements are shown in table 7.1. In the  
 1955 final analysis, the simulated events are weighted by the fractional difference to the measured  
 1956 values; the statistical uncertainty on the weight is taken as the sum in quadrature of the  
 1957 statistical uncertainties for the data and simulation efficiency measurements. The uncer-  
 1958 tainty on this measurement is taken as systematic uncertainty in the final measurement.

1959

1960 The correction for the trigger efficiency needs to take into account the differences in  
 1961 the HLT selections applied during different operating periods (see table 5.1). To determine  
 1962 the overall correction factor, we measure the trigger efficiency in data for each of the op-  
 1963 erating periods and compare it to the simulated efficiency of the HLT\_Mu9 selection. The  
 1964 overall efficiency in data is taken as the average of the three periods, weighted by integrated  
 1965 luminosity.

1966 The efficiency of the “cross–triggers” used in the run–range period 148822 – 149182  
 1967 (period C) cannot be measured in  $Z \rightarrow \mu^+\mu^-$  events as they require a reconstructed PFTau  
 1968 object at the trigger level. A single muon trigger (HLT\_Mu15) is also used in period C.  
 1969 The contribution of the cross–triggers is taken as a correction to the single muon trigger  
 1970 period C efficiency. The “muon leg” of the cross–triggers have the same requirements as

Muon selection	Efficiency		Ratio	Corection
	Data	Simulation		
VBTF identification	$99.2^{+0.1\%}_{-0.1\%}$	$99.1^{+0.1\%}_{-0.1\%}$	$1.001^{+0.001}_{-0.001}$	1.0
Particle Isolation	$76.8^{+0.4\%}_{-0.4\%}$	$78.3^{+0.3\%}_{-0.3\%}$	$0.981^{+0.006}_{-0.006}$	0.98
Trigger	$95.0^{+0.5\%}_{-0.5\%}$	$96.5^{+0.1\%}_{-0.2\%}$	$0.984^{+0.006}_{-0.006}$	0.98

Table 7.1: Efficiency of the various global muon selections applied in the analysis measured in data and simulated  $Z \rightarrow \mu^+\mu^-$  events. The “correction” column gives the event weight correction applied to the simulated events in the final analysis. The efficiency for each selection is the marginal efficiency with respect to the selection in the row above it.

muonTagAndProbeResults)

1971 the single muon triggers used in the run–range 147196 – 148058 (period B). The “cross–  
 1972 trigger” contribution is estimated as the difference between the efficiency in period B and  
 1973 the single–muon period C efficiency multiplied by a correction factor of  $0.9 \pm 10\%$  to account  
 1974 for the  $\tau$  leg efficiency. In the case that the measured single–muon period C efficiency is  
 1975 larger than the period B efficiency (due to statistical fluctuations and improvements in the  
 1976 trigger system), the period B efficiency is increased by 2%.

## 1977 §7.2 Hadronic Tau Identification Efficiency

⟨sec:HadTauIdEff⟩ The hadronic tau identification efficiency has been measured in 2010 7 TeV CMS data. The most straight forward to measure the tau ID efficiency would be to use a resonance which decays to taus and has a known cross section. One could then measure the tau ID efficiency in by comparing the observed yield  $N_{\text{obs}}$  in data with that expected from the known cross section, according to the cross section equation,

$$\varepsilon = \frac{N_{\text{obs}} - N_{\text{bkg}}}{\mathcal{L} \times \mathcal{A} \times \sigma \times \text{BR}_\tau}.$$

1978 The only suitable resonance for this method is  $Z \rightarrow \tau^+\tau^-$ . This method has been applied<sup>3</sup>  
 1979 in CMS  $Z \rightarrow \tau^+\tau^-$  cross section analysis ??, and measured a tau identification simulation  
 1980 to data correction factor of  $0.960 \pm 0.067$ .

<sup>3</sup>Actually, a slightly more complicated method is used. The analysis uses three decay channels, and the  $Z \rightarrow \tau^+\tau^-$  cross section and tau identification correction factors are fitted simultaneously. The central value of the  $Z \rightarrow \tau^+\tau^-$  cross section is driven by the  $Z \rightarrow \tau^+\tau^- \rightarrow e\mu$  channel, which is independent of the hadronic tau identification.

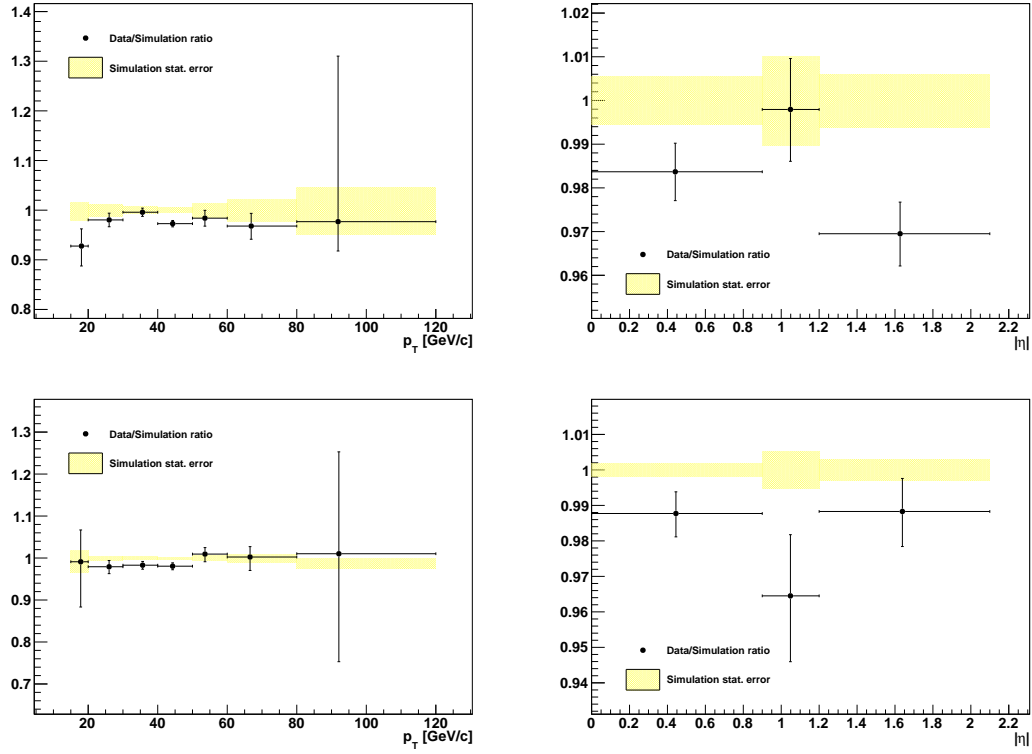


Figure 7.2: Ratio of muon isolation efficiency measured in data compared to simulated  $Z \rightarrow \mu^+\mu^-$  events.

`fig:MuonIsoCorrVersusPt?`

Unfortunately, this method cannot be used in this analysis. The measurement using the  $Z$  resonance operates on the assumption there is no New Physics contribution to the events in the  $Z$  bump. In the case that there was a Higgs signal at  $m_{A^0} = 90$  GeV/ $c^2$ , it would be indistinguishable from the  $Z$  and would appear as an increase of  $N_H$  in the observed yield. The analysis would be completely insensitive to a Higgs boson on the  $Z$  peak, and cause the efficiency to be overestimated by a factor

$$\delta\varepsilon = \frac{N_H}{\mathcal{L} \times \mathcal{A} \times \sigma \times \text{BR}_\tau}.$$

The solution to this problem is to use a “tag and probe” approach analogous to the muon efficiency measurement of Section 7.1. The tag and probe method is only sensitive to the shapes of the distributions, and will be independent of a Higgs contribution to the  $Z$  peak. This measurement has been performed by the CMS Tau Physics Object Group [47]. A loose hadronic tau preselection is applied to events which pass the selections (excluding the hadronic tau identification) of the CMS EWK  $Z \rightarrow \tau^+\tau^-$  cross section measurement [52].

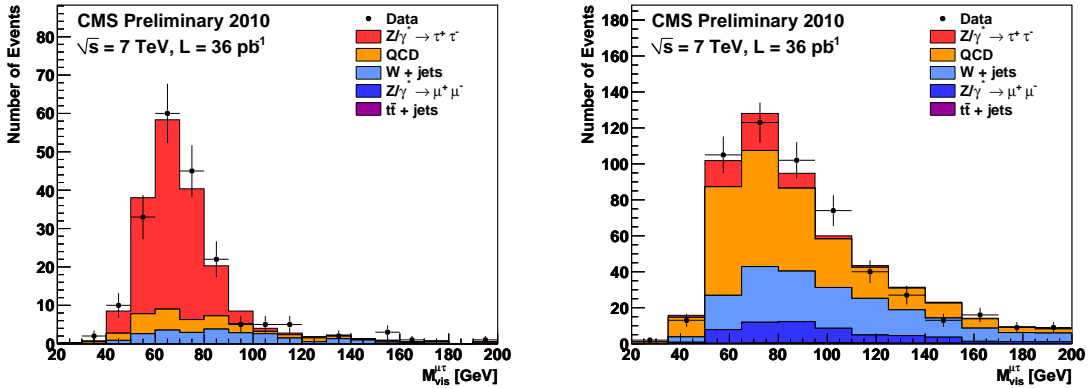


Figure 7.3: Visible mass spectrum of preselected events used to measure the hadronic tau identification efficiency in 2010 CMS 7 TeV data. The figure on the left (right) shows the preselected events that pass (fail) the hadronic tau identification. The different colors indicate the fitted yields of the different signal and background contributions. Reference: [47].

(fig:TauIdEffFits)

1987 The preselected sample is then split into two categories, those that pass the hadronic tau  
 1988 identification and those that fail. The signal and background yields in each category  
 1989 are fitted using the Template Method described in Section 6.3. An illustrative example of  
 1990 the fits for the yields is shown in Figure 7.3. The hadronic tau identification efficiency can  
 1991 then be computed using the relative size of the true tau yields in the passing and failing  
 1992 categories. The efficiency is measured [47] for the loose HPS + TaNC tau identification in  
 1993 the 2010 CMS dataset and is found to be  $1.06 \pm 0.30$ .

### 1994 §7.3 Muon and Tau Momentum Scale

1995 Muons are one of the best measured objects at CMS. The momentum scale of CMS muons  
 1996 has been measured [53] using the  $J/\psi$ ,  $\psi(2S)$  and  $\Upsilon$  di-muon resonant decays. The muon  
 1997 momentum resolution is found to be 3% or better for muons with  $p_T < 100$  GeV/ $c$ . We  
 1998 apply the muon momentum correction using the “MusCleFit” algorithm described in [53].  
 1999 The muon momentum correction and uncertainty varies as a function of  
 2000 muon  $p_T$  and  $\eta$ . The effect of the muon momentum correction uncertainty is a small effect  
 2001 in this analysis compared to the  $\tau$  and  $E_T^{\text{miss}}$  scale uncertainties.

2002 The uncertainty on the jet energy scale is determined from an analysis of the  $p_T$  bal-  
 2003 ance between photons and jets in  $\gamma + \text{jets}$  events [54]. The jet energy scale uncertainties

2004 determined by the JetMET group are applied to tau–jets as well as other jets in the event.  
 2005 The tau energy scale correction factor is currently taken to be 1.0 with an uncertainty of  
 2006 3%. The QCD jet energy scale has been measured to within 3% uncertainty. In the future,  
 2007 the energy scale of the tau is expected to be determined to a much better precision, as the  
 2008 neutral hadronic activity of a hadronic tau decay is expected to be zero. The jet energy  
 2009 scale of 3% can be confidently considered [47] an upper limit<sup>4</sup>, and is used in this analysis  
 2010 as the tau energy scale uncertainty.

## 2011 §7.4 Missing Transverse Energy Correction

(sec:ZRecoilCorr) 2012 In practice, the resolution of the reconstructed missing transverse energy is poor as it is  
 2013 sensitive to the mis–measurement of any object in the event. Furthermore, a fraction of the  
 2014 particles produced in the hard collision can be produced in the very forward region, outside  
 2015 of the fiducial region of the calorimeters. The resolution of the  $E_T^{\text{miss}}$  reconstruction can be  
 2016 measured in  $Z \rightarrow \mu^+ \mu^-$  events. The true  $E_T^{\text{miss}}$  in such events is expected to be zero. The  
 2017  $E_T^{\text{miss}}$  resolution in simulated  $Z \rightarrow \mu^+ \mu^-$  events is found to be smaller (better) than in the  
 2018 data.

2019 The  $E_T^{\text{miss}}$  resolution depends on the “recoil” of the  $Z$  boson. The reason for this effect  
 2020 is that for events where the  $Z$  is produced nearly at rest, the associated recoil products  
 2021 have very small transverse momentum and are produced at very high pseudorapidity. The  
 2022  $E_T^{\text{miss}}$  is corrected using a procedure called a “ $Z$ –recoil” correction, as described in [55].  
 2023 The resolution of the  $E_T^{\text{miss}}$  is measured in  $Z \rightarrow \mu^+ \mu^-$  events in simulation and data.  
 2024 The difference in the reconstructed  $E_T^{\text{miss}}$  resolution in both samples is parameterized by  
 2025 the magnitude of the transverse momenta of the particles recoiling against the  $Z$ .<sup>5</sup> The  
 2026 reconstructed  $E_T^{\text{miss}}$  in the simulated  $Z \rightarrow \tau^+ \tau^-$ ,  $Z \rightarrow \mu^+ \mu^-$ , and  $W + \text{jets}$  samples is  
 2027 “smeared” by a random amount in each event such that the final resolution matches the  
 2028 observed resolution in the data.

---

<sup>4</sup>The tau energy scale was roughly measured using the invariant mass of the hadronic decay products and shown to be compatible with 1.0, within 3%.

<sup>5</sup>The “recoil” particles are defined as all those not identified as  $Z$  decay products. This definition is equivalent to the total decay product transverse momentum  $q_T$  added reconstructed  $E_T^{\text{miss}}$ .

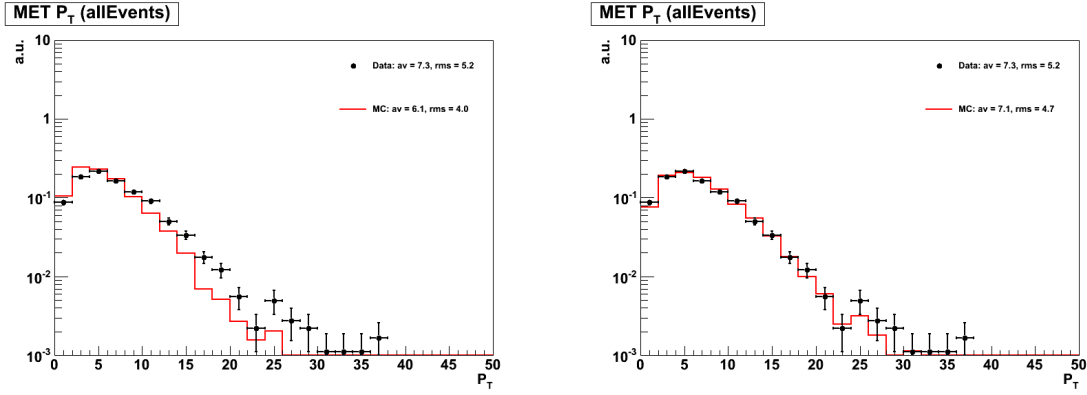


Figure 7.4: Missing transverse energy reconstructed in  $Z \rightarrow \mu^+\mu^-$  events selected in data compared to  $Z \rightarrow \mu^+\mu^-$  events in Monte Carlo simulation before (left) and after (right) the  $Z$ -recoil corrections to the  $E_T^{\text{miss}}$  resolution are applied.

(fig:ZrecoilCorrection)

2029         $Z$ -recoil corrections are determined as described in [55] and applied to simulated  
 2030         $Z \rightarrow \tau^+\tau^-$ ,  $Z \rightarrow \mu^+\mu^-$  and  $W + \text{jets}$  events, in order to correct for residual differences in  
 2031         $E_T^{\text{miss}}$  response and resolution between data and Monte Carlo simulation [56]. The correc-  
 2032        tions are obtained by an unbinned maximum likelihood fit (in data and simulation) of the  
 2033        transverse recoil vector  $\vec{u}_T = -(\vec{q}_T + E_T^{\text{miss}})$  as function of the transverse momentum  $\vec{q}_T$  of  
 2034        the  $Z$ -boson in directions parallel and perpendicular to the  $Z$ -boson transverse momentum  
 2035        vector. The effect of the  $Z$ -recoil correction is illustrated in Figure 7.4. The uncertainty on  
 2036        the  $Z$ -recoil correction factor from the maximum likelihood fit is treated as a systematic  
 2037        uncertainty in the final result.

## 2038        §7.5 Pile-up Event Weighting

?<sec:PUweighting>? The average number of pile-up interactions in the event can effect almost all aspects of  
 2039        the analysis. In general, increasing pile-up lowers particle identification efficiencies and  
 2040        lowers  $E_T^{\text{miss}}$  resolution. It is therefore important that the distribution of pile-up events  
 2041        in the simulation matches the distribution found in the data. Differences in the number  
 2042        of pile-up interactions between the data (averaged over the analyzed run-range) and pile-  
 2043        up Monte Carlo samples produced for “BX156” pile-up conditions are corrected for by  
 2044        reweighting Monte Carlo simulated events according to the number of reconstructed event

---

<sup>6</sup>The BX156 name comes from the fact that the pile-up scenario used in this simulation corresponds to an LHC configuration with 156 bunches.

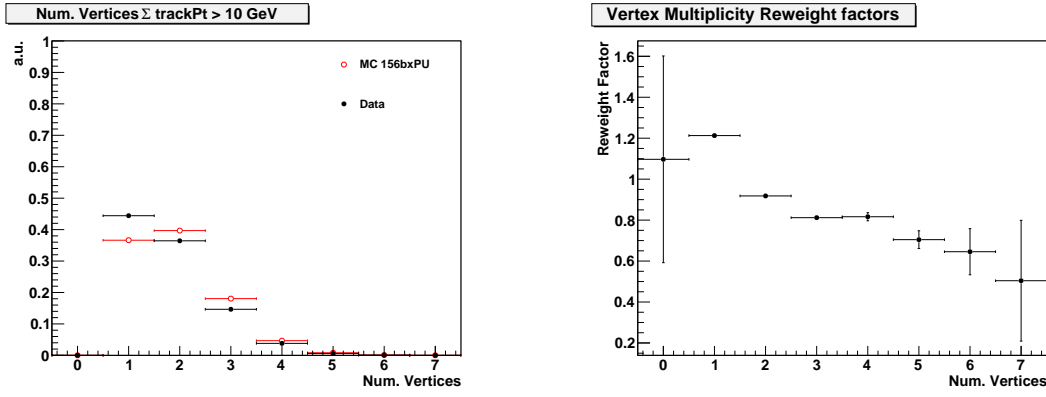


Figure 7.5: Vertex multiplicity distribution measured in the analyzed data-taking period compared to Monte Carlo simulation with “BX156” pile-up conditions (left) and resulting Monte Carlo reweighting factors (right).

{fig:pileUpReweighting}

2046 vertices, in order to match the distribution measured in a  $W \rightarrow \mu\nu$  dataset triggered by  
 2047 the HLT\_Mu15 High Level Trigger path. Vertices considered for this purpose are required  
 2048 to pass  $-24 < z_{vtx} < +24$  cm,  $|\rho| < 2$  cm, nDoF  $> 4$ . In addition, the total transverse  
 2049 momenta of all tracks fitted to the vertex is required to exceed 10 GeV/ $c$ , assuming that  
 2050 “softer” vertices have little or no effect on the “hard” event to pass event selection criteria.  
 2051 The average vertex multiplicity distribution measured in data is compared to Monte Carlo  
 2052 simulation with “BX156” pile-up conditions in Figure 7.5. Both distributions are similar,  
 2053 resulting in Monte Carlo reweighting factors close to unity.

2054

## Chapter 8

2055

# Systematics and Limit Extraction

(ch:systematics)

2056 In this chapter we discuss the systematic uncertainties affecting the search for the Higgs  
 2057 boson and the statistical techniques used to establish an upper limit on the Higgs  $\rightarrow \tau^+\tau^-$   
 2058 branching ratio times cross section ( $\sigma \times \text{BR}_\tau$ ). The limit can be interpreted as the largest<sup>1</sup>  
 2059 signal presence that could exist in the data and still be consistent with the null hypothesis.  
 2060 The limit on  $\sigma \times \text{BR}_\tau$  is roughly independent of the theoretical model<sup>2</sup>. In the conclusion,  
 2061 we will interpret the  $\sigma \times \text{BR}_\tau$  limit result in the context of the MSSM theory.

Proper determination of systematic uncertainties is one of the most challenging and important components in performing the measurement correctly. A systematic uncertainty is the effect of the uncertainty of some ancillary measurement (or assumption) that is used in the computation of the final result. An instructive example of how a systematic uncertainty can affect the final result is a counting experiment measuring the cross section of some signal particle in the presence of background. The formula for the cross section times the branching fraction is

$$\sigma \times BR = \frac{N_{sig}}{\mathcal{L} \cdot \mathcal{A} \cdot \epsilon} = \frac{N_{obs} - N_{bkg}}{\mathcal{L} \cdot \mathcal{A} \cdot \epsilon}, \quad (8.1) \quad \text{eq:CrossSectionE}$$

where  $N_{obs}$  is the number of events observed in data,  $N_{bkg}$  is the estimated number of background events in the observed data sample,  $\mathcal{L}$  is the integrated luminosity, and  $\mathcal{A} \cdot \epsilon$  is the acceptance times efficiency of the signal. All of the quantities in Equation 8.1 (with the exception of the observed count  $N_{obs}$ ) have some uncertainty which will effect the final measurement. Consider a situation where the expected number of background events is determined by fitting some sideband spectrum, and the fitted result has some error  $\delta N_{bkg}$ .

---

<sup>1</sup>At some stated level of statistical confidence; the convention for limits in experimental high energy physics is 95%.

<sup>2</sup>Provided that the width of the Higgs bosons in the given model is smaller than the resolution of the SVfit mass resolution.

The total relative effect of this error can be obtained by error propagation

$$\frac{\delta(\sigma \times BR)}{\sigma \times BR} = \frac{\partial(\sigma \times BR)}{\partial N_{bkg}} \frac{1}{\sigma \times BR} \delta N_{bkg} = \frac{-\delta N_{bkg}}{N_{obs} - N_{bkg}}. \quad (8.2) \quad \text{[eq:CrossSectionError]}$$

It is interesting to examine Equation 8.2 in two scenarios. In the limit that  $N_{obs}$  is large compared to  $N_{bkg}$ , the effect of the error on the background estimate  $\delta N_{bkg}$  does not affect the final result. In contrast, in a scenario when the data is dominated by background events, the relative error on the signal measurement due to the background estimation approaches infinity. The sensitivity of a measurement to a systematic uncertainty on a parameter depends on the context in which that parameter is used.

Experimental systematic uncertainties relevant for MSSM Higgs  $\rightarrow \tau^+ \tau^-$  search presented in this thesis are classified in three categories: normalization uncertainties on the signal and  $Z \rightarrow \tau^+ \tau^-$  background (events with true taus), normalization uncertainties on contributions from background with fake taus, and shape uncertainties. Normalization uncertainties on events with true taus are due to lepton reconstruction, identification, isolation and trigger efficiencies. These terms are equivalent to the efficiency  $\epsilon$  and acceptance terms  $\mathcal{A}$  of Equation 8.2 and affect the expected yield of MSSM Higgs  $\rightarrow \tau^+ \tau^-$  signal and  $Z \rightarrow \tau^+ \tau^-$  background events. The uncertainties on these effects are obtained by measuring the effect in data and simulation, according to the procedures of Chapter 7, and calculating a correction factor. The uncertainty associated with the measurement of the correction factor is the systematic uncertainty. The normalization uncertainties are assumed to be uncorrelated with the *shapes* of visible and SVfit mass distributions which are used to extract the MSSM Higgs  $\rightarrow \tau^+ \tau^-$  signal contribution in the analyzed dataset. Uncertainties on the shapes of the distributions are described by “morphing” systematics. These are due to uncertainties on the momentum/energy scale of identified electrons, muons, tau and other jets in the event. As the SVfit mass reconstruction algorithm uses the missing transverse energy, the shape of the SVfit distribution is sensitive to systematic uncertainties on the overall scale  $E_T^{\text{miss}}$  measurement. The “morphing” systematics affect the shapes of signal as well as background contributions. Normalization uncertainties on background contributions are estimated from the level of agreement between data and Monte Carlo simulation in background dominated control regions.

2089 §8.1 Signal normalization uncertainties

2090 The signal normalization uncertainties are due to imperfect knowledge of how improperly  
 2091 modeled effects in the detector affect our “acceptance” model, or the probability that a  
 2092 given signal event will pass one of the selections (detailed in Chapter 5). The general pro-  
 2093 cedure to quantify these uncertainties is to measure the effect in some control region in  
 2094 both the data and Monte Carlo. The ratio of data to Monte Carlo then gives a correc-  
 2095 tion factor which is applied to the simulation. An uncertainty on the measurement of the  
 2096 effect in control region (in data, simulation, or both) is then taken as the systematic un-  
 2097 certainties. The signal normalization uncertainties affecting this analysis on muon trigger,  
 2098 reconstruction, identification and isolation efficiencies are taken from the tag and probe  
 2099 analysis of  $Z \rightarrow \mu^+ \mu^-$  events presented in Section 7.1. A very conservative estimate of 30%  
 2100 is taken for the uncertainty on the tau reconstruction and identification efficiency. The tau  
 2101 identification uncertainty measurement is discussed briefly in 7.2. The dependency of the  
 2102 Higgs signal extraction on the tau identification efficiency has been studied, the result being  
 2103 that uncertainties on the tau identification efficiency affect the limit on cross-section times  
 2104 branching ratio for MSSM Higgs  $\rightarrow \tau^+ \tau^-$  production by a few percent only. An uncertainty  
 2105 of 11% is attributed to the luminosity measurement.

2106 §8.2 Background normalization uncertainties

2107 Uncertainties on the normalization of background processes are obtained from the study of  
 2108 background enriched control regions presented in Chapter 6. The main fake tau backgrounds  
 2109 in this analysis are QCD multi-jet and  $W +$  jets events. For a detailed discussion of the  
 2110 measurements, see Chapter 6. These backgrounds are produced copiously enough for the  
 2111 backgrounds to be studied in control regions dominated by a single background process  
 2112 with a purity exceeding 90% and an event statistics exceeding the expected contribution of  
 2113 that background to the analysis by more than one order of magnitude. Both backgrounds  
 2114 are found to be well modeled by the Monte Carlo simulation. An uncertainty of 10% is  
 2115 attributed to the contribution of QCD and  $W +$  jet backgrounds to the analysis. The  
 2116 cross-section for  $t\bar{t} + jets$  production makes it difficult to select a high purity sample of

2117  $t\bar{t}+jet$  events of high event statistics. From the study of the 19 events selected in the  $t\bar{t}+jets$   
 2118 background enriched control sample we assume an uncertainty on the  $t\bar{t}+jets$  background  
 2119 contribution in the analysis of 30%. The  $Z \rightarrow \mu^+\mu^-$  background has been studied with  
 2120 large statistical precision in two separate control regions, dominated by events in which  
 2121 the reconstructed tau–jet candidate is either due to a misidentified quark or gluon jet or  
 2122 due to a misidentified muon. Good agreement between data and Monte Carlo simulation is  
 2123 found in both cases. Sizeable uncertainties on the  $Z \rightarrow \mu^+\mu^-$  background contribution arise  
 2124 due to the extrapolation from the background enriched control regions to the data sample  
 2125 considered in the analysis, however: the contribution of  $Z \rightarrow \mu^+\mu^-$  background events to  
 2126 the analysis is due to events in which one of the two muons produced in the  $Z$  decay either  
 2127 escapes detection or fakes the signature of a hadronic tau decay. Both cases may be difficult  
 2128 to model precisely in the Monte Carlo simulation. The non–observation of a  $Z$  mass peak in  
 2129 the mu + tau visible mass distribution studied with the fake–rate method on the other hand  
 2130 sets a limit on possible contributions from  $Z \rightarrow \mu^+\mu^-$  background events. Conservatively,  
 2131 we assume an uncertainty of 100% on both types of  $Z \rightarrow \mu^+\mu^-$  background contributions.

### 2132 §8.3 Shape uncertainties

<sec:ShapeUncertainties>  
 2133 Shape uncertainties on the distributions of visible and “full” invariant mass reconstructed by  
 2134 the SVfit algorithm are estimated by varying the electron energy and muon momentum scale,  
 2135 the energy scale of tau–jets and other jets in the event and varying the missing transverse  
 2136 energy in Monte Carlo simulated events. After each variation the complete event is re–  
 2137 reconstructed and passed through the event selection. Shifted visible and “full” invariant  
 2138 mass shapes are obtained for each variation from the events passing all event selection  
 2139 criteria. The difference between shifted shapes and the “nominal” shapes obtained from  
 2140 Monte Carlo simulated events with no variation of energy or momentum scale or of the  
 2141 missing transverse energy applied is then taken as shape uncertainty.

2142 The systematic uncertainties on the muon and tau energy scales have been provided by  
 2143 the muon and tau Physics Object Groups and are described in Section 7.3. The modelling  
 2144 of missing transverse energy in different types of background events has been studied in  
 2145 the background enriched control regions described in Chapter 6. No significant deviations

2146 between data and Monte Carlo simulation have been found. Uncertainties due to missing  
 2147 transverse energy are estimated by varying parameters of the  $Z$ -recoil corrections within  
 2148 the uncertainties obtained when fitting (see Section 7.4) the  $Z$ -recoil correction factor pa-  
 2149 rameters in simulated  $Z \rightarrow \mu^+ \mu^-$  events versus  $Z \rightarrow \mu^+ \mu^-$  events selected in data.

## 2150 §8.4 Theory uncertainties

2151 The signal and background normalization as well as the shape uncertainties are all exper-  
 2152 imental uncertainties in nature. Additional theoretical uncertainties arise from imprecise  
 2153 knowledge of parton-distribution functions (PDFs) and of the exact dependency of signal  
 2154 cross-sections and branching ratios on  $\tan\beta$  and  $m_A$ . The PDFs describe how the energy  
 2155 of the protons is shared between the quarks and gluons. Since the longitudinal boost of  
 2156 the hard collisions depends on the PDFs, the signal acceptance is sensitive to errors in the  
 2157 PDFs. The uncertainties on the signal acceptance due to PDF uncertainties are estimated  
 2158 using tools developed by the CMS Electroweak working group [57]. The acceptance is com-  
 2159 puted with respect to MSSM Higgs  $\rightarrow \tau^+ \tau^-$  decays that have muons of  $p_T^\mu > 15$  GeV/ $c$   
 2160 and  $|\eta_\mu| < 2.1$ , jets produced in hadronic tau decays with visible  $p_T^{vis} > 20$  GeV/ $c$  and  
 2161  $|\eta_{vis}| < 2.3$  on generator level. Acceptance values are computed for the central value and  
 2162 44 eigenvectors of the CTEQ66 PDF set [58]. The systematic uncertainty on the signal  
 2163 acceptance is computed following the PDF4LHC recommendations [59, 60].

2164 The effect of Monte Carlo normalization, shape and theory uncertainties on the signal  
 2165 efficiency times acceptance is summarized in Table 8.1.

## 2166 §8.5 Limit Extraction Method

?<sec:statmethod>? The search for a new signal is performed by examining the observed distribution of the  
 2167 reconstructed di-tau mass  $m_{\tau\tau}$  as reconstructed by the SVfit algorithm. An “bump” in  
 2168 this spectrum would indicate the presence of a new particle. To make a statement about  
 2169 the presence of a bump with confidence, the shape under a potential bump must be well  
 2170 described. The background shape is decomposed into the combination of shapes from the  
 2171 difference background sources, which we refer to here as “templates.” The data and the

Source	Effect
Normalization uncertainties	
Trigger	$0.981 \pm 0.006$
Muon identification	$1.001 \pm 0.001$
Muon isolation	$0.984 \pm 0.006$
Tau-jet identification	$1.00 \pm 0.30$
Shape uncertainties	
Muon momentum scale	$\ll 1\%$
Tau-jet energy scale	$1 - 4\%^1$
Jet energy scale (JES)	$< 1\%^2$
$E_T^{\text{miss}}$ ( $Z$ -recoil correction)	1%
Theory uncertainties	
PDF	2% <sup>3</sup>

<sup>1</sup> decreasing with  $m_A$

<sup>2</sup> number quoted for  $gg \rightarrow A/H$  and  $b\bar{b} \rightarrow A/H$  sample as a whole;

in the subsample of events with b-tagged jets the effect of the JES uncertainty is 4%

<sup>3</sup> with small dependence on  $m_A$

Table 8.1: Effect of normalization uncertainties on the  $gg \rightarrow A/H$  and  $b\bar{b} \rightarrow A/H$  signal efficiency times acceptance.

(tab:ExpUncertainties)

2173 templates for each background distribution is binned in the observable  $m_{\tau\tau}$  variable. The  
 2174 normalization of each template represents the total yield expected for that source.

We can then define a likelihood for any configuration of our templates given the observed data. The likelihood is a “binned Poisson likelihood,” which is defined as the product of the Poisson probability in each bin. The Poisson probability  $P(n|\mu)$  is the probability to observe  $n$  events given an expectation of (on average)  $\mu$  events. The Poisson probability is given by the expression

$$P(k|\mu) = \frac{\mu^k e^{-\mu}}{k!}. \quad (8.3) \quad [\text{eq:PoissonProb}]$$

2175 The total likelihood for observed data given some configuration of templates is then simply

2176 a product of the Poisson probabilities (Equation 8.3) in each of the  $N_{bin}$  bins:

$$\mathcal{L} = \prod_{i=1}^{N_{bin}} \frac{\mu_i^{n_i} e^{-\mu_i}}{n_i!}, \quad (8.4) \text{?eq:CoreLikelihood}$$

2177 where the expected number of events  $\mu_i$  in the bin  $i$  is the sum of the number of events

2178 from all sources

$$\mu_i = \sum_{j=1}^{N_{source}} \mu_{ji}.$$

2179 The number of expected events in a source, in turn, can be written

$$\mu_{ji} = L \sigma_j \epsilon_{ji} \quad (8.5) \text{[eq:ShapeParameter]}$$

2180 where  $L$  is the integrated luminosity,  $\sigma_j$  is the cross section for source  $j$ , and  $\epsilon_{ji}$  is the  
2181 efficiency for source  $j$  in bin  $i$ .

2182 We incorporate the systematic uncertainties of the analysis by introducing a set of  
2183 “nuisance parameters”  $\vec{\beta}$  into the likelihood function. As the name suggests, we are not  
2184 interested in the actual value of the nuisance parameters. Each nuisance parameter param-  
2185 eterizes some phenomenon in the analysis. The shape templates (which can be defined purely  
2186 in terms of  $\sigma_j$  and  $\epsilon_{ji}$  in Equation 8.5) are now interpreted as functions of the set of nuisance  
2187 parameters  $\vec{\beta}$ . Existing knowledge about the value of the nuisance parameter is introduced  
2188 by extending the likelihood function with a constraint  $\mathcal{G}(\vec{\beta})$  that expresses the uncertainty  
2189 on the nuisance parameters. The templates  $\mu_{ji}$  can depend on the nuisance parameters in  
2190 two ways. Normalization uncertainties introduce multiplicative nuisance factors on the yield  
2191 of some (sub)set of the sources defined by Equation 8.5. As an example, consider a simplified  
2192 situation where there are only two sources:  $Z \rightarrow \tau^+ \tau^-$  and  $W + \text{jets}$  events. Both are sources  
2193 are sensitive to the efficiency of the muon trigger. Only the  $Z \rightarrow \tau^+ \tau^-$  sample is sensitive  
2194 to the efficiency of the hadronic tau identification algorithm, as the fake-rate in  $W + \text{jets}$   
2195 is measured in data. We would then introduce two multiplicative nuisance parameters,  $\beta_\mu$   
2196 and  $\beta_\tau$ , which respectively correspond to the two uncertainties. The expected number of  
2197 events in the  $i$ th bin is then given by a modified form of Equation 8.5

$$\mu_i = L \beta_\mu \sigma^W \epsilon_i^W + L \beta_\mu \beta_\tau \sigma^Z \epsilon_i^Z. \quad (8.6) \text{[eq:ShapeParameter]}$$

2198 From Equation 8.6, we can see that  $\beta_\mu$  affects both sources but  $\beta_\tau$  only affects the  $Z \rightarrow \tau^+ \tau^-$   
2199 source.

The shape uncertainties discussed in Section 8.3 are incorporated using a technique

$(1 - \alpha)\%$	$m = 1$	$m = 2$	$m = 3$
68.27	1.00	2.30	3.53
90.00	2.71	4.61	6.25
95.00	3.84	5.99	7.82
99.00	6.63	9.21	11.34

Table 8.2: Correspondence between a confidence level defined by  $(1 - \alpha)\%$  and the corresponding interval in  $2\Delta \ln \mathcal{L}$ . The  $2\Delta \ln \mathcal{L}$  interval is different depending the number  $m$  of parameters which are being simultaneously estimated.

(tab:ConfidenceIntervals)

called “vertical template morphing.” For each source, different templates are created for three different values of the morphing parameter, corresponding to -1, 0, and +1 standard deviation shifts in the nuisance parameter. To determine the number of expected events in the  $i$ th bin as a function of the morphing parameter, we interpret quadratically between the  $i$ th bin values of the three templates, and extrapolate linearly beyond them. The overall likelihood then, including nuisance parameters, can be written as

$$\mathcal{L} = \prod_{i=1}^{N_{bin}} \frac{[\mu_i(\vec{\beta})]^{n_i} e^{-\mu_i(\vec{\beta})}}{n_i!} \times \prod_{m=1}^{N_\beta} \mathcal{G}(\beta_m). \quad (8.7) \quad \text{[eq:LikelihoodNui]}$$

In Equation 8.7, we have introduced the assumption that the nuisance parameters are uncorrelated.

We wish to determine if the data is compatible with a new signal. To test for the presence of a bump, we examine the likelihood as a function of the signal cross-section. If the presence of a signal is unambiguous, one can simply determine the likelihood as a function of the cross-section. If the signal is known to be non-zero, confidence intervals about the maximum likelihood can be constructed by examining the change in the logarithm  $2\Delta \ln \mathcal{L}$  of the likelihood. The Frequentist interpretation of a confidence level  $1 - \alpha$  is that if the experiments were repeated  $N$  times, the interval corresponding to  $1 - \alpha$  would fail “cover” the *true* value of the observable in  $\alpha \times N$  of the experiments. The correspondence between confidence levels and intervals in  $2\Delta \ln \mathcal{L}$  is given in Table 8.2. Since the mass of a potential Higgs boson is unknown, we repeat this process for different signal masses. If there is not a significant signal, we can set upper bounds on the signal cross-section using one of several methods, which will be discussed below.

**Fixme:** Did I mix this up?

At this point, the likelihood still depends on the nuisance parameters. There are two methods of removing the dependence on the nuisance parameters, “marginalization” and “profiling.” Marginalization is the process of integrating the likelihood of Equation 8.7 over the entire range of all nuisance parameters. This effectively averages the effect of the different uncertainties into the marginalized likelihood function. The profiling method *maximizes* the likelihood in terms of the nuisance parameters. In the profiling method, the “profile likelihood” is created by maximizing the likelihood with respect to all of the nuisance parameters. One way to interpret the profiling method is that the values of nuisance parameters are being measured *in situ*, constrained by the observed data. While not a strictly Bayesian treatment, the profile likelihood method has been shown to give almost identical results to marginalization.

An interesting situation relating to the profiling of the nuisance parameters arises in this analysis in the context of the hadronic tau identification uncertainty. As discussed in Chapter 7, the Higgs–insensitive measurement of the tau identification efficiency has a high uncertainty of 30%. If the bump at the  $Z \rightarrow \tau^+ \tau^-$  resonance can be considered to Higgs free, the tau identification efficiency can be measured to a much greater precision, approximately 7% [52, 47]. When profiling the likelihood (as a function of cross section) for a Higgs with a mass  $m_{A^0} > m_Z$ , the likelihood contains the information that no Higgs contribution to the  $Z$  resonance is possible. This fact enables the profiling process to constrain the systematic uncertainty on the tau identification efficiency to the 7% level using the size of the  $Z$  resonance. Conversely, when the likelihood is evaluating the likelihood of the presence of a Higgs signal with  $m_{A^0} = m_Z$ , the likelihood cannot distinguish between a potential presence of Higgs events in the  $Z$  bump or a systematic undershoot of the tau identification efficiency in the simulation. In this case the profiling processing has no power to constrain the systematic to a value lower than the initial 30% value.

In the absence of the signal, or even in the presence of one, we can determine a upper 95% CL bound on the cross-section of the signal using the profile likelihood. In one method we simply use Bayes’ Theorem to convert the likelihood to a posterior density in the signal cross-section, and integrate to find the point below which 95% of the probability lies. The

Bayesian posterior PDF is computed as

$$\mathcal{P}(\sigma_H | \bar{x}, m_H) = \frac{\mathcal{L}(\bar{x} | \sigma_H m_H) \mathcal{P}(\sigma_H)}{\int \mathcal{L}(\bar{x} | \sigma'_H m_H) \mathcal{P}(\sigma'_H) d\sigma'_H}. \quad (8.8)$$

2239 The left hand side of Equation 8.8 represents the probability density for a given signal cross  
 2240 section, given the observed data  $\bar{x}$  and the assumed value  $m_H$  for the Higgs mass. We refer  
 2241 to this method as the “Bayesian” method of setting limits.

2242 In the other method, which is referred to as the “Delta Log Likelihood” (DLL) method,  
 2243 we compute two likelihoods. The first likelihood is computed for the “null hypothesis” case.  
 2244 The likelihood is profiled (maximized) assuming that no signal is present. We then construct  
 2245 the profile likelihood for increasing values of the signal yield. The upper limit is achieved  
 2246 when the logarithm of the profile likelihood is 1.92 units less than the value of the null  
 2247 hypothesis profile likelihood.

2248 In general the limits computed by the Bayesian and DLL methods are similar. However,  
 2249 the effect of upward or downward statistical fluctuations in the observed data affect the two  
 2250 methods in different ways. When the data fluctuates low, the DLL method will produce  
 2251 a more stringent limit than the DLL method. When the data fluctuates high, creating an  
 2252 apparent signal, the Bayesian method will (correctly) set a more stringent limit. In this  
 2253 thesis we report the results of both methods.

2254 In the results presented below we use nuisance parameters corresponding to the sys-  
 2255 tematic errors summarized in Table 8.3.

**Fixme:** Get

MET scale

Source	Method	Magnitude
Muon ID/trigger	Multiplicative	20%
$Z$ cross section	Multiplicative	5%
Jet to $\tau$ fake rate	Multiplicative	20%
$\mu \rightarrow \tau$ fake rate	Multiplicative	100%
$W$ +jets cross section	Multiplicative	10%
$t\bar{t}$ cross section	Multiplicative	40%
integrated luminosity	Multiplicative	10%
Tau energy scale	Morphing	2%
Missing $E_T$ scale	Morphing	XX%
Muon $p_T$ scale	Morphing	neg.
EM energy scale	Morphing	neg.

Table 8.3: Summary of systematic uncertainties represented by nuisance parameters in the likelihood, their representation method and magnitudes.  
 (tab-sys)

2256

## Chapter 9

---

2257

# Results

(ch:results)

## 2258 §9.1 Selected Events

2259 In the  $36 \text{ pb}^{-1}$  of 7 TeV data collected by CMS in 2010, the analysis selection criteria  
 2260 described in Chapter 5 selects a total of 573 events. The expected yields from each of  
 2261 the background sources, computed by the Template method (Section 6.3) and verified by  
 2262 the Fake-rate method (Section 6.2) are shown in Table 9.1. The total expectation from the  
 2263 Standard Model background is 577. The data agrees extremely well with the SM background  
 2264 expectation considering the expected statistical variance of the observed data (24 events), as  
 2265 well as the uncertainty on the integrated luminosity<sup>1</sup> and the tau identification uncertainty.

2266

2267 The distributions of the visible mass and SVfit mass in the final selected events are  
 2268 shown in Figure 9.3. Excellent agreement is seen between the shapes of the distributions. The  
 2269  $p_T$  spectrum of the transverse momentum are sensitive to mis-modeling of the kinematics  
 2270 and composition of the various background sources. Control plots showing the transverse  
 2271 momenta of the muon and visible hadronic tau in the final analysis selection are shown  
 2272 in Figure 9.1. The  $\eta$  and  $\phi$  distributions of the muon and tau objects are sensitive to  
 2273 detector effects, and the presence of cosmic muons. For example, muons from cosmic events  
 2274 will preferentially be produced in the  $\phi = 0$  direction. Spurious candidates resulting from  
 2275 poorly model noise in one of the CMS subdetectors will in general be localized in  $\eta - \phi$ . The  
 2276  $\eta$  and  $\phi$  distributions of the muon and tau candidates are shown in Figure 9.2 and show  
 2277 excellent agreement.

---

<sup>1</sup>The uncertainty on the CMS luminosity measurement was 11% at the time this analysis was performed. The measurement was later improved, and at the time of this writing the uncertainty on CMS 2010 integrated luminosity is 4% [61]. The improved luminosity measurement is not expected to change the results of this analysis significantly.

Process	Events in 36 pb <sup>-1</sup>
$t\bar{t} + \text{jets}$	6.6
$W + \text{jets}$	25.6
$Z \rightarrow \mu^+ \mu^-$	10.6
QCD	166.2
$Z \rightarrow \tau^+ \tau^-$	368.1
Standard Model sum	577.1
Data	573

Table 9.1: Number of Higgs  $\rightarrow \tau^+ \tau^- \rightarrow \mu + \tau_{had}$  candidate events passing the selection criteria described in Chapter 5.

ResultsLooseAHtoMuTau)

2278        The expected yields from an MSSM Higgs boson signal for  $\tan \beta = 30^2$  are summarized  
 resultsLooseAHtoMuTau)?  
 2279        in . The contributions from the gluon fusion production mode and the associated  $b$ -quark  
 2280        production modes are given separately. The yields are divided into the exclusive categories of  
 2281        events containing a  $b$ -tagged jet and those without. For a Higgs mass of  $m_{A^0} = 160$  GeV/c<sup>2</sup>,  
 2282        a total of 17 events are expected at  $\tan \beta = 30$ .

**Fixme:**

*Get cite*

## 2283        §9.2 Limits on Higgs Production

2284        We compute upper limits on the cross section times the branching ratio using the Bayesian  
 ?(sec:statmethod)?  
 2285        method described in Section . We compute an expected limit in the same manner as an  
 2286        observed limit, but with simulated data generated in “toy” experiments. A large number  
 2287        of pseudo-data sets are generated using the null hypothesis templates using Monte Carlo  
 2288        techniques. The pseudo-data sets are expected to have the same statistical sensitivity as  
 2289        the observed dataset. The upper limits are then computed using the pseudo-data. The  
 2290        process is repeated many times, and the spread of the obtained upper limits determines  
 2291        the expected upper limit band. The expected nominal upper limit, and the  $\pm 1$ , and  $\pm 2$   
 2292        confidence limits are shown in Table 9.3. The observed limit on the MSSM computed from  
 2293        the 413 events selected in this analysis is given in the right column of Table 9.3. The

**Fixme:** at  
*what value of  
 the nuisance?*

---

<sup>2</sup>Details of the relationship between the MSSM Higgs cross section and  $\tan \beta$  are discussed in detail in Section 9.3.

observed limit is compatible with the expected limit, within 1.5 standard deviations. The trend of the expected and observed limits versus the Higgs mass using both observables are shown in Figure 9.4. The use of the SVfit reconstructed mass as the observable increases the power of the limit significantly. The limit trend has some interesting features. When the Higgs mass is close to the mass of the  $Z$  resonance, the analysis have little power to set a limit on the presence of the Higgs. This is due to the large uncertainty on the tau identification efficiency. Essentially, when  $m_{A^0} = m_Z$ , the Higgs yield in the  $Z$  bump would have be larger than 30% of the  $Z \rightarrow \tau^+\tau^-$  yield for the profile likelihood to be able to recognize an excess of events. Below this value, the profile likelihood can simple shift the tau identification efficiency scale factor up by 30% and “eat” any potential excess of signal.

### §9.3 Interpretation in the MSSM

`(sec:MSSMInterp)` The limits on the cross section times branching ratio are roughly model independent,<sup>3</sup> and could be applied to set limits on the parameter space of a number of models. In this thesis, we interpret the results in the context of the MSSM. Specifically, we exclude a region in the  $\tan\beta - m_{A^0}$  parameters space of the MSSM. To find the upper limit band on  $\tan\beta$ , we find the minimum value of  $\tan\beta$  which provides the cross section and branching ratio product found in the corresponding row in Table 9.3.

The mapping between  $m_{A^0}$  and  $\tan\beta$  and the Higgs cross section is provided by the LHC Higgs Cross Section working group . The cross sections and branching ratios have been computed for the  $h^0$ ,  $H^0$ , and  $A^0$  MSSM Higgs states in both the  $ggA$  and  $qqA$  production modes, for a grid of points in  $\tan\beta - m_{A^0}$  space. In order to combine the  $ggA$  and  $qqA$  production modes, what we call our signal cross-section is the sum of the cross-section times branching ratio for both modes, assuming  $\tan\beta = 30$ . Additionally, as discussed in Section 1.2.3, the MSSM Higgs sector consists of two Higgs doublets, yielding five physical Higgs bosons. This search is sensitive to the three neutral Higgs particles the  $h^0, H^0$ , and  $A^0$ . The relative contributions of the three Higgs types depends on the mass

**Fixme:**  
get ref

---

<sup>3</sup>This assumption is only valid if the shape of the sum of all new physics contributions are also model independent, on the scale of the experimental resolution. For the values of  $\tan\beta$  this analysis is sensitive to, this is a valid approximation in the MSSM. In a model where the width of the Higgs boson resonance was larger than the resolution of the SVfit method, the limits of Table 9.3 would not be valid.

2320  $m_{A^0}$  of the CP-odd Higgs. An observed signal will have contributions from at least two  
 2321 Higgs states. For  $m_{A^0} \leq 130$  GeV/ $c^2$ , the  $A^0$  and  $h^0$  are approximately degenerate in mass  
 2322 and width. In this region the  $H^0$  has a very small relative cross section and a constant  
 2323 mass of  $m_{H^0} \approx 130$  GeV/ $c^2$ . For  $m_{A^0} \geq 130$  GeV/ $c^2$ , the  $h_0$  reaches a limiting mass of  
 2324  $\approx 130$  GeV/ $c^2$ , and the  $H^0$  and  $A^0$  become mass degenerate.

2325 The region in  $\tan\beta - m_{A^0}$  MSSM parameter space excluded by this analysis at 95%  
 2326 CL is shown in Figure 9.3. The limit is compared to the combined result from Run II of  
 2327 the Tevatron (this result is discussed in detail in Section 1.3.3). The result of this analysis  
 2328 sets a stronger limit than the Tevatron for large values of  $m_{A^0}$ . In the low  $m_{A^0}$  region, the  
 2329 analysis suffers due to the large tau identification efficiency uncertainty. This effect can be  
 2330 mitigated by using the  $e - \mu$  channel. The combined CMS result uses this approach, and  
 2331 will be discussed briefly in the conclusion.

**Fixme:**

check this!

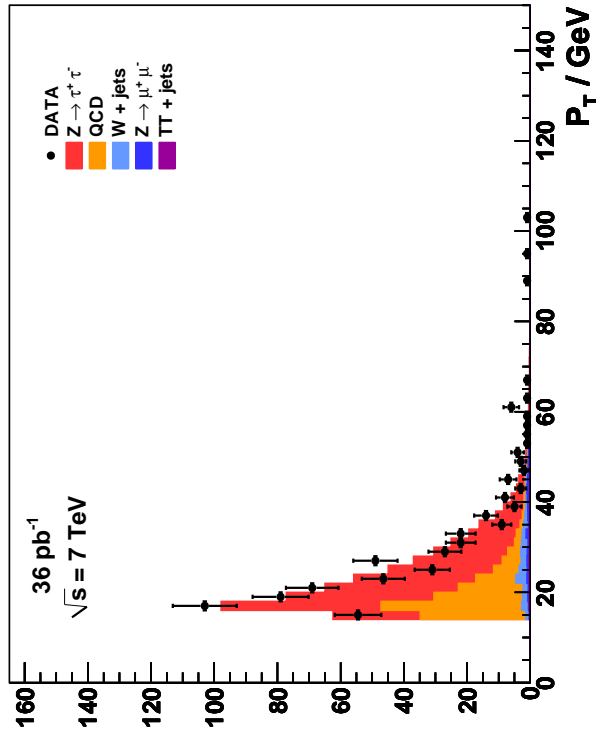
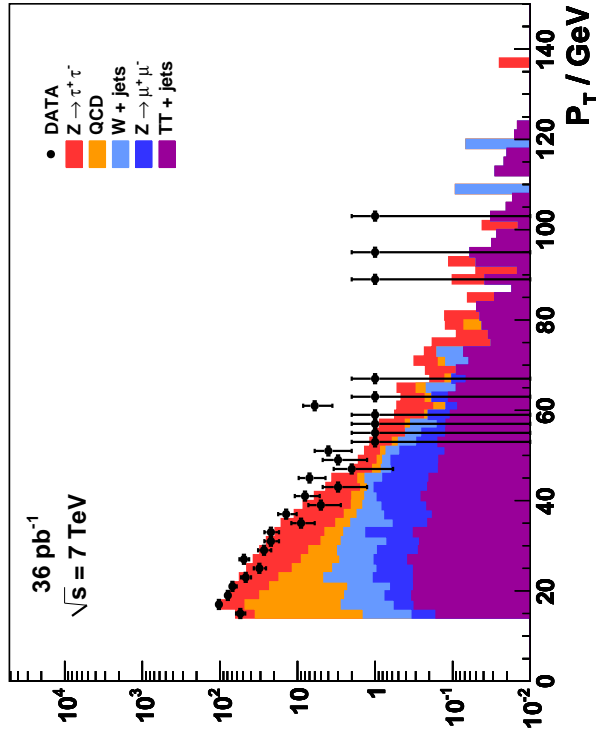
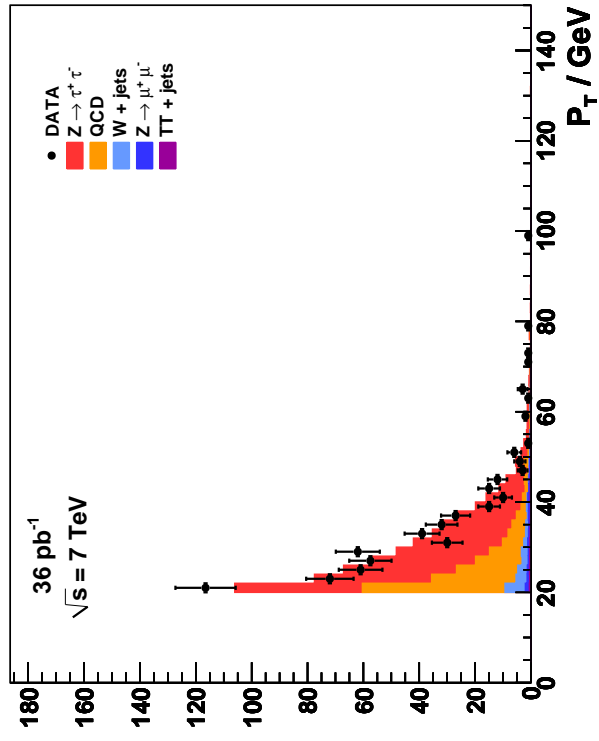
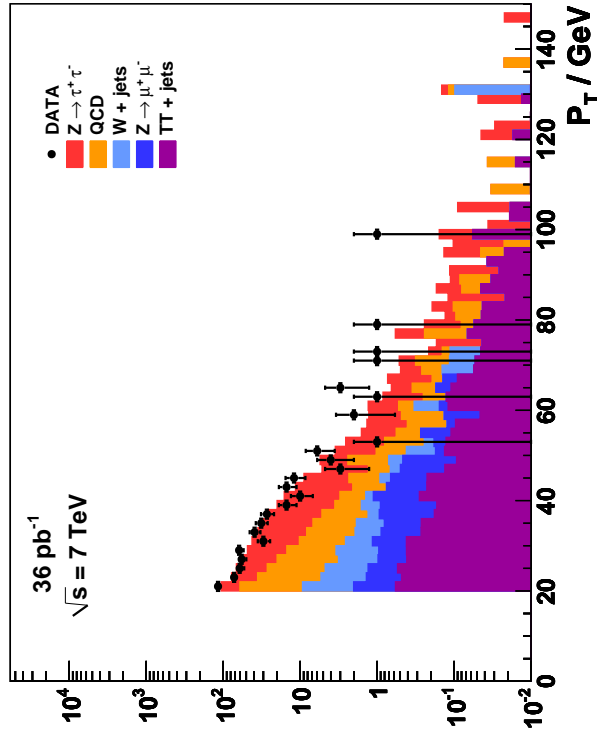
**Muon (final event sample)****Muon (final event sample)****Tau (final event sample)****Tau (final event sample)**

Figure 9.1: Distribution of the transverse momentum of the muon (top) and hadronic tau in  $Higgs \rightarrow \tau^+ \tau^- \rightarrow \mu + \tau_{had}$  candidate events passing the selection criteria described in Chapter 5. The distributions are shown in linear (logarithmic) scale on the left (right).  
finalControlPlots

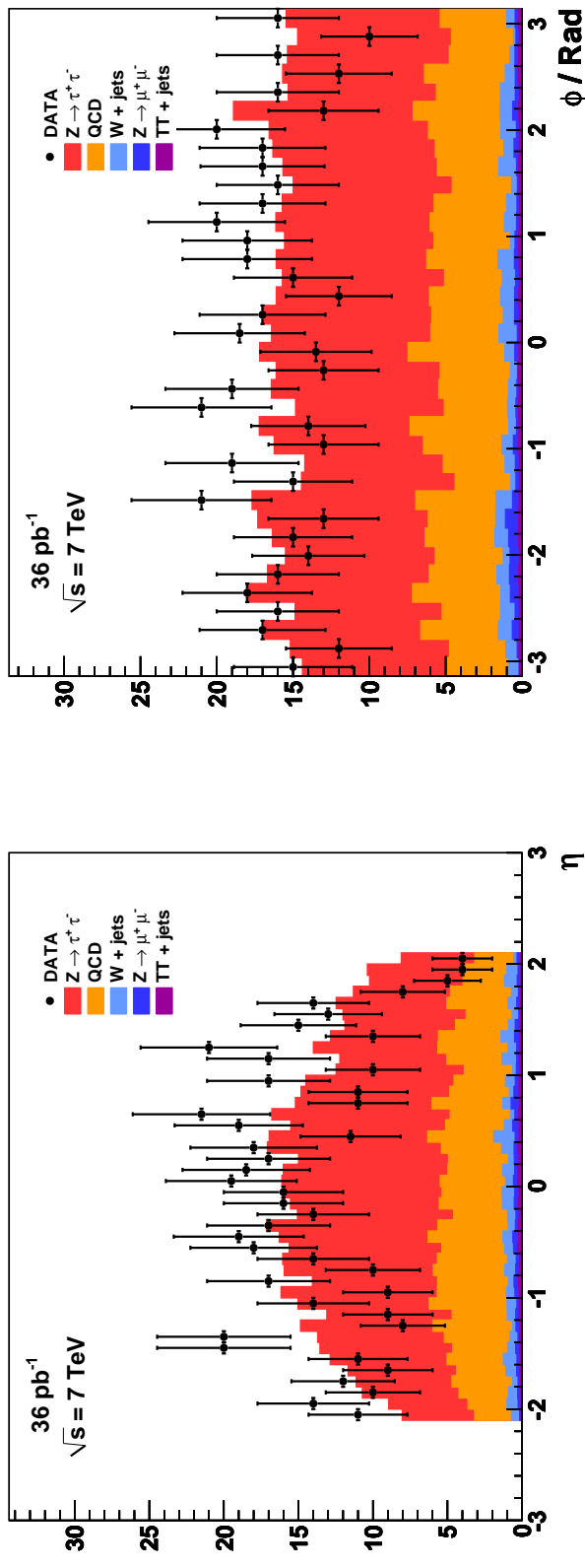
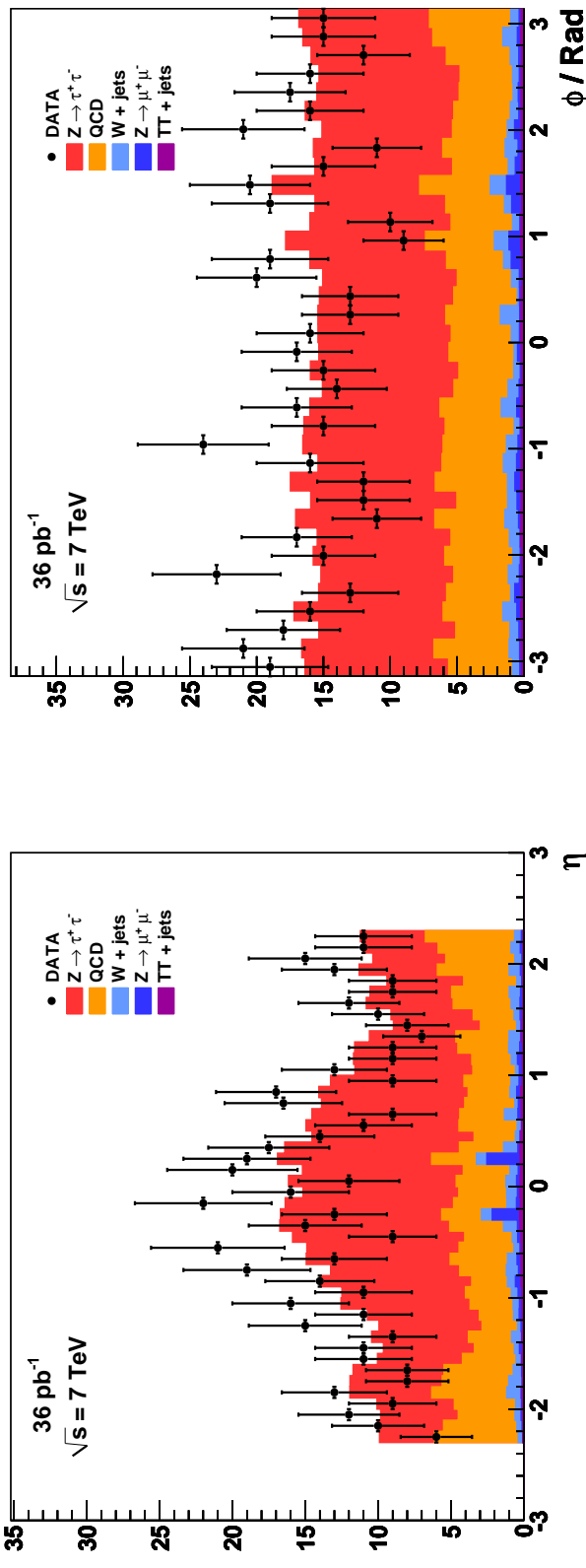
**Muon (final event sample)****Tau (final event sample)**

Figure 9.2: Distribution of the  $\eta$  (left) and  $\phi$  (right) of the muon (top) and hadronic tau (bottom) in Higgs  $\rightarrow \tau^+\tau^- \rightarrow \mu + \tau_{had}$  candidate events passing the selection criteria described in Chapter 5.

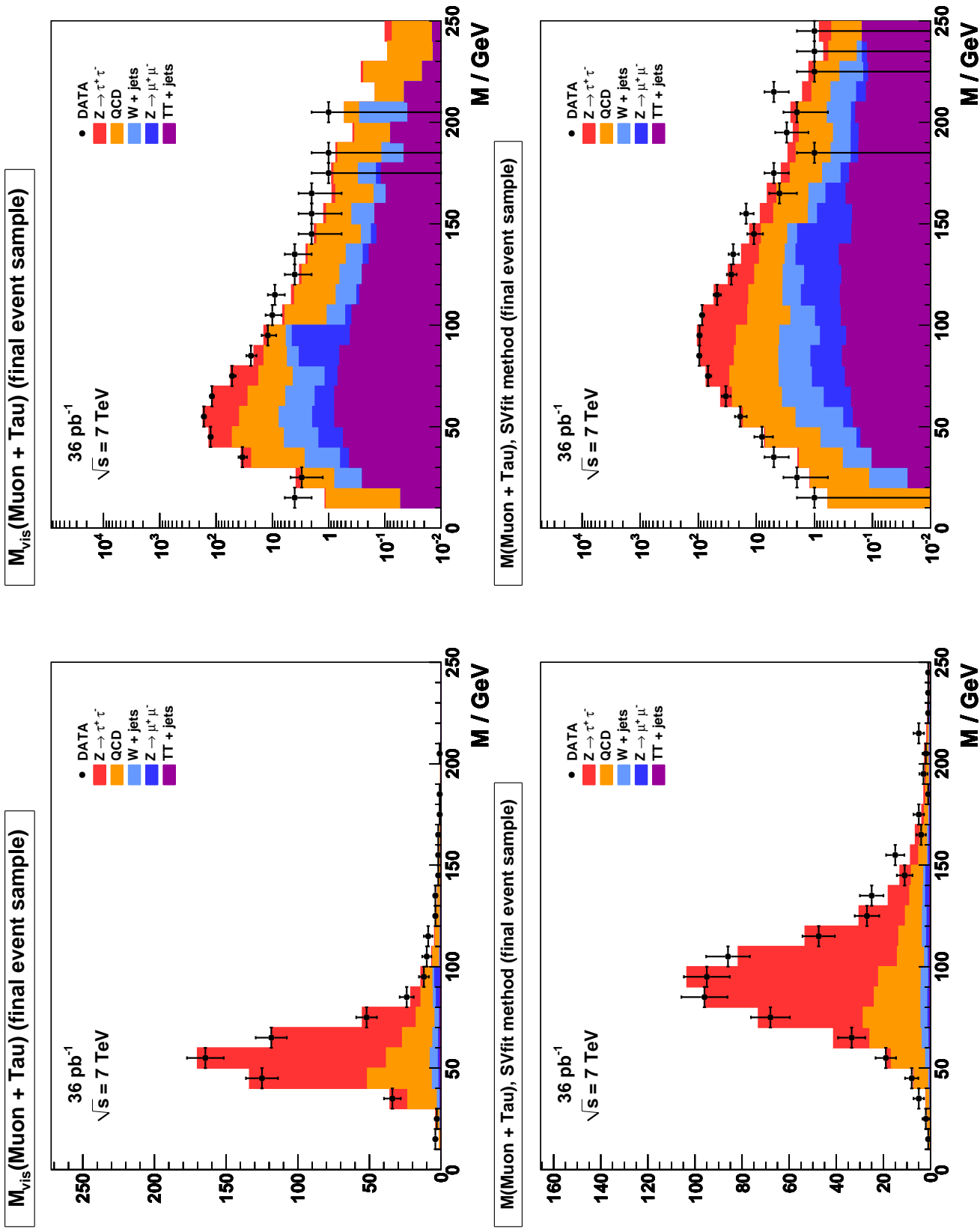


Figure 9.3: Distribution of visible (top) and “full”  $\tau^+\tau^-$  invariant mass reconstructed by the SVfit algorithm (bottom) in  $Higgs \rightarrow \tau^+\tau^- \rightarrow \mu + \tau_{had}$  candidate events passing the selection criteria described in Chapter 5. The distributions are shown in linear (logarithmic) scale on the left (right).

Process	Events without $b$ -tag	Events with $b$ -tag
Gluon fusion production		
A90	37.21	0.86
A100	27.40	0.40
A120	14.39	0.14
A130	11.81	0.18
A160	4.46	0.09
A200	1.51	0.03
A250	0.47	0.01
A300	0.15	0.0
A350	0.06	0.44
Associated $b$ -quark production		
bbA90	33.07	5.50
bbA100	30.18	4.77
bbA120	21.91	4.02
bbA130	18.34	3.35
bbA160	10.35	2.10
bbA200	4.85	1.29
bbA250	2.11	0.55
bbA300	0.97	0.26
bbA350	0.41	0.13

Table 9.2: Number of Higgs signal event expected to pass the selection criteria described in Section 5. The expected signal yield is given for MSSM parameter  $\tan \beta = 30$ , using the cross sections provided by the LHC Higgs Cross Section working group.

resultsLooseAHtoMuTau)?

Secondary Vertex Fit Limit						
Mass	$-2\sigma$	$-1\sigma$	Median	$+1\sigma$	$+2\sigma$	Observed
90	329.2	429.2	621.9	862.9	999.1	394.7
120	30.1	41.6	59.8	82.0	116.6	86.5
130	20.7	27.6	40.5	55.6	79.4	59.9
160	10.3	13.2	19.0	26.2	35.8	28.3
200	6.3	8.3	11.2	15.8	20.2	16.4
250	4.0	5.6	7.6	10.6	14.5	12.9
300	2.9	4.0	5.7	7.8	11.1	9.4
Visible Mass Limit						
Mass	$-2\sigma$	$-1\sigma$	Median	$+1\sigma$	$+2\sigma$	Observed
90	376.2	523.3	688.2	980.9	998.8	573.8
120	37.0	52.1	75.4	109.2	164.1	82.6
130	26.2	35.9	52.2	74.6	117.5	64.2
160	14.3	18.3	25.1	35.2	55.1	41.2
200	8.9	11.9	16.6	22.4	32.8	31.1
250	5.9	8.1	11.5	15.9	22.3	18.1
300	4.2	5.8	8.4	11.7	15.9	10.8

Table 9.3: Expected 95% CL upper limit bands and the observed limit using the Bayesian prescription. The limit is computed using both the SVfit mass (top) as well as the visible mass (bottom) as the search observable. Use of the SVfit mass significantly improves the strength of the limit considerably.

(tab-exp-limit-TaNC)

Higgs State	Included when		
	$m_{A^0} < 130 \text{ GeV}/c^2$	$m_{A^0} = 130 \text{ GeV}/c^2$	$m_{A^0} > 130 \text{ GeV}/c^2$
$A^0$	yes	yes	yes
$H^0$	yes	yes	no
$h^0$	no	yes	yes

Table 9.4: Logic for determining the MSSM Higgs cross section for a given mass of the CP-odd  $A^0$  Higgs. In some regions of parameter space, the contributions of one of the CP-even Higgs particles is ignored.

(gsXSectionCombination)?

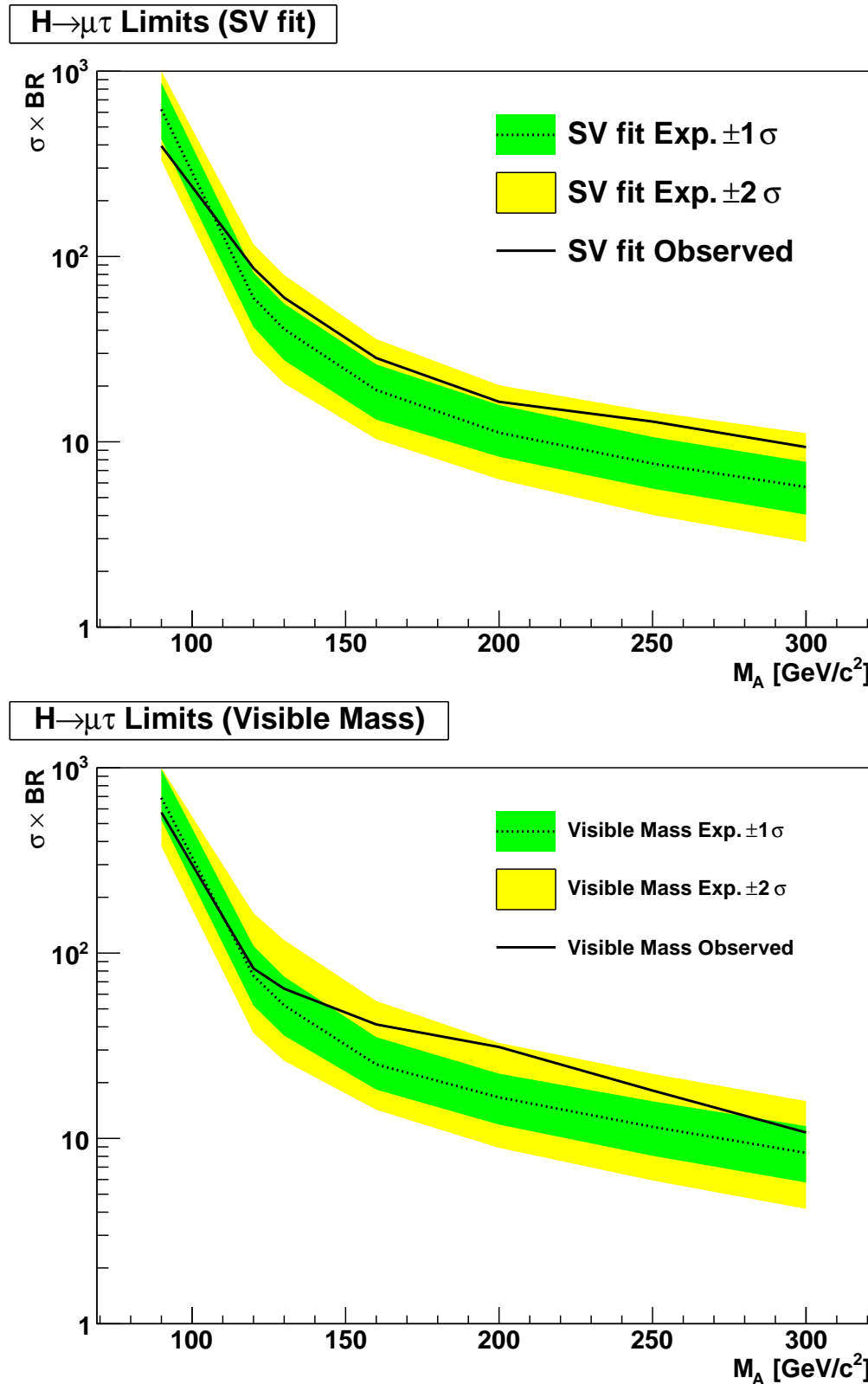


Figure 9.4: Observed and expected limits on the cross section times branching ratio of a Higgs boson versus Higgs mass. The top plot gives the limit computed using the SVfit mass as the observable, the bottom plot gives the limit computed using the visible mass. The dashed line gives the nominal expected limit. The green and yellow bands give the  $+1$  and  $+2$  standard deviations on the expected limit.

(fig:SVXSecLimits)

{fig:TanBetaLimit}

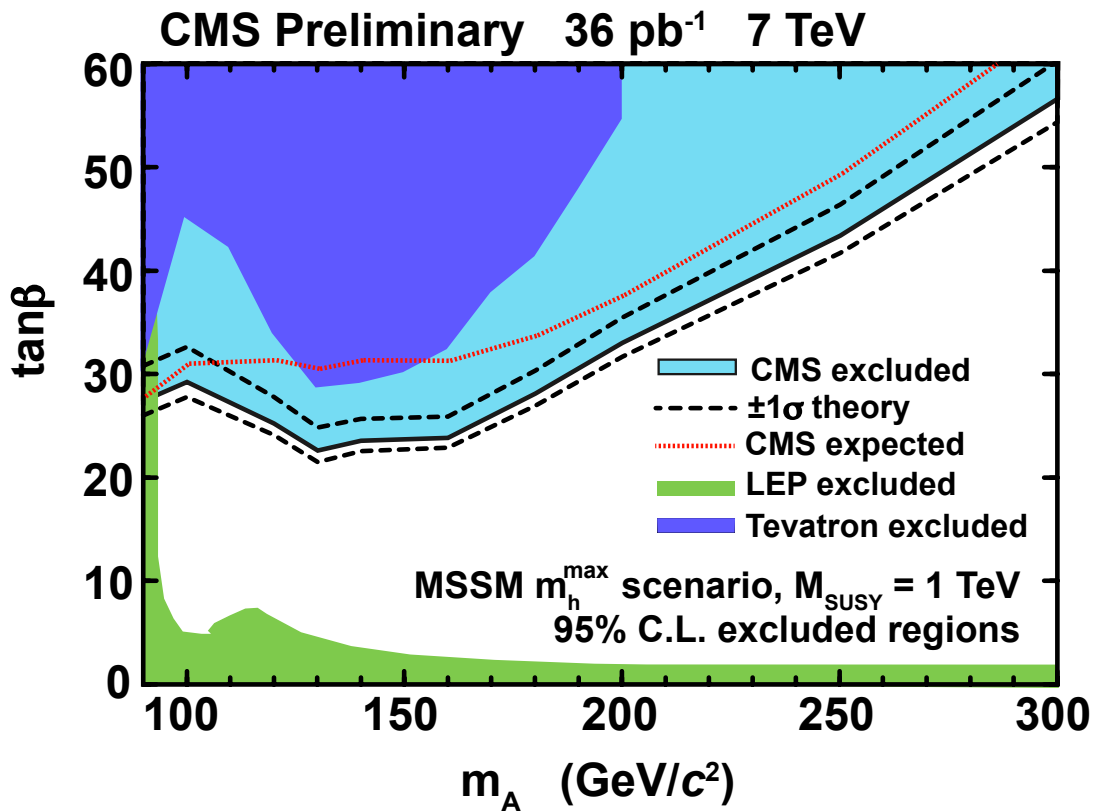
Figure 9.5: Region of MSSM  $\tan \beta - m_{A^0}$  parameter space excluded by this analysis.

---

## 2332 Conclusions

?<ch:conclusions>?  
 2333 This analysis has presented a search for MSSM Higgs bosons in the 2010 7 TeV CMS data  
 2334 set. Two new experimental methods, the TaNC tau identification algorithm, and the SVfit  
 2335 mass reconstruction method have been introduced in this thesis. Both methods increased  
 2336 the sensitive of the Higgs search. The search was performed using  $36 \text{ pb}^{-1}$  of data. The  
 2337 expected event yield from Standard Model sources is 577 events. In total, 573 events were  
 2338 selected; the observed is compatible with the Standard Model. No signal-like excess of  
 2339 events is observed. We set an upper limit on the production of Higgs bosons, and interpret  
 2340 this limit in the context of the MSSM.

2341 The analysis presented in this thesis was part of a larger study [1] performed by the  
 2342 CMS collaboration searching for the MSSM Higgs boson decaying to tau leptons. The CMS  
 2343 analysis used three channels, the  $H \rightarrow \tau\tau \rightarrow e - \tau_h$ ,  $H \rightarrow \tau\tau \rightarrow e - \mu$ , and the  $\mu - \tau_h$   
 2344 channel. The  $\mu - \tau_h$  channel search presented in this thesis is very similar to the CMS result.  
 2345 While not as pure as the  $\mu - \tau$  channel, the inclusion of the high-statistics  $e - \tau$  channel  
 2346 increases the sensitivity of the CMS analysis. The  $e - \mu$  channel has low statistics, but is  
 2347 not sensitive to the systematic uncertainty on the hadronic tau identification. The region of  
 2348 the MSSM parameter space excluded by combined CMS result is illustrated in Figure 9.3.  
 2349 At the time of this writing, the CMS result described in [1] sets the most stringent limits  
 2350 on the MSSM using a direct search.



ig:CMSTanBetaExclusion)

Figure 9.6: Region of MSSM  $\tan \beta - m_{A^0}$  parameter space excluded by the CMS combined analysis [1].

---

## 2351 Bibliography

- [HIG-200902] [1] CMS Collaboration, “Search For Neutral MSSM Higgs Boson Production via Decays to Tau Pairs in  $pp$  Collisions at  $\sqrt{s} = 7$  TeV”, *to be published* (2011).
- [Goldstone:1961eq] [2] J. Goldstone, “Field Theories with Superconductor Solutions”, *Nuovo Cim.* **19** (1961) 154–164. doi:10.1007/BF02812722.
- [PhysRev.127.965] [3] J. Goldstone, A. Salam, and S. Weinberg, “Broken Symmetries”, *Phys. Rev.* **127** (Aug, 1962) 965–970. doi:10.1103/PhysRev.127.965.
- [PhysRevLett.13.321] [4] F. Englert and R. Brout, “Broken Symmetry and the Mass of Gauge Vector Mesons”, *Phys. Rev. Lett.* **13** (Aug, 1964) 321–323. doi:10.1103/PhysRevLett.13.321.
- [PhysRevLett.13.508] [5] P. W. Higgs, “Broken Symmetries and the Masses of Gauge Bosons”, *Phys. Rev. Lett.* **13** (Oct, 1964) 508–509. doi:10.1103/PhysRevLett.13.508.
- [PhysRevLett.13.585] [6] G. S. Guralnik, C. R. Hagen, and T. W. B. Kibble, “Global Conservation Laws and Massless Particles”, *Phys. Rev. Lett.* **13** (Nov, 1964) 585–587. doi:10.1103/PhysRevLett.13.585.
- [Glashow:1961tr] [7] S. Glashow, “Partial Symmetries of Weak Interactions”, *Nucl.Phys.* **22** (1961) 579–588. doi:10.1016/0029-5582(61)90469-2.
- [Weinberg:1967tq] [8] S. Weinberg, “A Model of Leptons”, *Phys.Rev.Lett.* **19** (1967) 1264–1266. doi:10.1103/PhysRevLett.19.1264.
- [Salam:1968rm] [9] A. Salam, “Weak and Electromagnetic Interactions”, Originally printed in \*Svartholm: Elementary Particle Theory, Proceedings Of The Nobel Symposium Held 1968 At Lerum, Sweden\*, Stockholm 1968, 367–377.
- [Griffiths:IntroPartikel] [10] D. Griffiths, “Introduction to Elementary Particles”. Wiley-VCH, 2004.
- [Morii:SMandBSM] [11] S. M. T. Morii, C.S. Lim, “The Physics of the Standard Model and Beyond”. World Scientific, 2004.
- [UA1WDiscovery] [12] UA1 Collaboration, “Experimental observation of isolated large transverse energy electrons with associated missing energy at  $\sqrt{s} = 540$  GeV”, *Phys. Lett.* **B122** (1983) 103–116.
- [UA2WDiscovery] [13] UA2 Collaboration, “Observation of single isolated electrons of high transverse momentum in events with missing transverse energy at the CERN  $\bar{p}p$  collider”, *Phys. Lett.* **B122** (1983) 476–485. doi:10.1016/0370-2693(83)91605-2.

- UA1ZDiscovery** [14] UA1 Collaboration, “Experimental observation of lepton pairs of invariant mass around 95  $\text{GeV}/c^2$  at the CERN SPS collider”, *Phys. Lett.* **B126** (1983) 398–410.  
2383  
2384 doi:10.1016/0370-2693(83)90188-0.
- UA2ZDiscovery** [15] UA2 Collaboration, “Evidence for  $Z^0 \rightarrow e^+e^-$  at the CERN  $\bar{p}p$  collider”, *Phys. Lett.* **B129** (1983) 130–140. doi:10.1016/0370-2693(83)90744-X.  
2386
- Martin:1995zma** [16] S. P. Martin, “A Supersymmetry Primer”, *arXiv hep-ph* (sep, 1997). 128 pages.  
2388 Version 5 (December 2008) contains a change in convention that flips the signs of  
2389 sigma and sigmabar matrices. It also contains a total of about 2 pages of updates,  
2390 mostly on supersymmetry breaking issues. Errata and a version with larger type (12  
2391 pt, 142 pages) can be found at <http://zippy.physics.niu.edu/primer.html>.
- FeynmanDiag** [17] CERN Computing Newsletter.
- Rainwater:1998kj** [18] D. L. Rainwater, D. Zeppenfeld, and K. Hagiwara, “Searching for  $H \rightarrow \tau^+\tau^-$  in weak boson fusion at the LHC”, *Phys. Rev.* **D59** (1999) 014037, arXiv:hep-ph/9808468. doi:10.1103/PhysRevD.59.014037.  
2394  
2395
- PDG** [19] Particle Data Group Collaboration, “Review of particle physics”, *J. Phys.* **G37** (2010) 075021. doi:10.1088/0954-3899/37/7A/075021.  
2397
- MSTWXSection** [20]
- LHCHiggsXSecGroup** [21] LHC Higgs Cross Section Working Group Collaboration, “Handbook of LHC Higgs Cross Sections: 1. Inclusive Observables”, arXiv:1101.0593.  
2400
- MHMaxBenchmark** [22] M. Carena, S. Heinemeyer, C. Wagner et al., “MSSM Higgs boson searches at the Tevatron and the LHC: Impact of different benchmark scenarios”, *The European Physical Journal C - Particles and Fields* **45** (2006) 797–814. 10.1140/epjc/s2005-02470-y.  
2402  
2403  
2404
- CMSExperiment** [23] CMS Collaboration, “The CMS experiment at the CERN LHC”, *JINST* **3** (2008) S08004.  
2406
- CMS-PAS-TRK-10-004** [24] CMS Collaboration, “Measurement of Momentum Scale and Resolution using Low-mass Resonances and Cosmic-Ray Muons”, *CMS PAS CMS-PAS-TRK-10-004* (2010).  
2408  
2409
- CMS-PAS-TRK-10-005** [25] CMS Collaboration, “Tracking and Primary Vertex Results in First 7 TeV Collisions”, *CMS PAS CMS-PAS-TRK-10-005* (2010).  
2411
- CMS-PTDR** [26] G. L. Bayatian et al., “CMS Physics Technical Design Report Volume I: Detector Performance and Software”. Technical Design Report CMS. CERN, Geneva, 2006.  
2413
- CMS-PAS-PFT-08-001** [27] CMS Collaboration, “CMS Strategies for tau reconstruction and identification using particle-flow techniques”, *CMS PAS CMS-PAS-PFT-08-001* (2008).  
2415
- CMS-PAS-PFT-09-001** [28] CMS Collaboration, “Particle-Flow Event Reconstruction in CMS and Performance for Jets, Taus, and MET”, *CMS PAS CMS-PAS-PFT-09-001* (2009).  
2417

- [TMVA]** [29] A. Hoecker, P. Speckmayer, J. Stelzer et al., “TMVA - Toolkit for Multivariate Data Analysis”, *arXiv physics.data-an* (mar, 2007). Published in: PoSACAT:040,2007  
2419 TMVA-v4 Users Guide: 135 pages, 19 figures, numerous code examples and refer-  
2420 ences.  
2421
- [Kolmogorov]** [30] A. Kolmogorov, “On the representation of continuous functions of several variables by superposition of continuous functions of one variable and addition”, *Doklady Akademii Nauk SSSR* **114** (1957).  
2423  
2424
- [DavisTau]** [31] J. C. *et al.*, “Size of signal cones and isolation rings in the CMS tau identification algorithm”, *CMS Note* **2008/026** (2008).  
2426
- [CMS-AN-2010-082]** [32] M. Bachtis, S. Dasu, and A. Savin, “Prospects for measurement of  $\sigma(pp \rightarrow Z) \cdot B(Z \rightarrow \tau^+\tau^-)$  with CMS in pp Collisions at  $\sqrt{s} = 7$  TeV”, *CMS Note* **2010/082** (2010).  
2428  
2429
- [CMS-PAS-PFT-10-004]** [33] CMS Collaboration, “Study of tau reconstruction algorithms using  $pp$  collisions data collected at  $\sqrt{s} = 7$  TeV”, *CMS PAS CMS-PAS-PFT-10-004* (2010).  
2431
- [Antikt]** [34] G. P. S. M. Cacciari and G. Soyez, “The anti-kt jet clustering algorithm”, *JHEP* **04** (2008) 063, arXiv:0802.1189.  
2433
- [CMS-PAS-PFT-10-002]** [35] CMS Collaboration, “Commissioning of the Particle–Flow reconstruction in Minimum–Bias and Jet Events from  $pp$  Collisions at 7 TeV”, *CMS PAS PFT-10-002* (2010).  
2435  
2436
- [pythia6.4]** [36] S. M. T. Sjöstrand and P. Skands, “PYTHIA 6.4 Physics and Manual”, 2000.
- [taula]** [37] S. Jadach, Z. Was, R. Decker et al., “The Tau Decay Library Tauola: Version 2.4”, *Comput. Phys. Commun.* **76** (1993) 361.  
2439
- [geant]** [38] S. Agostinelli, J. Allison, K. Amako et al., “G4—a simulation toolkit”, *Nuclear Instruments and Methods in Physics Research Section A: Accelerators, Spectrometers, Detectors and Associated Equipment* **506** (2003), no. 3, 250 – 303.  
2441  
2442  
2443 doi:10.1016/S0168-9002(03)01368-8.
- [CMS-AN-2010-099]** [39] J. Conway, E. Friis, M. Squires et al., “The Tau Neural Classifier algorithm: tau identification and decay mode reconstruction using neural networks”, *CMS Note* **2010/099** (2010).  
2445  
2446
- [CDFMSSMHiggs]** [40] CDF Collaboration, “Search for MSSM Higgs decaying to  $\tau$  pairs in  $p\bar{p}$  collision at  $\sqrt{s} = 1.96$  TeV at CDF”, *Phys. Rev. Lett.* **96** (2006).  
2448
- [CMS-PTDRII]** [41] CMS Collaboration, “CMS technical design report, volume II: Physics performance”, *J. Phys.* **G34** (2007) 995–1579. doi:10.1088/0954-3899/34/6/S01.
- [improvedCollinearApprox]** [42] L. Bianchini, “Improved Collinear Approximation for VBF  $H \rightarrow \tau\tau \rightarrow 3\nu + \ell + \tau_{had}$ ”, *CMS Note* **2010/226** (2010).  
2452
- [tauDecayPolarization]** [43] B. K. Bullock, K. Hagiwara, and A. D. Martin, “Tau Polarization And Its Correlations As A Probe Of New Physics”, *Nucl. Phys.* **B 395** (1993) 499.  
2454
- [CMS-PAS-EWK-10-002]** [44] CMS Collaboration, “Measurements of Inclusive W and Z Cross Sections in pp Collisions at  $\sqrt{s} = 7$  TeV”, *CMS PAS EWK-10-002* (2010).  
2456

- [CMS-PAS-JME-10-005] [45] CMS Collaboration, “MET Performance in Events Containing Electroweak Bosons from pp Collisions at  $\sqrt{s} = 7$  TeV”, *CMS PAS JME-10-005* (2010).
- 2458
- [CMS AN 2010-008] [46] L. Lusito and C. Veelken, “Estimation of Background contributions to Tau analyses via Template Fitting”, *CMS Note 2010/088* (2010).
- 2460
- [CMS-PAS-TAU-11-001] [47] CMS Collaboration, “Performance of tau reconstruction algorithms in 2010 data collected with CMS”, *CMS PAS TAU-11-001* (2011).
- 2462
- [CDFFakerateD~~2464~~] [48] D. Jang, “Search for MSSM Higgs decaying to  $\tau$  pairs in  $p\bar{p}$  collision at  $\sqrt{s} = 1.96$  TeV at CDF”, *Ph.D. Thesis, Rutgers University* (2006).
- 2464
- [CDFFakerateAlmenar] [49] C. C. Almenar, “Search for the neutral MSSM Higgs bosons in the  $\tau\tau$  decay channels at CDF Run II”, *Ph.D. Thesis, Universitat de Valencia* (2008).
- 2466
- [CMS AN 2011-021] [50] J. Conway, E. Friis, and C. Veelken, “Measurement of the  $Z/\gamma^* \rightarrow \tau^+\tau^-$  Production Cross-section in the  $\mu + \tau_{had}$  final state using the HPS+TaNC Tau id. algorithm”, *CMS Note 2011/021* (2011).
- 2468
- 2469
- [MCEmbedding] [51] T. Früboes and M. Zeise, “The TauAnalysis/MCEmbeddingTools Package”.  
<https://twiki.cern.ch/twiki/bin/view/CMS/SWGuideTauAnalysisMCEmbeddingTools>
- 2471
- [CMS-PAS-EWK-10-013] [52] CMS Collaboration, “Measurement of the Inclusive  $Z \rightarrow \tau\tau$  Cross Section in  $pp$  Collisions at  $\sqrt{s} = 7$  TeV”, *to be published* (2011).
- 2473
- [CMS AN 2010-059] [53] S. Bolognesi, M. A. Borgia, R. Castello et al., “Calibration of track momentum using dimuon resonances in CMS”, *CMS Note 2010/059* (2010).
- 2475
- [CMS-PAS-JME-10-010] [54] CMS Collaboration, “Jet Energy Corrections determination at  $\sqrt{s} = 7$  TeV”, *CMS PAS JME-10-010* (2010).
- 2477
- [CMS AN 2010-032] [55] G. Bauer et al., “Modeling of  $W \rightarrow \ell\nu$  MET with Boson Recoil”, *CMS Note 2010/332* (2010).
- 2479
- [CMS AN 2010-460] [56] G. Cerati et al., “Search for MSSM neutral Higgs  $\rightarrow \tau^+\tau^-$  Production using the TaNC Tau id. algorithm”, *CMS Note 2010/460* (2010).
- 2481
- [EWK pdfUncertainty~~2480~~] [57] J. Alcaraz. <https://twiki.cern.ch/twiki/bin/view/CMS/SWGuideEWKUtilities>.
- [CTEQpdf~~2481~~] [58] P. M. Nadolsky et al., “Implications of CTEQ global analysis for collider observables”, *Phys. Rev. D* **78** (2008) 013004, arXiv:0802.0007.
- 2484
- [pdfAccS~~2480~~] [59] PDF4LHC Working Group. <http://www.hep.ucl.ac.uk/pdf4lhc/PDF4LHCrecov.pdf>.
- [pdfAccS~~2480~~] [60] R. C. G. D. Bourilkov and M. R. Whalley, “LHAPDF: PDF use from the Tevatron to the LHC”, arXiv:0605.0240.
- 2487
- [LumiI] [61] CMS Collaboration, “Absolute luminosity normalization”, *CMS Detector Performance Summary CMS-DPS-2011-002* (2008).
- 2489